Unravelling Extracellular Matrix Impact on Retinal Pigment Epithelium Mechanical Homeostasis and Functionality: A Multidimensional Approach with Stem Cell-Derived Models

Von der Fakultät für Mathematik, Informatik und Naturwissenschaften der RWTH Aachen University zur Erlangung des akademischen Grades einer Doktorin der Naturwissenschaften genehmigte Dissertation

vorgelegt von

Aleksandra Kozyrina, M.Sc.

aus

Rewda, Oblast Swerdlowsk, Russische Föderation

Berichter: *Priv.-Doz. Dr. Jacopo Di Russo*

Univ.-Prof. Dr. med. Rudolf Leube

Univ.-Prof. Dr. rer. nat. Geraldine Zimmer-Bensch

Tag der mündlichen Prüfung: *19.11.2024*

“One of the basic rules of the universe is that nothing is perfect.
Perfection simply doesn't exist…

Without imperfection, neither you nor I would exist”

– *Stephen Hawking*

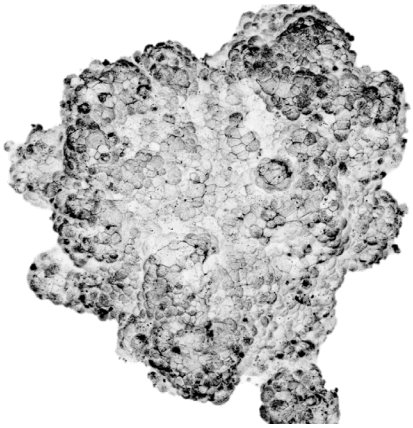

Table of content

Declaration of Authorship

Scientific contribution

Publications

Kozyrina AN, Piskova T, Doolaar I, Prapty T, Semeraro F, Yam L S, Haraszti T, Hubert M, Smith A-S, Di Russo J. *Laminin-defined Mechanical Status Modulates Retinal Pigment Epithelium Functionality.* Biorxiv, preprint, 2024.
https://doi.org/10.1101/2023.02.24.529913

Piskova T, **Kozyrina AN**, Di Russo J. *Mechanobiological implications of age-related remodelling in the outer retina.* Biomater Adv. 2023.
https://doi.org/10.1016/j.bioadv.2023.213343

Yoon S, Windoffer R, **Kozyrina AN**, Piskova T, Di Russo J, Leube RE. *Combining Image Restoration and Traction Force Microscopy to Study Extracellular Matrix-Dependent Keratin Filament Network Plasticity*. Front Cell Dev Biol. 2022.
https://doi.org/10.3389/fcell.2022.901038

Kozyrina AN, Piskova T, Di Russo J. *Mechanobiology of Epithelia From the Perspective of Extracellular Matrix Heterogeneity*. Front Bioeng Biotechnol. 2020.
https://doi.org/10.3389/fbioe.2020.596599

Conferences

Forces across scales, i3S, Porto, Portugal, 2024.
Kozyrina AN, Piskova T, Semeraro F, Doolaar I, Prapty T, Haraszti T, Hubert M, Windoffer R, Leube RE, Smith A, Di Russo J, *Laminin - induced mechanical homeostasis modulates retinal epithelium functionality.*

DGZ International meeting. Campus Saarbrücken Saarland University, Germany, 2023.
Kozyrina AN, Piskova T, Doolaar I, Prapty T, Semeraro F, Yam L S, Haraszti T, Hubert M, Smith A, Di Russo J, *Laminin alpha 5 - induced mechanical homeostasis modulates retinal epithelium functionality.*

4th International Symposium on Mechanobiology (ISMB). Sydney, Australia, 2022.
Kozyrina AN, Piskova T, Doolaar I, Prapty T, Semeraro F, Yam L S, Haraszti T, Hubert M, Smith A, Leube R, Di Russo J. *Extracellular Matrix Spatial Heterogeneity Drives Retinal Epithelium Mechanobiology.*

The international conference “Nanoengineering for Mechanobiology”. Camogli, Italy, 2022. Conference talk.

Kozyrina AN, Piskova T, Doolaar I, Windoffer R, Leube R, Di Russo J, *Extracellular Matrix Spatial Heterogeneity Drives Retinal Epithelium Mechanobiology.*

DGZ International meeting. Digital edition, 2021.

Kozyrina AN, Piskova T, Doolaar I, Steins T, Windoffer R, Leube R, Di Russo J, *Extracellular Matrix Heterogeneity Defines Retinal Epithelium Mechanobiology.*

Kármán Conference European Meeting on Intermediate Filaments. Kerkrade, Netherlands, 2021.

Kozyrina AN, Piskova T, Doolaar I, Steins T, Windoffer R, Leube R, Di Russo J, *Extracellular Matrix Heterogeneity and Retinal Mechanobiology: Does the keratin network control mesoscale properties of the pigment epithelium?*

The international conference “Nanoengineering for Mechanobiology” 5th edition. Digital edition, 2020.

Kozyrina AN, Piskova T, Di Russo J, *The mechanobiology of Retinal Pigment Epithelium heterogeneity*

Acknowledgements

I deeply appreciate everyone who contributed to my PhD journey. Without your guidance, support, and encouragement, this work would not be possible.

First of all, I am profoundly grateful to my supervisor, Dr. Jacopo Di Russo, whose insight, patience, and belief in my potential have been the driving force behind this work. You believed in me even when I stopped believing in myself. You motivated me and pushed me forward when my own strength was no longer enough. You knew how to find signs even in insignificant data. Without being unfounded, you made me who I am today, and for that, I am immensely grateful to you.

I would like to express my sincere gratitude to Prof. Rudolf Leube for his invaluable scientific insight and support throughout my PhD journey. I deeply appreciate the time and effort you invested in helping me refine my research, as well as your expertise, which consistently challenged me to think more critically and approach problems from new perspectives.

To my dearest "partner in crime," Teodora Piskova, thank you for teaching me that nothing is impossible if you truly desire it. Your encouragement to remain open-minded and embrace every opportunity the Universe offers has had a profound impact on me. To my friend and colleague, Felix Reul, thank you for the boundless optimism and infectious energy that you shared with us. You made even the most challenging days brighter. To the kind-hearted Vasudha Krishnamurthy, thank you for bringing harmony and calm to our hectic days. You have taught me the beauty of contemplation and opened my eyes to so many fascinating cultural experiences. I am incredibly grateful to you all for creating such a warm, supportive, and inspiring atmosphere and for being such wonderful friends.

I would also like to extend my appreciation to the incredible REMeD team, both past and present – thank you for creating an environment I was always eager to return to, even after a vacation. I would especially like to acknowledge Natalia Simon, Timmy Steins, Aiora Vilchez, Iris Doolaar, Iulia Scarlat, Taspia Prapty, Sebastian Schepl, Stacy Yam, Jonas Schimmel, Yuxin Ji and Gloria Zeiss for their unwavering support and friendship.

A special thanks goes to my dearest friend, Francesca Semeraro. Some of my fondest memories are from the times we shared—whether through the ups and downs of research or simply enjoying the little moments in life. Together, we shared almost everything, and

the towering stacks of dishes in the cold room will forever remind me of our sweet and occasionally sour adventures. I believe that the bond we've built will continue to connect us, no matter how many decades may pass.

I would also like to extend my appreciation to all my colleagues from the MOCA team for providing a uniquely enriching environment that greatly contributed to the success of my PhD journey. Thank you all for the diverse perspectives, occasional lively debates and memorable experiences that have greatly contributed to my personal and professional development. I am especially grateful to Prof. Reinhard Windoffer, Adam Breitscheidel, Dr. Marcin Moch, Dr. Nicole Schwarz, Dr. Hoda Moazzen, Dr. Jana Schieren, Dr. Anna Katharina Sternberg, Dr. Joana Ahlburg, Sabina Hennes-Mades, Laura Königs, Philipp Kolodziej, Liubov Izmaylova, Kyeongmin Kim and Elena Honscheid.

I would like to express my sincere gratitude to ME3T graduate school for making my research journey so rewarding. The supportive and intellectually dynamic environment you created, with the freedom to explore new ideas and have open discussions, made a huge difference. Your efforts in bridging diverse fields have greatly enriched my interdisciplinary research experience. I am also particularly grateful to Prof. Laura De Laporte, Prof. Rudolf Merkel, Prof. Ana-Sunčana Smith, Prof. Andreas Ludwig, Dr. Maxime Hubert, Dr. Aaron Babendreyer, Dr. Ramin Nasehi and my fellow PhD students Fiona Roll, Iris Doolaar and Laura Klasen. Your support and shared enthusiasm have been an invaluable part of my experience.

I would also like to acknowledge the Joachim Herz Foundation for its financial support through Add-on Fellowships for Interdisciplinary Life Science. Your dedication to professional and personal development and the creation of a supportive community have greatly enriched my PhD experience.

I want to extend my deepest thanks to my whole family for their unconditional love and constant encouragement. "Keep your head up," they would say, "everything is fine, we are with you," even when thousands of kilometres and multiple time zones lie between us. I am especially grateful to my dear soulmate, Andrey Babenyshev, for his endless patience, understanding, and unwavering belief in me, especially during the most challenging moments. You've been my rock and my anchor, always there to lift me up when I doubted myself. I couldn't have done this without you by my side.

Summary

Epithelial cells are interconnected, whereby they acquire mesoscale mechanical properties to accomplish specific tissue functions. In a homeostatic state, these mechanical properties rely on a balance between intercellular tension and adhesion to the underlying extracellular matrix (ECM). This balance is crucial for tissue function, particularly in postmitotic epithelium like retinal pigment epithelium (RPE), which due to lack of cell division, must undergo constant remodelling events to compensate for natural cell loss. The ECM, composed of a multitude of proteins, plays a pivotal role in regulating this force balance, influencing cell mechanics and behaviour. However, how changes in the ECM composition influence the ability of RPE to maintain their essential functions remains poorly understood.

Overall, RPE is a vital component of the retina, responsible for maintaining photoreceptor homeostasis and supporting vision. Daily, RPE cells phagocyte and recycle fragments of photoreceptor cells called photoreceptor outer segments (POS), to ensure their proper renewal and overall health of the tissue. In this research, I hypothesized that the biochemical and physical properties of the ECM, particularly the variations in laminin isoforms, which are key biochemical regulators within the ECM, directly influence RPE cell mechanics and functionality.

To study this, I developed several reductionist models using human stem cell-derived RPE cells. One model involved retinal spheroids in suspension culture, which allowed for the biochemical stimulation of cells with specific ECM components without mechanical interference from the environment. Another model included RPE cells cultured on soft hydrogels coated with different concentrations of laminins. This setup simulated the natural ECM environment of the retina and allowed control over the ECM cues. The mechanical properties of RPE cells were quantified using traction force microscopy, monolayer stress microscopy, and nanoindentation. Further, I explored how cellular contractility—an indicator of mechanical stress—affects their ability to phagocyte POS, a function essential for retinal health and vision.

The research revealed that the functionality of RPE cell is significantly influenced by laminin density and composition. Particularly, lower laminin 511 concentrations led to increased cellular strain and reduced phagocytic ability conversely to laminin 332. I demonstrated that the ratio between specific integrin receptors (β1 and β4) modulated

these interactions, altering the balance between actin and keratin cytoskeletal networks, which in turn determined the overall mechanical stability of the tissue. *In vivo* data supported these findings, showing that laminin density decreases towards the retinal periphery, aligning with reduced functional demand and indicating the presence of ECM-defined mechanical gradient within the RPE.

In conclusion, my work highlights the importance of ECM diversity in maintaining the mechanical homeostasis and functionality of RPE cells. The findings presented in this work highlight the crucial role of mechanics in visual function and offer valuable insights into retinal health and disease. This research provides a novel perspective on how ECM variations, particularly age-related remodelling, may disrupt cellular adhesion and mechanical balance, potentially leading to retinal disorders such as age-related macular degeneration. Further studies are needed to fully understand the extent to which these ECM-induced changes in RPE mechanical status contribute to retinal diseases and to explore potential treatments.

I. Introduction

Mechanobiology, the study of how physical forces and changes in the mechanical properties of cells and tissues influence biological processes, has emerged as a vital area of research with profound implications for understanding development, physiology, and disease. This interdisciplinary field bridges biology, engineering, and physics to explore how cells sense, transduce and respond to mechanical signals. The extracellular matrix (ECM) is of particular interest in mechanobiology, providing not only structural support but also biochemical and mechanical cues that influence cellular behaviour and tissue function. In epithelial tissues, which form protective barriers and interfaces within the body, the ECM plays a crucial role in maintaining structural integrity and tissue homeostasis. Overall, epithelial cells are highly interconnected, acquiring mesoscale mechanical properties that are essential for specific tissue functions. These functions rely on the balance of intercellular tension and adhesion forces to the underlying ECM, which cannot be fully explained from a single-cell perspective.

The central theme of this work is the retinal pigment epithelium (RPE), which is a specialized epithelial monolayer that plays an essential role in visual function. Located between the neural retina and the choroid, the RPE is involved in regulating the photoreceptor cell homeostasis, nutrient and waste transport, and the maintenance of the blood-retinal barrier. Its functionality is profoundly influenced by its mechanical environment, including forces generated by intraocular pressure, osmotic gradients due to constant intracellular transport, and mechanical forces from surrounding tissue and the underlying ECM. Understanding how all these factors impact RPE cells is critical for elucidating the mechanisms underlying retinal health and disease.

Considering the postmitotic nature of RPE, maintaining a proper balance of forces within the tissue is crucial, since the lack of cell division and the natural cell loss are compensated by active tissue remodelling. We hypothesise that the biochemical and physical properties of the ECM may contribute to epithelial organization and mechanics, which in turn may impact retinal functionality. Changes in the ECM may affect epithelial plasticity and increase susceptibility to retinal diseases.

The following sections of this chapter provide an overview of epithelial ECM remodelling in physiology, the role of cell adhesion receptors and fundamental concepts in epithelial mechanobiology with a specific focus on RPE.

1. Epithelial extracellular matrix composition and remodelling in physiology

The epithelial ECM is a crucial component of tissue architecture, providing structural support and biochemical signals that regulate cellular behaviour. The dynamic remodelling of this matrix is fundamental to various physiological processes, from tissue development and repair (Chaudhuri et al., 2020; Walma & Yamada, 2020) to homeostasis and adaptation (Frantz et al., 2010; Kozyrina et al., 2020). Understanding how epithelial ECM remodelling operates within physiological contexts is essential for comprehending how tissues maintain their integrity and function in both health and disease.

The ECM is a complex network of proteins and polysaccharides that surrounds cells in tissues, creating a specialized microenvironment. The composition and mechanical properties of the ECM can vary significantly between tissues, reflecting the specific functional requirements of each tissue type (Mouw et al., 2014). For the epithelial tissues, ECM is divided into two distinct components, namely basement membrane (BM) and interstitial matrix (IM) (Figure I-1A).

The BM is a specialized, thin layer of ECM that underlies epithelial cells and separates them from the underlying connective tissue. It is crucial for maintaining epithelial tissue integrity, supporting cell adhesion, and regulating cellular functions. The BM is composed of several key components including collagen type IV, laminins, nidogens and proteoglycans (Figure I-1A) (Kozyrina et al., 2020; Walma & Yamada, 2020). Unlike the BM, which is localized beneath cells, the IM extends throughout the interstitial spaces and forms a porous 3D lattice structure in the connective tissue. It is primarily produced by cells like fibroblasts and provides additional support and regulation (Zent & Pozzi, 2010). The composition of the IM includes fibrillar collagens (type I, II, III, and V), non-fibrillar collagens (e.g., XII and XIV), glycoproteins like elastin, fibronectin, proteoglycans and glycosaminoglycans (Figure I-1A) (Kozyrina et al., 2020; Mouw et al., 2014; Walma & Yamada, 2020).

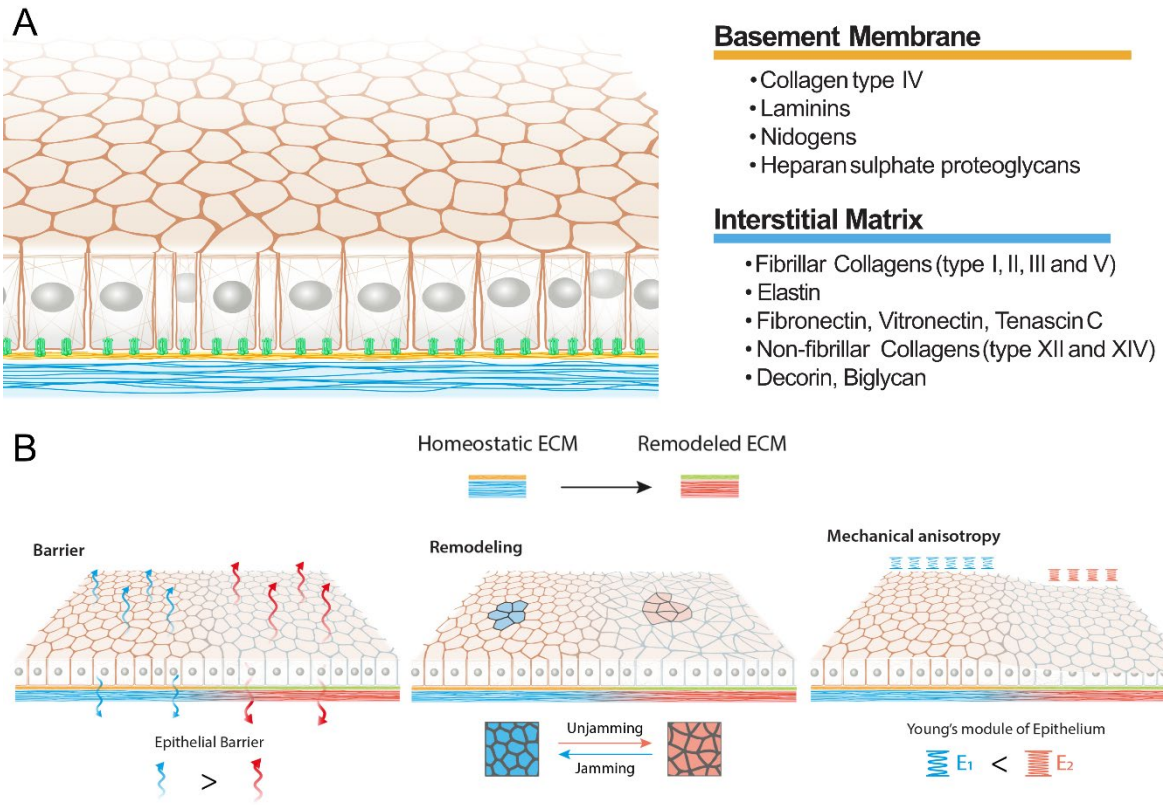

Figure I-1*. Epithelial extracellular matrix (ECM) in homeostasis and remodelling.* ***A.*** *Schematic representation of the epithelium above the ECM, highlighting two key layers: the basement membrane (BM) and the interstitial matrix (IM). The BM provides biochemical signalling to the cells, while the IM provides tissue elasticity and mechanical strength.* ***B.*** *Graphical representation of potential effects of ECM biochemical (yellow to green) and mechanical (blue to red) remodelling on epithelial tissue. Various adhesion conditions can influence epithelial characteristics, including barrier function, tissue remodelling, and mechanical anisotropy from left to right. The diagram illustrates an increase in permeability, a jamming-to-unjamming transition, and monolayer stiffening in response to ECM changes. Adapted from* (Kozyrina et al., 2020).

The BM and IM together form a dynamic and interactive ECM environment that supports epithelial function and tissue homeostasis. The BM regulates multiple cellular activities such as proliferation, migration, and differentiation (Yamada & Sixt, 2019; Yap et al., 2019). It acts as a barrier to prevent the invasion of cells and molecules, thereby maintaining tissue compartmentalization and function (Chang & Chaudhuri, 2019; Zent & Pozzi, 2010). The IM, on the other hand, offers structural support and flexibility, accommodating mechanical stresses and facilitating nutrient and waste exchange (Booij et al., 2010; Cox & Erler, 2011; Watt & Huck, 2013). The interplay between the BM and IM contributes to the overall mechanical properties of epithelial tissues, including their stiffness, elasticity, and resilience.

Moreover, the ECM is a highly dynamic structure that is constantly being remodelled through both enzymatic and non-enzymatic processes. It undergoes continuous and highly regulated post-translational modifications allowing tissues to

adapt to physiological demands (Figure I-1B) (Bonnans et al., 2014; Frantz et al., 2010). A complex interplay of cellular and molecular mechanisms regulates the remodelling process. It involves the synthesis and degradation of ECM components, mediated by coordinated secretion of remodelling enzymes, proteases and protease inhibitors. For example, the action of matrix metalloproteinases is counterbalanced by tissue inhibitors of metalloproteinases and regulated activity of other enzymes like lysyl oxidase to control the ECM degradation rate (Bonnans et al., 2014; Cox & Erler, 2011; Frantz et al., 2010).

During development, wound healing, and tissue regeneration, ECM remodelling is crucial for accommodating changes in tissue structure and function (Diaz-de-la-Loza et al., 2018; Serna-Morales et al., 2023; Walma & Yamada, 2020; Yamada & Sixt, 2019). For instance, during wound healing, ECM remodelling facilitates the repair process by enabling cell migration and new matrix deposition (Boekhorst et al., 2016). Additionally, the ECM plays a pivotal role in the epithelial-mesenchymal transition, a process where epithelial cells lose their polarity and adhesion properties to become more migratory mesenchymal cells (Scott et al., 2019). While this transition is vital during physiological processes, it is aberrantly activated in cancer and fibrosis, contributing to disease progression. Alterations in ECM composition, such as increased deposition of fibrillar collagens, promote this process by modulating cellular signalling pathways and altering the mechanical properties of tissues (Figure I-1B) (Rice et al., 2017; Wei et al., 2015; Zent & Pozzi, 2010).

In ageing, there is a gradual accumulation of molecular damage and alterations in ECM composition. Key changes include reduced ECM turnover, increased collagen crosslinking, tissue stiffening, and a decline in regenerative capacity (Booij et al., 2010; López-Otín et al., 2023). These alterations negatively impact tissue structure, function, and cellular behaviour, contributing to the overall decline in tissue integrity and function as organisms age (Cai et al., 2022; Watt & Huck, 2013). These ageing processes can be described as a series of thermodynamic events where the gradual increase in entropy leads to the system's inability to counteract disorder, leading to the accumulation of molecular damage, a decline in cellular function, and the eventual breakdown of physiological systems (Bortz, 1986).

Dysregulation of ECM remodelling is a hallmark of various diseases, including cancer and fibrosis (Cox & Erler, 2011; Saraswathibhatla et al., 2023; Zent & Pozzi, 2010).

In cancer, the ECM undergoes extensive remodelling, which facilitates tumour progression and metastasis. This process involves increased production of matrix metalloproteinases, which degrade ECM components and create a permissive environment for tumour invasion. Similarly, in fibrotic diseases, excessive ECM deposition leads to tissue stiffening and loss of function, driven by chronic inflammation and persistent activation of fibroblasts.

Overall, the ECM is one of the key regulators of tissue function and homeostasis. Understanding its biochemistry and mechanics in physiological contexts is essential for advancing our knowledge of tissue biology.

2. Cellular signalling at the basal interface

2.1. Basement membrane composition

Understanding the composition of the ECM and its remodelling processes is fundamental to exploring the complex cellular signalling that occurs at the interface between ECM proteins and cell adhesion receptors. This interface is not just a structural link but a dynamic signalling connection that drives critical cellular functions. Collagen, laminins, and proteoglycans, as key ECM components, engage with receptors like integrins, transmitting mechanical and biochemical signals into the cell (Figure I-2A). These interactions are important for maintaining the structural organization of epithelial tissues and ensuring their proper function. The BM, directly interfacing with cells, plays a crucial role in providing biochemical cues that modulate cellular behaviour and function. Collagen IV and laminins are central to this process, as they are key components that influence cellular signalling and tissue organization.

Collagen is the most abundant protein in animals, with 28 identified subtypes characterized by their triple-helical structure (Gordon & Hahn, 2009; B. Sun, 2021). Among these, collagen IV is a crucial component of the BM and is characterised by its distinctive structural features. Unlike other collagens that form parallel fibres, collagen IV assembles into a flexible network through non-parallel, head-to-head linking of its triple-helical molecules (Gordon & Hahn, 2009). This configuration allows it to form a sheet-like structure rather than a tight helix, providing greater flexibility. Collagen IV can be assembled from six different polypeptide chains (α1–α6), resulting in three primary isoforms: [α1(IV)]2α2(IV), [(α3)(α4)(α5)], and [(α5)2(α6)]. The most common isoform, [α1(IV)]2α2(IV), consists of two α1 chains and one α2 chain. The [(α3)(α4)(α5)] isoform

is found in the BM of kidney glomeruli and lung alveoli, while [(α5)2(α6)] is present in the epidermis, mammary glands, and alimentary tract epithelium (Kozyrina et al., 2020).

A

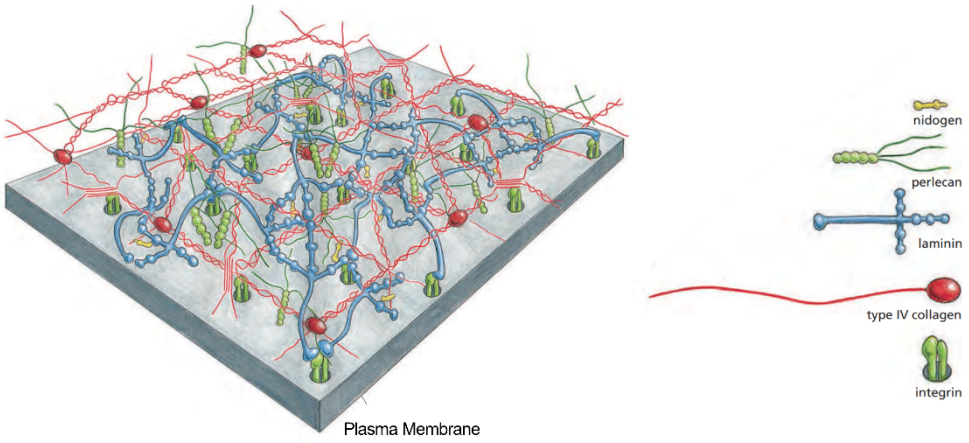

B

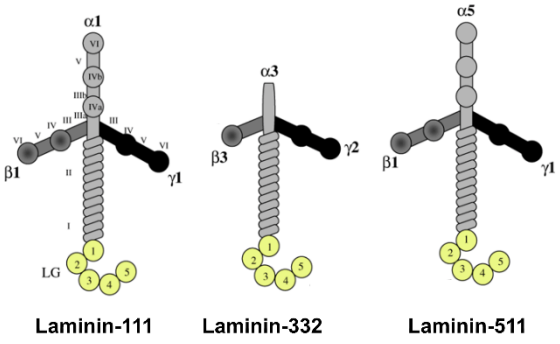

C

Location	ECM Protein	Integrin receptors
Basement Membrane	Laminin α1 Laminin α3	α6β1, α6β4, α3β1, α7β1
	Laminin α5	α6β1, α6β4, α3β1, α7β1, α5β1, αvβ1, αvβ3
	Collagen IV	α1β1, α2β1, α10β1, α11β1
Provisional Basement Membrane	Fibronectin Vitronectin	α5β1, αvβ1, αvβ3

Figure I-2. *Structural overview of basement membrane architecture and integrin-mediated adhesion.* ***A.*** *A molecular model of basement membrane composition illustrating the interactions between the proteins laminin, collagen type IV, and nidogen, and the proteoglycan perlecan (adapted from* (Alberts et al., 2015)*).* ***B.*** *Schematic representation of the structure of laminin-111, -332 and -511, highlighting their distinct structural differences (adapted from* (Sugawara et al., 2008). ***C.*** *The table summarizes the integrin receptors associated with the main epithelial laminins, collagen IV, together with fibronectin and vitronectin, which are aberrantly present in the basement membrane during tissue remodelling (adapted from* (Kozyrina et al., 2020).

Laminins, high-molecular-weight (≈400 to ≈900 kDa) glycoproteins and major components of the BM play a crucial role in the structural organization and integrity of tissues. Laminins have a cross- or T-shaped structure with a long arm formed by a coiled-coil assembly of the α, β, and γ chains stabilized by disulphide bonds (Figure I-2B). While the β and γ chains form the protein network, the C-terminal domain of the α chain remains free for interaction with cellular receptors, facilitating tissue-specific functions and signalling between intracellular and extracellular environments. The human genome encodes eleven laminin chains: five α chains (α1, α2, α3A/B, α4, α5), three β chains (β1, β2, β3), and three γ chains (γ1, γ2, γ3). This diversity allows for the assembly of 16 distinct laminin isoforms, although theoretically over 50 combinations are possible (Aumailley, 2012, 2021).

The expression of laminin isoforms varies by tissue type and developmental stage. During development, laminin 111 is predominant and crucial for cell polarization and tissue shaping (Lee & Streuli, 2014; Yurchenco, 2011). As tissues mature, laminin 111 is gradually replaced by other isoforms to maintain specific tissue homeostasis (Yurchenco, 2011). In contrast, laminins containing the α5 chain, such as laminins 511 and 521, are among the most ubiquitous isoforms in adult tissues. Additionally to their cell-binding domain, these laminins also carry exposed arginine-glycine-aspartic acid (RGD) sequences, which enhance cell adhesion to specific integrin receptors and influence cellular responses to mechanical forces (Di Russo et al., 2016). Laminin 332, found in the epidermal BM, interacts with cellular receptors to form hemidesmosomes (specialised junctional complexes), providing tissue structural support and cohesion under mechanical stress (Kiritsi et al., 2013; Rousselle & Beck, 2013). During wound healing, laminin 332 is deposited into the provisional matrix by leading keratinocytes, promoting cell migration and epidermal outgrowth (Wen et al., 2010). Laminins 211 and 221 are found in skeletal and cardiac muscles, while laminins 411 and 421 are prominent in endothelial basement membranes (Yap et al., 2019; Yousif et al., 2013).

2.2. Repertoire of cell adhesion receptors

While laminins and collagen IV serve as the main structural components of the BM, integrins are key transmembrane receptors that link these structural elements to the cell, mediating cell-ECM adhesion and signal transduction. These receptors enable cells to sense and respond to the dynamic changes within the ECM, facilitating essential cellular processes such as differentiation, migration, and survival (Flier & Sonnenberg, 2001). Integrins are heterodimeric cell adhesion molecules, composed of glycosylated α- and β-subunits, which form a bridge between the ECM and the cytoskeleton. This structural linkage is critical for maintaining cellular integrity and transmitting mechanical and chemical signals across the plasma membrane. In humans, the integrin family comprises 24 distinct receptors resulting from the combination of 18 α-subunits and 8 β-subunits (Clark & Brugge, 1995; Hynes, 2002). Each integrin heterodimer exhibits specific binding affinities for various ECM proteins, including laminins, fibronectin, and collagen (Figure I-2C). This diversity in subunit combinations allows integrins to mediate a wide range of interactions, not only with the ECM but also with other cells and pathogens, highlighting their role in various physiological and pathological processes (Ulanova et al., 2008).

The cellular adhesion to collagen IV is modulated by the β1 subgroup of integrins, with the major role of α1β1 and α2β1 (Figure I-2C). Both integrins interact with collagen IV and collagen I, but with different preferences: integrin α1β1 exhibits a stronger affinity for collagen IV, whereas α2β1 shows a greater binding strength to collagen I (Tulla et al., 2001). The loss of collagen IV-binding integrins such as α1β1 and α2β1 can impair adhesion to the basement membrane, resulting in weakened epithelial cell attachment and diminished capacity for wound healing and tumour angiogenesis (Gardner et al., 1996; Ghatak et al., 2016).

The primary laminin-binding integrins are α3β1, α6β1, and α6β4, which play crucial roles in the formation and maintenance of epithelial cell layers ((Pozzi et al., 2016) Figure I-2C). These integrins ensure stable adhesion to the BM, with α6β4 being specifically involved in the formation of hemidesmosomes—specialised junctional structures that anchor epithelial cells to the underlying matrix (Nievers et al., 1999). Integrin α6β1 is the most versatile receptor for laminin isoforms, while α3β1 and α6β4 primarily interact with laminin α3 and α5 chains, respectively (Belkin & Stepp, 2000). Additionally to classical laminin-binding integrins, the laminin α5 chain can promote cell adhesion through integrins αvβ3, αvβ1, and α5β1, due to RGD sequences at the N-terminal end (Kozyrina et al., 2020).

Hemidesmosomes are specialized adhesive structures in the epidermis that provide stable attachment of basal epithelial cells to the underlying BM. Unlike other integrin-cytoskeletal connections which link to actin filaments, hemidesmosomes are associated with the intermediate filament system. This involves the α6β4 integrin interacting with associated proteins like plectin and BP230 (Flier & Sonnenberg, 2001; Walko et al., 2015). The α6β4 integrin binds to the ECM protein laminin 332 and connects to the keratin intermediate filament network through P1a and BPAG1e (Chaudhari & Vaidya, 2014). This unique linkage helps maintain tissue integrity and may also serve as a site for signal transduction.

Despite the overlapping binding specificities of many integrins, the loss of almost any integrin α- or β-subunit results in significant biological defects in mice, underscoring their crucial role in tissue organization and function. For example, the α3β1 integrin is critical for cell migration and wound healing, and mice lacking α3 integrin die during the neonatal period due to severe defects in lung and kidney development (Dowling et al.,

1996; Kreidberg et al., 1996). Similarly, α6 integrin-null mice die at birth with severe skin blistering and defects in the cerebral cortex and retina (Arcangelis et al., 1999). The absence of the β4 gene disrupts hemidesmosome formation, leading to fragile skin that is prone to blistering, as observed in β4-null mice (Di Persio et al., 2000). Taken together, these findings suggest that laminin-binding integrins are essential for maintaining tissue integrity and proper organ function.

Integrins exhibit diverse distribution patterns across various tissues, reflecting their specialized roles in cellular interactions and tissue maintenance. Despite sharing the common β1 subunit, integrins α3β1 and α6β1 have unique functions and distinct distribution patterns. Integrin α3β1 is most abundant in the skin, kidneys, lungs, intestines, bladder, and stomach, where it mediates the adhesion of epithelial cells to laminin 332 and 511 and maintains cell-cell contacts (Di Persio et al., 1997; Yalcin et al., 2015). Conversely, integrin α6β1 is found on platelets, leukocytes, gametes, and some epithelial cells, binding to various laminin isoforms with the highest affinity for laminin 111, 511, and 332 (Delwel et al., 1994). Integrin α6β4 is found at the base of most epithelial cells, in a subset of endothelial cells, and in some peripheral nerve cells. It facilitates cell adhesion to laminins, essential for forming hemidesmosomes and mediate tissue homeostasis (Nievers et al., 1999; Weaver et al., 2002).

2.3. Mechanotransduction and integrin signalling

Mechanotransduction is the cellular mechanism that transforms mechanical stimuli from the surroundings into biochemical intracellular signals, allowing cells to sense and respond to their physical environment. Integrins, along with mechanosensitive ion channels, are central to this process and facilitate the interactions between cells and the ECM. Integrins, as their name suggests, serve to integrate the extracellular and intracellular environments, playing a key role in bidirectional signalling across the plasma membrane.

Integrin activation involves both inside-out and outside-in signalling pathways, which dynamically modulate cellular adhesion and signalling in response to various stimuli (Chastney et al., 2021; Hynes, 1992). Inside-out signalling is initiated by intracellular signals, such as the binding of proteins like talin and kindlin to the cytoplasmic tails of integrin β subunits, causing conformational changes that increase integrin affinity for ECM ligands (Harburger & Calderwood, 2008). This process is crucial

for cellular responses to internal cues, including changes in the cytoskeleton and signalling from other receptors. Conversely, outside-in signalling begins when integrins bind to ECM ligands, leading to integrin clustering and the recruitment of intracellular signalling molecules to their cytoplasmic domains. This interaction forms focal adhesions, which are multiprotein complexes that facilitate further signal transduction and regulate processes such as cell migration, spreading, proliferation, and survival (Lauffenburger & Horwitz, 1996). Together, these mechanisms allow integrins to dynamically link the extracellular environment with intracellular processes, thereby coordinating cell behaviour and responses.

A leading concept in the field to explain the mechanism of coupling between integrins and actin during cell migration, originally proposed by Mitchison and colleagues, is called the 'molecular clutch' hypothesis (Mitchison & Kirschner, 1988). This model conceptualizes the dynamic linkage between the ECM and the cell's actin cytoskeleton through integrin-based adhesions (Figure I-3). The molecular clutch model describes how these integrin-actin connections transmit mechanical forces, with the engagement of the clutch modulating the coupling of retrograde actin flow and generating traction forces on the ECM. This process involves mechanosensitive proteins (e.g. talin and vinculin) that adjust the strength of integrin-cytoskeleton linkages, activating signalling pathways like FAK/Src and RhoA/ROCK, which regulate cell behaviour. The key insight of the molecular clutch model is that mechanotransduction depends on the force loading rate, which is determined by ECM stiffness (Figure I-3B, C) (Chaudhuri et al., 2020). Changes in substrate stiffness influence the speed of the clutch engagement, dictating whether actin polymerization results in cell membrane extension and modulation of actin retrograde flow, thus coordinating cell migration and other responses to mechanical cues.

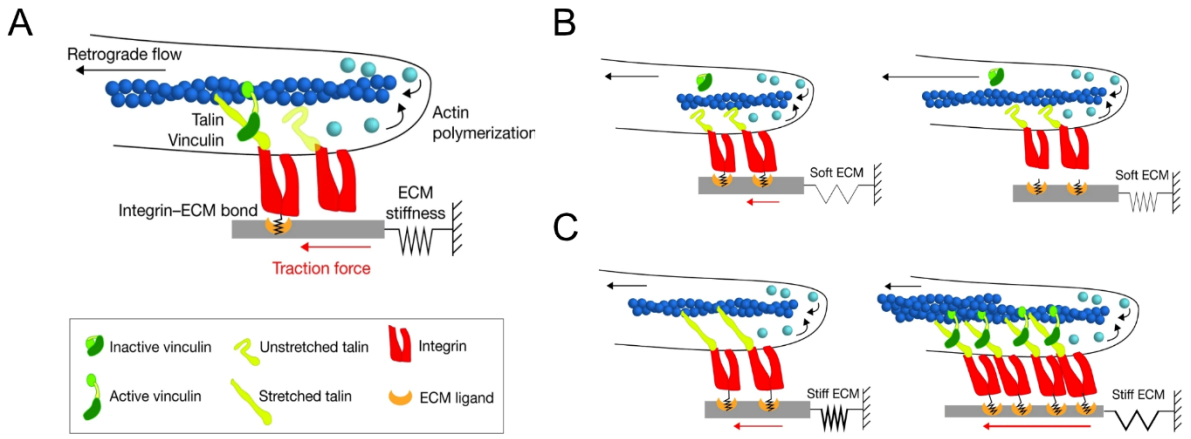

Figure I-3. *Schematic representation of molecular clutch model.* ***A.*** *A summary of the mechanosensitive molecular clutch model.* ***B.*** *On soft substrates, load transmission is slower than the integrin–ECM bond lifespan, causing bond dissociation before talin unfolds or vinculin binds.* ***C.*** *On stiff substrates, the load is transmitted faster than the bond lifespan, promoting talin unfolding, vinculin binding, and actin reinforcement. The illustration was adapted from* (Swaminathan & Waterman, 2016).

Additionally, the density of adhesion receptors is a key factor in regulating cellular behaviour. Studies on single cells have shown that altering integrin ligand density and cell confinement can significantly impact migration modes. Specifically, a combination of low adhesion density, which typically reduces migration speed, and increased cell contractility due to confinement can induce a switch to an amoeboid migration mode across various cell types (Y.-J. Liu et al., 2015). Moreover, the recent study on migrating keratinocyte monolayers using specific nanospasing of $\alpha_5\beta_1$ integrin demonstrated the crucial role of the optimal integrin density for effective migration (Di Russo et al., 2021). These findings underscore that, within the framework of the molecular clutch model, cellular contractility is governed by a delicate balance between ECM mechanical properties and biochemical signalling, both of which are critical for proper cellular function.

3. Fundamentals of epithelial mechanobiology

3.1. Diversity of epithelial organisation and mechanobiological implications

Epithelial tissues are fundamental components of the human body, serving as barriers, interfaces, and functional units in various organs and systems. Characterized by close cell-cell adhesion, they form continuous sheets covering surfaces and lining cavities (Figure I-4A). This structural arrangement allows epithelia to perform diverse functions, including protection, absorption, secretion, and sensation of environmental changes (Mescher, 2013).

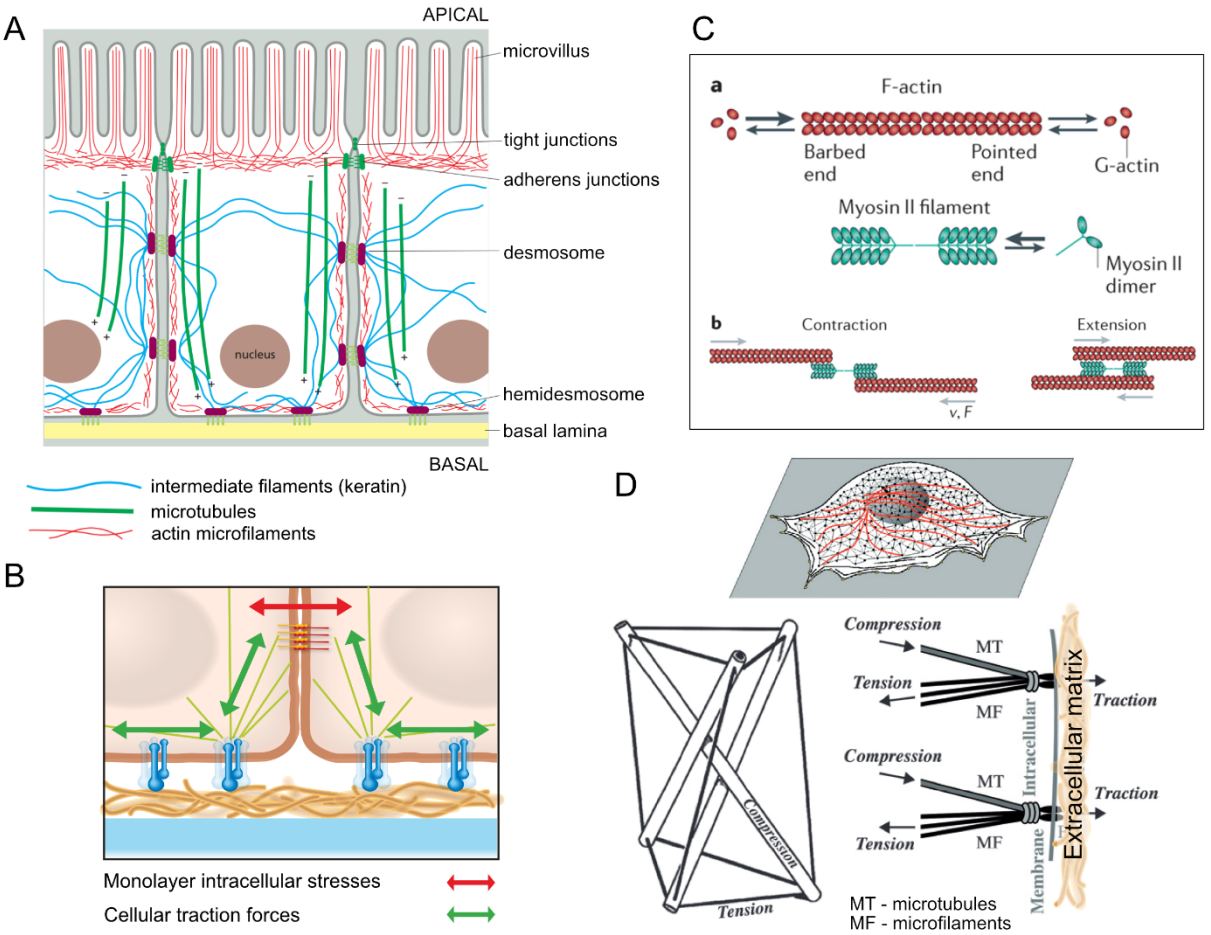

***Figure I-4**. Mechanobiological overview of epithelial cells: junctions, polarity, and force transmission. model. **A.** Cytoskeleton organization in polarized epithelial cells. Actin filaments (red) form microvilli at the apical surface, increasing nutrient absorption. A circumferential actin band links to adherens junctions, connecting cells. Intermediate filaments (blue) anchor to desmosomes and hemidesmosomes, reinforcing the cell layer and attaching it to the ECM. Microtubules (green) run vertically, guiding cellular transport and organization. Adapted from* (Alberts et al., 2015). ***B.** Schematic illustration of the cell monolayer interacting with ECM via integrin receptors (blue). The arrows traction forces exerted by cells on the ECM (green) and stresses across the monolayer (red), highlighting mechanical interactions within the tissue. **C.** Schematic representation of actomyosin contractility. (a) F-actin has barbed (open) and pointed (closed) ends, with arrows indicating the association and dissociation of G-actin monomers. Faster association with the barbed end is shown by larger arrows. Myosin II filaments, consisting of bipolar myosin dimers with a central bare zone, interact with F-actin. (b) Myosin II filaments translocate F-actin towards the barbed ends, creating a characteristic force (F) and velocity (v) relationship. This process results in filament contraction (left) or extension (right), depending on myosin II's position relative to the filaments' centre. Adapted from* (Murrell et al., 2015). ***D.** Schematic representation of tensegrity force balance. The figure illustrates the balance of forces between tensed actin microfilaments (MF), compressed microtubules (MT) within the cell, and traction forces at focal adhesions (FA). Contractile tension is partially transmitted to FAs and balanced by traction, while the rest is internally balanced by MT compression. Adapted from* (Stamenović & Ingber, 2008).

Epithelial tissues vary widely in structure and function, reflecting their specialized roles in different parts of the body. They can be classified based on the number of cell layers (simple or stratified) and cell shapes (squamous, cuboidal, or columnar) (Mescher, 2013). For instance, simple squamous epithelium, composed of a single layer of flat cells, is found in areas where rapid diffusion or filtration is needed, such as the alveoli of the

lungs and the glomeruli of the kidneys. Stratified squamous epithelium, which protects against mechanical stress, lines the skin, mouth, and oesophagus. Cuboidal and columnar epithelia, which can be simple or stratified, are commonly found in glandular tissues and the lining of the digestive and respiratory tracts, where they facilitate absorption and secretion.

Mechanobiology explores how mechanical forces and the properties of cells and tissues influence biological functions. Epithelial tissues are central to this field since in addition to the abovementioned roles, they can sense, transmit and respond to mechanical forces to maintain homeostasis and drive biological processes. Acting as barriers and interfaces, epithelia are constantly exposed to diverse mechanical environments, ranging from the dynamic stretching of the skin to the fluid shear stress in the blood vessels and the mechanical rigidity of bone-lining cells. These forces can arise from various sources, including fluid flow, tissue movements, and interactions with the ECM (Eyckmans et al., 2011; Nagatomi, 2011).

Epithelial cells possess a unique ability to maintain structural integrity and proper function while adapting to environmental changes through a process defined as epithelial mechanical homeostasis (Macara et al., 2014). Throughout their lifetime, epithelial cells continuously generate and respond to mechanical forces, using a range of cellular mechanisms to sustain structural balance and preserve tissue function and integrity. At their interface with the ECM, epithelial cells generate traction forces mediated by integrins through actin-dependent focal adhesions and keratin-associated hemidesmosomes, which are essential for various cellular processes, including migration, division, and morphogenesis (Figure I-4B) (Nievers et al., 1999; Ridley et al., 2003). Additionally, epithelial cells are interconnected by junctional complexes, such as tight junctions, adherens junctions, and desmosomes, which maintain tissue integrity and facilitate the transmission of mechanical forces across the tissue (Figure I-4A) (Rübsam et al., 2017). These junctions link to the cytoskeleton, allowing cells to sense and respond to mechanical stress by modulating cytoskeletal dynamics and signalling pathways. This intricate network of junctional complexes serves as anchoring points that distribute mechanical stress across the tissue, ensuring the maintenance of mechanical homeostasis (Maruthamuthu et al., 2011). The balance between traction forces and adhesion forces between neighbouring cells creates a dynamic equilibrium crucial for tissue integrity and function, which is a fundamental aspect of epithelial mechanobiology.

3.2. Epithelial mechanical homeostasis

The interplay between actin filaments and keratin intermediate filaments is critical in maintaining the mechanical integrity and function of epithelial tissues. Actin, through its dynamic interactions with myosin motors, drives essential processes like cell motility, shape changes, and contractility, forming the basis of the actomyosin network that generates forces critical for cellular movement and tissue morphogenesis (Figure I-4C). Keratins, particularly K8/K18, on the other hand, provide structural resilience and mechanical strength, reinforcing the epithelial cell layers through desmosomal and hemidesmosomal attachments (Klymkowsky et al., 1983). Keratins also influence cell stiffness and migration by directing actin dynamics, enhancing migration persistence, and affecting deformability and invasion capabilities (Pora et al., 2020; Seltmann et al., 2013). The joint correct function of actin and keratin networks ensures that epithelial cells can withstand mechanical stresses and maintain tissue homeostasis. Disruptions in the balance between actin and keratin can impair actomyosin contractility, leading to altered cell shape, tissue rigidity, and potential pathologies such as skin blistering and cancer (Holle et al., 2017; J. S. Kim et al., 2012; Pora et al., 2020; Seltmann et al., 2013).

At the cellular level, actomyosin contractility is crucial for maintaining tissue mechanical homeostasis and arises from the interactions between actin filaments and non-muscle myosin II, forming an organized cytoskeletal network that generates ATP-driven contractile forces (Nobes & Hall, 1995). Key regulators of this process are the small Rho family GTPases, particularly RhoA and Rac, which modulate nearly every aspect of actin dynamics (Geiger et al., 2009). These GTPases also modulate many events to regulate the apicobasal polarisation of epithelial cells required for their specialisation (Mack & Georgiou, 2014). Particularly, RhoA activates Rho-associated kinase (ROCK) which leads to phosphorylation of the myosin light chain (MLC) and inhibition of MLC phosphatase. In turn, this increases myosin II ATPase activity and enhances cellular contractility. ROCK also phosphorylates LIM kinase, which stabilizes actin filaments and promotes the formation of stress fibres. In contrast, Rac promotes actin polymerization and branching by activating the Arp2/3 complex, resulting in the formation of lamellipodia and filopodia. Therefore, Rac supports dynamic cell movement and shape changes, balancing the contractile forces regulated by RhoA (Nobes & Hall, 1999).

Actomyosin contractility is essential in epithelial tissues for determining cell shape, motility, and force transmission through cadherin-based adherens junctions

(Wickström & Niessen, 2018). During processes like tissue elongation and folding, actomyosin dynamics drive cell intercalations and coordinate cell flattening (Shun Li et al., 2024). This contractility, regulated by pathways such as the previously mentioned RhoA and small GTPases, is crucial for maintaining cell junctions, mechanical properties, and epithelial barrier integrity (Citalán-Madrid et al., 2013; Gumbiner, 2005; Martin & Goldstein, 2014). Disruptions in actomyosin function can impair differentiation, compromise barrier function, and contribute to diseases like Crohn's and ulcerative colitis (Citalán-Madrid et al., 2013). Additionally, actomyosin is crucial for force transmission and transcriptional changes necessary for branching morphogenesis in epithelial organs (J. M. Kim et al., 2021). By driving the apical-to-basal formation of contractile cables in epithelial monolayers, actomyosin contractility enables the efficient extrusion of apoptotic cells (Le et al., 2021), maintains homeostatic cell numbers in crowded epithelia (Eisenhoffer et al., 2012), and ultimately plays a vital role in preserving tissue homeostasis.

3.3. Epithelial mechanobiology from the extracellular matrix perspective

In epithelial mechanobiology, the ECM serves as more than just a passive scaffold but rather as an active regulator of cellular behaviour, providing both structural support and biochemical signals. The ECM acts as a compression-resistant substrate that counteracts the tensile forces generated by the cytoskeleton and cell-cell junctions (Mouw et al., 2014; Saraswathibhatla et al., 2023). Variations in ECM composition can impact key cellular processes. Its mechanical properties—such as stiffness, elasticity, and topography—play a significant role in regulating epithelial cell functions and tissue homeostasis. Accounting for the dynamic interplay between cells and the ECM, cells use mechanotransduction pathways described above to sense and respond to ECM properties, exerting mechanical forces known as traction forces. Higher traction forces from a stiffer ECM can drive epithelial cell differentiation, whereas a softer ECM fosters stem cell growth. Local variations in ECM properties can create differences in mechanical forces within tissues, affecting their stability and function (Saraswathibhatla et al., 2023). Previous research has shown that epithelial tissues from asthmatic patients exhibit different traction forces compared to non-asthmatic individuals. Specifically, asthmatic epithelial cells display a lower threshold for mechanical stress, leading to increased sensitivity and susceptibility to phase transitions (J.-A. Park et al., 2016). This hypersensitivity is often linked to ECM remodelling, highlighting the importance of ECM-

derived mechanical cues in maintaining epithelial mechanical homeostasis and influencing disease outcomes (Kozyrina et al., 2020; Saraswathibhatla et al., 2023). Cellular traction forces can be influenced by the biochemical properties of the ECM alone. For instance, switching the ECM ligand from collagen I to fibronectin, while keeping stiffness constant, can alter traction force magnitudes (Maruthamuthu et al., 2011; Ohashi et al., 2009). This indicates that the biochemical composition of the ECM can independently affect cellular mechanics by modulating focal adhesion dynamics and cytoskeletal organization.

By intricate balance of the actomyosin machinery, cells can generate and transmit mechanical forces that define cell morphology and tissue architecture. The tensegrity model, conceptualized by Donald Ingber, provides a compelling framework for understanding the dynamic mechanical equilibrium of cells (Figure I-4D) (Ingber, 1993). Tensegrity, short for "tensional integrity," describes a structural system in which isolated components under compression are supported within a network of continuous tension. In the context of cellular and tissue architecture, this model describes how the living cytoskeleton maintains stability through a tensile prestress. This prestress arises from contractile actomyosin filaments that generate tensional forces, which are counterbalanced by intracellular compression-supporting structures such as microtubules and intermediate filaments, as well as extracellular connections to the ECM and neighbouring cells (Figure I-4D). This results in a dynamic, interconnected scaffold within each cell, where the actin cytoskeleton, microtubules, and intermediate filaments collectively support tissue integrity. The model illustrates how mechanical forces are distributed and integrated across both intracellular and extracellular components to sustain cellular and tissue architecture (Ingber et al., 2014).

The shape of epithelial cells is also significantly influenced by the ECM (Iskratsch et al., 2014; Mouw et al., 2014). In the homeostatic state of adult epithelia, cells in crowded regions generally acquire a hexagonal organisation, creating a honeycomb pattern that minimizes energy and balances mechanical forces (Bi et al., 2015). On stiffer substrates, cells spread out and flatten due to increased traction forces and focal adhesion formation, which requires extensive cytoskeletal reorganization. This spreading results in a more polarized cell shape, which is crucial for directional migration and effective tissue organization. Conversely, on softer substrates, cells tend to be more rounded with less pronounced cytoskeletal organization (Keese & Giaever, 1991).

Computer simulations using the vertex model can predict cell shape transitions between jammed and unjammed states. A key metric in these simulations is the dimensionless shape factor $q = \frac{P}{\sqrt{A}}$, where P is the perimeter and A is the area of the cell. This shape index quantifies cell morphology, indicating roundness or elongation. The shape factor helps in constructing a jamming phase diagram, revealing that epithelia remain jammed when intercellular stresses and traction forces are below a certain threshold. This jamming-unjamming transition is significant not only in normal development but also in pathological conditions such as asthma and cancer (Mongera et al., 2018; Palamidessi et al., 2019; J.-A. Park et al., 2016).

4. Retinal pigment epithelium and its extracellular matrix

4.1. Outer retinal physiology

The fundamental principles of epithelial mechanobiology provide insights into how cells within tissues sense and respond to mechanical stimuli. The described processes are crucial not only for understanding epithelial tissues in general but also have profound implications for specialized epithelial structures in the body. One such specialized tissue is the outer retina, comprising several layers, including the photoreceptor layer, the retinal pigment epithelium (RPE) and its ECM (Figure I-5A).

In the retina, the most prominent ECM structure is Bruch's membrane, situated at its outermost part, also known as the outer retina (Booij et al., 2010). Bruch's membrane is crucial for nutrient exchange between the choroid vessels and the retina, and it provides structural support and adhesion to the RPE (Piskova et al., 2023). Structurally, Bruch's membrane has a complex organisation composed of five distinct layers: the RPE basement membrane, the inner collagenous layer, the elastic layer, the outer collagenous layer, and the basement membrane of the choroid capillaries (Booij et al., 2010). This multilayer organization maintains the homeostasis of the outer retina layers, primarily regulating the diffusion and reciprocal exchange of ions, molecules, and nutrients between the RPE and choroid (Fields et al., 2020). Additionally, with its elasticity, Bruch's membrane plays a crucial mechanical role in withstanding intraocular pressure and may have other biomechanical roles in accommodating eye changes during vision (Curcio & Johnson, 2013).

The RPE is a specialized and highly polarised monolayer of postmitotic cells that directly interfaces with the light-detecting neural tissue (Figure I-5A). In the developing

eye, the RPE organizes the retina (German et al., 2008; S. M. Raymond & Jackson, 1995), while in the adult, it plays a key role in the visual cycle (Bok, 1993; Strauss, 2005). The RPE plays an essential role in visual functions by providing metabolic and functional support for the photoreceptor cells in the retina (Lakkaraju et al., 2020). At the apical surface of the RPE, cells possess special membrane protrusions (microvilli) that increase membrane surface area and ensure efficient diffusion for absorption and secretion (Lehmann et al., 2014). These microvilli tightly adhere to the interphotoreceptor matrix, maintaining tissue organization. The actin-binding protein ezrin, which belongs to the ezrin/radixin/moesin family, facilitates the connection between actin filaments and plasma membrane proteins, thereby supporting the integrity of the RPE microvilli (Bonilha et al., 1999; Kivelä et al., 2000). These cells are also densely packed with pigment granules, primarily melanin, which gives them a dark appearance and reduces damage to the retina and internal nerves from ultraviolet light (Piskova et al., 2023; Yang et al., 2021).

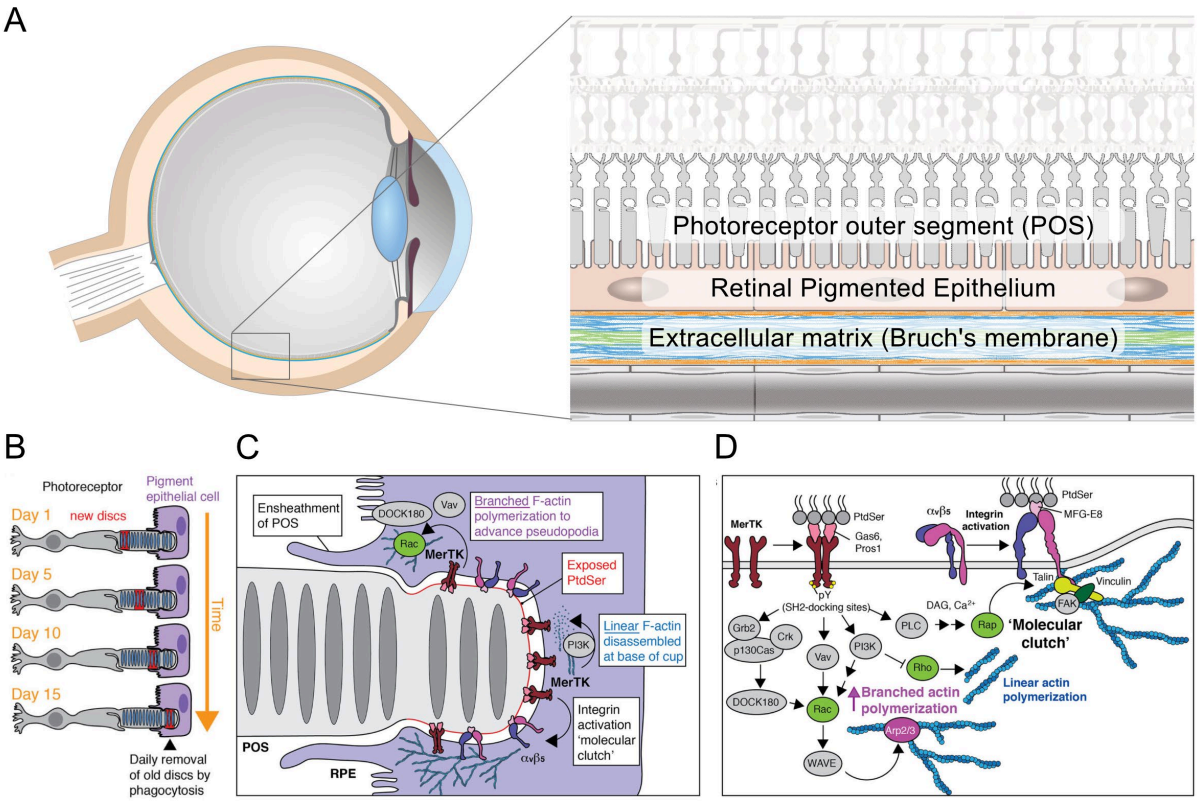

Figure I-5. *The retinal pigment epithelium in outer retina physiology.* ***A.*** *The schematic structure of the outer retina layers described in this work: photoreceptor cells with photoreceptor outer segments (POS), retinal pigment epithelium (RPE) and its extracellular matrix (ECM), Bruch's membrane. Adapted from* (Kozyrina et al., 2024). ***B.*** *The RPE beneath the retina is essential for photoreceptor function, as it regulates the turnover of POS through phagocytosis. This process removes the oldest membrane discs, which are prone to phototoxic damage, while new discs are continuously formed at the base of the POS.* ***C.*** *Phagocytosis of the POS by the RPE, driven by actin polymerization, begins when PtdSer is exposed and binds to bridging molecules and MerTK receptors.* ***D.*** *Actin remodelling, mediated by MerTK, facilitates the engulfment of POS. Integrins, particularly*

αvβ5, also play a role in binding PtdSer and assisting in the phagocytic process. Adapted from (Kwon & Freeman, 2020).

Despite being highly specialised, RPE shares common functions with other epithelia, particularly its role as a barrier in forming the blood-retinal barrier (Bok, 1993). Positioned between the neurosensory retina and the choroid, the RPE uses highly organized intercellular junctions to regulate the transport of nutrients, ions, and water between the retina and the choroid. This barrier maintains the immune privilege of the eye, creating a controlled environment that protects retinal neurons from potential pathogens and inflammatory damage. Additionally, it plays a key role in homeostasis, ensuring that the retinal environment remains optimal for photoreceptor function (Klettner & Dithmar, 2020).

4.2. Retinal pigment epithelial functions in the visual cycle

The RPE plays several critical roles in maintaining retinal health and function, particularly within the visual cycle. This biochemical process regenerates retinal, a molecule essential for vision. Light absorption by visual pigments in photoreceptors converts 11-cis-retinal to all-trans-retinal, initiating the phototransduction cascade and sending visual signals to the brain. All-trans-retinal is then reduced to all-trans-retinol and transported to the RPE, where it is converted back to 11-cis-retinal by the RPE-specific 65 kDa enzyme (RPE65) (Bok, 1993; Kwon & Freeman, 2020; Yang et al., 2021).

One of the main activities of RPE cells is the daily phagocytosis of shed photoreceptors' outer segment (POS) fragments (Figure I-5B) (Lakkaraju et al., 2020; R. W. Young & Bok, 1969). This process is crucial for the renewal and maintenance of photoreceptor cells, which are essential for the functionality of the retina and vital for proper vision. The number of POS per RPE cell is not constant within the eye, with an average of 25-30 POS per RPE cell in the central and macular area, decreasing towards the periphery (approximately 15 POS) (Volland et al., 2015), indicating a gradient of functional demand.

For POS phagocytosis, RPE cells use an evolutionary conserved molecular machinery that is shared with other cell types (Klöditz et al., 2017). The phagocytic process involves the recognition, binding, and ingestion of the shed POS, which are then degraded and recycled. The presence of phosphatidylserine (PtSer) on the surface of the shed POS acts as an "eat me" signal, initiating the engulfment by the RPE (Figure I-5C) (Ruggiero et al., 2012). This recognition is mediated by integrin receptors, particularly

αvβ5 integrin, on the apical surface of the RPE. Specifically, the integrin ligand MFG-E8 (milk fat globule-EGF factor 8) bridges PtSer on POS with apical αvβ5 integrin receptors on the RPE, facilitating the phagocytosis (Finnemann, 2003; Kwon & Freeman, 2020; Nandrot et al., 2004). MFG-E8, a secreted glycoprotein, can bind to αvβ3 and αvβ5 integrins via its RGD motif (Hanayama et al., 2002). Mice deficient in αvβ5 integrin fail to exhibit the coordinated daily burst of RPE phagocytosis and subsequently develop age-related blindness (Nandrot et al., 2004). This interaction triggers the activation of focal adhesion kinase, which subsequently stimulates the engulfment receptor Mer tyrosine kinase (MerTK) (Feng et al., 2002; Finnemann, 2003). Activation of MerTK requires its extracellular ligands, Protein S and Gas6, and is essential for POS internalization.

Once recognized, the RPE extends its membrane around the POS, forming phagocytic cups with the help of F-actin structures (Figure I-5C, D) (Yingyu Mao & Finnemann, 2015). The assembly of these cups is controlled by the Rho GTPase family. Inactivation of the RhoA pathway is a crucial downstream effect of MerTK signalling, such that manipulating cytosolic ROCK activity can restore phagocytic capacity to MerTK-deficient RPE (Yingyu Mao & Finnemann, 2021). Additionally, the phagocytosis process activates Rac1, which promotes the nucleation of Arp2/3-branching of the F-actin cytoskeleton (Yingyu Mao & Finnemann, 2015, 2021). While branched networks of F-actin propel and advance broad regions of the plasma membrane, they must be stabilized and connected to adhered transmembrane proteins to prevent retrograde flow and collapse. These stability points, known as "molecular clutches," limit the slipping of branched F-actin networks and enhance phagocytosis efficiency (Figure I-5D) (Kwon & Freeman, 2020). This process is similar to the integrin-dependent molecular clutch model where F-actin recruitment and reorganization are essential for cellular adhesion to substrates (Mitchison & Kirschner, 1988; Oria et al., 2017).

Overall, POS phagocytosis is a fundamental function of RPE cells that is finely tuned by multiple molecular mechanisms associated with cellular mechanics. This suggests that RPE mechanical status might play a crucial role in maintaining photoreceptor homeostasis and our vision.

4.3. Structural and functional interplay in retinal integrity

Epithelial homeostasis and function largely rely on the balance between cell-cell and cell-ECM adhesion forces. This balance is particularly critical in postmitotic epithelia

like RPE, where the lack of cell division and the natural cell loss are compensated by active tissue remodelling.

The RPE monolayer exhibits morphological heterogeneity within different retinal locations. In the central retina (macula of humans), RPE cells are arranged in a tightly packed, honeycomb-like structure, optimizing support for the high photoreceptor density and visual acuity requirements (Volland et al., 2015). In contrast, towards the retinal periphery, RPE cells become more elongated and less organized, corresponding with a decrease in cell density and the number of cellular neighbours (Bhatia et al., 2016). This gradient in cellular arrangement suggests variations in mechanical status across the retinal landscape.

Maintaining structural integrity is crucial for the RPE to support photoreceptor cells and maintain the blood-retinal barrier. Like other epithelial tissues, the RPE relies on a delicate balance between cytoskeletal elements to preserve cell shape, mechanical stability, and functionality. A rich presence of F-actin stress fibres has been associated with diminished phagocytic activity, whereas a lack of stress fibres coupled with contiguous lateral circumferential F-actin correlates with high phagocytic activity, indicative of a healthy, functional RPE (Müller et al., 2018). In ageing, RPE morphology is significantly impaired, characterized by a decreased cell number and compensatory increases in cell size and multinucleation (Chen et al., 2016; Tarau et al., 2019). These changes suggest an adaptive response to maintain the epithelial continuum necessary for retinal function. However, this adaptation results in reduced functional capacity due to alterations in cytoskeletal dynamics and increased cellular stress. The RhoA-ROCK pathway is known to modulate the cytoskeletal architecture and functional capacity of the RPE. Inhibiting the ROCK pathway has been shown to enhance phagocytic function and improve monolayer mechanics, suggesting therapeutic potential for age-related RPE dysfunction (Yingyu Mao & Finnemann, 2021). These insights highlight the importance of maintaining cytoskeletal balance and monolayer organization for optimal phagocytosis and retinal integrity.

Along with RPE, Bruch's membrane exhibits regional heterogeneity across the retina, reflecting the distinct functional demands of different areas. Bruch's membrane is thinner in the macula, where high-acuity vision occurs, and thicker in the peripheral retina, which supports peripheral and low-light vision (Booij et al., 2010; Curcio & Allen,

1990; Hussey et al., 2022). This variation is due to differences in the collagenous and elastin layers, with the macula having a 3 to 6 times thinner elastin layer that allows for greater flexibility (Booij et al., 2010; Chong et al., 2005). This structural difference correlates with a higher density of photoreceptors in the macula and a thicker RPE layer, which supports the region's specialized function (Boulton & Dayhaw-Barker, 2001; Volland et al., 2015).

Over time, Bruch's membrane exhibits collagen cross-linking, increased thickness and accumulation of minerals like calcium and zinc within the interstitial matrix (Booij et al., 2010). The most notable age-related change in Bruch's membrane is the appearance of drusen, which are local deposits of amorphous extracellular material formed by the aberrant accumulation of lipids and proteins, negatively influencing its permeability (Piskova et al., 2023). These deposits are a hallmark of ageing and diseases like age-related macular degeneration (AMD), where the ECM alterations contribute to disruption of the RPE function and its ability to maintain retinal health.

Overall, the interplay between Bruch's membrane composition and RPE function is crucial for understanding how different retinal regions manage mechanical stress to maintain their integrity and functional capacity. Although some components of Bruch's membrane are known to vary spatially along the visual axis, the influence of the ECM variation on RPE mechanical homeostasis remains an open question.

II. Project aims and objectives

The extracellular matrix (ECM) is crucial for maintaining tissue function and regulating cellular behaviour, particularly in epithelial tissues like the retinal pigment epithelium (RPE). This research aims to characterise how changes in the biochemical composition of ECM laminins—specifically laminin isoforms—affect RPE mechanics and functionality, with a focus on their implications for retinal health and disease.

The primary objective is to determine how different laminin isoforms affect the mechanical properties of RPE cells. This involves studying how different laminin isoforms influence cellular mechanics, including contractility and elasticity, to describe the ECM's role in regulating epithelial mechanical status and maintaining tissue integrity.

Another objective is determining how ECM-defined mechanical gradients within the RPE impact retinal functionality, particularly its ability to perform essential functions, such as phagocytosis of photoreceptor outer segments. This function is vital for vision, and disruptions could contribute to retinal disorders. Understanding how ECM-derived mechanical properties impact RPE functionality will provide insights into how these changes may contribute to retinal disorders.

In summary, this research aims to characterise the relationship between ECM laminin composition, cellular mechanics, and RPE function. By linking specific ECM properties to RPE behaviour, the study offers new insights into the ECM's role in maintaining retinal function, contributing to the broader context of retinal health and disease prevention.

III. Materials and methods

1. Materials

1.1. Cells

***Table III-1**. List of cells.*

Name	Origin	Source of supply	Used passages
ARPE-19	Human retinal pigment epithelial cell line	ATCC, CRL-2302	P9 – P30
hiPSC-RPE (iCells)	Retinal pigment epithelial cells derived from human induced pluripotent stem (iPS) cells	Fujifilm, 01279	P1

1.2. Cell culture supplies, inhibitors, extracellular matrix proteins

***Table III-2.** List of cell culture supplies.*

Cell culture supplies	**Produced by**
Accutase Solution	Sigma-Aldrich, A6964-100ML
Albumin bovine (BSA) Fraction V	Serva, 11930.03
CellAdhere Dilution Buffer	StemCell Technologies, 07183, 100 ml
CELLBANKER 2® freezing media	AMSBIO, 11891, 100 ml
Dimethyl sulfoxide (DMSO)	Sigma-Aldrich, D4540, 500 ml
Dulbecco's Modified Eagle Medium (DMEM)/F-12	Gibco, 31331-028
Dulbecco's Phosphate-Buffered Saline (DPBS) Calcium/Magnesium	Thermo Fisher Scientific, 14040-091, 500ML
Ethylenediaminetetraacetic acid (EDTA)	Sigma-Aldrich, E5134-1KG
FBS Good, EU-approved regions, filtrated bovine serum, 0.2 µm sterile filtered	PAN-Biotech, P40-37500
Gentamicin	GIBCO, 15750-060, 10 ml
Human protein S	Coachrom Diagnostica, pp012A
Hydrocortisone Solution	Sigma-Aldrich, H6909-10ML
KnockOut Serum	Thermo Fisher Scientific, 10828-028, 500ML
MEM α, GlutaMAX™ Supplement, no nucleosides	Gibco, 32561-029
Methyl cellulose	Sigma-Aldrich, M7027-100G
N-2 supplement	Gibco, 17502048
Penicillin Streptomycin Solution	Gibco,15140122
Recombinant Human MFG-E8 Protein, CF	R&D systems, 2767-MF-050
Paraformaldehyde, prilled, 95%	Sigma-Aldrich, 441244-1KG
Taurine	Sigma-Aldrich, T0625

3,3′,5-Triiodo-L-thyronine sodium salt (T3)	Sigma-Aldrich, T5516-1MG
Trypsin-EDTA solution	Sigma-Aldrich, T4049-500ML
Inhibitors	
RHO ACTIVATOR II	Cytoskeleton, CN03-A
ROCK-Inhibitor (Y-27632)	Sigma-Aldrich, 0503-1MG
Extracellular matrix proteins	
Biolaminin 111	BioLamina, LN111-02
Biolaminin 211	BioLamina, LN211-02
Biolaminin 332	BioLamina, LN332-0502
Biolaminin 511	BioLamina, LN511-0502
Human Collagen Type IV, Collagen from human placenta	Sigma-Aldrich, C7521-10MG
VITRONECTIN-XF	StemCell Technologies, 07180, 2 ml

1.3. Chemicals

Table III-3. *List of chemicals.*

Name	**Produced by**
Acrylamide (40%)	Bio-Rad, 1610140
Agarose, universal	VWR International, 35-1020 & 443666A
(3-Aminopropyl)triethoxysilane (APTES)	Sigma Aldrich, 440140-100ML
Ammoniumpersulphate (APS)	Sigma-Aldrich, 248614-100G
Aqua B. Braun, Ecotainer® (ddH_2O)	Braun, 0082479E
Biozym LE Agarose	Biozym Scientific GmbH, 840004
Bis-acrylamide (2%)	Bio-Rad, 1610142
Eco-sil speed, Addition-curing duplicating silicone for dentistry (Dental glue)	Picodent, 1300 7100
Ethanol absolute ≥99,9%	VWR Chemicals, 1.00983.2511P
Fluorescein isothiocyanate isomer I (FITC)	Thermo Fisher Scientific, F1906
Glutaraldehyde (25%)	Sigma-Aldrich, 354400
Glutaraldehyde Fixative	Agar Scientific, AGR1010
Glycerol	Carl Roth, 3783.1
HEPES	Carl Roth, HN77.4
Latex beads, carboxylate-modified polystyrene, fluorescent yellow-green 1.0 um	Sigma-Aldrich, Sigma, L4655
2-Mercaptoethanol	Carl Roth, 4227.2
Mowiol 4-88	Sigma-Aldrich, 81381
Paraformaaldehyd, prilled, 95%	Sigma-Aldrich, 441244-1KG
PBS Tablets	Gibco 18912014

N,N,N′,N′-Tetramethylethylenediamine (TEMED)	Sigma-Aldrich, 411019-100ML
Triton X-100	Sigma-Aldrich, T8787
Tris(hydroxymethyl)aminomethane (TRIS)	Biomol GmbH, T0244
2-Propanol ≥99,7%	VWR Chemicals, 20842.330
Sodium dodecyl sulphate (SDS)	SERVA Electrophoresis GmbH
Sodium hydroxide (NaOH)	Merk, 1064981000

1.4. Labware

Table III-4. *List of labware.*

Name	**Produced by**
Cell Culture Flask, CELLSTAR®, 50 ml (T25)	Greiner Holding, 690160
Cell scraper S, 240mm	VWR International, TPPA99002
Coverslip d=18 mm	Epredia, CB00180RA120MNZ0
Disposal Biopsy Punches 4mm, 6mm, 8mm	PMF medical
Eppendorf® Protein LoBind tubes, 0.5 mL	Eppendorf, EP0030108094
Eppendorf® Protein LoBind tubes, 1.5 mL	Eppendorf , EP0030108116
Eppendorf Tubes 5.0 ml	Eppendorf, 0030119460
Filter tip, sterile, 20 µL/ 200 µL/ 1000 µL	Starlab International GmbH
Flowmi 40µm Cell Strainer	SP Bel Art, H13680-0040
Greiner Cryo.s™ vials, cryo tubes, 2 ml	Greiner Bio-One GmbH, 122280
Nanoindenter tips	Optics11 Life
Parafilm® M	Sigma-Aldrich, P7793
Pipette tips, 20 µL/ 200 µL/ 1000 µL	Sarstedt
Safe-Lock Tibes 0.5 ml, amber	Eppendorf, 0030 121.155
Serological pipette, sterile, 2 mL/ 5 mL/ 10 mL/ 25 mL	Greiner Bio-One GmbH
12 Well glass bottom plates	Cellvis, P12-1.5H-N
24-Well CytoOne® Plate	Starlab, CC7682-7524
35 mm Glass bottom dishes	Cellvis, D35-10-0-N
100 x 20 mm CytoOne® Dish	CytoOne CC7672-3394

1.5. Laboratory equipment

Table III-5. *List of laboratory equipment.*

Devices	**Produced by**
Becton Dickinson (BD) LSR Fortessa Cell Analyzer	BD Biosciences
Chiaro Nanoindenter	Optics 11 Life
Eppendorf 5417R Refrigerated Centrifuge	Eppendorf, Z366021

Field Emission Microscope Quattro S	Thermo Fisher Scientific
Incubator HERAcell™ 150i CO2	Thermo Fischer Scientific, 51032720
Mini centrifuge	Roth T464.1
Zeiss ApoTome.2 Fluorescent Microscope: ApoTome.2 Axio Imager.M2 AxioCam 305 (camera) AxioCam MRm (camera) Filters: 38HE, 43HE, 49, 50 HXP 120 C Objective: Plan-Apochromat 20×/0.8 DIC Objective: Plan-Apochromat 63×/1.4 Oil DIC	Carl Zeiss Microscopy
Zeiss Axio Observer 7 Inverted Fluorescent Microscope: Axio Observer.Z1 7 AxioCam 305 (camera) Filters: 43 Heating Unit XL S2 (Pecon GmbH) Incubator XLmulti S1 (Pecon GmbH) Incubator XLmulti S1 (Pecon GmbH) Objective: EC Plan-Neo-Fluar 20×/0.50 Ph2 Objective: Plan- Apochromat 10×/0.45 Ph1 Solid-State Light Source Colibri 5 TempModule S1 (Pecon GmbH) Vibration isolated workstation	Carl Zeiss Microscopy
Zeiss LSM 710 Duo with Airyscan Confocal Microscope: Axio Observer.Z1 Laser cassette 405 cw (diode laser 405 nm) Laser module LGK 7872 ML8 (Ar: 458, 488, 514 nm) Laser module LGK 7786 P (HeNe: 543 nm) Definite Focus HXP 120 Compact Light Source IsoStation Vibration Isolated Workstation (Newport Corporation) Objective: LD C-Apochromat 40×/1.10 Water Korr UV-VIS-IR Objective: Plan-NeoFluar 20×/0.8 M27	Carl Zeiss Microscopy
UVO Cleaner model 42-220	Jelight Company, Inc.
Additional supplies	
Immersion medium Immersol W 2010	Carl Zeiss Microscopy, 444969-0000-000

Immersion oil Immersol 518 F fluorescence free	Carl Zeiss Microscopy, 444960-0000-000
Objective LD C-Apochromat 40×/1.10 Water Korr UV-VIS-IR	Carl Zeiss Microscopy
Objective Plan-Apochromat 63x/1.4 Oil DIC	Carl Zeiss Microscopy
Piuma & Chiaro Probe – Stiffness 0.025 N/m – Tip Radius 10 µm – Single Ferrule	Optics 11 Life
Plan- Apochromat 10×/0.45 Ph1	Carl Zeiss Microscopy

1.6. Laboratory kits

Table III-6. *List of laboratory kits.*

Name	**Produced by**
Click-iT™ EdU Cell Proliferation Kit for Imaging, Alexa Fluor™ 488 dye	Thermo Fischer, C10337
COMBO RHOA/RAC1/CDC42 activation kit	Cytoskeleton, 3X10R BK030
DC™ Protein Assay Kit II	Bio-Rad, 5000112
LIVE/DEAD™ Fixable Near IR(780) Viability Kit	Thermo Fisher Scientific, L34992
MicroTissues® 3D Petri Dish® micro-mold mixed spheroid kit	Sigma Aldrich, Z764094-6EA
SiR-Actin Kit – Live cell actin probe	Spirochrome, SC001
SiR-Tubulin Kit – Live cell microtubule probe	Spirochrome, SC002

1.7. Antibodies

Table III-7. *List of antibodies.*

Name	**Origin**	**Source**	**Concentration (µg/ml) / Dilution**
Primary antibodies			
Anti-Cytokeratin-8 (TROMA-1)	rat	From Troma-1 cells	Rat serum
Anti-human Desmoglein 2	rabbit	Proteintech, 21880	1:1000
Anti-human laminin 332	rabbit	Gift from Monique Aumailley	Rabbit serum, 1:2000
Anti-human fibronectin	rabbit	Sigma, F3648	2.5
Anti-human ezrin (clone 3C12)	mouse	Abcam, ab4069	20
Anti-human ZO-1	rabbit	Thermo Fisher, 61-7300	5
Anti-integrin α3 (Clone P1B5)	mouse	Merk/Calniochem, CP11L	1-5
Anti-integrin α6 (Clone GOH3)	rat	Santa Cruz, sc-19622 L	1:50-1:500
Anti-integrin β1 (Clone 12G10)	mouse	Abcam, ab30394	1:100
Anti-integrin β4	rabbit	Abcam, ab236251	1:50-1:200
Anti-mouse collagen type IV	mouse	Merck Millipore, AB756P	12.5
Anti-mouse laminin 111 (pan-Laminin)	rabbit	Gift from Lydia Sorokin	Rabbit serum, 1:2000
Anti-mouse laminin α5	rabbit	Gift from Lydia Sorokin	Rabbit serum, 1:1000
Anti-phospho-Myosin Light Chain 2 (Ser19)	rabbit	Cell Signalling, 3671	1:50
Desmoplakin 1/2	Guinea pig	PROGEN Biotechnik GmbH. DP-1	Stabilized antiserum
Anti-RhoA	mouse	Cytoskeleton, ARH05	1:500-1:1000
Antibodies used for adhesion assay			
Integrin β1 (clone P5D2)	mouse	Santa Cruz, sc-13590 L	2000 (1:100)
Integrin β4 (clone ASC-8)	mouse	Merk, MAB2059Z	1000 (1:50)
Integrin αvβ3 (clone LM609)	mouse	Merk, MAB1976Z	1000 (1:50)
Integrin α2 (clone P1E6)	mouse	Merk, MAB1950Z	1000 (1:50)
Integrin α3 (clone P1B5)	mouse	Merk, MAB1952Z	1000 (1:50)
Integrin α5 (clone P1D6)	mouse	Merk, MAB1956Z	1000 (1:50)
Integrin α6 (clone GOH3)	rat	Santa Cruz, sc-19622 L	2000 (1:100)
Antibodies used for flow cytometry			
Integrin β1-PE (clone 12G10)	mouse	Santa Cruz, sc-59827 PE	200 (1 mg for 10^6 cells)

Integrin β4-Alexa Flour 488 (clone A9)	mouse	Santa Cruz, sc-13543 AF488	200 (1 mg for 10^6 cells)
Integrin α3-Alexa Flour 647 (clone P1B5)	mouse	Santa Cruz, sc-13545 AF647	200 (1 mg for 10^6 cells)
Integrin α6-Brilliant Violet 421 (clone GOH3)	rat	BioLegend, 313623	25000 (5 µl for 10^6 cells)
Secondary antibodies			
Anti-mouse-IgG AF488	goat	Invitrogen, A11001	4
Anti-mouse-IgG AF594	goat	Invitrogen, A11005	4
Anti-mouse-IgG AF647	goat	Jackson/Dianova, 111-605-144	10
Anti-rabbit-IgG AF594	goat	Invitrogen, A11012	4
Anti-rabbit-IgG AF647	goat	Molecular Probes, A21235	10
Anti-rat-IgG AF555	goat	Invitrogen, A21434	4
Anti-rat-IgG AF647	goat	Thermo Fisher, A21247	10
Fluorescent stains			
Hoechst 33342		Thermo Fisher, H3570	1:1000
Phalloidin iFluor 647		Abcam, ab176753	1:500
Phalloidin iFluor 488		Abcam, ab176759	1:500

1.8. Plasmid constructs

Table III-8. *List of AAV plasmid constructs.*

Name	**Produced by**
Custom shRNA AAV5 virus (>2x10^{11} GC/ml, 10x25 µl) made from vector pAAV[shRNA]-mCherry-U6>hITGB1[shRNA#1] (Vector ID: VB230129-1083pte)	VectorBuilder
Custom shRNA AAV5 virus (>2x10^{11} GC/ml, 10x25 µl) made from vector pAAV[shRNA]-mCherry-U6>hITGB1[shRNA#2] (Vector ID: VB230129-1084bae)	VectorBuilder
Custom shRNA AAV5 virus (>2x10^{11} GC/ml, 10x25 µl) made from vector pAAV[shRNA]-mCherry- U6>hITGB1[shRNA#3] (Vector ID: VB230129-1085nbd)	VectorBuilder
Scamble control shRNA AAV5 virus (>2x10^{11} GC/ml, 10x25 µl) made from vector pAAV[shRNA]-mCherry-U6>Scramble_shRNA (Vector ID: VB010000-0024wah)	VectorBuilder

1.9. Buffers

Cell culture media

ARPE-19 media:

DMEM/F-12 Glutamax Supplement 500 mL
10% FBS Good, filtrated bovine serum, 0.2 μm sterile filtered 50 mL
1% Penicillin Streptomycin Solution 5 mL

hiPSC-RPE cell culture media:

MEM alpha 93.3 mL (91.3%)
KnockOut Serum 5 mL (5%)
N-2 Supplement 1 mL (1%)
Hydrocortisone, 50 μM 0.11 mL (55 nM)
Taurine sterile solution in ddH2O 50 mg/ml 0.5 mL (250 μg/ml)
Triiodo-L-thyronine (T3) sterile solution for future use (20 μg/ml):
3,3′,5′-Triiodo-L-thyronine (T3) 1 mg
NaOH 1 N 1mL
MEM alpha sterile 49 mL
Dilute the solution 1:1000 immediately before use in MEM alpha
Triiodo-L-thyronine (T3) diluted in MEM alpha 0.07 mL (14 pg/ml)
Gentamicin, 50 mg/ml 0.05 mL (25 μg/ml)

Buffers for hydrogel surface functionalisation

0.5 M HEPES buffer pH 6:

ddH2O 400 mL
HEPES 59.575 g
NaOH 10 M to adjust the pH to 6
ddH2O to achieve total volume of 500 mL

25 mM HEPES buffer pH 6:

ddH2O 400 mL
HEPES 2.978 g
NaOH 10 M to adjust the pH to 6
ddH2O to achieve total volume of 500 mL

PAA hydrogel solutions

Table III-9. *The composition of PAA hydrogel solutions.*

Young's Modulus	**1 kPa**	**4 kPa**	**18 kPa**	**35 kPa**
Total Solution Volume is 15ml	0.03% Bis 5 % Acry	0.1% Bis 5% Acry	0.07% Bis 10% Acry	0.264% Bis 8% Acry
ddH2O	12.78 ml	12.255 ml	10.63 ml	10.02 ml
Acrylamide (40%)	1.875 ml	1.875 ml	3.75 ml	3 ml
Bis-Acrylamide (2%)	225 µl	750 µl	525 µl	1.98 ml

5X Laemmli buffer

TRIS 312.5 mM

Glycerol 50% (vol/vol)

2-mercaptoethanol 25% (vol/vol)

SDS 350 mM

FACS buffer

Stock solution: EDTA 100 mM (1.489 g) in $PBS^{-/-}$ (40 mL)

BSA 3% (1.2 g)

EDTA 5 mM (1:20 diluted stock solution)

$PBS^{-/-}$40 mL

1.10. Software

Table III-10. *List of used software.*

Name	**Developed by**
Affinity Designer Graphic Design Software	Serif
Fiji image processing package	National Institutes of Health, USA
FlowJo	BD Biosciences
GraphPad Prism 10 Software	GraphPad Software, Inc.
Imaris Image Analysis Software	Oxford Instruments
MATLAB & Simulink Software R2021a	The MathWorks, Inc.
Microsoft Office Professional plus 2016	Microsoft
Nanoindenter DataViewer v2	Optics11 Life
ZEN software: 3.3 blue edition, 2.1 black edition SP3	Carl Zeiss

2. Methods

2.1. RPE mechanical heterogeneity in vivo

To perform characterisation of the intercellular stress heterogeneity of retinal pigmented epithelium *in vivo*, a computational force-inference toolkit CellFit written by G. Wayne Brodland was used (Brodland et al., 2014). Briefly, retina flat mounts stained for F-actin as described here (Kozyrina et al., 2024) were imaged using Plan-Apochromat 63 x/1.4-NA, DIC M27 oil immersion objective on Zeiss LSM 710 (Carl Zeiss) confocal microscope with Airyscan capabilities. Obtained images were then segmented and analysed using the following workflow. Briefly, maximum intensity projection was created to catch most of the signal from the cellular membrane, the resulting picture was converted into 16-bit format and saved in the main folder. The membrane outlines were segmented using Seedwater Segmenter (Mashburn et al., 2012) with sigma set to 15 to capture all the cells. The created classification result called "Outline" can now be opened in Fiji software (National Institutes of Health, USA) and segmented using the Trainable Weka Segmentation plugin considering cellular membrane as one class of objects and cytoplasm – as another. The created 8-bit image was converted into a binary mask using threshold, then skeletonized using Skeletonize (2D/3D) Fiji plugin and saved in the main folder. This classified image was, in the end, opened in CellFit, where the output results containing intracellular tension and intercellular pressure values were created as a ".csv" file. The resulting standard deviations of the pressures within one field of view were plotted and statistically compared for different retina regions (centre, mid periphery, far periphery) in GraphPad Prism 10 software.

The same flat-mount retina regions previously imaged for the nuclear marker (DAPI) were further analysed to assess differences in nuclear geometry along the visual axis. Briefly, maximum intensity projections of the nuclear signal were classified using the Trainable Weka Segmentation plugin Fiji, converted into the binary mask and each nucleus was saved as a separate region of interest (ROI). Then, the area, perimeter, major and minor axis, angle, circularity and roundness of all ROIs were measured and compared between the retinal regions in GraphPad Prism 10 software. Additionally, Circular Statistics Toolbox CircStat (Directional Statistics, (Berens, 2009)), (Matlab, MathWorks) was applied to obtain more descriptive directional statistics to better characterize nuclear orientation patterns within the retina.

2.2. Cell culture

ARPE-19

Epithelial ARPE-19 cell line was cultured until confluence in T25 flasks using Dulbecco's Modified Eagle Medium/Nutrient Mixture F-12 (DMEM/F-12, GlutaMAX Supplement, ThermoFisher, 31331-028) containing 10% (vol/vol) Fetal Bovine Serum (FBS, PAN-Biotech, P40-37500) and 1% (vol/vol) Penicillin-Streptomycin (Gibco,15140122). As an initial step of the splitting, a double wash with 5 mM EDTA/$PBS^{-/-}$ solution was conducted to cleanse the cell monolayer. Importantly, the cells were intentionally kept moist after the final washing step and incubated at 37°C in a 5% CO_2 humid atmosphere for 10 minutes allowing the chelate solution to properly bind calcium and magnesium into a hexadentate and weaken cell-cell adhesion. The EDTA solution was then removed, and the Trypsin/EDTA solution (Sigma-Aldrich, T4049-500ML) (1.5 ml for T25 flask at 0.05% concentration) was added to detach the cells. Cell detachment was observed at room temperature within approximately one minute after which medium containing FBS was added at 3.5 ml into a T25 flask. The cell suspension was transferred into a 15 ml falcon tube, centrifuged at 106 g for five minutes and resuspended in an appropriate amount of fresh medium. Finally, the detached cells were seeded onto a fresh cell culture flask at a 1:10 ratio or used as required for subsequent experimental procedures.

hiPSC-RPE

Differentiated human induced pluripotent stem cell-derived retinal pigment epithelial (hiPSC-RPE) cells were obtained from FUJIFILM Cellular Dynamics (Fujifilm, 01279). They were seeded onto 24-well plates pre-coated with 2.5 μg/ml Vitronectin XF (StemCell Technologies, 07180) that was diluted in CellAdhere Dilution Buffer (StemCell Technologies, 07183) at densities ranging from 1600 to 1800 cells/mm^2 after thawing. The cells were cultured to confluence in a humidified incubator set at 37°C with 5% CO_2. Upon reaching confluence, the cells were detached and resuspended in CELLBANKER 2® freezing media (Amsbio LLC, 11891) for cryopreservation at an approximate density of 750.000 cells per vial, stored in liquid nitrogen for future experiments. Cell detachment was facilitated by incubating the cells with 5 mM EDTA in PBS without Ca^{+2} and Mg^{+2} ($PBS^{-/-}$) for 30 minutes followed by treatment with TrypLE Express dissociation agent (Gibco, 12605-010) for five minutes at 37°C. During these steps, all solutions were transferred into a sterile 15 ml falcon tube after incubation to prevent undesired cell loss. Before

seeding, cells were centrifuged at 300 g for 5 minutes and then resuspended in the cell culture media at the required density.

To characterise the cellular proliferation rate, hiPSC-RPE were cultured in a 24-well plate according to the manufacturer's instructions. The cell monolayer was imaged with a 10x objective using an inverted microscope every second day for up to 30 days in culture. Then, the representative ROI of 600x600 pixels^2 or 0.099722992 mm^2 was chosen for every image. The number of cells within every ROI was measured manually using a multi-point tool in the Fiji image processing package (National Institutes of Health, USA). For this step, I used cells from freshly thawed commercial vials (P0) and cells that had been split and plated once (P1).

For the main experiments, cells were thawed, cultured for up to two weeks until confluence, and then used according to specific experimental conditions. The hiPSC-RPE medium consisted of MEM α (Thermo Fisher, 32561-029), 5% (vol/vol) knock-out serum replacement (Gibco, 10828-028), 1% (vol/vol) N-2 supplement (Gibco, 17502-048), 55 nM hydrocortisone (Sigma-Aldrich, H6909), 250 µg/ml taurine (Sigma, T0625), 14 pg/ml triiodo-L-thyronine (Sigma, T5516), and 25 µg/ml gentamicin (Gibco, 15750-060) (see the buffer section). Media exchange was performed every second day to maintain cell viability and functionality throughout the culture period.

2.3. Formation of spheroids

Hanging drop technique

In the experimental procedure, ARPE-19 cells were split according to the above-mentioned protocol, transferred into a 15 ml Falcon tube and centrifuged at 700 rpm (106 g) for four minutes. Following centrifugation, the pellet was resuspended in 3 ml of media, and the resulting cell suspension underwent cell counting in the Neubauer counting chamber. Subsequently, the suspension was appropriately diluted to achieve the desired 3-50*10^4 cells/ml concentration. This calibrated cell density serves as the foundation for the subsequent steps.

In preparation for the experimental setup, small drops (ranging from 25 to 30) of the 20 µl cell suspension were carefully dispensed onto the lid of a sterile cell culture Petri dish. The cell suspension was used in a concentration of 3, 20 or 50*10^4 cells/ml resulting in 600, 4000 or 10000 cells per droplet. To create a humidified environment for cell growth and interaction, 5 ml of PBS$^{-/-}$ was added to the bottom of the Petri dish.

For the final step, the Petri dish lid was quickly inverted, now covered with cell drops, onto the PBS-filled dish. This construction was then placed in an incubator set at 37°C with a 5% CO_2 and 95% humidity environment. The incubation period spans from three up to 20 days according to the initial cell density (see results chapter), allowing for optimal cell growth, interaction, and observation of experimental outcomes.

Formed spheroids were then transferred into a 12-well glass-bottom plate covered with 35 kPa polyacrylamide hydrogel (PAA) to allow nutrient exchange and perform proper visualisation. Initially, each well contained 1 ml of the polymer solution (see buffer section) that was mixed as mentioned in the following chapter (Methods section, subchapter 2.6), polymerised under an inert atmosphere for 30 minutes and sterilised for at least 30 minutes under ultraviolet (UV) light before spheroid transfer. Next, formed spheroids were gently transferred onto the hydrogel using a 1000 µL pipette with a cut tip. Spheroids were then cultured for the next several days while being monitored simultaneously to ensure the formation of a stable 3D structure.

3D MicroTissue moulds (3D Petri Dish)

First, to produce a 3D Petri Dish, an agarose solution of 3.5% (wt/vol) concentration was prepared by dissolving 1.75 g of agarose powder (Biozym Scientific GmbH, 840004) in 50 ml of $PBS^{-/-}$ and heating it in microwave until boiling to fully dissolve. The prepared agarose solution was maintained at 65°C for future use to prevent solidification. Subsequently, 0.5 ml of the prepared agarose solution was slowly added to each mould, any air bubbles should be avoided and removed. After a couple of minutes, the agarose was gelled and moulds were flexed to release the formed 3D Petri Dish. The agarose 3D Petri Dishes were then immersed in a sufficient amount of $PBS^{-/-}$ and sterilized under UV light for a minimum of 30 minutes to prevent contamination during subsequent experimental procedures. Before cell seeding, agarose moulds were equilibrated in fresh culture media solution two times for 15 minutes and then transferred into sterile cell culture 12-well plate.

Cell seeding part

After trypsinization, ARPE-19 cells were counted, washed and resuspended at an appropriate concentration. Culture media for seeding contained 2.5 mg/ml of methylcellulose (Sigma-Aldrich, M7027-100G) to increase media viscosity and promote faster spheroid formation. Each mould was filled with 190 µl of cell solution containing

$1.3*10^6$ cells ($6.8*10^6$ cells/ml) to achieve approximately $16*10^3$ cells per spheroid, considering 81 micro-wells within each agarose mould. According to the manufacturer's guidelines, the nominal diameter of the spheroid at this cell density was 500 µm. Similarly, hiPSC-RPE cells, after detachment from the 24-well plate, were washed once and resuspended in 190 µl methylcellulose-containing media. Since the optimal cell density for spheroid formation depends on cell type, hiPSC-RPE cells were cultured at approximately $0.4*10^6$ cells per agarose mould ($2.1*10^6$ cells/ml) or $5*10^3$ cells per spheroid. The bottom of the well plate was then covered with 0.5 ml of cell culture media to avoid agarose dehydration.

Next day after the cell seeding, the surrounding area of the 12-well plate around the agarose mould was gently filled with 1.5 ml of fresh cell culture media (2 ml in total). To prevent undesirable liquid flow and disruption of cell agglomerates, the well plate should be tilted slightly and medium should be added very slowly from the bottom of the well plate. Two days after cell seeding, the media was changed again with fresh media or with bolus-dose addition of laminin 521 or laminin 111 at 10 µg/ml per mould.

2.4. Immunofluorescence staining of spheroids

After the defined incubation time required for the formation and growth of proper spheroids, spheroids were transferred into a 1.5 ml Eppendorf LoBind tube for the immunofluorescence staining. The protocol involved fixation in 2% (wt/vol) PFA for 30 minutes at 4°C with gentle rotation, followed by permeabilization using 0.1% (wt/vol) Triton X-100 in $PBS^{-/-}$ for 30 minutes at room temperature, and subsequent blocking for one hour at room temperature with 1% (wt/vol) BSA in $PBS^{-/-}$ with gentle rotation. Immunostaining procedures included overnight incubation at 4°C with gentle shaking in a solution of the primary antibody, diluted in blocking solution (1% BSA in $PBS^{-/-}$), followed by three 10-minute washes with $PBS^{-/-}$ to remove excess primary antibody. Secondary antibody staining was conducted for two hours at room temperature with gentle shaking, along with the addition of DAPI (1 µg/ml, Invitrogen D1306) for nuclear staining. All antibody stock solutions were centrifuged for one minute in a mini centrifuge (Roth T464.1) to avoid antibody aggregates in the staining solution and ensure better visualisation. Detailed information and concentrations of primary and secondary antibodies that were used can be found in the materials section (see Table III-7). The excess secondary antibody and DAPI were then removed by three 10-minute washes with $PBS^{-/-}$. Samples were transferred into 12-well glass-bottom plates using $PBS^{-/-}$ for imaging.

All steps were conducted with precautions taken to minimize exposure to light during the staining and imaging processes.

For live imaging of spheroids, a fluorogenic SiR-actin cell-permeable probe was used (Spirochrome, SC001) that stains F-actin with high specificity. Briefly, at the desired time point, formed hiPSC-RPE spheroids were transferred into a new sterile agarose mould and incubated in cell media containing 500 nM SiR-actin (1:2000 dilution of 1mM stock solution) for three to four hours. Before imaging, the dye-containing media was removed and samples were immersed into fresh media in sufficient amounts for imaging. Spheroids were transferred into 1% BSA-coated sterile 12-well glass-bottom plates 1% BSA solution for one hour before the imaging. The coating was required to inhibit the adhesion of cells to the glass bottom and disruption of the structure of spheroids. Each condition was imaged for no more than two hours providing us with reliable parameters for the sphericity of the samples. All samples were imaged using Plan-NeoFluar 20×/0.8 M27 objective on a Zeiss LSM 710 confocal microscope with Airyscan capability (Carl Zeiss).

2.5. Analysis of spheroid sphericity

After the abovementioned preparation, fixed or living hiPSC-RPE spheroids were imaged using a Zeiss LSM 710 confocal microscope (Carl Zeiss). Imaged Z-stacks were imported into Imaris Image Analysis Software (Oxford Instruments) to create a 3D reconstruction of the spheroid surface. Then, the projection of the spheroid shape on an imaging plane was characterised in terms of sphericity. The intensity threshold was applied to identify the shape of the spheroid projection, whose perimeter and area were measured by the Particle Analysis plugin in the Fiji image processing package (National Institutes of Health, USA) and used for further calculations.

$$\Phi = \frac{\pi * \sqrt{\frac{4A}{\pi}}}{P} \quad (1),$$

where Φ – sphericity ($\Phi \in (0; 1]$), P and A – perimeter and area of the projection of spheroid.

2.6. *Hydrogel preparation*

In preparation for creating the hydrogel substrates, the glass surface of the Petri dish required a chemical functionalisation (Figure III-1). First, Petri dishes were rinsed for five minutes in a water solution of 0.1 M NaOH (Merk, 1064981000), then thoroughly washed with ddH2O in a large beaker. Next, the dishes were treated with 4% (3-Aminopropyl) triethoxysilane (APTES) (vol/vol) (Sigma Aldrich, 440140) in isopropanol for five minutes, followed by thorough rinsing in ddH2O. To functionalize the amine of APTES with an aldehyde group of glutaraldehyde, each Petri dish was filled with 1% glutaraldehyde (vol/vol) diluted with ddH2O from the 25% stock solution (Sigma Aldrich, 354400). The reaction between amines and glutaraldehyde lasted 30 minutes at room temperature, with subsequent washing of the glassware in ddH2O. Glass-bottom Petri dishes were then dried at 60°C for one hour and stored in a dry, dark place to prevent dust accumulation for up to 2 months.

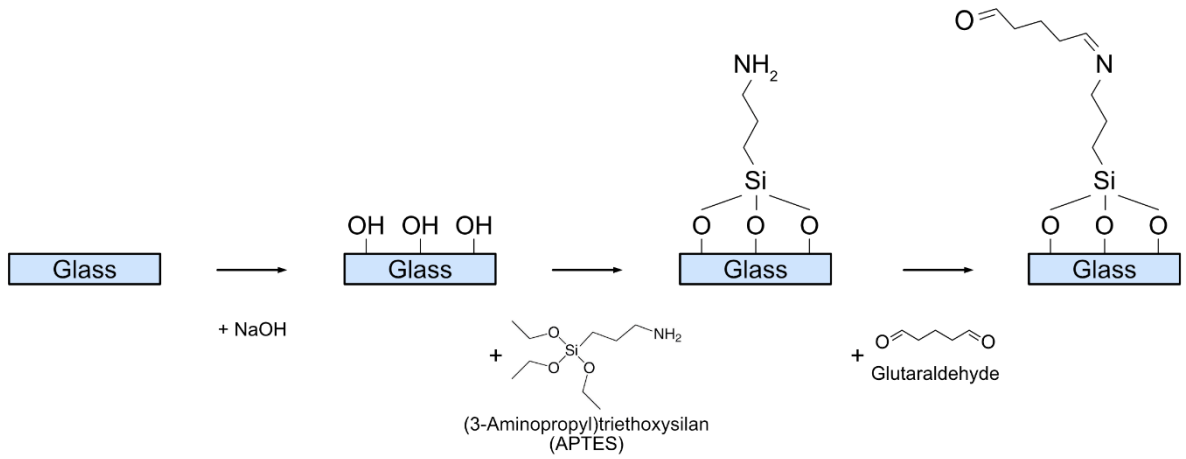

Figure III-1. *Procedure of APTES-glutaraldehyde-based activation of the glass surface.*

For the formation of the hydrogel substrates, acrylamide and bis-acrylamide monomers were crosslinked through a free-radical polymerization process initiated by an ammonium persulfate (APS) and N,N,N′,N′-Tetramethylethylenediamine (TEMED) system (Figure III-2). The starting solution was prepared by using 40% acrylamide (Bio-Rad, 1610140) and 2% bis-acrylamide (Bio-Rad, 1610142) in distilled water. The ratio between acrylamide and bis-acrylamide was adjusted to achieve hydrogels with different Young's modulus (see buffer section). Briefly, the corresponding ratios were 5% / 0.03% (wt/vol) for 1 kPa, 5 % / 0.1 % (wt/vol) for 4 kPa, 10% / 0.07 % (wt/vol) for 18 kPa and 8% / 0.264% (wt/vol) for 35 kPa. For hydrogels intended for traction force microscopy, 1 µm yellow-green carboxylate-modified polystyrene microbeads (Sigma, L4655) were included in the solution.

To prepare 1 ml of polymer solution, 990.5 µl of acrylamide/bis-acrylamide mix was combined with 4 µl Beads (or equal volume of distilled water), 5 µl APS (0.5% (vol/vol)) (Sigma Aldrich, 248614, from a pre-prepared 10% (wt/vol) stock solution in distilled water) and 0.5 µl TEMED (0.05% (vol/vol)) (Sigma Aldrich, 411019) in the order listed. During this step, it was crucial to mix the solution quickly and very thoroughly, while carefully avoiding the formation of any air bubbles, since the presence of oxygen inhibits polymer chain formation. To obtain flat hydrogel substrates, this solution was then pipetted between glutaraldehyde-activated glass-bottom Petri dishes (Cellvis, D35-20-0-N) and a hydrophobic 18 mm glass coverslip. Polymerised hydrogels were rinsed with $PBS^{-/-}$ and left on a shaker overnight to ease the removal of an upper glass coverslip. Then, using a biopsy punch and curved forceps, the unnecessary polymer part was cut out to have a fixed and precise hydrogel area for further experiments.

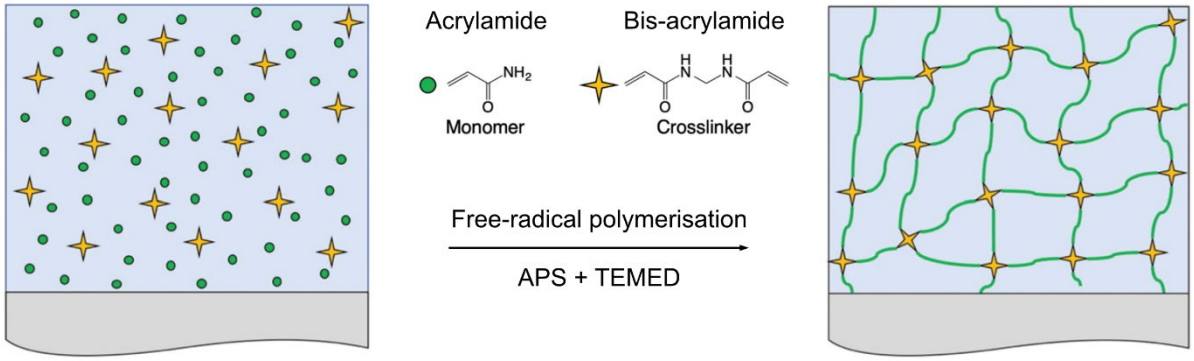

Figure III-2. *Schematic of hydrogel network formation using APS/TEMED-based free-radical polymerisation. Adapted from (Simič et al., 2021).*

2.7. Hydrogel surface functionalisation with protein

Due to the protein-repellent nature of polyacrylamide hydrogels, the ECM protein of interest should be covalently bonded to the hydrogel surface to allow for proper cellular adhesion. The crosslinking reaction of ECM proteins on the hydrogel surface was carried out according to the protocol described by Przybyla L. and colleagues (Przybyla et al., 2016). Briefly, for functionalisation solution, stock solutions of 0.5 M HEPES NaOH pH 6 (see buffer section) and 0.2% (wt/vol) bis-acrylamide in distilled water, 0.2% (vol/vol) tetramethacrylate (Sigma, 408360) and 3% (wt/vol) hydroxy-4′-(2-hydroxyethoxy)-2-methylpropiophenone (Sigma, 410896) in ethanol were prepared (see Table III-11). Acrylic acid N-hydroxysuccinimide ester (Sigma, A8060) was initially dissolved in DMSO (10 mg/ml), kept in aliquots at -20°C and reconstituted before the reaction in 50% ethanol at the final concentration of 0.03 % (wt/vol).

Table III-11. *Components of functionalisation solution for protein coating of the hydrogel (volumes for two dishes). Underlined solutions were degassed.*

Component	**Volume (µl)**
ddH2O	433.3
0.5M HEPES NaOH pH 6	100
Ethanol (100%)	65
Bis-Acrylamide (0.2%)	50
0.2% (V/V) Tetramethacrylate in EtOH	10
0.03% (0.3mg/ml) N-hydroxysuccinimide ester in 50% EtOH	333.3 (10 + 323.3)
3% 2-Hydroxy-4′-(2-hydroxyethoxy)-2-methylpropiophenone in EtOH	8.33
Total Volume (µl)	1000

First, calculating 1 ml solution per two gels, in 5 mL Eppendorf tube 433.3 µl of distilled water, 100 µl of 0.5 M HEPES NaOH pH 6, 65 µl of ethanol absolute and 50 µl of bis-acrylamide were combined (Table III-1, underscored solutions), and degassed under vacuum for 20 min. Then, 10 µl tetramethacrylate, 8.33 µl hydroxy-4′-(2-hydroxyethoxy)-2-methylpropiophenone and 10 µl of the ester, quickly reconstituted in 323.3 µl of 50% ethanol, were added to the degassed solution. The completed functionalization solution was applied over the surface of hydrogels, previously partly dehydrated in a 70% ethanol solution for 5 minutes. The timeframe between reconstitution of the ester in 50% ethanol and transferring the functionalisation solution onto the hydrogels should be minimised. Then, the hydrogels were exposed for 10 minutes to UV light in UVO Cleaner to initiate the reaction. During these steps, it is crucial to protect the solution from the light, and excess of oxygen and be quick since the reaction is time-sensitive and the ester is prone to degradation. For the same reason, the temperature of reactive solutions was critical, thus, everything was kept on ice for controllable conditions.

After the UV initiation of the reaction, Petri dishes were immediately transferred onto an ice surface to slow down the ester degradation. Following sequential double washing with 25 mM ice-cold HEPES buffer (see buffer section) and ice-cold $PBS^{-/-}$ for a cumulative duration of 20 minutes, the gel surface underwent overnight incubation at 4°C with the desired ECM protein solution. Human recombinant laminin-511 (Biolamina, LN511-0202), laminin-332 (Biolamina, LN332-0202), laminin-211 (BioLamina, LN211-02) were prepared at the desired concentration in PBS containing Ca^{2+} and Mg^{2+} ($PBS^{+/+}$),

alone or mixed with 30 µg/ml collagen type IV (Sigma-Aldrich, M7027-100G). The specific details about the concentrations and dilution volumes can be found in Table III-12. Vitronectin (StemCell Technologies, 07180) was used without dilution at a concentration of 250 µg/ml. Subsequently, the resulting hydrogels were washed in $PBS^{+/+}$ and sterilized in PBS solution for 30 minutes under UV light before their use as cell culture substrates.

Table III-12. *Protein dilutions for the hydrogel functionalisation (total volume 50 µl).*

Laminin concentration (µg/ml)	**Laminin (µl)**	**Collagen IV (µl)**	**PBS+/+ (µl)**
30	15	1.5	33.5
20	10	1.5	38.5
10	5	1.5	43.5
5	2.5	1.5	46
2.5	1.25	1.5	47.25
1	0.5	1.5	48

To assess surface protein saturation, gels were chemically crosslinked and coated with laminin-511 at concentrations of 5, 10, 20 or 30 µg/ml in combination with collagen type IV (30 µg/ml) in $PBS^{+/+}$ (see Table III-12). Stock concentration of laminins was 100 µg/ml and of collagen IV – 1 µg/ml. After overnight incubation at 4°C, gels were thoroughly washed with $PBS^{+/+}$ to eliminate unbound proteins, and fixed with 2% PFA for 10 minutes at room temperature. Subsequently, gels were blocked with 1% BSA and stained with primary Anti-mouse laminin α5 (provided by Lydia Sorokin) and secondary Anti-mouse IgG AF594 (Invitrogen, A11005). Throughout each step, gels were washed with $PBS^{-/-}$ for a minimum of one hour. Stained gels were imaged with a 63x Oil-immersion Plan-Apochromat objective on ApoTome.2 Fluorescence Microscope (Carl Zeiss), capturing at least 10 regions per gel. The average intensity of each image was quantified using the Fiji image processing package (National Institutes of Health, USA), and the resulting data were plotted in GraphPad Prism 10.

2.8. Cell seeding on hydrogel

First, the two components of the addition-curing duplicating silicone for dentistry or "dental glue" (Picodent, 1300 7100) were mixed in a 1:1 ratio. Subsequently, small droplets (up to 20 mm in diameter) formed from this mixture were left to polymerise on a flat, sleek glass, or plastic surface for 10 minutes. Then, the inner part of the droplets was cut with a biopsy punch of a certain size (4, 6 or 8 mm in diameter according to the experimental settings). Each side of these dental glue rings underwent UV-initiated

sterilisation in a cell culture plastic Petri dish for a minimum of 30 minutes separately and then together with functionalised hydrogels. In the last step, dental glue rings were placed in contact simultaneously with the wall and bottom of the Petri dish at an angle to the horizontal plane, thereby increasing the efficiency of the sterilisation, as shown in Figure III-3. Hydrogels were coated with protein as described before and sterilised under UV light in $PBS^{+/+}$ containing gentamicin (25 µg/ml). After sterilisation, the $PBS^{+/+}$ was removed from the hydrogels and, after allowing them to dry slightly, gently placed dental glue rings around them using curved forceps, avoiding using high force since the glass bottom of the Petri dish is fragile. The small volume of the media (up to 50 µl) was immediately placed in the dental glue hole on top of the hydrogel surface for equilibration of the hydrogels. These experimental conditions allow us to culture cells as confined monolayers in experimentally reproducible conditions.

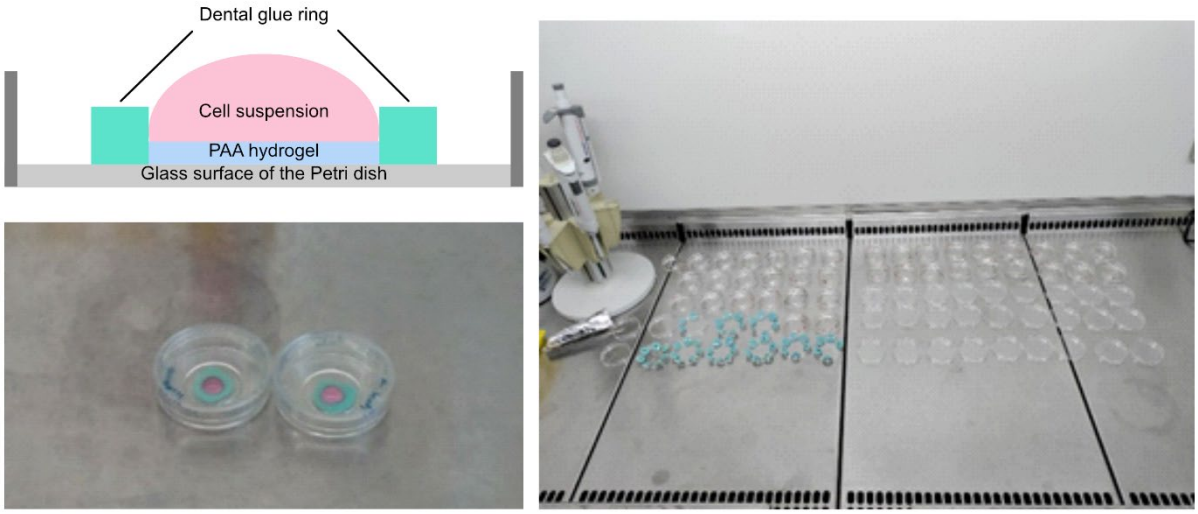

Figure III-3. *Experimental setup for seeding cells on hydrogels.*

ARPE-19 were split according to the abovementioned protocol and seeded on top of the previously functionalised sterile PAA hydrogel (8 mm in diameter) at a density of $5*10^4$ cells or 10^3 cells/mm^2 in 50 µl of the media. Here, APRE-19 were cultured for one week using hiPSC-RPE media that contains specific components and growth factors, required for RPE homeostasis and proper function.

hiPSC-RPE were previously cultured in a 24-well plate until confluence, split using PBS/EDTA and TrypleX (see the cell culture protocol). For seeding onto PAA hydrogels, hiPSC-RPE cells were used at a density corresponding to 5000-6000 cells/mm^2 (see Table III-13), mirroring the RPE density in the human macula, and cultured for one week. The actual seeding density was slightly higher to compensate for the partial cell death along with the preceding experimental steps.

Table III-13. *Amount of hiPSC-RPE cells according to the size of the hydrogel.*

Hydrogel diameter	Number of hiPSC-RPE cells	Volume	Set of experiments
4 mm	80-100*10^3	32 µl	Immunofluorescent staining
5mm	120 – 150*10^3	50 µl	POS internalisation
6 mm	150-180*10^3	72 µl	TFM and Flow Cytometry

2.9. Immunofluorescent staining of cells on hydrogel

Cells grown on hydrogels were initially quickly washed with warm (approximately 37°C) $PBS^{+/+}$ and then fixed using warm (approximately 37°C) 2% (wt/vol) PFA for eight minutes at room temperature. Following fixation, the cells were permeabilized with 0.3% (vol/vol) Triton X-100 for two minutes and subsequently blocked with 1% (wt/vol) BSA for 30 minutes at room temperature. Primary antibodies or Phalloidin-iFluor 647 Reagent (Abcam, ab176759) in $PBS^{-/-}$ containing 1% (wt/vol) BSA were incubated with cells overnight at 4°C. The next day, samples were washed three times for ten minutes each, then secondary antibodies were diluted in a $PBS^{-/-}$ solution containing DAPI (1 µg/ml) (Invitrogen, D1306) and incubated with the sample for 30 minutes at room temperature, followed by a 30-minutes wash. To ensure better visualization and prevent antibody aggregates in the staining solution, all antibody stock solutions underwent one-minute centrifugation in a mini centrifuge (Carl Roth, T464.1). Detailed information and concentrations of primary and secondary antibodies utilized in this study can be found in the materials section (see Table III-7). Imaging of the samples was conducted in a $PBS^{-/-}$ solution to correspond with the immersion type of the objective. After the imaging, the samples were mounted in a Molviol solution to ensure long-lasting protection of the staining. Using a 1000 µl pipette, a small amount of Molviol solution was carefully applied to the centre of the monolayer. Then, I carefully lowered a clean 18 mm coverslip onto the sample, being careful not to trap air bubbles underneath. The mounted samples were kept drying overnight at room temperature and later transferred to a cold room (at 4°C) for longer storage.

For live imaging of the one-week-old RPE monolayers on hydrogels, cells were treated with fluorogenic SiR-actin (500 nM) (same concentration as for spheroids; see Methods, subchapter 2.4). The incubation time of two hours was enough to achieve a sufficient quality of actin labelling. Both fixed and living monolayers were imaged using Plan-Apochromat 40x water immersion objective on a Zeiss LSM 710 confocal microscope with Airyscan capability (Carl Zeiss). Orthogonal projections from Z-stacks obtained with

confocal live-imaging of F-actin were used to measure the average junction height of cultured RPE monolayers for the monolayer stress microscopy using Fiji image processing package (National Institutes of Health, USA).

2.10. Scanning Electron Microscopy

After being cultured for one week on PAA gels with a specific coating, hiPSC-RPE cells were fixed using 3% glutaraldehyde (Agar Scientific, AGR1010) for 4 hours at 4°C, followed by a wash in 0.1 M Sorensen's Phosphate Buffer. Then, the samples were dehydrated via ascending alcohol series of 30%, 50%, 70%, and 90% ethanol for 10 minutes each, followed by three immersions in 100% ethanol. Critical Point Drying was conducted using liquid CO_2. Before imaging, cell monolayers were coated with a 10 nm gold/palladium layer. The imaging was performed using Field Emission Microscope Quattro S (Thermo Fisher Scientific).

2.11. Proliferation assay

Proliferation levels in hiPSC-RPE monolayers on PAA hydrogels were evaluated using the Click-iT EdU proliferation assay kit (Thermo Fisher Scientific, C10337) according to the manufacturer's instructions. Cells were treated with a combination of cell culture supernatant and 5-Ethinyl-2'-Desoxyuridin (EdU) (20 µM in hiPSC-RPE cell culture medium), resulting in a final EdU concentration of 10 µM, and incubated for 24 hours. Following this incubation period, cells were fixed as described earlier and processed for imaging. Since EdU is incorporated into newly synthesized DNA, proliferating cells were distinguished by positive staining of their nucleus with EdU-Alexa Fluor 488. An overview of the entire gel area was captured using the tiles option on an Axio Observer 7 microscope (Carl Zeiss). The ratio of proliferating cells was determined by comparing them with DAPI-positive nuclei and quantified using the particle analysis plugin of Fiji software (National Institutes of Health, USA).

2.12. Photoreceptor outer segment internalisation assay

Photoreceptor outer segments (POS) were harvested in batches from porcine eyes obtained from a local slaughterhouse, following previously established protocols (Parinot et al., 2014). In brief, the eyes were dissected under a red safelight lamp as the sole source of illumination, and the neural retina was extracted. POS were then isolated through retinal mechanical homogenization and subsequent ultracentrifugation in a sucrose gradient. Following isolation, POS were labelled with 2.5 mg/ml FITC dye (Thermo Fisher,

F1906), suspended in DMEM (Thermo Fisher, 31331-028) containing 2.5% (wt/vol) sucrose, and stored in low-bind aliquots at −80°C for future use.

For the internalization assay, POS aliquots were thawed in a water bath, washed with hiPSC-RPE medium, centrifuged at 2300g for 5 minutes, and resuspended in hiPSC-RPE cell medium to achieve a ratio of approximately 10 POS per RPE cell in culture (one aliquot in 191 µl for four 5 mm gels). Human MGF-E8 protein (R&D Systems, 2767-MF-050) and human protein-S (Coachrom, pp012A) were added at concentrations of 2.4 µg/ml and 2 µg/ml, respectively, to facilitate internalization. The total volume of media was chosen to be 50 µl of final solution per one 5 mm gel. Subsequently, hiPSC-RPE monolayers were washed twice with warm media and then incubated for four hours at 37°C with the prepared mixture.

After the incubation period, monolayers were gently washed four times with warm $PBS^{+/+}$ and fixed for fluorescence staining as described previously (see Methods, subchapter 2.9). The imaging of the samples was performed as Z-stacks using a Plan-Apochromat 40x water immersion objective on a Zeiss LSM 710 confocal microscope with Airyscan capability (Carl Zeiss). Phagocytosis efficiency was determined by calculating the projected area of internalized POS divided by the total projected POS area in the same field of view. Internalized POS were identified in orthogonal views from confocal optical sections (0.5 µm) using F-actin staining (Phalloidin iFluor 647) to differentiate between apically bound and internalized segments. Automated analysis was performed using the particle analysis plugin of Fiji software (National Institutes of Health, USA), following the application of a binary mask on the images.

2.13. Traction force and monolayer stress microscopy

Traction force quantification and monolayer stress calculations were conducted following established protocols (Di Russo et al., 2021; Vishwakarma et al., 2018). Initially, a one-week-old epithelial monolayer cultured on a PAA gel containing fluorescent beads was imaged using an Axio Observer 7 microscope (Carl Zeiss) to capture the bead signals. Subsequently, the monolayer was detached using a 0.5% (wt/vol) SDS solution in $PBS^{-/-}$, followed by washing steps and a 20-minute incubation of the gel in cell media to prevent gel shrinkage caused by the solvent change.

The positions of the fluorescent beads within the hydrogel after cell detachment (representing the relaxed state of the gel) were compared with their positions in the gel,

deformed by cells, before detachment (tensed state of the gel). The resolution and bit depth of both images were standardised to 1500*1252 (giving the pixel size of 0.8995) and 8-bit respectively, and the brightness and contrast were uniformly adjusted using the manually written macro in Fiji software (National Institutes of Health, USA) (see Appendix 1). After applying the template matching plugin, bead displacement vectors were calculated using the particle image velocimetry (PIV) plugin in Fiji software (Iterative PIV basic). The PIV interrogation window sizes were set to 128 (SW1), 64 (SW2) and 32 (SW3), with a correlation threshold of 0.8. Traction forces were then derived from these vectors using the Fourier transform traction cytometry (FTTC) plugin in Fiji.

Subsequently, based on the obtained traction force data, average normal stress vectors were computed using a force balance algorithm implemented in MATLAB (MathWorks), as detailed in previous studies (Di Russo et al., 2021; Vishwakarma et al., 2018) (see Appendix 1). For the ARPE-19 monolayers, the average cell height was assumed to be 5 μm, which is comparable to the height of most epithelial cell cultures. Since hiPSC-RPE cells are highly polarised, to ensure computational accuracy, the average cell junctional height for each measured sample was determined using live F-actin staining with SiR-actin (Spirochrome, SC001) and incorporated into the force balance algorithm.

The force correlation length was determined using the characteristic length scale from the spatial autocorrelation function of average normal stresses, as previously described (Hardin et al., 2013) (see Appendix 1). In brief, this length scale reflects how far the force propagates across the monolayer and is obtained from the spatial autocorrelation function, *C(r)*, of the average normal stress. *C(r),* is calculated as:

$$C(r) = \frac{1}{N\ var(\bar{\sigma})} \sum_{i,j=1}^{N} \sum_{|r_i - r_j| = r} \delta\bar{\sigma}_i \,.\, \delta\bar{\sigma}_j \qquad (2),$$

where $\delta\bar{\sigma}_i$ is the local deviation of the average normal stress at position r_i from its spatial mean $\bar{\sigma}_i$and $var(\bar{\sigma})$ is the variance of these deviations. The stress correlation length was identified as the distance at which the stress correlation function became negligible, specifically where the function dropped to 0.01.

2.14. Elasticity measurements of hiPSC-RPE monolayers

Experimental measurements of the monolayer elasticity were conducted using a Chiaro Nanoindenter System from Optics 11 Life, which was integrated into a Zeiss Axio

Observer 7 microscope (Carl Zeiss). This microscope setup included an environmental chamber maintaining a temperature of 37°C throughout the experiments. A preheated probe with a radius of 10 µm and a stiffness of 0.025 N/m (Optics 11 Life) was used to perform indentations in Displacement control mode, penetrating 10 µm into the cell monolayer.

Data analysis was performed using the DataViewer V2.4.0 software (Optics 11 Life). The generated load-displacement curves were analysed by fitting them with a Hertzian contact model based on a predetermined indentation depth ranging from 0 to 3 µm to determine apical stiffness. A Poisson's ratio of 0.5 was applied, and a maximum load of 30% was chosen to set the contact point. Only results exhibiting a proper fit ($R^2 > 0.95$) were considered for the subsequent statistical analysis using GraphPad Prism 10 software.

2.15. Active RhoA levels

To explore the level of active RhoA in hiPSC-RPE cells as a function of laminin isoform and density, a pull-down assay using RhoA/Rac1/Cdc42 Activation Assay Combo Biochem Kit™ (Cytoskeleton, BK030) was performed. After one week in culture, the lysates from cell monolayers were prepared for analysis according to the manufacturer's instructions. Briefly, cell culture dishes were first placed on ice, the medium was aspirated, and samples were washed with ice-cold $PBS^{+/+}$. After aspirating the PBS, dishes were tilted on ice for an additional minute to ensure the removal of all remnants of PBS, as residual PBS could adversely affect the assay. Following this, cells were lysed in ice-cold Cell Lysis Buffer supplemented with 1X Protease Inhibitor Cocktail (25 µl per gel), and lysates were gently harvested with a cell scraper, taking care not to remove the gel from the glass or break it. The resulting lysates were transferred into pre-labelled low-binding 1.5 mL Eppendorf tubes on ice and immediately clarified by centrifugation at 10000 g, 4°C for one minute. Finally, cell lysates were snap-frozen in liquid nitrogen and stored at -80°C for future use.

Before comparing active RhoA levels between different conditions, we measured the concentration of total available protein on one gel after a week in culture using DC™ Protein Assay Kit II (Bio-Rad, 5000112). Every 6 mm gel contained approximately 34.7 µg of protein in lysate meaning that a minimum of 10 identical gels should be pulled together to obtain sufficient quantities for analysis (300 – 800 µg of total cellular protein).

For the pull-down assay, active RhoA should be conjugated with Rhotekin-RBD Affinity beads (Part # RT02-S). Frozen lysates were thawed in a room-temperature water bath and immediately transferred to ice upon thawing. Supernatants of lysates from 11 gels were combined in one 1.5 mL low-bind Eppendorf tube. Equivalent protein amounts of lysate (estimated 300 – 400 µg total cell protein) were combined with a pre-determined amount of Rhotekin-RBD: 30 µl (50 µg) per assay. All further steps were performed in a 1.5 ml low-binding tube. The sample was incubated at 4°C on a rotator at 1100 rpm for one hour. Then, beads were pellet by centrifugation at 5000 g, 4°C for one minute. Without disturbing the pellet, about 90% of the supernatant was transferred to another tube and 200 µl was saved for further analysis of inactive RhoA and the reference housekeeping genes. The saved supernatant volume was boiled for 5 minutes together with 50 µl of 5X Laemmli buffer (final proportion is 1X).

Meanwhile, the beads were washed once with 500 µl of Wash Buffer by pipetting up and down without inverting the tube. Beads were centrifuged at 5000 x g, 4°C for three minutes, the supernatant was removed without disturbing the pellet, and the sample was boiled for two minutes with 15 µl of 2X Laemmli buffer. The samples were analysed by SDS-PAGE and Western blotting.

2.16. Rho pathway manipulations

To tune Rho-dependent pathways, we exposed RPE monolayers to Rho activator II (Cytoskeleton, CN03-A) and the Rho kinase (ROCK) inhibitor Y-27632 (Sigma Aldrich, Y0503). In brief, one-week-old RPE monolayers cultured on soft (4 kPa) hydrogels coated with high laminin density (20 µg/ml) were treated with Rho activator II (1 µg/ml) aiming to enhance actomyosin contractility. Cells were incubated with the drug-containing media for three hours before conducting POS phagocytosis assay or traction force measurements. An equivalent volume of water was used as a solvent control. To suppress actomyosin contractility on surfaces with low laminin density (2.5 µg/ml), the ROCK inhibitor (25 µM) was added into the media one hour before POS phagocytosis assay or traction force measurements. An equivalent volume of DMSO was used as a solvent control. For traction force microscopy, each dish was first imaged under a control condition, then incubated with the drug and imaged again. The reference images of the beads were acquired after the cell detachment. Subsequent analyses were carried out following the procedures outlined in the respective chapters.

2.17. AAV-mediated β1 integrin knock-down

To assess the importance of β1 integrin-mediated adhesion in controlling RPE monolayer mechanics, adeno-associated viral vector (AAV) transduction of shRNA was performed to knock down β1 integrin expression in mature monolayers. The AAV5 serotype was chosen as a capsid for our vector since previously it showed the best transfection efficiency among AAV2.7m8, AAV5, AAV2 and AAVrh10. To perform knockdown, I mixed together pAAV[shRNA]-mCherry-U6>hITGB1[shRNA#1] (Vector ID:VB230129-1083pte), pAAV[shRNA]-mCherry-U6>hITGB1[shRNA#2] (Vector ID:VB230129-1084bae) and pAAV[shRNA]-mCherry-U6>hITGB1[shRNA#3] (Vector ID:VB230129-1085nbd) vectors and used pAAV[shRNA]-mCherry-U6>Scramble_shRNA (Vector ID:VB010000-0024wah) as scramble control (Vector Builder) (see Appendix 2).

Briefly, after four days on a hydrogel, cells were genetically modified. Considering that by that time 6 mm hydrogel contained roughly 150–250*10^3 cells and multiplicity of induction was recommended at 10^4-10^6 genome copy (GC) per cell, 10 µl of virus was used for each gel since every vial contained more than 2x10^{11} GC/ml. Virus aliquots were first thawed on ice, and transduction media for one gel was prepared as follows: 10 µl virus solution, 30 µl of fresh hiPSC-RPE media and 30 µl of conditioned media from the same dish. Then, cell media was aspirated from the petri dish and replaced with 70 µl AAV-containing media inside a dental glue ring. Part of the media around the ring was left intact to maintain the proper humidity level in subsequent steps. After the incubation for 24 hours at 37 °C in a humidified 5% CO_2 incubator, virus-containing media was removed and replaced with a fresh complete cell culture medium. The gene expression analysis and subsequent changes in traction forces were performed on day three and onward. Both transfection efficiency observation and traction force measurements were performed using the Axio Observer 7 microscope (Carl Zeiss).

2.18. Characterisation of cellular adhesion

Cell adhesion assay was adapted and modified based on the method described by Di Russo et al. (Di Russo et al., 2016). Briefly, a confluent monolayer of hiPSC-RPE cells cultured in a 24-well plate underwent detachment. This process involved incubating the cells for 30 minutes with 750 µl of 5 mM EDTA in $PBS^{-/-}$, without enzymatic treatment, to prevent undesired receptor cleavage. Following detachment, the cells were gently washed with an additional 750 µl of EDTA in $PBS^{-/-}$, and the entire solution was transferred into a 15 ml Falcon tube. After cell counting, the suspension was centrifuged at 300 g for

5 minutes. The resulting pellet was resuspended in ice-cold media, constituting half the volume required for the experiment, and transferred to low protein binding tubes.

In blocking experiments, the ice-cold medium was supplemented with a blocking antibody at a concentration of 20 µg/ml and incubated for 15 minutes on ice. Azide-free blocking antibodies used in the experiment are listed in the materials section (see Table III-7, antibodies used for adhesion assay). Subsequently, the cell suspension was diluted (1:2) with an equivalent volume of warm media and promptly transferred onto the hydrogel surface. After a 15-minute incubation at 37°C and 5% CO_2, the hydrogel surfaces were gently washed with warm $PBS^{+/+}$ to remove unattached cells. Then, adhered cells were fixed with 2% (wt/vol) PFA at room temperature for 8 minutes and stained for F-Actin using Phalloidin-iFluor 488 Reagent (Abcam, ab176753) for subsequent analysis. Quantification of attached cells was achieved using the particle analysis plugin in Fiji software (National Institutes of Health, USA), and the results were normalized to the mean value from the control samples within the same set of hydrogels, expressed as a percentage of adhesion.

2.19. Flow Cytometry

After one week in culture, hiPSC-RPE cells were gently detached from the hydrogel substrate. Briefly, cells were incubated for 30 minutes at 37°C and 5% CO_2 in sterile 10 mM EDTA solution in $PBS^{-/-}$(see buffer section), followed by a subsequent treatment with Accutase solution (Sigma Aldrich, A6964) for 15 minutes. Throughout this process, gentle shaking facilitated cellular detachment. Subsequently, cells were delicately rinsed from the surface with an additional 1 ml of EDTA in $PBS^{-/-}$, then transferred into a 15 ml tube and centrifuged for 5 minutes at 300 g. During the detachment, the aspiration of solutions should be neglected to avoid cell loss.

After centrifugation, cells were dispersed in ice-cold $PBS^{-/-}$ and divided into two distinct tubes: one to undergo comprehensive antibody panel staining (see Table III-14), while the other would be specifically stained for β4 integrin. In the first tube, viability staining with the LIVE/DEAD™ Fixable Near IR(780) Viability Kit (Thermo Fisher Scientific, L34992) was conducted during a 15-minute incubation on ice, ensuring protection from light. After centrifugation at 300 g at 4°C for 4 minutes, cells were fixed with 1 ml of 1% (wt/vol) PFA for 5 minutes on ice, then resuspended in 100 µl of $PBS^{-/-}$

containing 3% BSA (wt/vol) and 5 mM EDTA (FACS buffer, see buffer section) for a subsequent 6-minute centrifugation at 300 g at 4°C.

Fluorescently conjugated antibodies (see Table III-7, antibodies used for flow cytometry) were added following the manufacturer's guidelines and incubated with the cells for 45 minutes on ice protected from light. After a thorough washing step, the cells were resuspended in 400 µl of FACS buffer and filtered using the Flowmi(R) Cell Strainer (MERK, BAH136800040) directly into the flow cytometry tube for subsequent measurements.

The stained cells were analyzed using a BD LSRFortessa flow cytometer equipped with 405, 488, 561, and 640 nm lasers (see Table III-14). Data analysis was conducted using the FlowJo software.

Table III-14. *Antibody panel used for flow cytometry experiments.*

Laser		**Channel Name**	**Filter**	**Panel**
Violet – 405 nm	V1	V450	450/40	Integrin α6 – BV421
Blue – 488 nm	B1	FITC	530/30	Integrin β4 – AF488
Yellow/Green – 561 nm	Y/G1	PE	586/15	Integrin β1 – PE
Red – 640 nm	R1	APC	670/14	Integrin α3 – AF647
	R3	APC-Cy7	780/60	Viability

2.20. Statistics

GraphPad Prism 10 Software (GraphPad Software, Inc.) was used to perform statistical analysis of all the experiments. Before further statistical evaluation, the data was tested for normal distribution of the values (normality test). The respective figure captions provide details regarding sample conditions and the specific statistical test used for each dataset.

IV. Results

The extracellular matrix (ECM) is critical to the structural and functional integrity of the retinal pigment epithelium (RPE), which overall supports retinal health and vision. The ECM is not only a scaffold for cellular attachment but also transmits biochemical and mechanical signals that influence cellular behaviour. Understanding the ECM's role in regulating RPE mechanical homeostasis and functionality is essential for advancing our knowledge of retinal health and disease.

Although other models have provided valuable insights, human induced pluripotent stem cell-derived RPE (hiPSC-RPE) models offer a more physiologically relevant system for studying human-specific cellular responses and disease mechanisms. This research project aims to investigate the complex interplay between ECM components and RPE mechanical status and functionality using the hiPSC-RPE model. By using a multidimensional approach, I analysed how variations in ECM properties influence RPE morphology, biomechanics, and functionality.

1. Outer retina characterisation *in vivo*

1.1. Relevant background work

Understanding the mechanical and biochemical landscape of the RPE and its underlying ECM is crucial when studying retinal function and pathology. Previous studies have described the relationship between the retinal structure and its function in relation to visual angle, showing that both mice and humans exhibit the highest density of photoreceptor cells in the central region (macula in humans), which gradually decreases towards the periphery (Volland et al., 2015). In our group, we characterised the mechanical properties of the RPE and the biochemical composition of Bruch's membrane in adult BALB/C mice (25-30 weeks) (Figure IV-1) (Kozyrina et al., 2024). As previously shown (Bhatia et al., 2016; Ortolan et al., 2022), we identified three regions based on their radial distance from the optic nerve: "centre" (300-1200 µm), "mid periphery" (1200-2000 µm), and "far periphery" (2000-3000 µm) (Figure IV-1A). Together with my colleagues, we showed the presence of substantial differences in RPE cell organisation along this radial gradient, in agreement with previous reports (Bhatia et al., 2016; Y.-K. Kim et al., 2021; Ortolan et al., 2022).

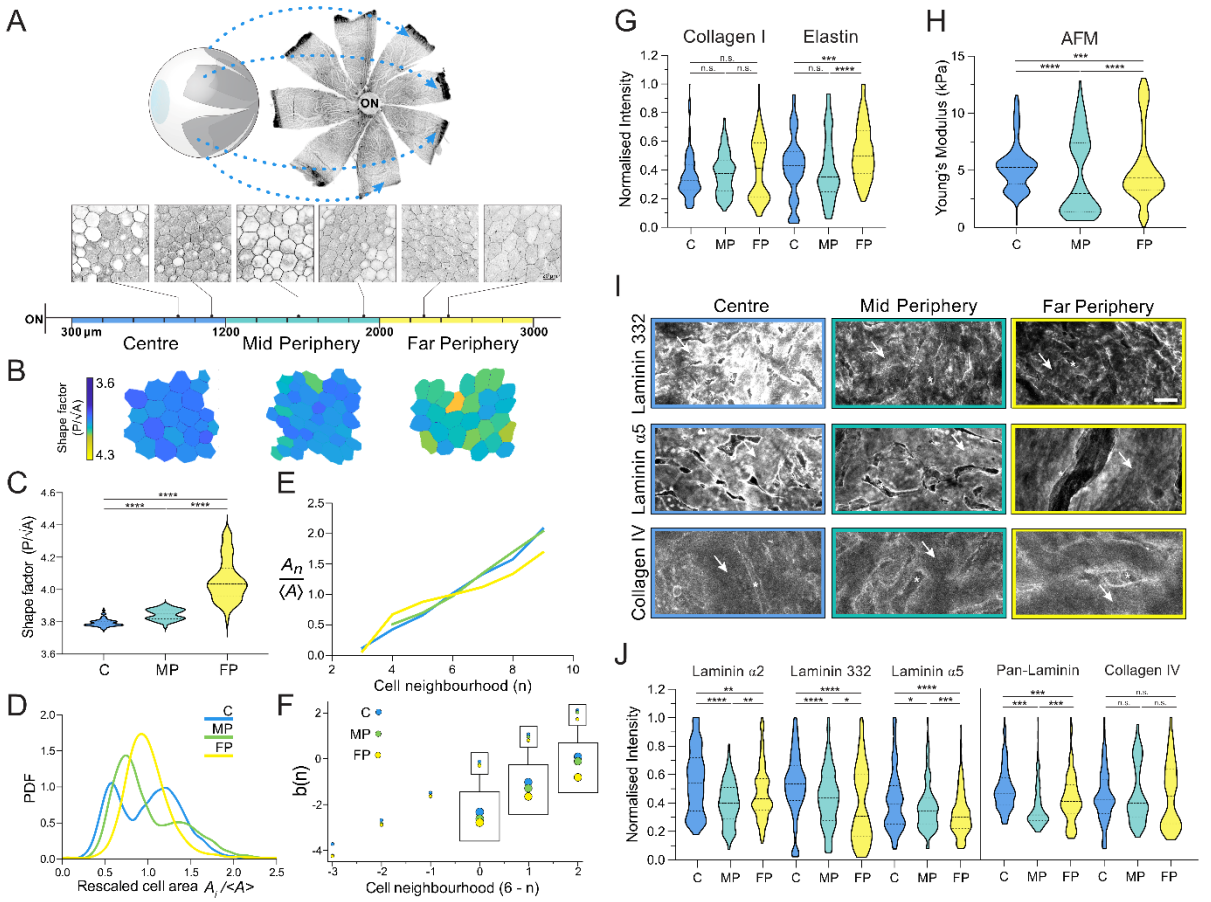

Figure IV-1. *Spatial heterogeneity of murine retinal pigment epithelium topology and Bruch's membrane composition (adapted from Kozyrina et. al, 2024).* ***A.*** *Murine retina flat mount illustrating the regions selected for analysis, with representative F-actin staining of the RPE. Regions were defined by their distance from the optic nerve head: centre (300-1200 µm), mid periphery (1200-2000 µm), and far periphery (2000-3000 µm).* ***B.*** *Representative cell shape index maps for the three regions. The shape index is calculated as the perimeter divided by the square root of the area for each cell ($P/\sqrt{A}$).* ***C.*** *Violin plot depicting the mean RPE shape factors from different regions of the eye, analysed from 7 mice.* ***D.*** *Probability density function (PDF) of the rescaled cell areas, defined by $A_i/\langle A\rangle$, where A_i is the individual cell area and $\langle A\rangle$ is the average cell area within a given image. The analysis includes more than 5500 cells from 3 mice.* ***E.*** *Lewis' law illustrates the relationship between rescaled cell area and the number of neighbours, comparing three different regions from 3 mice.* ***F.*** *Aboav-Weaire's law shows the variation of the topological parameter b(n), depending on the number of neighbours for each neighbouring cell across different retinal regions from 3 mice.* ***G.*** *Violin plots of mean fluorescence intensity of interstitial matrix components in Bruch's membrane. Data were collected from 3 mice and normalized to the highest intensity per mouse.* ***H.*** *Violin plots of the regional Young's modulus of Bruch's membrane from 5 mice.* ***I.*** *Representative immunofluorescent images of Bruch's membrane stained for laminin 332, laminin α5, and collagen type IV. Arrows indicate the RPE basement membrane surface, and stars indicate preparation artefacts. Scale bar: 20 µm.* ***J.*** *Violin plots showing the mean fluorescence intensity of basement membrane components: laminin α2, laminin 332, laminin α5, pan-laminin, and collagen type IV. Each region's quantification includes at least 7 sectors from 3 to 6 mice. Statistical significance was tested using the Mann-Whitney test: *p < 0.05; **p < 0.01; ***p < 0.001; ****p < 0.0001; ns = not significant.*

In the central region, RPE cells display a classic honeycomb arrangement, which transitions to a monolayer of more elongated cells towards the far periphery (Figure IV-1A). To quantify these morphological variations, we performed morphometric analyses of RPE cells across these regions (Figure IV-1B, C, D). The increase in cellular elongation was quantified using a shape factor ($P/\sqrt{A}$) for each cell by dividing the perimeter of the

cell P by the square root of its corresponding area A. This shape factor, which is independent of cell size, is thought to represent epithelial rigidity. It reflects the balance between cortical tension and the energy of cell-cell adhesion, with lower shape factor values indicating a greater influence of cortical tension (Bi et al., 2015). In our system, the cellular shape factor increased from an average of 3.8 in the central region to over 4.0 in the far periphery, indicating increased intercellular tension (Figure IV-1B, C).

Interestingly, distinct cell populations were identified in the central and mid peripheral regions when comparing normalised cell area and perimeter distributions (Figure IV-1D). Further topological analysis by Dr. Maxime Hubert using Lewis' law (Chiu, 1995; S. Kim et al., 2014; Lewis, 1926) and Desh's law (Rivier, 1985) demonstrated different curve behaviours across retinal regions, most notably between the centre and far periphery (Figure IV-1E). To gain deeper insights into monolayer topology, Aboav-Weaire's law was employed (Aboav, 1970, 1980; Chiu, 1995), correlating the number of neighbours *n* of each cell with the average number of neighbours *m(n)* of adjacent cells (Figure IV-1F). This relation describes the mean number of neighbours that neighbouring cells have via the topological parameter *b(n)*:

$$b(n) = (n-6)\mu_{m(n)} - \sigma_n^2 \qquad (3),$$

where $\mu_{m(n)}$ is the mean size of the neighbourhood among the neighbours, and σ_n^2 is the central second moment of the distribution of neighbours, that is, its variance (Kozyrina et al., 2024). This analysis revealed a linear relationship indicative of functional epithelium, with shifts between values suggesting topological variation from centre to periphery (Figure IV-1F). Collectively, these morphometric and topological analyses of over 5500 cells from three mice underscored the existence of regional mechanical heterogeneity in the RPE monolayer.

In epithelium, ECM mechanical cues are primarily dictated by the composition and crosslinking density of the interstitial matrix (Kozyrina et al., 2020). Using confocal microscopy and immunofluorescence staining, my colleague, Teodora Piskova, quantified collagen type I and elastin levels in Bruch's membrane across different retinal regions. The fluorescence intensity patterns observed were consistent with literature reports (Chong et al., 2005; Newsome et al., 1987), showing regional variability (Figure IV-1G). Additionally, atomic force microscopy (AFM) measurements of Young's modulus revealed a highly variable stiffness distribution in Bruch's membrane. The mode stiffness was

5.5 kPa in the centre, 1.5 kPa in the mid periphery, and 4 kPa in the far periphery (Figure IV-1H). Since the mechanical heterogeneity of the ECM does not follow the trend of diminishing RPE functionality, the logical explanation was the absence of a direct link between ECM elasticity and RPE functional demand.

From a biochemical perspective, the basement membrane plays a pivotal role in epithelial homeostasis, primarily through laminin isoforms (Kozyrina et al., 2020). The analysis by Teodora Piskova of laminin and collagen type IV in Bruch's membrane revealed significant regional differences in laminin isoforms, while collagen type IV levels remained constant (Figure IV-1I, J). Notably, laminin α2-containing isoforms displayed a biphasic distribution, with higher fluorescence intensity in the centre and far periphery, and lower in the mid-periphery. Laminin 332 and α5-containing isoforms exhibited the highest intensity in the centre, gradually diminishing towards the periphery, mirroring photoreceptor density and functional demand. Additionally, no laminin α1 or α4 isoforms were detected.

1.2. Mechanical status of RPE in vivo correlates with the decline of Bruch's membrane biochemical components

To further characterise the heterogeneity of RPE organisation among different retinal regions and compare it between mice of different ages, I used the CellFIT, a Python-based package of force inference equations and assessment tools that estimates the forces in triangular cellular junctions based on their geometries (Brodland et al., 2014). This analysis allows the description of intracellular pressure variance in both adult (23-29 weeks) and old (50 weeks) mice along the visual axis (Figure IV-2). Immunofluorescent confocal images of RPE stained for F-actin were made in the central, mid peripheral, and far peripheral regions of the retina (Figure IV-2A, B, top). The images were segmented using a watershed segmentation algorithm (Mashburn et al., 2012), and the resulting binary masks were analysed using CellFIT (Figure IV-2A, B, bottom). Since the results from inference algorithms are relative to the field of view, one could only speculate on the variability of mechanical parameters such as intracellular pressures and cellular membrane tensions within one image. Thus, the standard deviation of intracellular pressures was chosen as the most optimal parameter to describe the heterogeneity of epithelial mechanics.

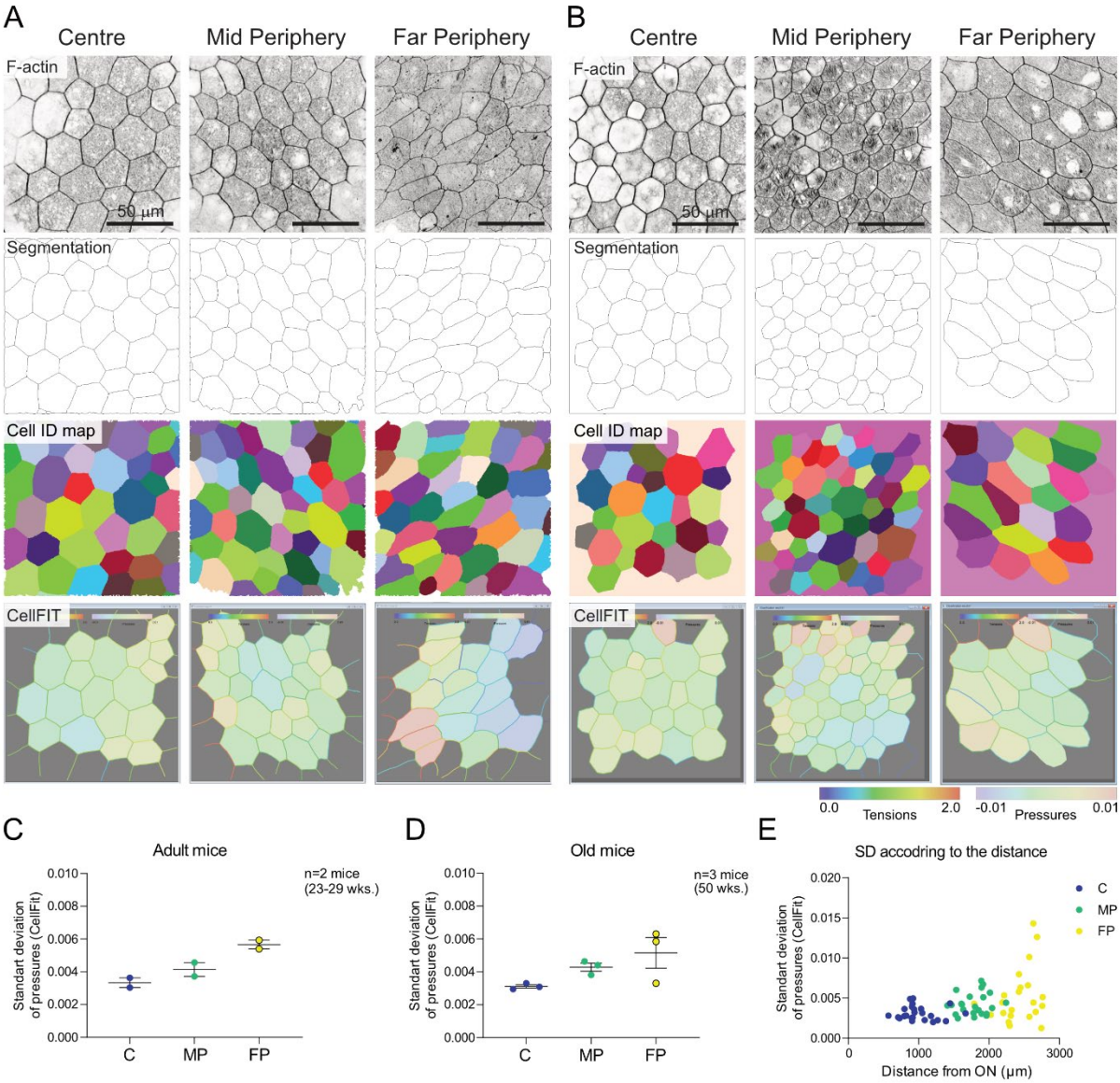

Figure IV-2. *Characterisation of RPE mechanical heterogeneity in vivo for adult (23-29 weeks) and old (50 weeks) mice using CellFIT analysis.* ***A, B.*** *Representative images of RPE actin staining, its segmentation performed in Fiji and resulting CellFIT maps for different regions in the eye for adult (A) and old (B) mice. The regions are divided according to the distance from the optic nerve head: centre (300–1200 µm), mid periphery (1200–2000 µm) and far periphery (2000–3000 µm).* ***C.*** *Scatter dot plot representing standard deviation of intracellular stresses for different regions in adult mice. Each dot shows the average standard deviation ± SEM from at least two independent mice.* ***D****. Scatter dot plots showing the standard deviation of intracellular stresses for different regions in old mice. Data are shown as the average value for each mouse ± SEM.* ***E.*** *Scatter dot plot showing the spatial distribution of standard deviations of pressures in old mice. Each dot represents a single imaged region within the retina. The data were statistically tested with the Kruskal-Wallis test with Dunn's correction for multiple comparisons. Each region contains the quantification of at least 8 eye sectors from two for adult and three from old mice.*

The CellFIT analysis revealed an overall increase in the standard deviation of pressures for both adult and old mice, indicating more variable cell geometry along the visual axis (Figure IV-2C, D). This variability was also evident in scatter plots showing the distribution of these standard deviations relative to the distance from the optic nerve (Figure IV-2E). These results suggest that RPE cells exhibit different mechanical statuses

and become more heterogeneously organised from the centre to the far periphery. This mechanical heterogeneity was observed in both adult and old mice.

1.3. Nuclear geometry varies in RPE between the central and peripheral retina indicating different levels of monolayer strain

The nuclear geometry of cells can provide important insights into the intracellular strain and mechanical properties of tissues (Lammerding, 2011). In confined epithelial monolayers, differences in nuclear shape and orientation may reflect the varying mechanical conditions experienced by cells (Yanlan Mao & Wickström, 2024). Since the overall RPE monolayer has region-dependent mechanical statuses, I was curious to know if nuclear geometry is somewhat affected. To investigate the link between the region-specific spatial position of the cells and the changes in nuclear geometry that they experience, I analysed the nuclear signal from RPE cells from the centre and far periphery within the retina (Figure IV-3). Immunofluorescent confocal images of the epithelial nuclei were obtained and segmented using a trainable Weka segmentation plugin in Fiji (Figure IV-3A). The resulting binary images were then used to quantify the nuclear geometry and perform circular statistics of their orientations. Visible from the images, nuclei in the peripheral region appeared to be more elongated compared to those in the central region. The quantification of geometry shows a reduction in nuclear roundness and circularity, accompanied by a higher aspect ratio towards the far periphery, indicating varying mechanical strains within the RPE monolayer along the visual axis (Figure IV-3B).

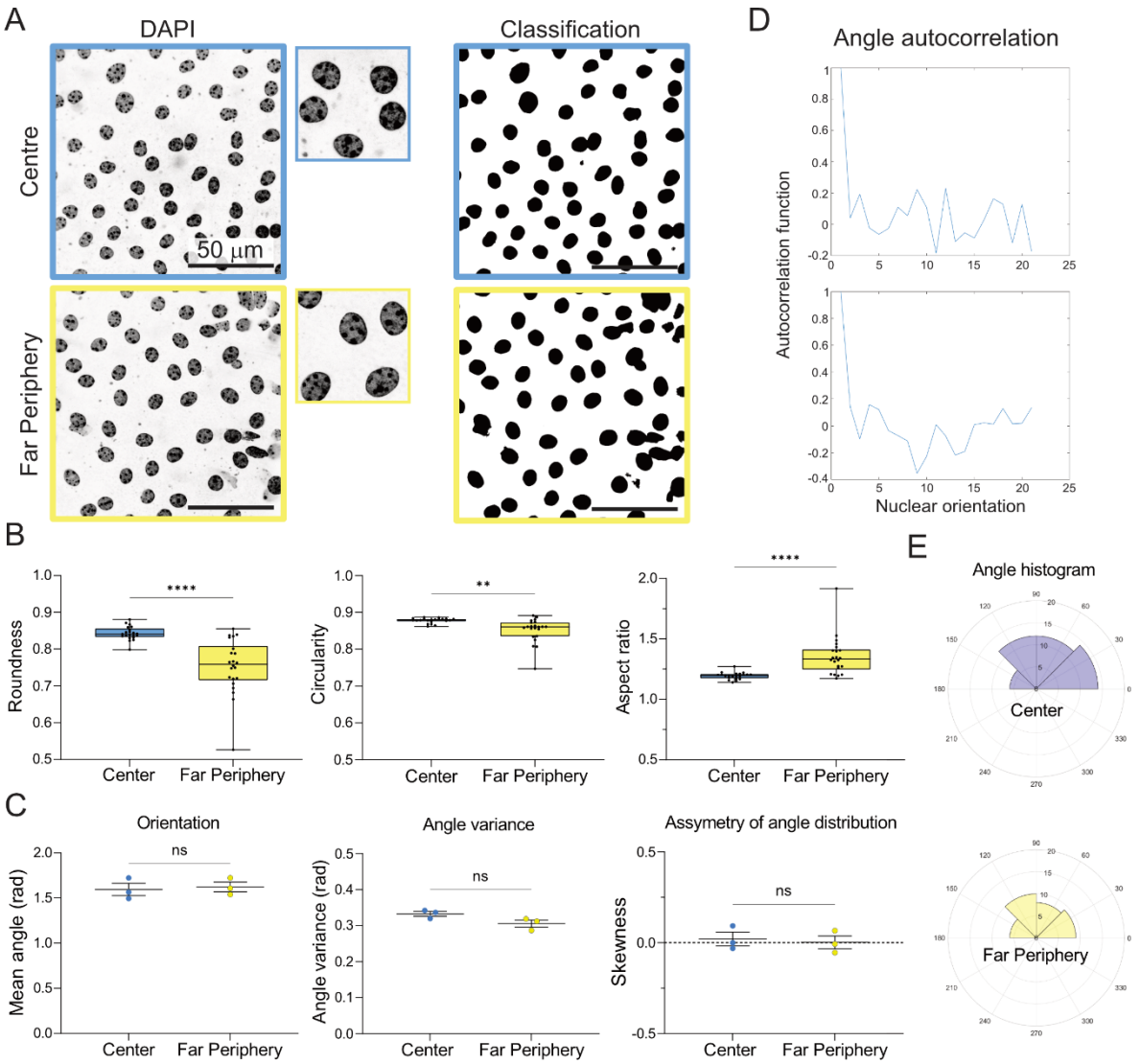

Figure IV-3. *Characterisation of RPE nuclear mechanics in vivo for central versus far-peripheral retinal region.* ***A.*** *Representative images of nuclear staining (DAPI) (left) (images were obtained by Teodora Piskova) and their segmentation using trainable Weka segmentation plugin in Fiji (right) for centre and far periphery.* ***B.*** *Box and whisker plot showing a difference of nuclear geometry in terms of roundness, circularity and elliptical aspect ratio performed in Fiji based on classified images (A). Each dot represents the average value for the particular parameter within the individual image.* ***C.*** *Circular statistics analysis in Matlab shows no difference in nuclear orientation, angle variance and asymmetry of angle distribution for both regions. Each dot represents results within one image (A).* ***D.*** *Representative autocorrelation functions of nuclear orientation within the field of view show no particular direction of the major elliptical axes of the nuclei for both regions. Graphs were performed using circular statistics analysis in Matlab.* ***E.*** *Representative angle histogram showing the orientation of major nuclear axis within the field of view. The statistical analysis was performed using the Wilcoxon matched-pairs signed rank test. For all statistical analysis, each retinal region (centre or far periphery) contains the quantification of four to eight sectors from three individual adult mice.*

To further explore the potential connection between the region-dependent mechanical status and the nuclear orientation, I conducted circular statistics analysis in Matlab (Berens, 2009). Despite the observed elongation of nuclei in the periphery, the mean angle, angle variance, and asymmetry of angle distribution did not differ significantly between the central and far peripheral RPE regions (Figure IV-3C).

Additionally, the circular statistics showed no significant trend in nuclear orientation for both regions, as visible in the autocorrelation functions of nuclear orientation (Figure IV-3D). Representative angle histograms confirmed the absence of a specific orientation pattern (Figure IV-3E). The non-significant results on the nuclear orientation might be attributed to the challenges associated with imaging and segmentation of curved retinal tissue. These technical difficulties could mask potential differences in nuclear orientation.

Altogether, these results highlight the complex relationship between the biochemical composition of Bruch's membrane and the mechanical homeostasis of the RPE, together mediating retinal function and resilience.

1.4. Epithelial mechanics depend on the strength of monolayer tight junctions

Epithelial tight junctions are multiprotein junctional complexes forming continuous intercellular barriers to maintain tissue integrity and mechanics in a homeostatic state (Alberts et al., 2015). We were interested to know whether the removal of the tight junctional proteins, members of the Zonula Occludens protein family, ZO-1 and ZO-2 *in vivo* would result in significant mechanical outcomes. This part of the work was done together with collaborators from the Translational Retinal Research Laboratory (Singapore, Singapore). Prof. Su Xinyi and colleagues provided us with representative immunofluorescent RPE images from mice in which ZO-1 (T1KO), ZO-2 (T2KO) or both (DKO) were knocked out (Figure IV-4).

The imaging was performed using F-actin labelling of the RPE in the central retinal regions (Figure IV-4A). The segmentation and further analysis with CellFIT were performed as described in previous chapters. Notably, the cell monolayer became less uniformly organised which is the most prominent in double knockout mice (DKO). The change in morphology of the cells was so dramatic that the segmentation for CellFIT analysis in proper quality was not possible (Figure IV-4A, right). The standard deviation of intracellular pressures revealed a slight, although non-significant, increasing trend for knocked-out mice when compared to the wild type (Control) (Figure IV-4B). Our observations of cellular morphology were confirmed by an analysis of the cellular shape index ($P/\sqrt{A}$) (Figure IV-4C). The analysis reveals the presence of more stretched and elongated cells in the mice lacking ZO-1 or ZO-2, as well as an increased distribution of values. Overall, the cellular shape index encodes cellular mechanical properties defined

by the balance of cell-cell adhesion and cortical tension, with higher values when the first component is predominant (Bi et al., 2015).

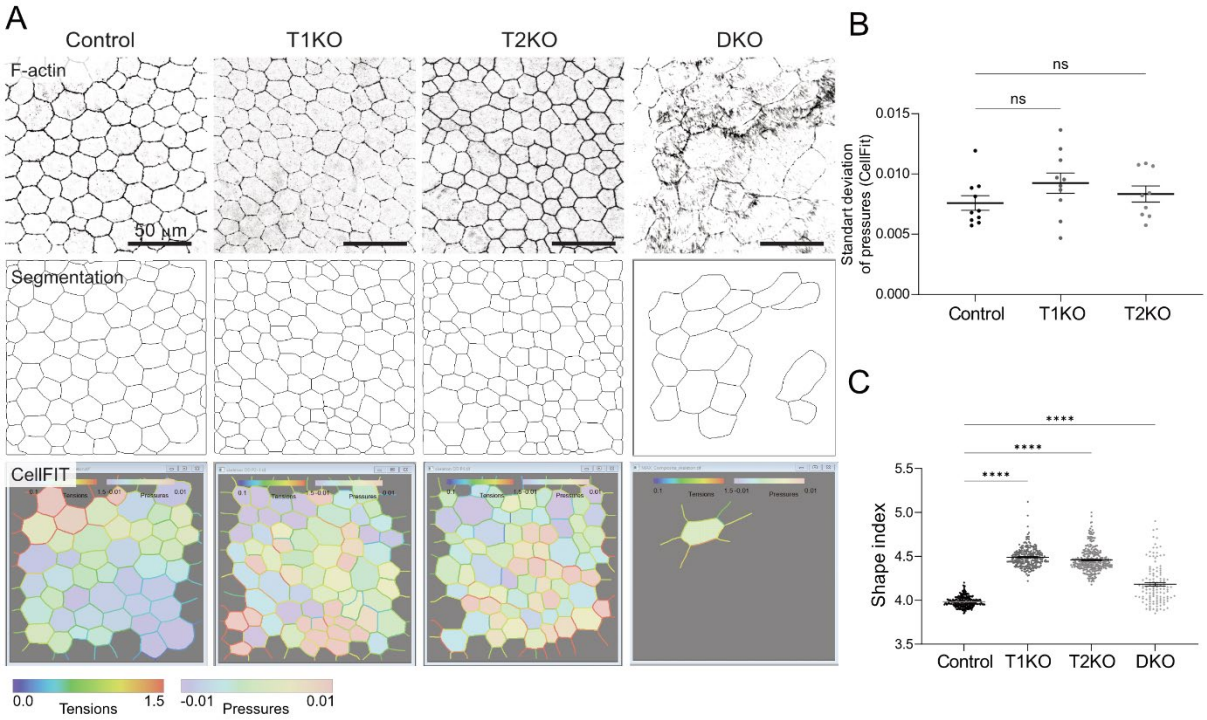

Figure IV-4. *Characterisation of RPE mechanics in central regions for mice lacking ZO-1 (T1KO), ZO-2 (T2KO) and both proteins (DKO).* ***A.*** *Representative images of RPE actin staining (top), its segmentation (middle) and resulting CellFIT maps (bottom) for wild-type mouse (Control), T1KO, T2KO and DKO.* ***B.*** *Scatter dot plot representing the standard deviation of intracellular stresses for Control, T1KO and T2KO mice obtained with CellFIT analysis. Each dot shows data from single image from at least five regions for the left and the right eyes. Statistical analysis was performed using ordinary one-way ANOVA with Dunnett's correction for multiple comparisons compared to the control column.* ***C.*** *Scatter dot plot of the cellular shape factor analysis. Shape index is quantified as $P/\sqrt{A}$ where P and A – cellular perimeter and area respectively. Each dot represents a single cell from at least five different regions of the left and right eyes from one individual mouse. Since the data points were not normally distributed, statistical analysis was performed using the Kruskal-Wallis test with Dunn's correction for multiple comparisons compared to the control column. All data are shown as mean value ± SEM.*

Taken together, this highlights that the alteration in the strength of intercellular adhesion affects the force balance within the epithelium, leading to the overall change in monolayer mechanics. This effect could be explained by the compensational mechanisms within the cell monolayer to maintain tissue integrity in conditions with weaker tight junctions. The absence of significant differences between the control and double knockout mice could be explained by insufficient imaging quality and unreliable segmentation. However, overall larger cells and a trend towards higher shape index are visible for DKO.

2. Three-dimensional approach to study the exclusive role of ECM biochemistry on RPE mechanobiology *in vitro*

2.1. Hanging drop technique provides suboptimal culture conditions for spheroid formation

The characterization of RPE cell topology and morphology within the retina *in vivo* indicated a potential correlation between laminin density within the basement membrane and the mechanical status of the epithelial monolayer (Kozyrina et al., 2024). Due to the complexity and experimental limitations of *in vivo* models, we aimed to develop a relevant *in vitro* system to dissect the role of individual ECM components on RPE behaviour. To explore this relationship, first, I decided to study the exclusive effect of ECM biochemical composition on epithelial mechanobiology using RPE spheroids. The benefit of this suspension system includes eliminating mechanical cues from the environment and focusing exclusively on biochemical signals derived from the ECM. To begin with, I used spontaneously arising human RPE cell line ARPE-19 as a cell culture model to create a robust and reproducible 3D spheroid model for studying RPE cell behaviour and characteristics.

First, I explored a hanging drop technique to facilitate spheroid formation (Figure IV-5) (Foty, 2011). ARPE-19 cells were cultured in suspension within small drops inverted on the lid of a petri dish (Figure IV-5A, left). After a certain time in these drops (formation time), spheroids were transferred onto polyacrylamide (PAA) hydrogel and monitored for morphological changes over three days (Figure IV-5A). I observed a correlation between the initial cellular density and the time required for stable spheroid formation (Figure IV-5B, different density is indicated by the frame colour). For example, spheroids formed from 4000 cells required more than three days to achieve a stable 3D structure (Figure IV-5A). On the contrary, spheroids initiated with 10,000 cells per droplet developed into properly formed structures within the observed timeframe. However, maintaining spheroids for 14 days without media exchange in drops seemed detrimental to cell viability.

Immunofluorescent images of ARPE-19 spheroids revealed a multi-layered cellular structure without luminal formation, as observed by a dense F-Actin network and the presence of cellular nuclei within the spheroids (Figure IV-5C). Orthogonal projections further confirmed the compact multicellular organisation. The observed

gradient in fluorescent intensity across the Z-projection of the spheroid was an imaging artefact arising from the spheroid size and the depth of light penetration.

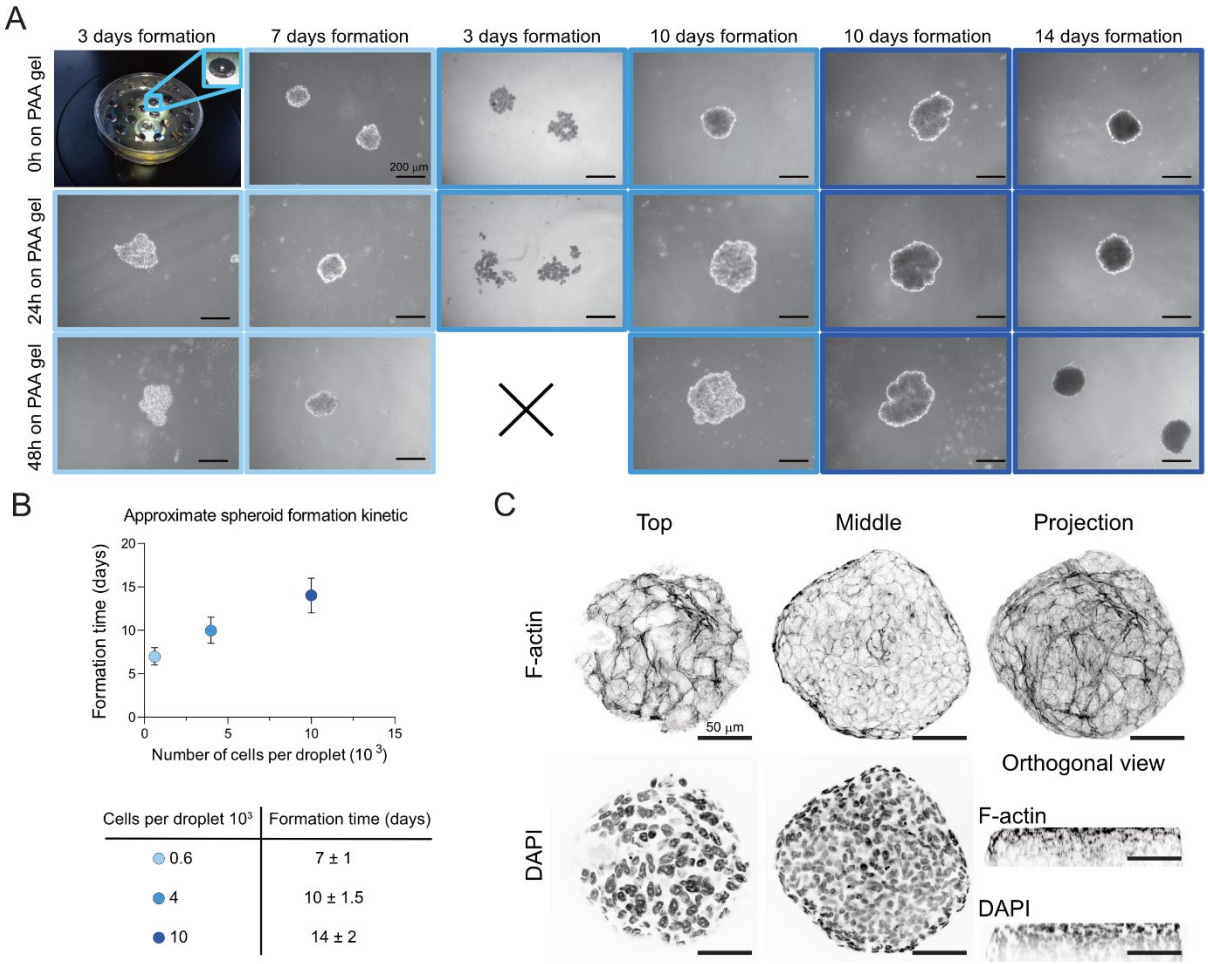

Figure IV-5. *Establishment and characterisation of ARPE-19 spheroids using the hanging drop technique.* ***A.*** *Representative bright field images of ARPE-19 spheroids immediately after transfer onto PAA hydrogel (0h on PAA gel), and after 24h and 48h on hydrogel. These images depict spheroids formed from cell suspensions with different initial cell densities (indicated by frame colour) and various durations in a droplet culture. The colour of the image borders represents the density as follows: light blue – 600 cells per droplet (*$3 * 10^4$ *cell/ml), blue – 4000 cells per droplet (*$20 * 10^4$ *cell/ml), dark blue – 10000 cells per droplet (*$50 * 10^4$ *cell/ml). Scale bar 200 µm.* ***B.*** *Characterization of the formation kinetics of stable ARPE-19 spheroids at various cell densities based on observational data.* ***C.*** *Representative immunofluorescent confocal images of 9 days-old ARPE-19 spheroid stained for F-actin (Phalliodin) and nuclear marker (DAPI), revealing a multi-layered cellular structure without lumen formation. Scale bar 50 µm.*

These results indicate that while the hanging drop technique is effective for initiating the formation of ARPE-19 spheroids, it does not provide optimal culture conditions for their long-term maintenance and development. The technique's limitations, such as insufficient nutrient diffusion and structural instability at lower cell densities, suggest the need for alternative or supplementary methods to achieve more reliable and physiologically relevant 3D RPE cell models.

2.2. *3D Petri dish moulds offer enhanced control for spheroid formation and characterisation*

To optimise the culture conditions for ARPE-19 spheroids, I explored a new approach using 3D Petri Dish moulds. This method aimed to provide a more controlled environment for spheroid formation and characterization compared to the previous technique. Prior to cell seeding, the mould needed to be prepared according to the manufacturer's instructions (Figure IV-6A). The green object indicates the mould, which was filled with red-coloured agarose hydrogel to create the desired structure. Figure IV-6B illustrates the prepared agarose moulds after sterilization and their placement into a 12-well plate for subsequent cell culture experiments.

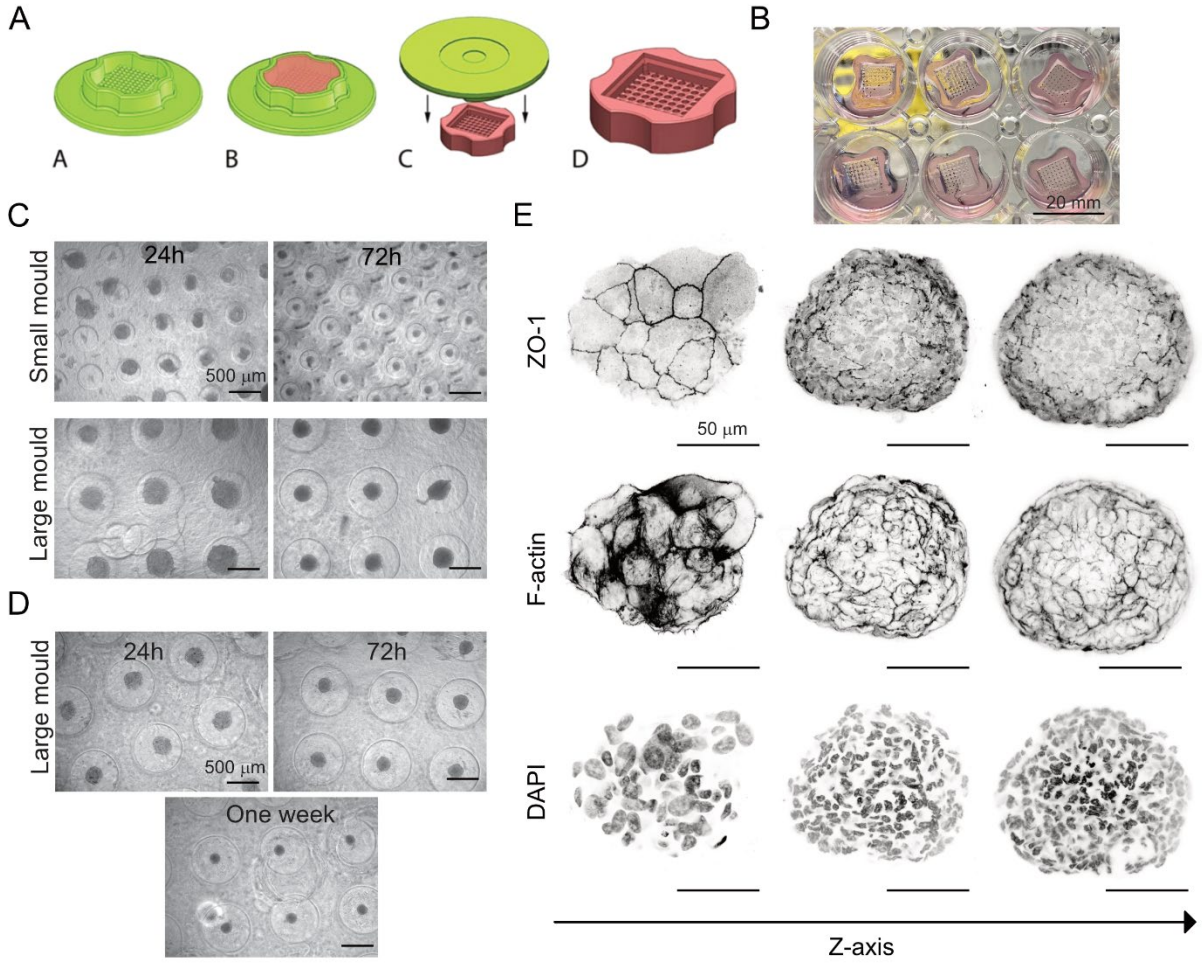

Figure IV-6. *Establishment and characterisation of ARPE-19 spheroids using 3D Petri Dish moulds.* ***A.*** *Schematic representation of mould preparation. The green object represents the mould, into which the red-coloured agarose hydrogel is inserted.* ***B.*** *Formed agarose moulds were sterilised, transferred into a 12-well plate and used in cell culture.* ***C.*** *The bright field pictures of ARPE-19 spheroids 24 hours and 72 hours after cell seeding indicated the comparison of small versus large. The moulds were produced using 90 kPa PAA hydrogel, cell density was used according to the manufacturer's instructions. Scale bar 500 µm.* ***D.*** *Representative bright field images of ARPE-19 spheroids formation in large moulds produced with 3.5% agarose. Scale bar 500 µm.* ***E.*** *Immunofluorescent confocal images of tight junctions (ZO-1), F-actin (Phalloidin) and nuclei (DAPI) for different Z positions within ARPE-19 spheroid (top, middle, bottom). Scale bar 50 µm.*

The use of 3D moulds offered precise control over spheroid size and facilitated extended culture durations. Initially, spheroids seeded in small (16x16 array) and large (9x9 array) PAA moulds were compared over a three-day culture period (Figure IV-6C). However, PAA moulds were floating and had holes due to air bubbles formed during polymerisation, resulting in uneven cell distribution and uncovered spaces. To address these challenges, the protocol was refined by using 3.5% agarose for mould fabrication, which improved the uniformity of spheroids and supported their maintenance in culture for over a week (Figure IV-6D). The larger size of the agarose moulds appeared to be optimal for subsequent handling and comprehensive characterization studies.

Similar to spheroids formed using the hanging drop technique, ARPE-19 spheroids exhibited a multicellular structure without luminal formation, as evidenced by the presence of tight junctions (ZO-1), F-Actin, and nuclei (DAPI) distributed uniformly throughout the spheroid (Figure IV-6E).

These results demonstrate that 3D Petri dish moulds offer a promising alternative for the generation and characterization of epithelial spheroids. The method allows for precise control over spheroid size, morphology, and cellular organization, thereby improving the reproducibility of 3D models for studying ECM-derived RPE mechanobiology. However, given that ARPE-19 cells do not fully replicate the features of RPE cells *in vivo*, there remains a critical need to develop more physiologically relevant culture systems.

2.3. Establishment of hiPSC-RPE culture for the in vitro study of ECM-derived RPE mechanobiology

Human induced pluripotent stem cell-derived RPE (hiPSC-RPE) cells have been successfully used to model mature RPE and study its functionality (Müller et al., 2018; M. J. Song et al., 2023). Building on this, I aimed to explore the role of ECM cues in RPE behaviour using terminally differentiated hiPSC-RPE cells, which closely mimic human-specific retinal processes. By leveraging the versatility of hiPSC-RPE cells in resembling RPE features, and their functionality, they represent a promising *in vitro* model.

Since those cells were never used within our laboratory and maintaining the culture is quite advanced compared to cell lines, I first needed to develop a protocol for properly maintaining these cells in culture. According to the manufacturer's protocol, cells should be seeded in vitronectin-coated vessels at a density of $0.3*10^6$ cells for a 24-

well plate ($1.58*10^5$ cells/cm^2). Figure IV-7A shows representative bright field images of hiPSC-RPE cells cultured for up to 29 days on vitronectin-coated cell culture well plates. Over time, the cells exhibited the characteristic polygonal morphology similar to native RPE cells. Initially, the cells were sparse and scattered (Figure IV-7A, top) but gradually proliferated to form a confluent monolayer with a uniform appearance (Figure IV-7A, bottom).

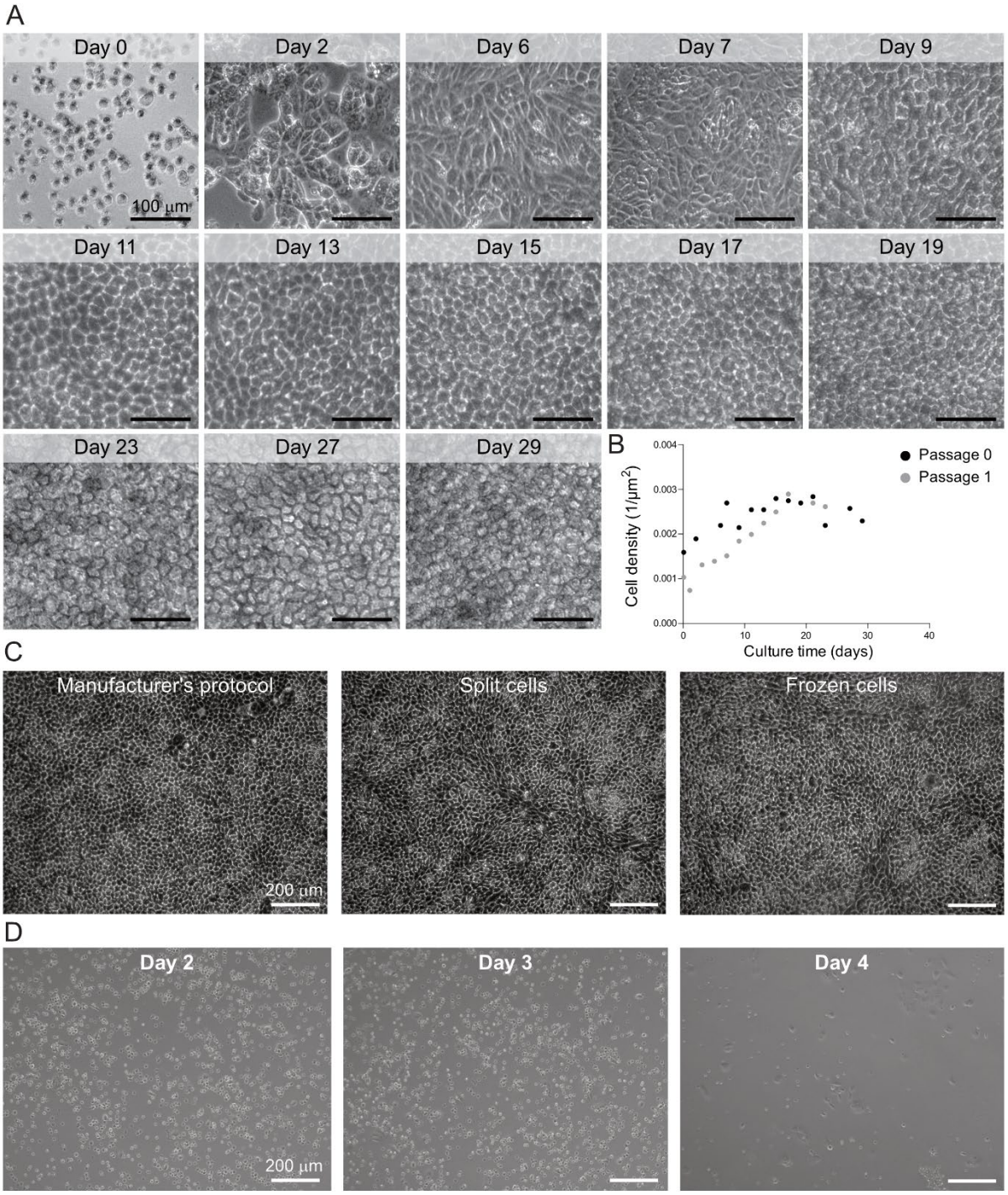

(Description on the next page)

Figure IV-7. *Establishment and characterisation of PSC-derived RPE cells on vitronectin-coated cell culture well plate.* ***A.*** *Representative bright field images of hiPSC-RPE cultured for up to 29 days. Scale bar 100 µm.* ***B.*** *Quantification of the increase in cell density over time for a commercial vial (P0) and for cells that underwent one freezing-thawing cycle (P1).* ***C.*** *Representative bright field images of two-week-old hiPSC-PRE indicating stable cellular morphology upon freezing-thawing cycles and splitting compared to the manufacturer's protocol. Scale bar 200 µm.* ***D.*** *Bright field images of cells cultured on a well plate representing the impact of cell density on monolayer formation. Scale bar 200 µm.*

In the cell culture protocol provided by the manufacturer, cells were typically obtained directly from the commercial vial, thawed, and then seeded onto the substrate. However, ensuring optimal cell recovery after cryopreservation is a critical step, particularly when working with hiPSC-derived lines. Additionally, given the intricate nature of cellular adhesion on artificial matrices such as hydrogels, which can introduce additional stress to cells, I identified the need to refine culturing conditions to improve cell quality and viability.

To address this, I optimised a cell culture protocol on confluent hiPSC-RPE monolayers and implemented a splitting step using incubation with EDTA and TrypleX. If a commercial vial (P0) was used, following this procedure, cells were frozen with CELLBANKER® Cell Freezing Media and stored in liquid nitrogen for future use. This approach allowed us to scale up our total cell number by splitting and freezing P0. Moreover, we managed to develop a controllable and reproducible system where, for every experiment, we thawed P1 cells and culture them until confluence in a well-plate, followed by a final splitting step directly before seeding onto hydrogels.

First, I validated the quality of our optimisation culturing cells on 24-well plates. To estimate the average proliferation rate, the cell density of hiPSC-RPE cultures was quantified over time using a multi-point tool in Fiji (Figure IV-7B). The graph illustrates the increase in cell density from day 1 to day 30 for two groups: cells from a commercial vial (P0) and cells that underwent one freezing-thawing cycle (P1). The P0 group showed a steady increase in cell density, reaching a plateau at approximately day 14. The P1 group also exhibited significant growth, reaching the same maximum density with a slight delay compared to the P0 group at approximately 20 days in culture. However, the proliferation rates were similar. Considering the initially lower cell density, likely due to reduced survival after freezing, this suggests that the freeze-thaw cycle did not significantly impair the proliferative capacity of the hiPSC-RPE cells.

Additionally, cells demonstrate stable cellular morphology after undergoing freezing-thawing cycles and splitting if compared with commercial protocol as observed

in representative bright field images of two-week-old hiPSC-RPE cells (Figure IV-7C). The cells retained their polygonal shape and formed a cohesive monolayer, indicating that the cryopreservation process did not adversely affect their structural integrity.

However, it is crucial to consider that hiPSC-RPE cells require close contact with neighbouring cells for proper maintenance and communication. This requirement, combined with their relatively low proliferation rate (doubling approximately every two weeks), necessitates precise control of seeding density. As observed in bright field images, when cells are cultured on well plates at low density, they struggle to maintain the proliferation rate needed to form a confluent monolayer and may occasionally die due to the lack of cell-cell contacts (Figure IV-7D). This highlights the importance of optimal seeding density for the efficient establishment of hiPSC-RPE cultures.

2.4. 3D Petri dish moulds provide a reliable environment for hiPSC-RPE spheroids culture

Next, I used previously introduced 3D tissue agarose moulds to establish and characterise hiPSC-RPE spheroid culture, aiming to develop a stable model for studying the influence of ECM biochemical composition on spheroid organisation and morphology. After two weeks in culture, cells acquired a retinal epithelium phenotype, indicated by the development of pigmentation (Figure IV-8A). Since epithelial cells strongly rely on intercellular communication, initial cellular density plays a crucial role in the formation of stable 3D structures. Spheroids seeded with 420 cells per spheroid exhibited less compact and cohesive structures unable to form 3D structures compared to those seeded with 2500 cells per spheroid (Figure IV-8B, C).

To further examine the reproducibility of the method during the culture expansion, I compared hiPSC-RPE cells sourced directly from a commercial vial (P0) and cells subjected to one freezing-thawing cycle (P1) regarding their ability to form spheroids (Figure IV-8D). Both groups showed similar rates of spheroid formation and comparable morphology, indicating that a single freezing-thawing cycle did not significantly impact the ability of hiPSC-RPE cells to form spheroids under these conditions. Furthermore, cells from P1 formed more uniform spheroids, facilitating standardization of our culture conditions to ensure consistent treatment before experiments.

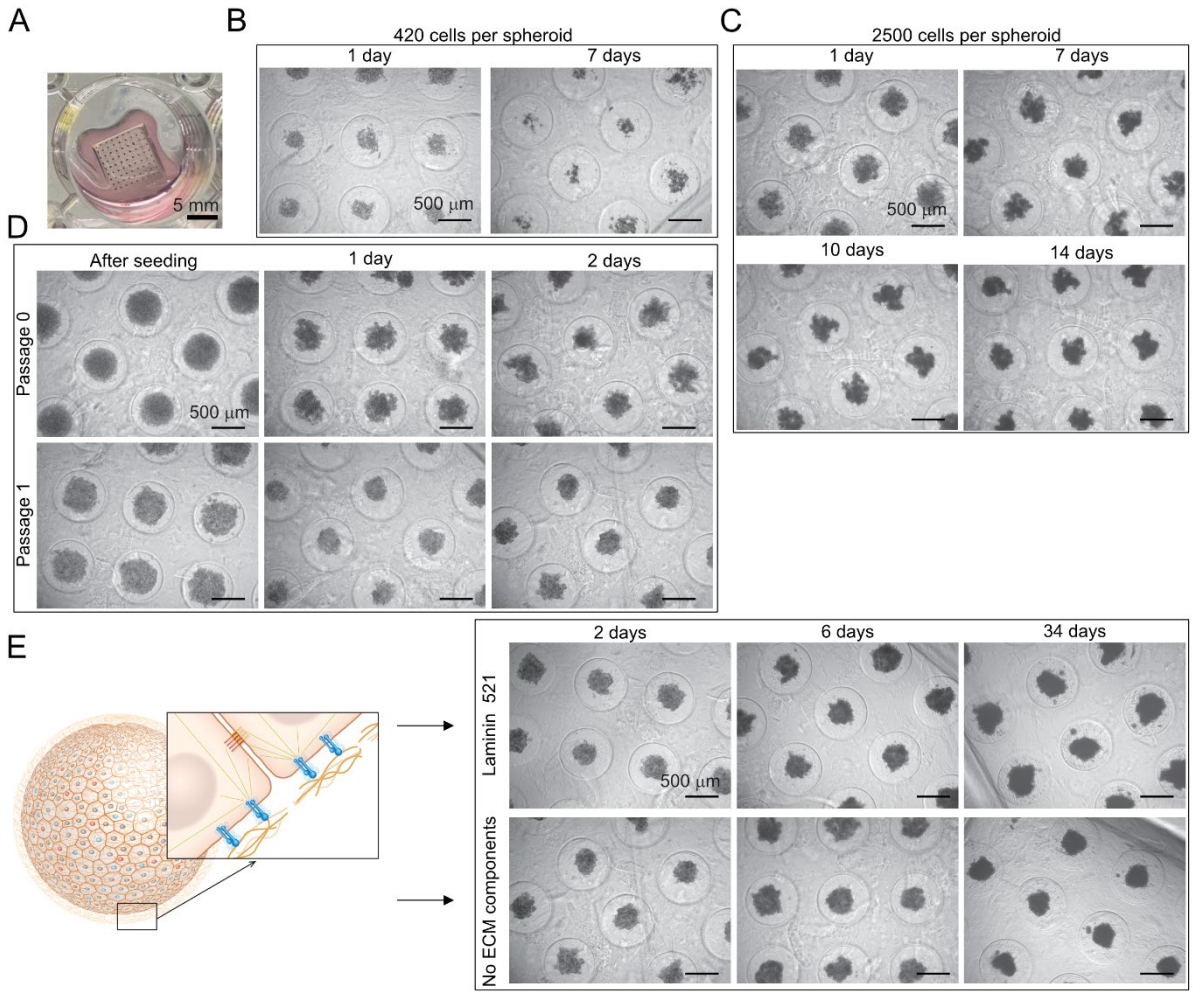

Figure IV-8. *Establishment of hiPSC-RPE spheroids using 3D Petri Dish moulds.* ***A.*** *Two-weeks-old spheroids in agarose mould transferred into 12-well plate showing signs of cellular pigmentation. Scale bar 5 mm.* ***B, C.*** *Bright field images of spheroids in large moulds at low (420 cells per spheroid) (B) and high (2500 cells per spheroid) (C) cell density highlighting the importance of sufficient cell number for stable spheroid formation. Each mould contains 81 micro-wells for individual spheroids.* ***D.*** *Comparison of spheroids formed using cells from commercial vial (P0) and cells after one freezing-thawing cycle (P1) showing similar formation speed and spheroid morphology.* ***E.*** *Experimental strategy and representative bright field images of spheroids used to study the exclusive impact of ECM biochemistry on RPE mechanobiology. After one day of spheroid culture, bolus doses of laminin 521 or laminin 111 were added to the media for further characterisation. The scale bar for bright field images of moulds is 500 µm.*

The experimental approach was aimed at studying ECM biochemical cues exclusively, without the influence of physical cues, on hiPSC-RPE mechanobiology. Spheroids were cultured for one day before exposure to bolus doses of either laminin 521 (composed of laminin α5, β2, and γ1) or laminin 111 (composed of laminin α1, β1, and γ1) (Figure IV-8E). Initial observations suggest that laminin 521 may alter spheroid morphology, leading to differences in size and structure compared to spheroids cultured without ECM component addition (Figure IV-8E).

These data highlighted the versatility and reliability of 3D Petri dish agarose moulds for generating hiPSC-RPE and investigating the impact of specific ECM

components on spheroid morphology. Such advancements are crucial for developing more physiologically relevant *in vitro* models to study RPE mechanobiology.

2.5. ECM components modulate RPE spheroid morphological organisation and mechanics

To further elucidate the role of specific ECM components in controlling structural and functional organisation of hiPSC-RPE spheroids, I performed morphological and immunofluorescent characterisation of spheroids formed under different ECM biochemical stimuli. After several days in viscous media, the cells organised into hollow single-layered spheroids (acini) with a high degree of polarization, as suggested by the internal apical actin belt (Figure IV-9A). These acini were formed without the exogenous addition of ECM to the media, making this an ideal system to exclusively investigate biochemical cues from the ECM without interference from physical cues. Additionally, 3D tissue moulds were convenient for a long-term culture.

As observed in the maximum intensity projections of the F-Actin signal, RPE cells developed an organised actin network illustrating stable structural integrity (Figure IV-9B). Additionally, some morphological alternations might be observed between spheroids without ECM addition and those cultured in the presence of laminin 521.

Characterisation of other molecular markers like Ezrin, ZO-1 (tight junctions) and cytokeratin-8, confirmed the presence of a single-layered structure and illustrated a polarised cellular organisation within the spheroid (Figure IV-9C). However, these results cannot be conclusive since the polarity orientation identified by ezrin seems to be opposite from the actin and ZO-1 polarisation. Further studies are needed to characterise this system to a higher degree. The immunofluorescent signal from cytokeratin-8 illustrates the absence of a proper keratin network formation which might be related to the limitations of the suspension culture, which does not provide sufficient mechanical stimuli (Figure IV-9C). After several weeks in culture, spheroids were positive for ECM components such as Pan-Laminin and vitronectin, presented on the outer side of the acini (Figure IV-9D, E), aligning with the polarity orientation suggested by the actin cytoskeleton and tight junctions.

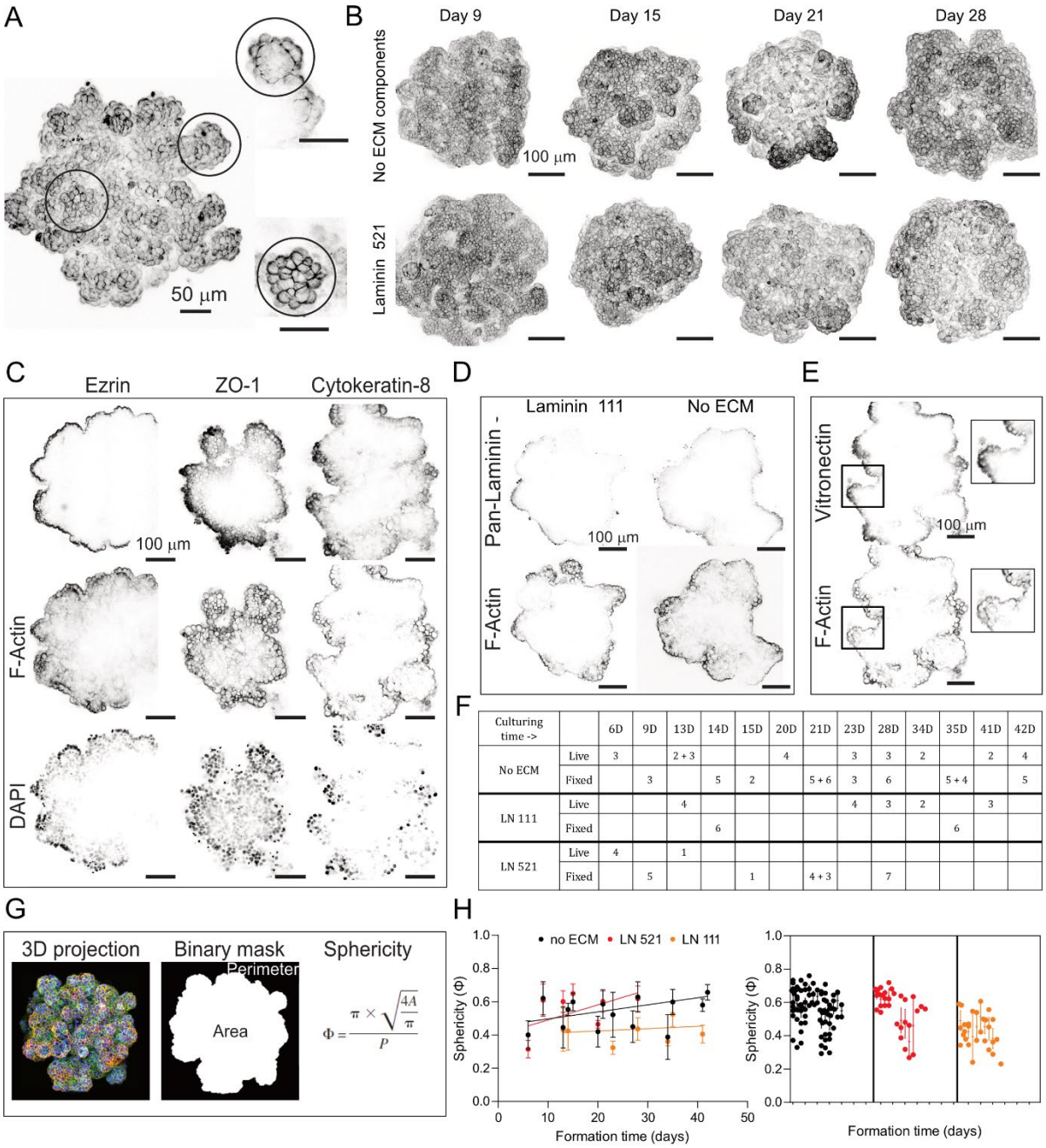

Culturing time ->		6D	9D	13D	14D	15D	20D	21D	23D	28D	34D	35D	41D	42D
No ECM	Live	3		2 + 3			4		3	3	2		2	4
	Fixed		3		5	2		5 + 6	3	6		5 + 4		5
LN 111	Live			4					4	3	2		3	
	Fixed				6							6		
LN 521	Live	4		1										
	Fixed		5			1		4 + 3		7				

Figure IV-9. *Characterisation of the role of ECM biochemical composition on epithelial mechanobiology using hiPSC-RPE spheroids.* ***A.*** *Maximum intensity projection (left) and single z-stacks (right) of live F-actin confocal image of 23-days-old hiPCS-RPE spheroid showing formation of single cell layer (top) and apical actin belt (bottom). Scale bar 50 µm.* ***B.*** *Representative maximum intensity 3D projections of confocal images depicting the F-actin cytoskeleton in spheroids formed either without adding ECM components (top) or with laminin 521 (bottom). Scale bar 100 µm.* ***C.*** *Representative immunofluorescent confocal images of single Z-stack within spheroid showing microvilli (Ezrin), tight junctions (ZO-1), keratin (Cytokeratin-8) and F-actin (Phalloidin) network. DAPI was used as a nuclear marker. Scale bar 100 µm.* ***D, E.*** *Representative immunofluorescent images of RPE spheroids (21 days) stained for ECM components such as Pan-laminin (D) and vitronectin with zoomed-in regions of interest (right) (E). F-actin labelling of the same spheroids was performed using phalloidin. Scale bar 100 µm.* ***F.*** *Table illustrating the number of imaged RPE spheroids used for subsequent analysis of their sphericity.* ***G.*** *Workflow for analysis of spheroid sphericity using Fiji as described in the methods section. Maximum intensity 3D projections of F-actin confocal images (left) were processed using a threshold to generate a binary mask (middle), from which the projected area and perimeter values were extracted using a measurement tool in Fiji. The resulting sphericity was calculated using these parameters as shown here (right).* ***H.*** *A scatter dot plot with linear approximation (left) and nested graph (right) illustrating the sphericity of RPE spheroids relative to the time of spheroid formation upon stimulation with either laminin 521 or laminin 111. The condition without the addition of ECM components was used as a control.*

To characterise the morphological variability associated with ECM-governed signals, spheroids were imaged at different time points regarding the actin cytoskeleton organisation (Figure IV-9F). Next, I created a pipeline to quantify the sphericity of spheroids using the maximum intensity projections of the actin signal and obtaining spheroid area and perimeter to measure the sphericity (Figure IV-9G). Spheroids were imaged with a confocal microscope to acquire better resolution and ensure the accuracy of the measurements. Overall, the shape and sizes of spheroids were very heterogeneous, leading to a high standard deviation of the values (Figure IV-9H).

Qualitative analyses showed that the addition of a single laminin 511 bolus dose to the medium slightly increased the sphericity of the culture compared with controls (Figure IV-9H). On the contrary, the presence of laminin 111 promoted the formation of more irregular and less coherent constructs. This suggests the activation of signalling pathways, which lead to differential cell-cell adhesion and biochemically-driven alteration of spheroid morphology independently from the ECM rigidity.

Altogether, within the 3D Petri dishes, RPE cells formed properly structured spheroids with organized, single-layered cellular architecture, making them reliable and reproducible for 3D culture systems. This also demonstrates the effectiveness of 3D Petri dish moulds in forming stable hiPSC-RPE spheroids. Overall, these preliminary morphological and immunofluorescent characterizations highlight the influence of ECM biochemical composition on spheroid morphology and organization. Further work is required to better quantify spheroid mechanics, including the evaluation of intracellular stresses and 3D imaging to capture the complete spheroid shape. This integrated approach provides valuable insights into the complex interactions between ECM components and epithelial cell behaviour. Thus, this system holds significant potential for advancing our understanding of RPE mechanobiology.

3. Reductionist approach to study ECM-derived RPE mechanobiology *in vitro*

3.1. ARPE-19 as a cell culture model for establishing an in vitro bottom-up approach

In parallel with a three-dimensional system, I was developing another experimental strategy to study the effect of ECM conditions on cellular behaviour. To explore the relationship between individual ECM components and their density variation on RPE mechanobiology, we established a bottom-up approach using PAA hydrogels with

Young's modulus of 4 kPa, which closely mimics the elasticity of retinal ECM. PAA hydrogels offer several advantages as substrates: their optical transparency facilitates microscopy imaging, and their linear elastic stress-strain response within the range of cellular forces allows for the quantification of monolayer mechanics using traction force and monolayer stress microscopy. Additionally, the protein-repellent nature of PAA hydrogels enables complete control over the biochemical composition of the surface coating since protein attachment requires an additional chemical modification step (Funaki & Janmey, 2017). Despite being reductionist by the principle, this approach offers a highly controllable system, closely mimicking the native RPE conditions within certain rational approximations, with more straightforward characterisation and analysis.

For the experimental strategy, retinal epithelial cell monolayers were cultured on PAA hydrogels with defined stiffness and surface coating for one week (Figure IV-10A). As observed *in vivo*, ECM laminins decrease in density from the central part of the retina towards the far periphery. To replicate this, I functionalised the hydrogels following the method of Przybyla et al. (Przybyla et al., 2016), using specific concentrations of laminin, which reached saturation at a coating concentration of around 20 µg/ml (Figure IV-10B).

First, I used the ARPE-19 cell line as a more simplified model of RPE cells. After one week in culture on PAA hydrogels, the cells exhibited a disorganized actin cytoskeleton, as shown in F-actin confocal images (Figure IV-10C). Even after two weeks in culture, F-actin did not resemble the actin structure seen *in vivo* RPE cells (Figure IV-10D). Despite these issues, after one week in culture, ARPE-19 cells demonstrated positive staining for desmoplakin, indicating the formation of desmosomes, and proper keratin network formation, as observed via cytokeratin-8 staining. However, cells formed a multi-layered structure, visible with DAPI nuclear staining, which complicates the calculation of epithelial mechanics (Figure IV-10E). On the basal side, cells expressed epithelial adhesion receptors such as integrin α6, β4 and β1 (Figure IV-10F).

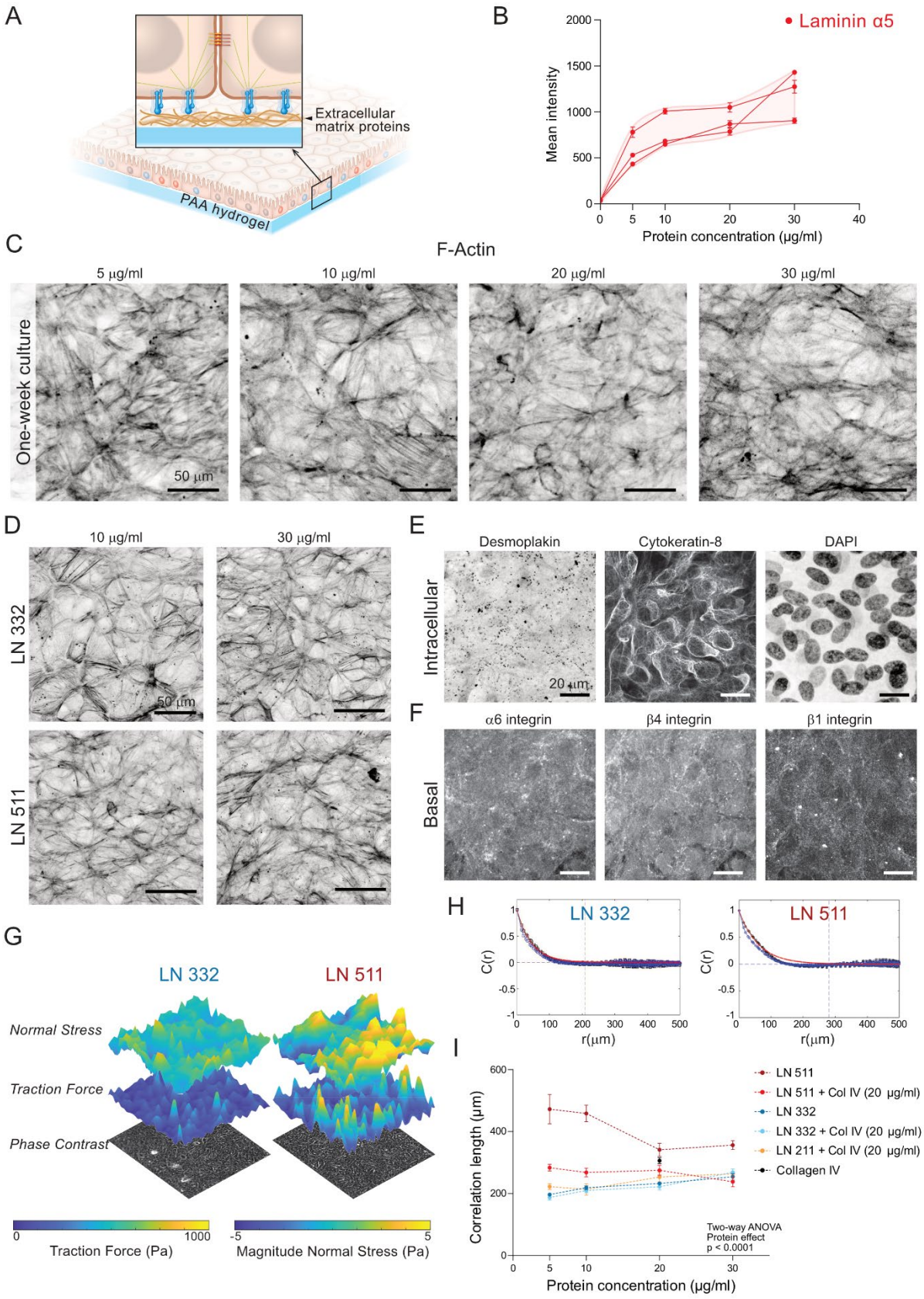

Figure IV-10. *Characterisation of ECM-derived mechanics of ARPE-19 monolayers cultured on soft polyacrylamide hydrogels.* ***A.*** *Schematic representation of the in vitro bottom-up experimental approach using PAA hydrogel surface coated with specific ECM protein as a culture substrate.* ***B.*** *Line graph of the mean fluorescent intensity of the hydrogel surface fixed and stained with laminin α5 antibody right after chemical crosslinking with different concentrations of laminin 511 combined with collagen type IV (30 µg/ml). This*

relation indicates a correlation between laminin concentration and its surface density. Each line represents an individual dilution series. Images were taken from 10 different areas of the gel. Data are shown as mean ± SEM. ***C.*** *Representative actin cytoskeleton confocal images of one-week-old ARPE-19 cells cultured for one week on PAA hydrogel coated with different concentrations of laminin 332. Scale bar 50 µm.* ***D.*** *Representative confocal images of two-weeks-old monolayers showing the heterogeneous organisation of actin cytoskeleton on laminin 332 or laminin 511 at 10 µg/ml or 30 µg/ml.* ***E.*** *Representative confocal images of one-week-old ARPE-19 cells showing positive staining for desmoplakin, cytokeratin-8 and nuclear marker DAPI representing a double-layered cell sheet. Scale bar 20 µm.* ***F.*** *Immunofluorescent confocal images of cell-adhesion receptors integrin α6, integrin β4 and integrin β1 at the basal side of the cells.* ***G, H.*** *Representative traction force and monolayer stress profiles (G) and autocorrelation curves (H) of ARPE-19 cultured for one week on high concentration (20 µg/ml) of laminin 332 and laminin 511 without collagen.* ***I.*** *Quantification of ECM-derived difference in cellular coordination (correlation length). Culturing ARPE-19 cells on laminin 511 alone or combined with collagen IV with following TFM, MSM and correlation length characterisation was performed by Teodora Piskova. Each dot represents the average value from at least three experiments, data are shown as mean ± SEM. Statistical analysis was performed using ordinary two-way ANOVA with Tukey's correction for multiple comparisons.*

Using the reductionist approach, I studied how ECM laminins affect monolayer contractility by altering the biochemistry of PAA surface coatings. By incorporating fluorescent beads into our hydrogels, we could visualise and measure the substrate deformation caused by cells, allowing us to quantify the cell adhesion forces under different conditions. Based on these deformation maps, traction force microscopy (TFM) and monolayer stress microscopy (MSM) were employed to measure cell-matrix adhesion forces and intracellular stresses. To explore epithelial biomechanics in response to ECM-derived signals, I applied these techniques to ARPE-19 cells (Di Russo et al., 2021; Vishwakarma et al., 2018). Traction plots revealed that ARPE-19 cells exhibit significantly higher contractility forces when seeded on laminin 511 (composed of laminin α5, β1, and γ1) compared to laminin 332 (composed of laminin α3, β3, and γ2) (Figure IV-10G). Considering that obtaining a confluent monolayer on laminin 511 was overall challenging, insufficient cellular adhesion can explain increased traction forces, leading to a stronger interaction with the substrate needed for cell survival. To accurately quantify the intracellular stresses experienced by the cells, we included the average height of the cell monolayer (approximately 5 µm), in our calculations. The monolayer stress profiles also indicated higher overall stresses for cells cultured on laminin 511 (Figure IV-10G).

Since epithelial cells are interconnected and transmit forces across the monolayer, we aimed to quantify the autocorrelation of normal stresses to assess intracellular cooperation (Di Russo et al., 2021; Vishwakarma et al., 2018). The correlation length represents the size of the cell cluster within which cells behave and move cooperatively. Representative autocorrelation curves indicated an increase in correlation length for cells cultured on laminin 511, with correlation lengths extending up to 300 µm, compared to 200 µm for cells on laminin 332 (Figure IV-10H). We further compared the behaviour of

ARPE-19 monolayers cultured on PAA hydrogels with varying concentrations of ECM proteins identified *in vivo*. For these conditions, we used laminin 332 and laminin 511 alone, as well as laminin 211 (composed of laminin α2, β1, and γ1), laminin 332, and laminin 511 combined with collagen IV (20 μg/ml). Quantitative analysis showed that monolayers cultured on laminin 511 exhibited higher levels of intracellular communication and coordinated stress distribution, while the presence of collagen IV drastically reduced the correlation length. No significant differences were observed between different concentrations within the same coating (Figure IV-10I).

Based on these observations—such as the heterogeneous organization of the actin cytoskeleton, the formation of multi-layered structures on the hydrogel, and the lack of a protein- and density-dependent response in ARPE-19 mechanics—we concluded that while ARPE-19 cells are useful for establishing a cell culture system on PAA hydrogels, they are not the most physiologically relevant model for studying and characterizing RPE mechanobiology *in vitro*.

3.2. hiPSC-RPE as a cell culture model for establishing an in vitro bottom-up approach

To further explore the role of specific laminin isoforms and their concentration gradients, I established a protocol to culture hiPSC-RPE cells on PAA hydrogels coated with various concentrations of different laminin isoforms. As mentioned previously, the hydrogels were functionalized according to the method described in Przybyla et al. (Przybyla et al., 2016), using specific concentrations of laminins. hiPSC-RPE cells adhered and formed a confined monolayer when seeded on soft (4 kPa) PAA gels coated with laminins (Figure IV-11A, left). The protein-repellent nature of the polymer allows precise control over the biochemical cues defined by the coating. Staining fibronectin confirmed the absence of aberrant ECM protein deposition by the cells during culture (Figure IV-11B). Only intracellular signal for fibronectin was observed for cells cultured on laminin 511-coated hydrogel for one week.

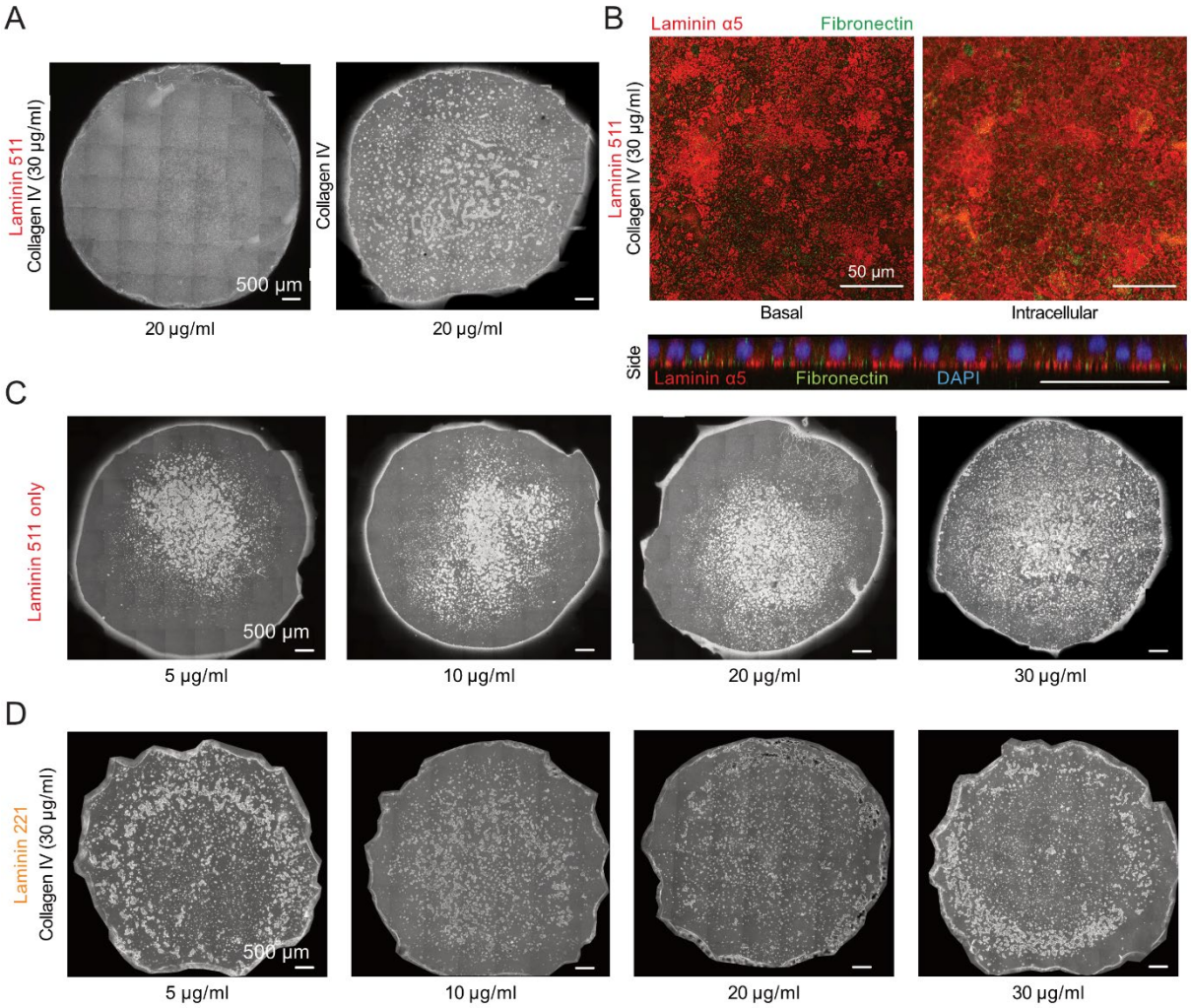

Figure IV-11. *Significance of polyacrylamide hydrogel coating biochemical composition for monolayer formation.* ***A.*** *Visual comparison of a cohesive hiPSC-RPE monolayer formed on a 4 kPa polyacrylamide gel, coated with a combination of laminin 511 (20 µg/ml) and collagen type IV (30 µg/ml), versus a fragmented monolayer observed on a surface coated solely with collagen type IV (20 µg/ml). Scale bar 500 µm.* ***B.*** *Immunofluorescent microscopy images depict the laminin 511-coated gel surface, stained for extracellular matrix (ECM) proteins, revealing the absence of fibronectin deposition after one week of cellular culture. The top row illustrates the presence of laminin α5 (red) and the absence of fibronectin (green) signals at the basal surface and within the monolayer. Notably, the fibronectin signal appears predominantly intracellular, as depicted in the side view of the monolayer. Scale bar 50 µm.* ***C, D.*** *Representative overview images showing colonies of hiPSC-RPE cells seeded on hydrogels coated with varying concentrations of laminin 511 alone (C) and laminin 221 in combination with collagen type IV (30 µg/ml) (D). The overviews of cell colonies on laminin 511 only (C) were performed by Teodora Piskova. These images highlight insufficient cellular adhesion and monolayer formation compared to standard experimental conditions. Scale bar 500 µm.*

Due to the reductionist experimental approach, certain coating conditions, however, were not conducive to obtaining intact RPE monolayers. For example, coatings with laminin 511 alone or laminin 211 alone and in combination with collagen type IV did not support RPE monolayer formation (Figure IV-11A, right, C, D). Since hiPSC-RPE cells failed to form a proper monolayer on laminin 511 without collagen IV, I focused subsequent experiments on comparing different conditions. Specifically, I compared laminin 511 with laminin 332 in combination with collagen IV (30 µg/ml), or laminin 332

with and without collagen IV. For simplification, laminin 511 always means in combination with collagen IV.

These results indicate that the biochemical composition of the hydrogel coating significantly affects cell adhesion strength and monolayer formation and suggest that laminin 511 and 332, but not laminin 211, are primarily responsible for supporting RPE adhesion *in vivo*.

3.3. hiPSC-RPE cells on hydrogels develop an organised cytoskeletal network and epithelial features comparable to in vivo

The cytoskeleton plays a crucial role in maintaining the structural integrity and function of epithelial cells (DuFort et al., 2011; Iskratsch et al., 2014). Unlike the ARPE-19 cell line, which fails to fully recapitulate the cytoskeletal organisation of native RPE, our observations of one-week-old hiPSC-RPE cultures show promising results. When cultured on PAA hydrogels with different laminin coatings, hiPSC-RPE forms a columnar polarized monolayer with well-organized actin filaments and pronounced intracellular actin visible with live F-actin staining (Figure IV-12A). This is a significant improvement over the ARPE-19 cells. Additionally, representative confocal microscopy images of hiPSC-RPE cells stained live with SiR-tubulin demonstrate the organization of microtubule networks. These microtubules are visible at the basal layer, intracellular regions, and the apical side, contributing to intracellular transport and cellular stability (Figure IV-12B).

Interestingly, upon examining the organization of the actin cytoskeleton, I noted a significant influence of the substrate on monolayer mechanics. The staining of F-actin revealed a dramatic change in the organization of the actin cytoskeleton when hydrogels were coated with vitronectin, which is typically abundant during remodelling processes, or when cells were cultured on a very soft substrate (1 kPa) (Figure IV-12C). As observed at the orthogonal projections of cytoskeletal elements, cells cultured on laminin 511 formed columnar and highly polarized monolayers, with an average junctional cell height of around 15 µm, while those cultured on laminin 332 exhibited a height of approximately 10 µm (Figure IV-12D). Cell height measurements were performed using orthogonal projections of live F-actin staining of one-week-old monolayers.

Additionally to microfilaments, when looking at intermediate filament organisation, I noticed the absence of proper cytokeratin-8 network formation after one week in culture, regardless of the protein coating concentration (Figure IV-12E). This

suggests that while actin and microtubule networks are established, intermediate filament organization may require additional time or specific conditions to form properly.

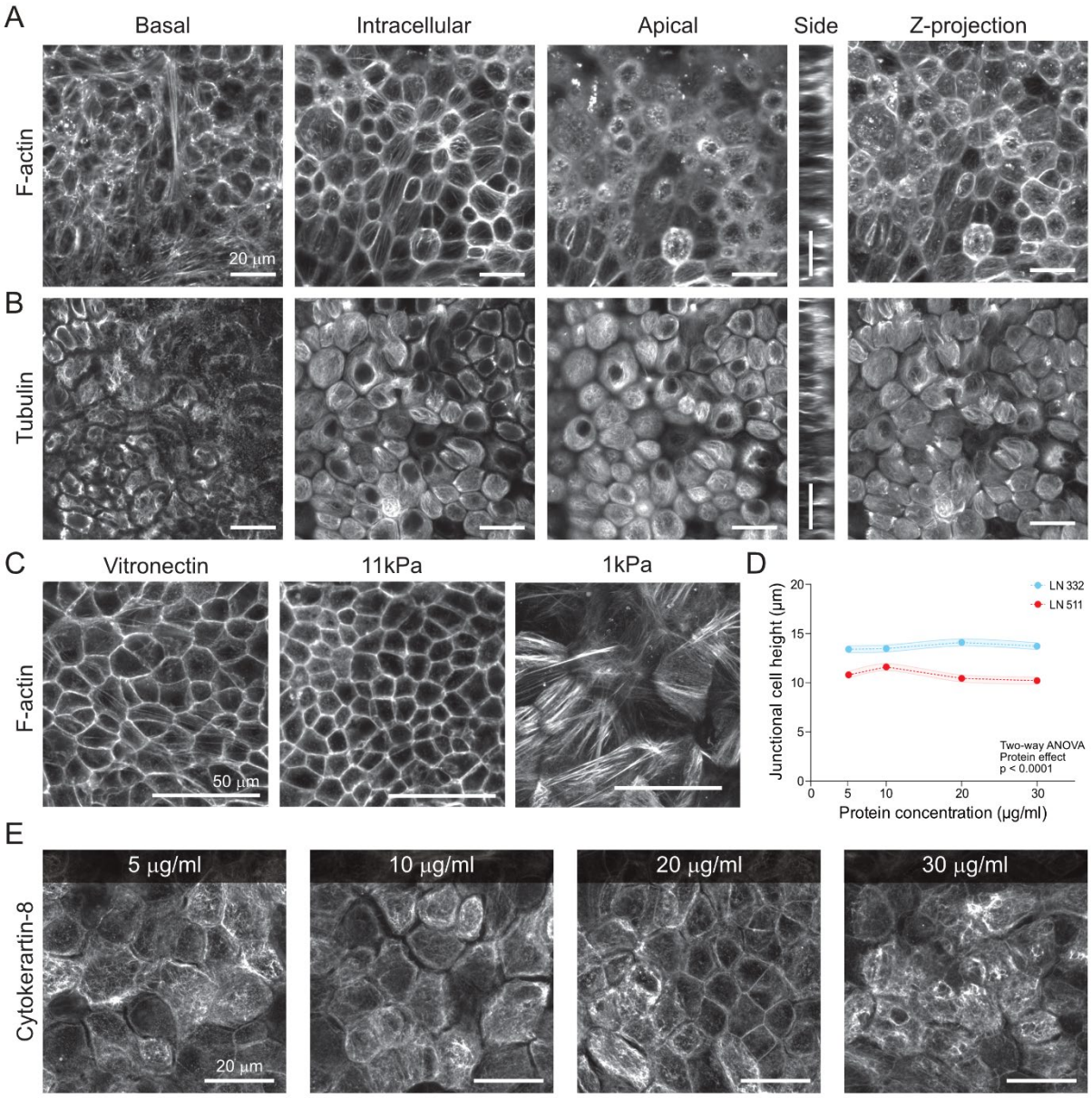

Figure IV-12. *Cytoskeletal organisation of one-week-old hiPSC-RPE monolayers cultured on polyacrylamide hydrogels with different coatings.* ***A, B.*** *Representative confocal microscopy images of a one-week-old monolayer, stained live with SiR-Actin (F-actin) (A) or SiR-Tubulin (B), illustrating organization of networks at the basal cell layer, intracellularly, and at the apical side. The side view demonstrates polarized cell sheet formation. Scale bar 20 µm.* ***C.*** *Confocal images of cell monolayer fixed and stained for F-actin with Phallodin highlighting the importance of substrate conditions for monolayer homeostasis. Scale bar 50 µm.* ***D.*** *Average cell height measured at the adherence junction levels of one-week-old hiPSC-RPE monolayer. Measurements are means from at least three independent experiments ± SEM.* ***E.*** *Representative images of keratin-8 staining indicating the absence of proper network formation after one week in culture regardless of the protein coating concentration. Scale bar 20 µm.*

Next, I characterised the cellular organization and epithelial features of hiPSC-RPE monolayers. Demonstrating their terminally differentiated state, one-week-old hiPSC-RPE monolayers exhibited clear expression of retinal pigment epithelium-specific 65 kDa protein (RPE65) (Strunnikova et al., 2010; Yang et al., 2021), as evidenced by

immunofluorescent staining (Figure IV-13A). Additionally, consistent with previous observations, after one week in culture, the cells displayed polarization, evident apical microvilli, and the formation of tight junctions, as indicated by the immunofluorescent staining of the microvilli marker ezrin and the junctional protein ZO-1 (Figure IV-13B, C).

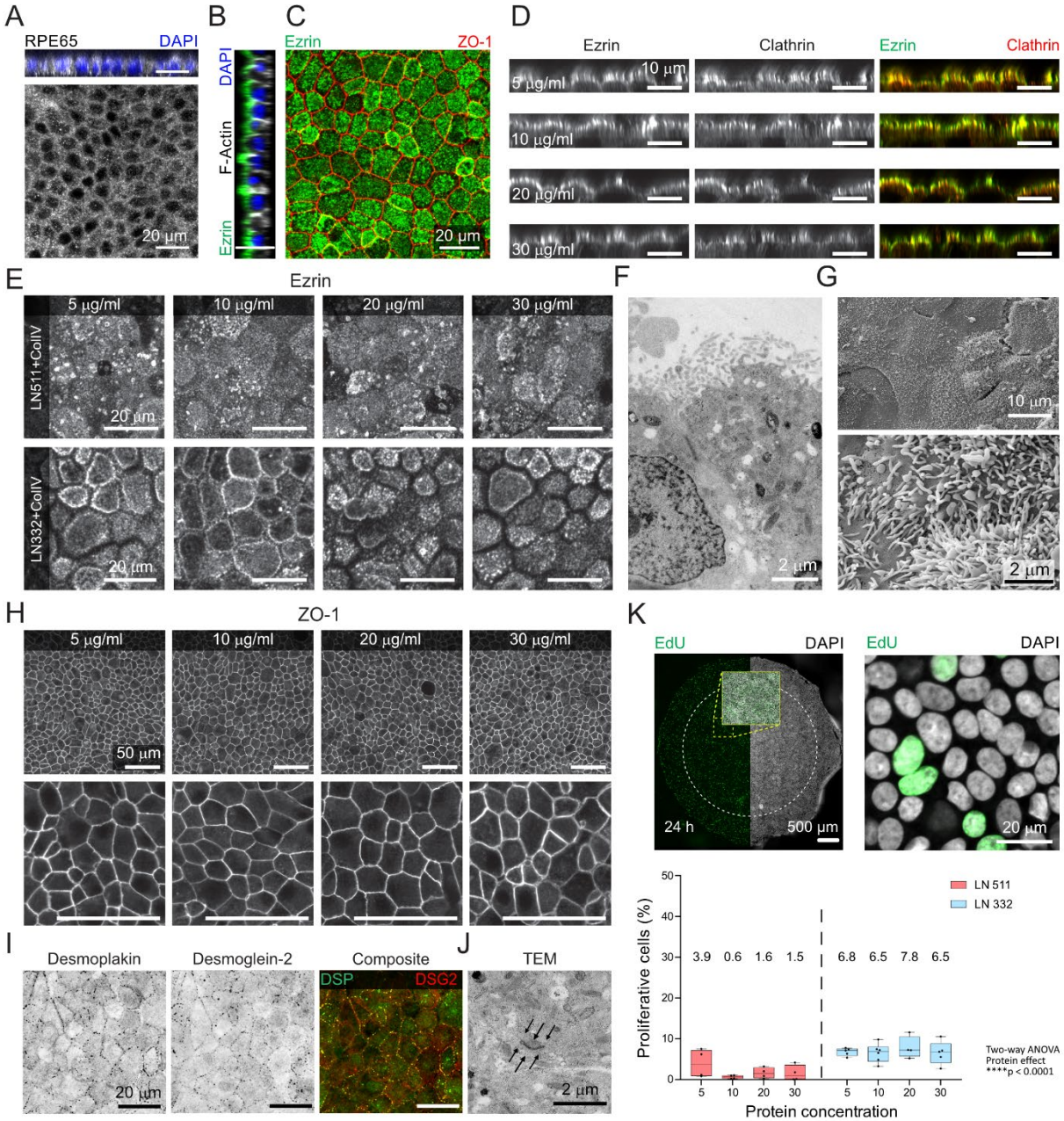

Figure IV-13. *Cellular organisation and epithelial features of hiPSC-RPE monolayers cultured on soft polyacrylamide hydrogels.* ***A.*** *Immunofluorescent confocal image of one-week-old monolayer stained for retinal pigment epithelium-specific 65 kDa protein (RPE65) and nuclear marker (DAPI). Scale bar 20 µm.* ***B, C*** *Representative confocal images of hiPSC-derived RPE cultured on PAA hydrogel with Young's modulus of 4 kPa, coated with laminin 511 or laminin 332 in the presence of collagen type IV (30 µg/ml). After one week in culture, cells form a polarized monolayer, as observed in confocal cross-sections stained for the microvilli marker ezrin (A) and tight junctions (ZO-1) (B). DAPI staining marks the nuclei. Scale bar 20 µm.* ***D.*** *Orthogonal projections of the hiPSC-RPE cells cultured on hydrogel coated with different concentrations of laminin 332 (5 – 30 µg/ml) in the presence of collagen IV (30 µg/ml) stained with ezrin and clathrin. Scale bar 10 µm.* ***E.*** *Representative confocal images of the cellular apical surface of cells cultured on laminin 511 or laminin 332 in the presence of collagen type IV (30 µg/ml) stained for ezrin. Scale bar 20 µm.* ***F, G.*** *Magnified structure of*

RPE apical microvilli visualised by transmission electron microscopy (TEM) (F) and scanning electron microscopy (SEM) with different magnifications (G). Scale bar 2 µm and 10 µm respectively. ***H.*** *Representative confocal images of tight junctions in RPE cells among different hydrogel coating concentrations. Scale bar 50 µm.* ***I, J.*** *Polarised epithelial monolayer is characterised by the formation of desmosomes as illustrated on the immunofluorescent images of cells stained for desmoplakin and desmoglein-2 (I) and transmission electron micrograph (J). Scale bar 20 µm and 2 µm respectively.* ***K.*** *Cellular proliferation rates within 24 hours were obtained using the EdU labelling assay for cells cultured on the PAA hydrogel surface. The distribution of proliferating cells within a gel is illustrated in an overview image of the gel (left) and a confocal image of the monolayer stained for EdU and nuclei (DAPI) (right). The scale bar is 500 µm and 20 µm respectively. The percentage of proliferative cells, determined by the ratio of nuclei with incorporated EdU, was quantified based on fluorescent signals in the central region of the gel to avoid potential edge effects (indicated by a white circle). The data represent average values ± SEM from at least 4 independent experiments. Statistical analysis was performed using Ordinary two-way ANOVA with Tukey's multiple comparisons test, ****p < 0.0001.*

The colocalization of ezrin and clathrin further suggests the potential for clathrin-dependent endocytosis (Figure IV-13D), a mechanism crucial for nutrient uptake and transfer across the RPE (Kwon & Freeman, 2020; Lehmann et al., 2014). The immunofluorescent images of the apical cell surface demonstrate the variability in microvilli organisation between laminin 511- and laminin 332-based hydrogel coating, indicating the influence of ECM cues on apical internalisation processes (Figure IV-13E). However, no significant differences were observed for protein concentrations. The apical microvilli are also visible at high magnification detected by transmission and scanning electron microscopy (Figure IV-13F, G).

Taking into account typical epithelial features, such as the formation of junctional protein complexes, the presence of uniform tight junctions was observed across all protein coating concentrations, as seen by representative ZO-1 immunofluorescent staining (Figure IV-13H). In addition, the immunofluorescent images of cells stained for desmoplakin and desmoglein-2 (Figure IV-13I), along with a transmission electron micrograph (Figure IV-13J), illustrate the presence and organization of desmosomes within the cell-cell junctions.

After a week of culture, hiPSC-RPE cells exhibited a low proliferative state determined by the EdU labelling assay, as illustrated by the representative overview and confocal images (Figure IV-13K, top). The percentage of proliferative cells appeared to be less than 8% within a 24-hour, and interestingly, cells cultured on laminin 332 demonstrated greater amounts of newly formed DNA (Figure IV-13K, bottom).

Altogether, culturing hiPSC-RPE cells on PAA hydrogels provides a robust human-relevant *in vitro* model with near-physiological features for studying RPE mechanobiology. The optimized conditions allow for the formation of well-organized,

polarized low-proliferative monolayers with characteristic epithelial features, closely replicating the native environment and cellular architecture of the human RPE. This model offers a valuable platform to study RPE homeostasis and pathophysiology.

3.4. Biophysical characterisation of monolayer mechanics reveals surface density-dependent RPE contractility

Following the comparative approach between *in vivo* and *in vitro* systems, we performed morphometric and topological analysis of the monolayer cultured on different laminin isoforms and densities. Representative F-actin staining images and subsequent segmentation of cellular membranes revealed no significant differences in monolayer organization across the various conditions (Figure IV-14A). These qualitative observations were quantitatively confirmed through the calculation of the average cellular area, perimeter and elongation, which remained consistent regardless of the laminin isoform or density used (Figure IV-14B). Additionally, we showed that the cellular neighbourhood also remained constant irrespective of the underlying surface biochemistry (Kozyrina et al., 2024). Overall, these data demonstrate a stable relationship among laminin densities and isoforms, excluding their direct role in controlling monolayer morphology and topology *in vivo*.

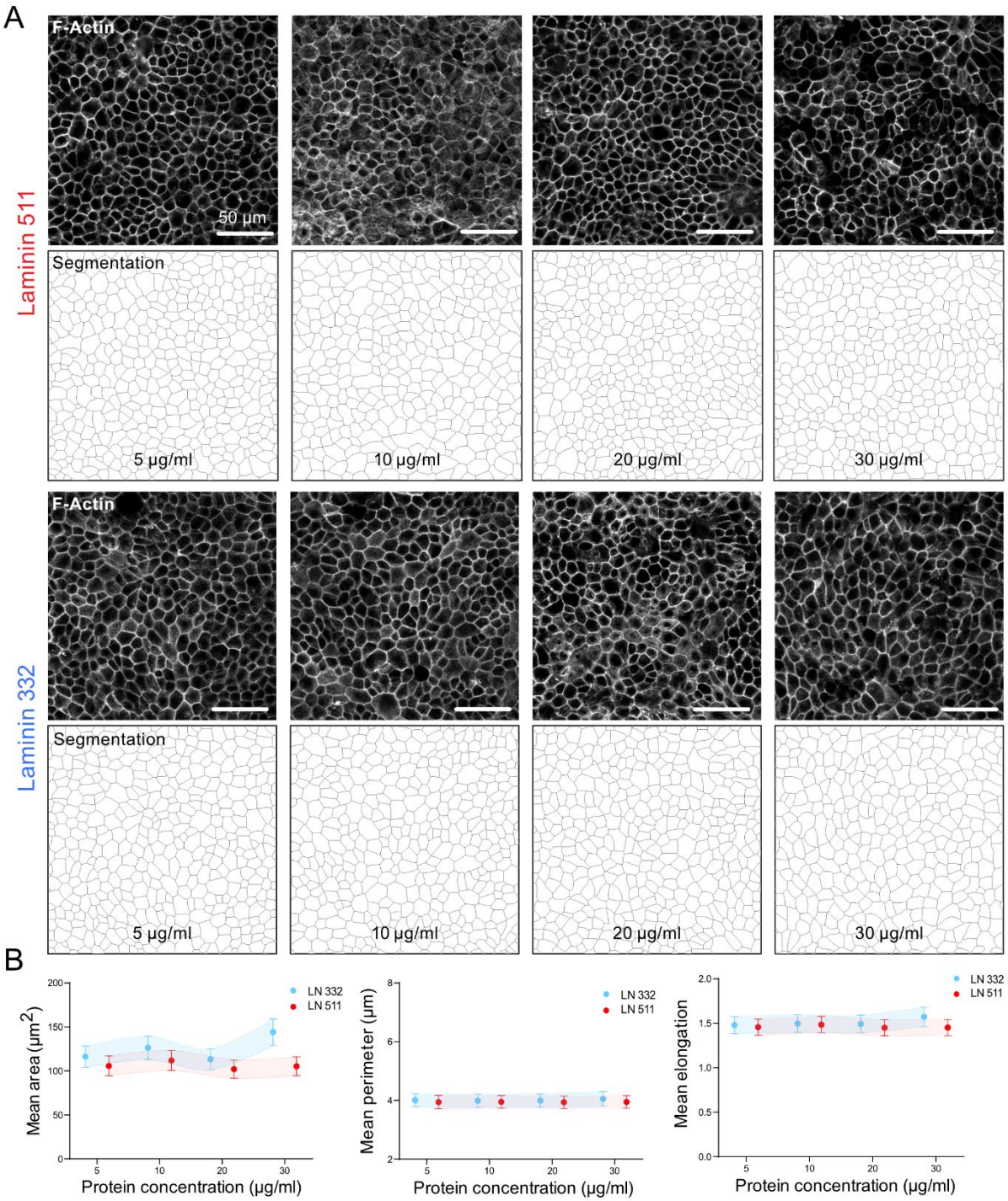

Figure IV-14. *Actin cytoskeleton segmentation and characterization shows a stable of hiPSC-RPE cell morphology on polyacrylamide hydrogels.* ***A.*** *Representative confocal images of one-week-old hiPSC-RPE monolayers cultured on 4 kPa PAA hydrogels coated with different concentrations of laminin 511 (top) or laminin 332 (bottom) both in the presence of collagen type IV (30 µg/ml). The top row displays the actin cytoskeleton network in the stained samples and the bottom row shows segmented images used for morphometric analysis. Culturing cells on laminin 511 was performed by Teodora Piskova. Scale bar 50 µm.* ***B.*** *Morphometric analyses of the cells reveal the absence of significant difference in cellular mean area, mean perimeter and mean elongation between different laminin isoforms and densities from 3 independent experiments. The morphometric analysis was performed by Dr. Maxime Hubert. Figure adapted from* (Kozyrina et al., 2024).

Although the experimental *in vitro* data did not match the expected behaviour of the monolayer with respect to laminin concentration, this discrepancy could be attributed

to other *in vivo* factors or limitations in our experimental model. Another crucial aspect of monolayer characteristics, related to the overall mechanical status of the epithelium, is contractile forces. As mentioned earlier, our *in vitro* system provides a direct and accessible way for measuring monolayer contractility using traction force microscopy (TFM) and monolayer stress microscopy (MSM) (Di Russo et al., 2021; Vishwakarma et al., 2018). Therefore, we next investigated whether variations in hydrogel biochemistry, particularly laminin isoform and density, impact monolayer contractile forces. Traction force and monolayer stress profiles revealed a direct relationship between monolayer contractility and the biochemistry of the hydrogel coatings (Figure IV-15A-E). The quantification showed that laminin 511 promotes higher traction forces than laminin 332 when combined with collagen IV. The most significant difference was observed at the lowest laminin density (170 Pa vs 80 Pa respectively at 5 µg/ml) (Figure IV-15B).

The difference in traction at the lowest laminin 511 density might be attributed to a gradual increase in cell adhesion to collagen type IV, which remained constant across the conditions. To investigate this, we examined the effect of collagen type IV on monolayer traction forces using laminin 332 as a control, since laminin 511 alone does not support monolayer formation (Figure IV-15B). Our quantification revealed an overall decrease (~40%) in traction in the presence of collagen type IV, ruling out its role in the increased traction observed at the lowest laminin 511 density. These findings confirmed that the observed changes in contractility are laminin-specific and highlighted the importance of collagen IV for sufficient cellular adhesion (Figure IV-15B).

Using the data from traction forces and monolayer heights (Figure IV-12D), we calculated intercellular normal stresses for various conditions as previously described in the literature (Di Russo et al., 2021; Vishwakarma et al., 2018) (Figure IV-15B, C). Similar to previous observations, the quantification showed a significant increase in the magnitude of normal stresses when cells are cultured without collagen IV without altering the density-dependent curve behaviour. Also, we observed a substantial difference in monolayer absolute stresses at the lowest coating density of laminins (5 µg/ml), averaging ~1 Pa for laminin 511 and 0.6 Pa for laminin 332 (Figure IV-15B). Despite the variations in absolute contractility, stress vectors averaged close to 0 Pa for both coatings and densities, indicating near-equilibrium of stresses within the monolayers. The

presence of collagen IV in laminin 332 coating did not significantly alter the average stresses (Figure IV-15C).

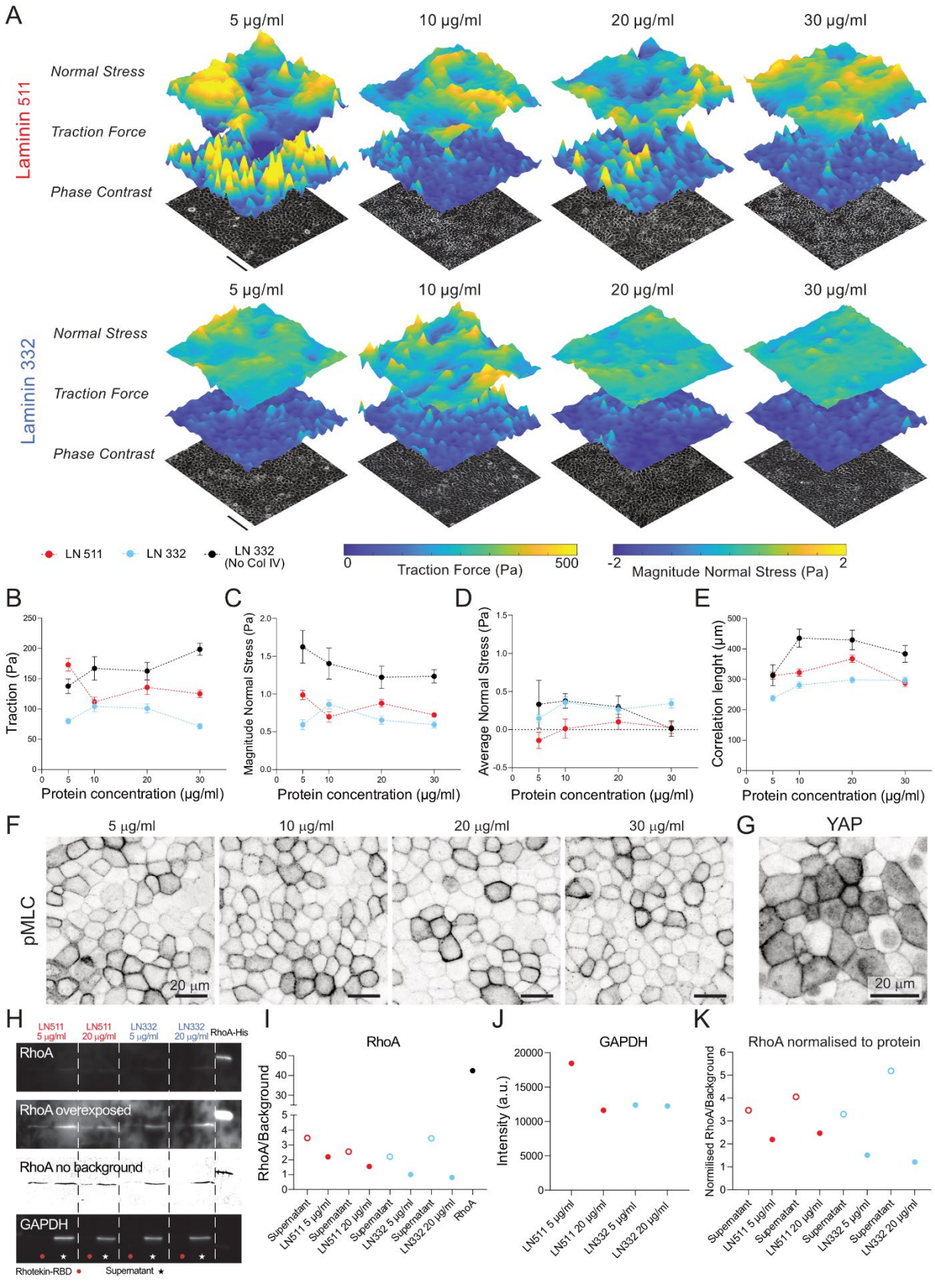

(Description on the next page)

Figure IV-15. *Reductionist approach demonstrated the effect of laminin density on RPE contractility levels according to the biochemistry of PAA surface coating.* ***A, B, C, D.*** *Representative traction force and monolayer stress profiles for different coating conditions (A) and their quantifications (B, C, D) show a significant increase in contractility of RPE monolayers at the lowest laminin 511 density (in combination with collagen IV, 30 µg/ml), and overall with laminin 332 coating in the absence of collagen IV.* ***E.*** *Characterisation of multicellular cooperation (correlation length) showing higher cellular cooperation for conditions with higher contractility. Culturing cells on laminin 511 with the following contractility quantifications was performed by Teodora Piskova.* ***F, G.*** *Representative confocal images of phosphorylated myosin light chain (pMLC) and yes-associated protein 1 (YAP1) representing heterogeneous actomyosin contractility among monolayer. Scale bar 20 µm.* ***H.*** *Western blot analysis demonstrating the expression levels of active RhoA in cells cultured for one week on 4 kPa PAA gels coated with low (5 µg/ml) or high (20 µg/ml) concentrations of laminin 511 or laminin 332 in the presence of collagen type IV (30 µg/ml). The experiment was performed using a pull-down assay with rhotekin-RBD affinity beads. The blot was probed with antibodies against RhoA and GAPDH (as a loading control). Due to poor blot quality, some image manipulations were performed to acquire the quantitative data, such as a signal from RhoA was overexposed and then the background was removed using background subtraction in Fiji. The average intensity of the background on the blot image "RhoA no background" was used to normalise all RhoA signals.* ***I, J, K.*** *Densitometry quantification of the RhoA expression levels relative to the background (I), expression levels of GAPDH (J), used further to normalise RhoA levels to the protein amount (K). The signal from samples was used as total RhoA from the supernatant and active RhoA from the beads.*

Using the values and orientation of normal stresses, we validated the effect of hydrogel coating conditions on epithelial collective behaviour using the autocorrelation function as previously described. This parameter can also be considered as a fingerprint of monolayer material properties, where a lower correlation length, despite showing weaker cooperation, represents a more flexible material with high adaptability. This is supported by the observed enhanced correlation length for cells cultured without collagen IV, which undergo a more challenging process of cell adhesion. Our results showed that hiPSC-RPE cells exhibited an overall lower correlation length when cultured on laminin 332 in combination with collagen IV across all experimental conditions (Figure IV-15E). Additionally, no direct relationship was observed between the correlation length and laminin coating concentration, given the divergent effects seen with traction forces at low laminin concentration (5 µg/ml). This suggests a more complex relationship between overall contractility levels and multicellular cooperation.

To further assess the overall mechanical status, I analysed molecular markers of cellular contractility within RPE monolayers. First, I studied the phosphorylation of the myosin II regulatory light chain (MLC), a key regulatory event driving actomyosin contractility (Bresnick, 1999). However, the phosphorylated myosin light chain (pMLC) signal did not reveal any ECM-specific patterns that would define monolayer actomyosin activity, making it challenging to quantify its localisation in relation to laminin concentration (Figure IV-15F). Additionally, substrate adhesion is known to modulate F-actin conformation and tension, which regulate transcriptional factors such as YAP/TAZ

(Totaro et al., 2018). Similar to pMLC, yes-associated protein 1 (YAP1) displayed a heterogeneous distribution within the monolayer (Figure IV-15G).

To explore the influence of laminin isoform and density on cellular RhoA activity, I performed a pull-down assay followed by quantification with Western blot. The rhotekin-RBD beads were used to selectively bind active RhoA levels from the lysate, allowing us to estimate monolayer contractility by comparing the levels of active RhoA to total RhoA in the supernatant (Figure IV-15H). Due to the low protein content in the samples, the fluorescent signal from RhoA appeared weak on the Western blot. To obtain quantifiable data, the image was overexposed, and the background was accurately subtracted. Despite some remaining background, the signal from RhoA was estimated relative to the average background (Figure IV-15I). GAPDH was used as a loading control, revealing slight variations in protein levels across samples (Figure IV-15J). Consequently, the RhoA values were normalized to protein content, resulting in the data presented in Figure IV-15K. Due to the complexity of the experimental setup and the necessity to pool over 15 different samples to achieve sufficient signal, the data represent values from a single experiment. While these observations are not conclusive, they suggest that cells cultured on laminin 511 exhibit higher levels of active RhoA compared to those cultured on laminin 332. This finding aligns with previous traction force measurements.

3.5. hiPSC-RPE elasticity and viscoelastic behaviour are independent of laminin surface density

Next, we aimed to determine whether the coating density could generally impact RPE viscoelastic properties, potentially regulating its apical processes and subsequent interaction with the neural retina *in vivo*. To investigate this and further characterise monolayer biomechanics, we performed indentation experiments using a spherical probe with a radius of approximately 10 µm to measure the elasticity of the hiPSC-RPE monolayers (Figure IV-16). Representative bright field images of one-week-old hiPSC-RPE monolayers live stained for F-actin (SiR-actin) illustrate the cellular deformation under mechanical stress during indentation (Figure IV-16A). The cantilever displacement graph (Figure IV-16B) shows the characteristic profile of cantilever bending, indentation depth, and piezo displacement during the indentation. Figures C and D depict the load versus indentation dependency plots for the apical (up to 3 µm) and bulk elasticity (3–10 µm) of the monolayers. The contact fit, loading, holding, unloading, and fitting curves are indicated by yellow, light blue, dark blue, and red colours respectively. These curves were

used further to calculate the effective Young's modulus of the monolayer in DataViewer software (Optics11 Life).

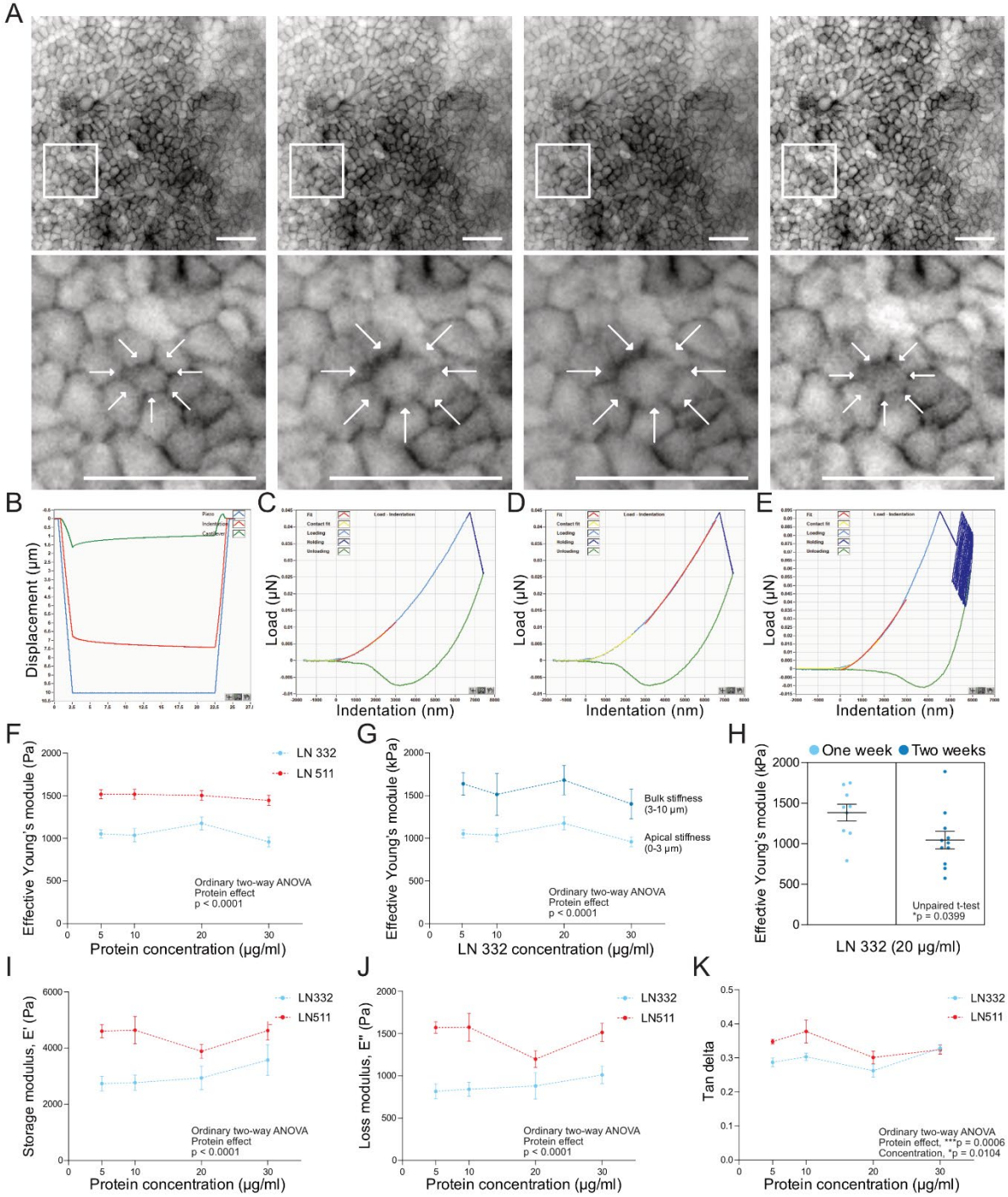

Figure IV-16. *Effect of laminin isoform and concentration on the elasticity and viscoelastic properties of hiPSC-RPE monolayers.* ***A.*** *Representative images of one-week-old hiPSC-RPE monolayer live stained for F-actin (SiR-actin) during the indentation process (A) according to the indentation profile (B). Scale bar 50 µm.* ***B.*** *The graph of cantilever displacement (µm) from time (s) represents the movement of the cantilever for further analysis of monolayer elasticity. The following dependence curves are highlighted in colours: green – bending of the cantilever, red – indentation depth over time, and light blue – piezo displacement over time.* ***C, D.*** *Dependency plot of load (µN) from indentation (nm) for the apical (up to 3 µm) (C) and bulk elasticity (3 – 10 µm) (D). The following dependence curves are highlighted in colours: yellow – contact fit, light blue – loading, dark blue – holding, green – unloading, and red – fitting curve.* ***E.*** *The plot of load (µN) versus indentation (nm) during the dynamic mechanical analysis (DMA).* ***F.*** *Quantification of the effective Young's modulus of the apical*

side of monolayer in different conditions. The measurements were performed according to profile B and analysed using the fitting curve C. ***G.*** *Comparison between apical (up to 3 µm) (C) and bulk (3 – 10 µm) effective Young's modulus for cell monolayers cultured on laminin 332 in combination with collagen IV (30 µg/ml).* ***H.*** *Comparison of the apical effective Young's modulus for one-week-old and two-weeks-old monolayers cultured on laminin 332 (20 µg/ml) with collagen IV (30 µg/ml). Each dot represents a single indentation point, and the overall graph shows a comparison between two hydrogels seeded with cells simultaneously. Statistical analysis was performed using an unpaired t-test.* ***I, J, K.*** *Analysis of monolayers viscoelasticity showing storage modulus (I), loss modulus (J) and tan delta (K) among coating concentrations for laminin 511 and laminin 332. The experimental part related to laminin 511 was performed by Teodora Piskova. All data are shown as average ± SEM from at least 4 independent experiments (F, G, I, J, K). Statistical analyses were performed using ordinary two-way ANOVA with Tukey's multiple comparisons test (F, G, I, J, K).*

The effective Young's modulus is a measure of the stiffness of a material, reflecting its ability to deform under defined stress. In the context of cell monolayers, it quantifies how resistant the cells are to deformation when a force is applied. The viscoelastic properties of the hiPSC-RPE monolayers were analysed via dynamic mechanical analysis (DMA) whose working principle lies in the application of a small, oscillatory force to a material and measuring its response (Figure IV-16E).

Quantification of the effective Young's modulus for the apical side of the monolayer under various coating conditions indicated that RPE monolayers on laminin 511 are stiffer (~1.5 kPa) compared to those on laminin 332 (~1 kPa), regardless of the protein surface density (Figure IV-16F). I further compared the effective Young's modulus for apical and bulk regions (Figure IV-16G) and the temporal changes in modulus for one-one-week-old versus two-weeks-old monolayers cultured on laminin 332 and collagen IV (Figure IV-16H). The results indicate that the mechanical properties of the monolayer evolve over time, making the monolayer softer and highlighting the dynamic nature of cellular biomechanics. This apical softening might be related to the monolayer maturation and increase in height that leads to the positioning of the nuclei – the stiffest cellular region – further from the apical side or overall softening of the cytoplasm.

The analysis of DMA gives us information about the viscoelastic behaviour of cell monolayer including the storage modulus G', loss modulus G'', and tan delta tan δ across different coating concentrations for laminin 511 and laminin 332 (Figure IV-16I, J, K). Briefly, the storage modulus reflects the amount of energy stored in the material during deformation, the loss modulus indicates the viscous energy dissipated as heat, and the tan delta, as the ratio of the previous two components, measures the material's damping behaviour. The characterisation shows that while the viscoelastic properties of the monolayer remained consistent across different coating concentrations, cells cultured on laminin 511 exhibited higher storage and loss moduli compared to those on laminin 332

(Figure IV-16I, J). This suggests that laminin isoform, rather than its concentration, influences the stiffness and energy dissipation capacity of the monolayer.

3.6. Laminin-defined traction levels modulate RPE efficiency to phagocyte photoreceptor outer segments

Similar to how the contractile actomyosin cytoskeletal network governs cell shape and motility by transmitting force dynamics through cellular junctions, epithelial contractility levels play a critical role in determining overall tissue functionality and reactivity (Balcioglu et al., 2020; Malinverno et al., 2017; J.-A. A. Park et al., 2015; Vishwakarma et al., 2018). To investigate the relationship between RPE monolayer mechanics and their functional capacity, we assessed the ability of RPE monolayers cultured on PAA hydrogels to perform their fundamental function – bind and phagocytose photoreceptor outer segment (POS) fragments. These POS fragments were isolated from porcine eyes and fluorescently labelled with FITC for visualization (Parinot et al., 2014) (Figure IV-17A, B, C).

Our quantification revealed that RPE monolayers on high laminin coating concentrations (10-30 µg/ml) exhibited comparable phagocytic efficiencies between laminin 332 and laminin 511. However, at a lower coating concentration of 5 µg/ml, a significant reduction in phagocytic efficiency (~50%) was observed in RPE on laminin 511 (Fig. IV-17B, C). Interestingly, this divergent effect between laminin isoforms disappears at an even lower concentration (2.5 µg/ml), suggesting that at this concentration, collagen IV dominates the biochemical signalling, and the cells no longer respond to laminin. Additionally, culturing cells on 1 µg/ml laminin 511 was not feasible due to insufficient adhesion (Figure IV-17B). These findings suggest a strong correlation between traction force levels in RPE monolayers and their functional capacity, indicating a potential cause-effect relationship between laminin-defined traction and RPE functionality.

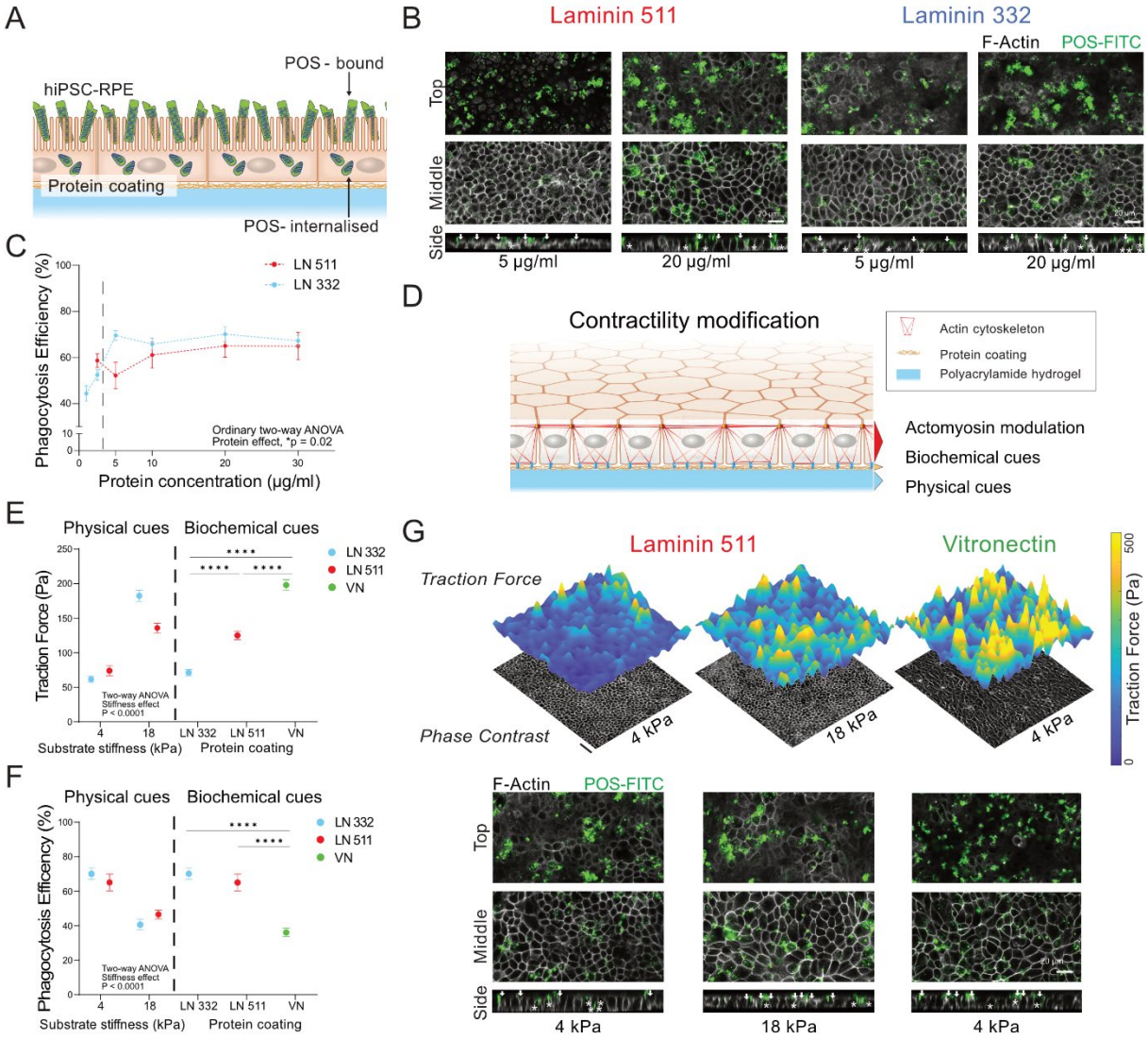

Figure IV-17. *Functional capacity of hiPSC-RPE cells in vitro.* ***A.*** *Schematic representation of the photoreceptor outer segment (POS) internalisation assay on hiPSC-RPE monolayer.* ***B.*** *Average phagocytosis efficiency ± SEM for different laminin isoforms and coating conditions based on at least 4 independent experiments. Phagocytosis efficiency was calculated as the ratio of internalised POS to total POS. The experiments with laminin 511 (5 - 30 µg/ml) were performed by Teodora Piskova. Statistical significance was tested using ordinary two-way ANOVA with Tuckey's multiple comparisons test for coating concentration between 5 and 30 µg/ml.* ***C.*** *Representative confocal images of the hiPSC-RPE cells on PAA hydrogel coated with laminin 511 or laminin 332 in the presence of collagen type IV. The top row indicates FITC-labelled POS fragments on the apical surface of the cells. The middle row shows an optical section of the cell monolayer with internalised POS fragments. Orthogonal projections in the bottom row highlight bound (arrows) and internalized (stars) POS fragments.* ***D.*** *Schematic representation of the experimental strategy to modulate monolayer contractility.* ***E, F.*** *Quantification of mean traction forces (E) and phagocytosis efficiency (F) ± SEM in hiPSC-RPE cells under different ECM physical (elasticity) and biochemical (coating) cues. PAA hydrogels were coated with laminin 511 or laminin 332 in the presence of collagen type IV or with vitronectin (VN). TFM measurements on VN were performed by Iris Doolaar. Statistical analysis was performed using ordinary two-way ANOVA with Tuckey's multiple comparisons test (physical cues) and Mann-Whitney test (biochemical cues), ****p<0.0001.* ***G.*** *Representative plots of traction forces and immunofluorescent images from POS internalisation assay under different physical or biochemical conditions.*

To further investigate whether POS phagocytosis efficiency is directly influenced by RPE traction forces independent of ECM biochemical composition, I modulated the ECM physical properties (hydrogel stiffness) and biochemical nature of adhesion

(laminins vs vitronectin) mimicking the ECM remodelling events (Figure IV-17D). I compared the RPE efficiency in internalizing POS under these varied conditions against the maximum efficiency observed on laminins (at a concentration of 20 µg/ml). RPE monolayers were first cultured on stiffer hydrogels (18 kPa) coated with laminin 511 or 332 (20 µg/ml) in the presence of collagen type IV (30 µg/ml), resulting in significantly increased traction forces compared to monolayers on 4 kPa gels (~140 Pa for laminin 511 and 170 Pa for laminin 332). This increase in traction force corresponded to a decreased efficiency in POS internalization (~40%) (Figure IV-17E, F, G). Similarly, RPE monolayers on 4 kPa hydrogels with a high concentration of vitronectin (250 µg/ml) also exhibited higher traction forces (~200 Pa) and a reduced ability to internalize POS (~36%).

To differentiate the role of cellular contractility from potential ECM signalling effects, I modulated actomyosin contractility in RPE monolayers using a ROCK inhibitor to reduce contractility or a RhoA activator to increase it (Figure IV-18A, B, C). RPE monolayers on soft (4 kPa) surfaces coated with collagen type IV (30 µg/ml) and low laminin concentrations (2.5 µg/ml), which initially exhibited low POS phagocytosis activity (~50%), were treated with the ROCK inhibitor. Conversely, cells on high-density laminins (20 µg/ml) with collagen type IV were treated with a RhoA activator to promote contractility. The treatments effectively modulated traction forces, with reduced traction following ROCK inhibitor treatment and increased traction after RhoA activation (Figure IV-18A). The phagocytic efficiency of RPE monolayers was directly affected by changes in actomyosin contractility. Independently of the laminin type, phagocytic efficiency increased from ~50% to ~70% following ROCK inhibitor treatment and decreased from ~70% to ~50% following RhoA activation (Figure IV-18B).

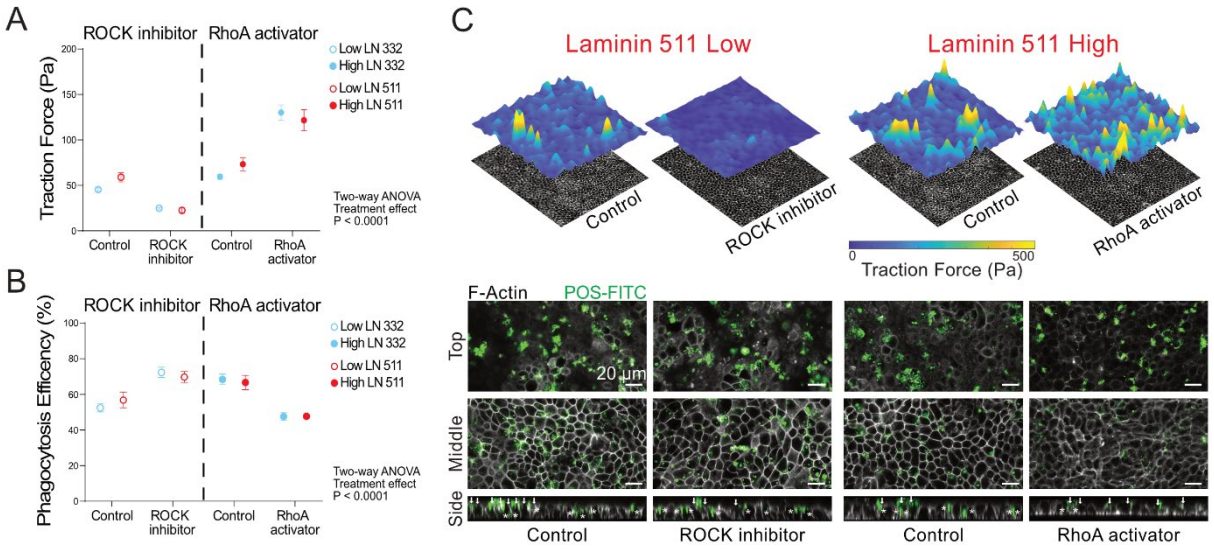

Figure IV-18. *Laminin-defined RPE contractility modulates POS phagocytosis.* ***A, B.*** *Drug treatment modulating the actomyosin contractility levels using ROCK inhibitor and RhoA activator shows an inverse relationship between monolayer contractility (traction forces) (H) and POS phagocytosis efficiency (I). Data are presented as mean ± SEM. Statistical analysis was performed using ordinary two-way ANOVA with Tuckey's multiple comparisons test, ****p<0.0001.* ***C.*** *Representative traction force plots and immunofluorescent images of POS internalisation assay after drug treatment.*

Overall, these data indicate that low laminin 511 density, as opposed to laminin 332, decreases RPE functional capacity by promoting higher traction forces.

3.7. The epithelial contractility is defined by the variability of integrin receptors involved in cellular adhesion

Integrins are heterodimeric transmembrane receptors that facilitate the interaction between cells and their microenvironment to control numerous cellular processes, including migration, differentiation, and tissue architecture (Flier & Sonnenberg, 2001; Harburger & Calderwood, 2008; Wickström & Niessen, 2018). In epithelial cells, integrins mediate adhesion to the basement membrane, impacting cellular mechanics and function (Kozyrina et al., 2020; Di Russo et al., 2023). At the level of the ECM, the alpha chain of laminins defines the specificity for integrin adhesion, commonly with one of the following isoforms: α6β1, α3β1, α6β4 and α7β1 (Pozzi et al., 2016). Intracellularly, members of the integrin β1 family connect to the actin cytoskeleton through talin, while integrin α6β4 links to the keratin network via plectin (Alberts et al., 2015). On the extracellular side, both integrin β1 and β4 interact with several proteins, including the α3 and α5 chains of laminins (Aumailley, 2012; Hynes, 2002). Considering the direct role of subtract nanostructure in modulating epithelial homeostasis (Di Russo et al., 2021; J. L. Young et al., 2016, 2020), I explored the repertoire of integrin receptors mediating adhesion of hiPSC-RPE cells on PAA hydrogels coated with different densities of laminin 511 and laminin 332 (Figure IV-19A).

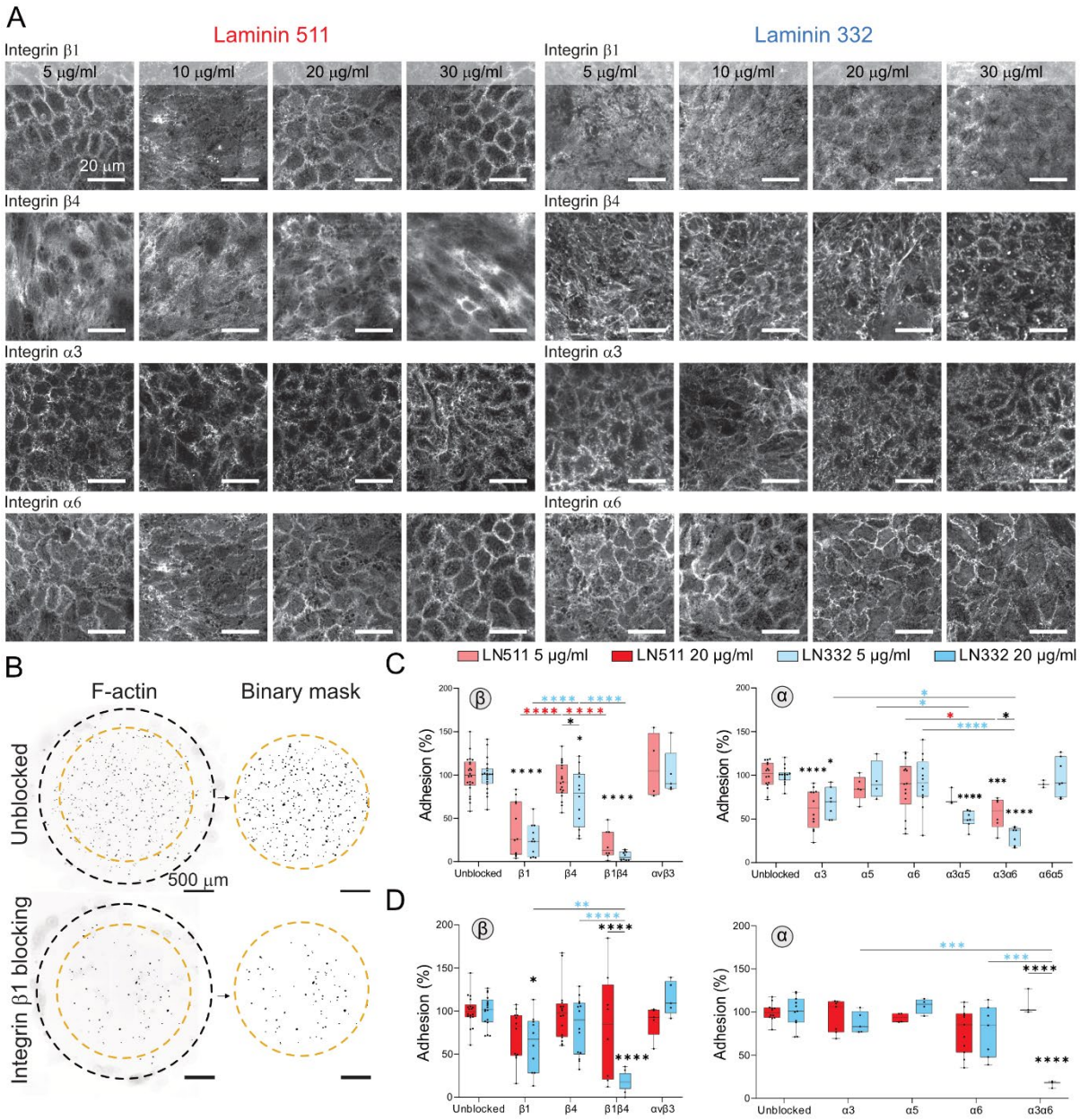

Figure IV-19. *Repertoire of integrin receptors mediating RPE cell adhesion to laminin-coated hydrogels.* ***A.*** *Immunofluorescent images showing the localization of integrin receptors on the basal side of hiPSC-RPE cells cultured on hydrogels coated with varying concentrations of laminin 511 or laminin 332. Cells were stained for integrin subunits β1, β4, α3, and α6, highlighting their distribution and expression patterns in response to different laminin coatings. Scale bar 20 μm.* ***B.*** *Representative hydrogel overviews of cells stained for F-actin with phalloidin, showing unblocked cells (top) and cells with adhesion blocked using anti-integrin β1 (bottom). The black circle indicates the hydrogel area, while the orange represents a region of interest (ROI) used for analysis. The binary masks represent the hydrogel surface, which has been thresholded and converted to a binary image for quantification using a particle analysis plugin in Fiji. Scale bar 500 μm.* ***C, D.*** *Box and whisker plots depicting the percentage of RPE cell adhesion on low (5 μg/ml) (C) or high (20 μg/ml) (D) density laminin 332 or laminin 511-coated hydrogels, after incubation with integrin beta or alpha subunits blocking antibodies, and control (unblocked). Statistical significance: * p < 0.05, ** p < 0.01, *** p < 0.001 ****p<0.0001, defined using ordinary two-way ANOVA with Tuckey's multiple comparisons test. Asterisks positioned directly on the box and whisker indicate significance relative to the control. Asterisks of different colours indicate the following comparison: red – comparison between laminin 511 conditions, light blue – comparison between laminin 332 conditions, and black – comparison between laminin 511 and laminin 332 within one particular blocking condition. Adhesion assay experiments were conducted together with Francesca Semeraro.*

The expression and distribution of integrin subunits β1, β4, α3, and α6 were assessed via immunofluorescent staining of hiPSC-RPE cells cultured on laminin-coated hydrogels (Figure IV-19A). Overall, the basal localisation of integrin subunits in response to varying concentrations of laminin 511 and laminin 332 represents a heterogeneous distribution across different conditions. This variability may partly originate from the limitations of immunofluorescence as a method for studying cellular adhesion nature. However, the presence of positive fluorescent signals suggests a potential role for these integrin isoforms in mediating RPE adhesion processes.

To access the functional relevance of specific integrin isoforms, I performed an adhesion assay on hydrogels coated with low (5 μg/ml) or high (20 μg/ml) laminin concentration. Briefly, cells were incubated with blocking antibodies against integrin β (β1, β4, [αv]β3) or α (α3, α5, α6) subunits, transferred on hydrogel for a fixed period with subsequent washing, and adhesion was quantified by staining F-actin with phalloidin. Figure IV-19B provides representative hydrogel overviews, highlighting the adhesion patterns of unblocked cells and those treated with anti-integrin β1 antibodies. The number of adherent cells was quantified in the designated region of interest using particle image analysis in Fiji.

In conditions with low laminin coating concentrations, blocking β1 integrin significantly reduced adhesion on both laminin 332 (~75%) and laminin 511 (~62%) coatings (Figure IV-19C, left). In contrast, blocking β4 and αvβ3 integrin subunits showed no significant reduction in adhesion, with only a slight decrease observed with β4 on laminin 332. To rule out a possible compensation effect of integrin β1 at this condition, I concurrently blocked β1 and β4 integrins and obtained reduced adhesion on laminin 511 and nearly complete inhibition of adhesion on low-density laminin 332 (~94%).

For the α subunits, blocking with the α3 integrin antibody alone led to a significant decay of adhesion strength. However, similarly to β subtypes, simultaneous blocking integrin α3 and α6 subunits resulted in a substantial reduction of adhesion, suggesting the cooperative role of those two subunits in the adhesion process (Figure IV-19C, right). Additionally, the differential effects of simultaneous blocking of integrins β1 and β4 and integrins α3 and α6 on low-density laminin 511 and laminin 332 suggests a different repertoire of receptors involved in adhesion at those two conditions.

Interestingly, at high laminin concentrations, no significant effect was observed with single subunit blocking, which could be explained by higher binding probability, resulting in lower resolution of the method (Figure IV-19D). However, as hypothesized, concurrent blocking of integrin β1 with β4 and integrin α3 with α6 confirmed the divergent receptor involvement in adhesion on laminin 332 versus laminin 511.

These findings highlight the differential roles of integrin β1, β4, α3, and α6 subtypes in mediating RPE cell adhesion to laminin-coated hydrogels.

3.8. The role of integrin β1 in RPE adhesion is concealed by compensatory mechanisms when studied alone

To differentiate adhesion mediated by between integrin β1 or β4, I targeted specific intracellular processes and modulated integrin β1 reactivity, followed by a comparison between cells cultured on laminin 332 or laminin 511 coatings. First, I introduced an adeno-associated virus (AAV) shRNA knockdown vector to modulate the expression levels of integrin β1 (Figure IV-20A). This vector was labelled with mCherry and included one of three different hITGB1 shRNA sequences (shRNA#1, shRNA#2, or shRNA#3), all of which were used in equal proportions in our experiments to ensure efficient knockdown of integrin β1. As a negative control for a virus carrier, I used a scramble shRNA AAV5 virus with scrambled sequence instead of functional hITGB1 (see Appendix 2). Semi-confluent cell monolayers were transduced on day four of culture and observed for over a week to monitor the subsequent changes.

As can be seen from the immunofluorescent images, limitations of the imaging method prevented us from clearly visualising the reduction in integrin β1 expression using a confocal microscope (Figure IV-20B). However, the overall immunofluorescent signal of the virus increases 48 hours after transduction and remains stable even after six days, indicating efficient transduction efficiency (Figure IV-20C).

To characterise the biomechanical changes in monolayers subjected to β1 integrin knockdown, I performed traction force experiments and compared cellular contractility levels under different coating conditions right before the transduction and 96 hours later (Figure IV-20D). Quantification showed a minimal difference in the overall traction forces between viral transduction and scramble control. However, the only promising difference was observed when double the amount of shRNA (2xAAV) was used on cells cultured on low-density laminin 511 (5 μg/ml).

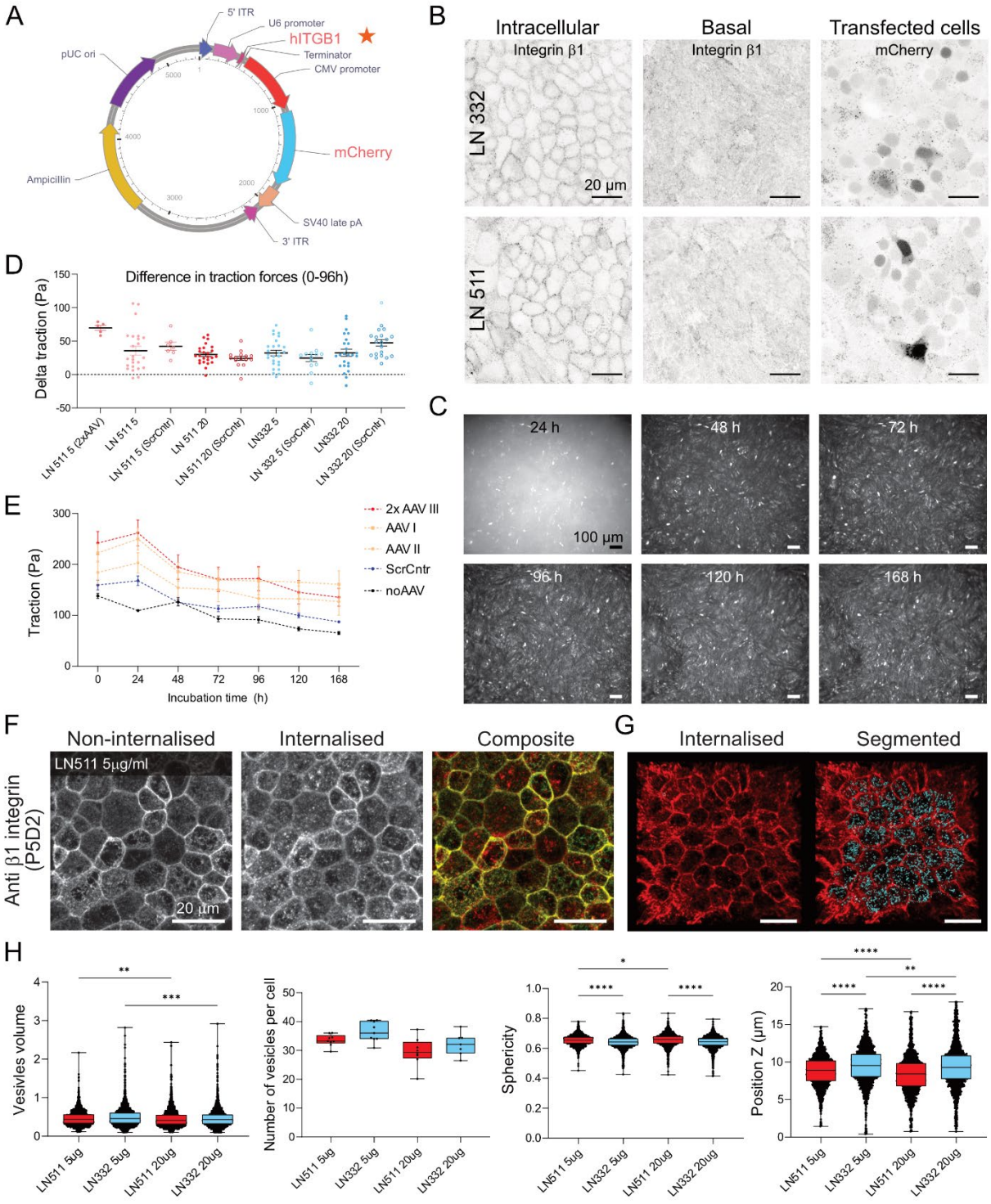

Figure IV-20. *Modulation of integrin β 1-mediated adhesion.* ***A.*** *A schematic map of the human ITGB1 shRNA knockdown AAV5 vector labelled with mCherry. Star indicates the position where either shRNA#1, shRNA#2 or shRNA#3 were located (see Appendix 2). The mixture of all three was used in equal proportions for the experiments.* ***B.*** *Representative immunofluorescent confocal images of transfected cells showing a signal of integrin β1 within the cells (Intracellular) and at the basal side of the cells (Basal) together with the fluorescent signal of mCherry indicating transfected cells. Cells were cultured on hydrogel coated with low concentration (5 µg/ml) of laminin 332 or laminin 511 for one week. Scale bar 20 µm.* ***C.*** *Representative immunofluorescent images of the mCherry signal within the monolayer indicate increased transfection efficiency over time. hiPSC-RPE were cultured for four days on hydrogel prior to transduction. Observations were performed starting from 24h after the transduction until day seven. Scale bar 100 µm.* ***D.*** *Characterisation of traction forces reveals variability in adhesion force difference between the time point before transduction and 96h later across various coating conditions (laminin 511 or laminin 332 at 5 µg/ml or 20 µg/ml). The values were compared to a*

scramble control for the particular condition. The highest difference refers to the condition where cells were cultured at low concentrations of laminin 511 and transfected with double the amount of viral shRNA. ***E.*** *Time progression of traction forces when cells cultured on hydrogels coated with a low concentration of laminin 511 showed no difference with any control condition.* ***F.*** *Representative immunofluorescent confocal images of one-week-old hiPSC-RPE cells during anti-integrin β1 antibody internalisation assay indicating non-internalised receptors (before permeabilisation), internalised vesicles (after permeabilisation) and composite of these two channels.* ***G.*** *The same image (F) was segmented in Imaris and used for further analysis.* ***H.*** *Quantification of the internalisation efficiency among different coating conditions. Box and whisker plots show comparison of vesicle volume, number of vesicles in one cell (density), sphericity and Z-position for low (5 µg/ml) and high (20 µg/ml) concentration of laminin 332 or laminin 511 on hydrogel. Statistical analysis was performed using Kruskal-Wallis test with Dunn's correction for multiple comparisons.*

For a better understanding of the temporal effect of integrin knockdown on RPE contractility, I observed an evolution of traction forces exerted by the monolayers cultured on laminin 511 at 5 µg/ml under various transduction conditions. A slight increase in traction forces was observed 24 hours post-transduction, likely due to the primary effects of incubation with the viral RNA during this period. Over time, traction forces generally decreased, but it was challenging to distinguish between virus-induced mechanical changes and a natural decrease in contractility due to the monolayer maturation process. Hence, despite being a promising model for studying integrin β1-mediated adhesion, the combination of AAV transduction and traction force measurements did not give us promising results. This lack of effect could be explained either by the sensitivity of the method or, more likely, by compensatory mechanisms involving other integrins.

Unlike many other cell-surface receptors that undergo synchronized ligand-induced internalization and degradation, integrins are continuously trafficked within cells (Bridgewater et al., 2012; J. Z. Kechagia et al., 2019). Therefore, I aimed to study integrin β1 functional involvement by characterising the difference in its endocytosis. Briefly, RPE cells were incubated with the blocking anti-integrin β1 (P5D2) antibody to neutralise active transmembrane domains and promote receptor internalisation. The number of internalization events provided insights into the stability of integrin-laminin bonds. Immunofluorescent images distinguish between non-internalised receptors (before permeabilisation), internalised vesicles (after permeabilisation), and a composite of these two channels (Figure IV-20F). This assay allowed for the analysis of integrin β1 internalisation efficiency. The images were segmented using Imaris software for further analysis (Figure IV-20G). Quantitative analysis of the internalisation efficiency included measurements of vesicle volume, number of vesicles per cell (density), sphericity, and Z-

position for low (5 µg/ml) and high (20 µg/ml) concentrations of laminin 332 and laminin 511 on hydrogel (Figure IV-20H).

Vesicle volumes were higher at low laminin concentrations compared to high for both laminins. The difference in vesicle density was not significant, however, a trend of reduced number of vesicles was observed with laminin 511 compared to laminin 332. This may suggest a more stable integrin-laminin bond and a higher impact of integrin β1-mediated adhesion on laminin 511. Between the two laminins, vesicles were more spherical and located lower along the Z-axis for laminin 511 compared to laminin 332. The difference in Z-position aligned with the overall junctional cell height difference (Figure IV-12D).

This analysis illustrated differences in integrin β1 endocytosis across various coating conditions, providing insights into the role of laminin concentration and isoform in modulating integrin β1 function. However, these results are not conclusive as they heavily depended on the quality of segmentation, which presented significant challenges. Therefore, an additional approach was needed to quantify receptor functionality in a more reliable and accurate manner.

3.9. Integrin β4/β1 ratio modulates RPE adhesion and mechanical homeostasis along the visual axis

To determine the repertoire of receptors involved in RPE adhesion with response to different ECM cues, I used flow cytometry to characterise the surface distribution of target integrins (Figure IV-21). Since the greatest difference in integrin impact on cellular adhesion was observed at low protein density, so laminin 511 and laminin 332 at a coating concentration of 5 µg/ml were used as culture substrates. Single RPE cells were acquired from one-week-old monolayers and stained for key α (α3, α6) and β (β1, β4) integrin subunits, previously identified with adhesion assay (Figure IV-19C, D).

For the reliable data analysis, the flow cytometry gating strategy began with identifying cells (Figure IV-21A), isolating single cells (Figure IV-21B), and selecting a population of single living cells (negative viability marker) (Figure IV-21C). Additionally, because the emission spectrum of AlexaFluor488, to which anti-integrin β4 was conjugated, overlaps with the autofluorescence of the cells due to their pigmentation, an additional gating strategy was implemented to separate cells exclusively positive for β4 (Figure IV-21D). Representative histograms showed the surface expression of PE-

conjugated integrin β1 and AF488-conjugated β4 on hiPSC-RPE cells cultured on low-density laminin 332 and laminin 511, compared to unstained controls (Figure IV-21E).

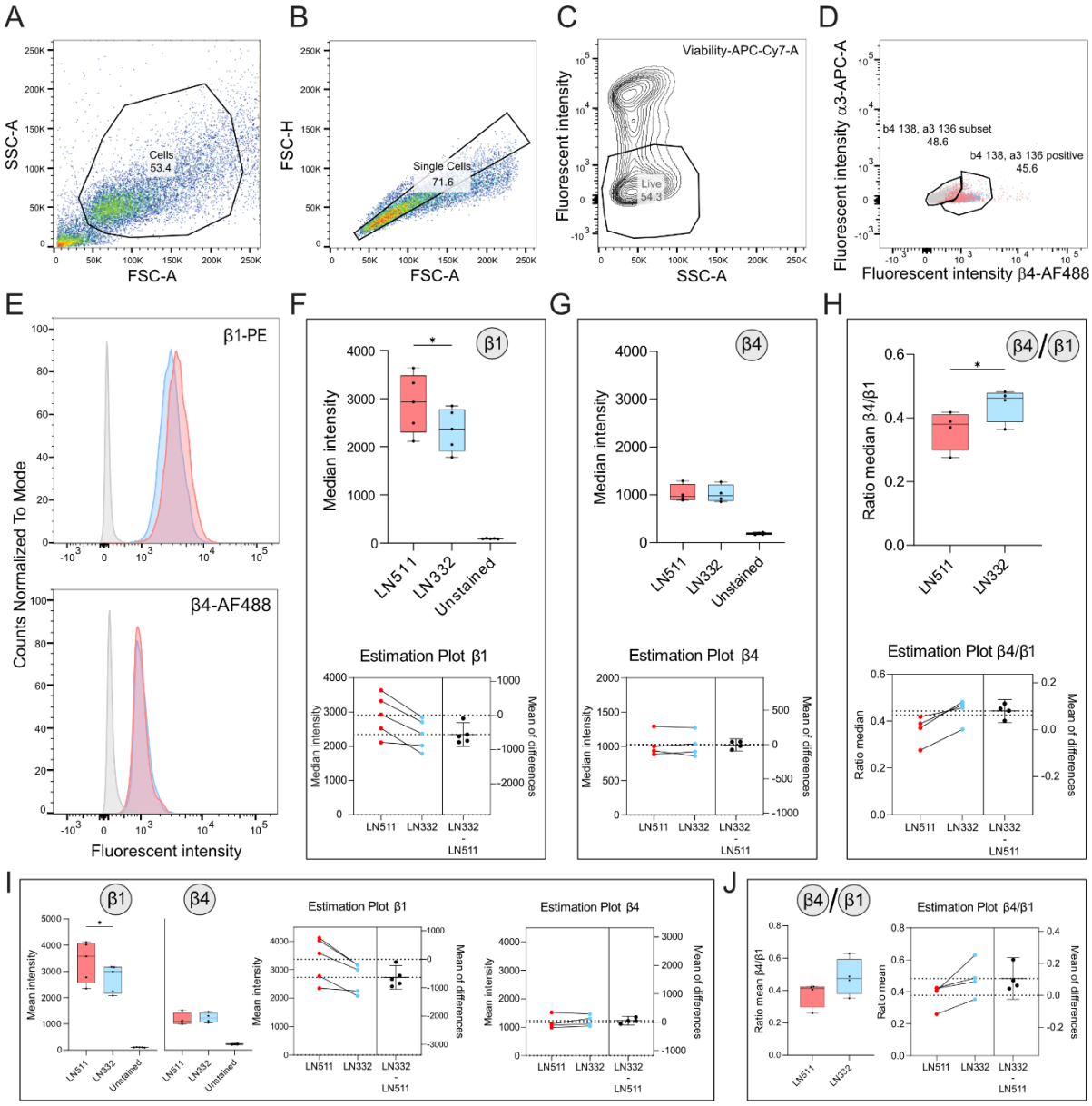

Figure IV-21. *Flow cytometry analysis of integrin β expression in hiPSC-RPE cultured on low density (5 µg/ml) laminin 511 or laminin 332.* ***A, B, C, D.*** *Representative dot plots illustrating the gating strategy to identify cells (A), single cells (B), contour plot to extract a population of single living cells (C) and gating strategy for β4-positive cells (D).* ***E.*** *Representative flow cytometry histograms showing surface expression of PE-conjugated integrin β1 (top) and AF488-conjugated β4 (bottom) on hiPSC-RPE cells cultured for one week on low-density laminin 332 (light blue), laminin 511 (red), and unstained control (grey).* ***F, G, H.*** *Box and whisker plots illustrate the distribution of intensity medians and the relative estimation plots from independent experiments for β1 (F) and β4 (G) integrins, as well as their ratio (H).* ***I.*** *Box and whisker plots of the mean intensity of integrin β1 and integrin β4 staining (left) and corresponding estimation plots (right) acquired from flow cytometry data.* ***J.*** *Box and whisker (left) and estimation (right) plots showing the ratio between mean intensity of integrin β4 and integrin β1 staining. Statistical analysis was done using a paired t-test to compare results between laminin 511 and laminin 332 coatings, * $p < 0.05$.*

My quantification of median and mean fluorescent intensities revealed distinct integrin profiles for RPE cells adhering to laminin 511 and laminin 332. Specifically, cells

adhering to low-density laminin 511 exhibited a significantly higher surface presence of β1 integrin compared to those adhering to laminin 332 (Figure IV-21E, F). In contrast, the surface levels of β4 integrin were similar between coating conditions (Figure IV-21G). Further analysis showed that RPE cells on laminin 332 displayed a significantly higher ratio of integrin β4 to β1 compared to those on laminin 511 (Figure IV-21H, I, J).

Additionally, no significant differences were observed in the expression of α3 and α6 integrins across the different conditions as shown by the quantification of both median and mean fluorescence intensity (Figure IV-22A-D). Estimation plots, which connect both conditions for each experiment, further confirm the absence of any noticeable trends between laminins (Figure IV-22E, F).

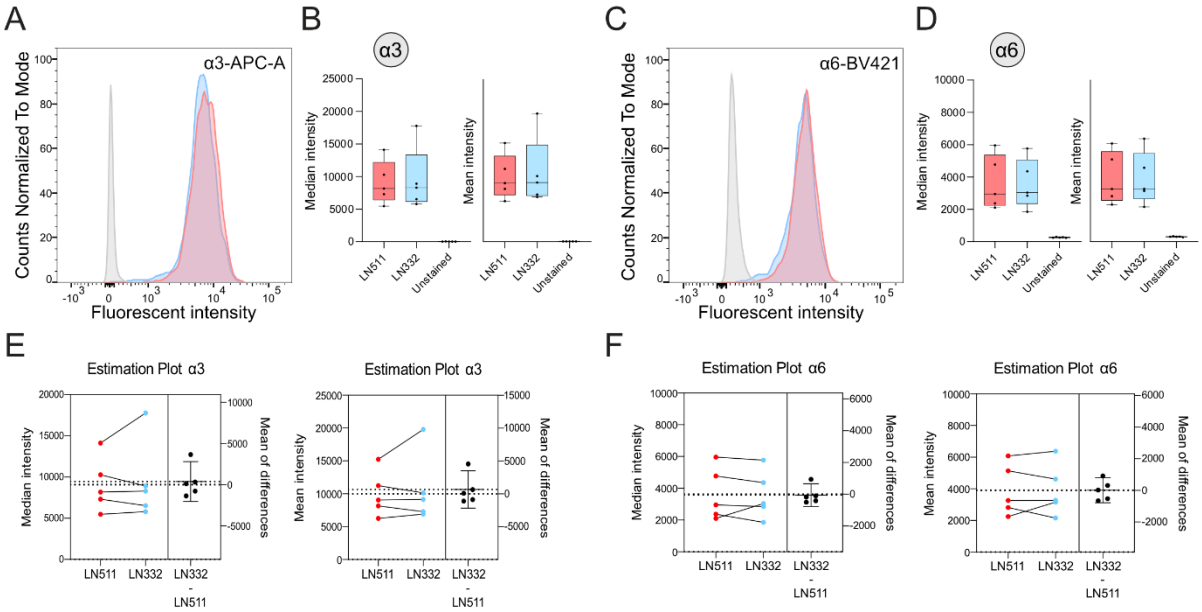

Figure IV-22. *Flow cytometry analysis of integrin α expression in hiPSC-RPE cultured on low density (5 µg/ml) laminin 511 or laminin 332.* ***A, B, C, D.*** *The results from flow cytometry analysis of staining for APC-A-conjugated integrin α3 and BV421-conjugated integrin α6 showing representative histograms, box and whisker plots of median and mean fluorescent intensity (A, B, C, D) and corresponding estimation plots (E, F). The grey-coloured histogram represents the signal from unstained cells. Statistical analysis was done using a paired t-test to compare results between laminin 511 and laminin 332 coatings, * $p < 0.05$.*

These results suggest that integrins α6β1 and α3β1 primarily support adhesion to laminin 511, while adhesion to laminin 332 involves integrins α6β1, α3β1, and α6β4. The observed differential expression and integrin ratio highlighted the subtle regulatory mechanisms governing RPE cell adhesion, which are crucial for maintaining mechanical homeostasis along the visual axis. Overall, these data provide valuable insights into the ECM-derived integrin-mediated adhesion of RPE cells, contributing to our understanding of their role in retinal health and disease.

V. Discussion

The findings of my work highlight the complex relationship between the extracellular matrix (ECM) and the retinal pigment epithelium (RPE), emphasising its crucial role in maintaining retinal health and vision. Overall, the ECM's dual function to regulate both biochemical and mechanical signals is key to maintaining the structural and functional integrity of the RPE cells. By establishing a physiologically relevant stem cell-derived model, we gain novel insights into human-specific cellular responses and mechanisms. This platform effectively demonstrates how ECM properties influence RPE morphology, mechanical properties, and functional behaviours in human-relevant contexts, recapitulating key aspects of human pathophysiology.

Here, I will interpret these findings within the framework of existing research, consider potential translational applications, and discuss study limitations and future research directions.

1. Extracellular matrix gradient *in vivo* drives retinal epithelium mechanobiology

Our findings demonstrate a direct role of laminin density in regulating RPE functional capacity through epithelial contractility. The uniqueness of the work lies in the fact that we are the first to report the presence of a relative density gradient of specific laminin isoforms in Bruch's membrane *in vivo* (Kozyrina et al., 2024). The Bruch's membrane has the highest laminin content at the retinal centre, whereas, at the far periphery, laminin 332 and α5-containing isoforms have the lowest density. This laminin density gradient correlates with a different topology and a gradual increase in the RPE cellular shape factor, with lower laminin density corresponding to more elongated cells. Cellular shape factor and cell-to-neighbourhood relationship directly correspond to the mechanical properties of the epithelial monolayers and contractility (Bi et al., 2015; Chouhan et al., 2024; Wyatt et al., 2015). When considering the distribution of mechanical properties using the cell-inference algorithm, the variability of intracellular stresses shows an increasing trend towards the far peripheral region in both adult and aged mice, suggesting heterogeneous mechanical load. However, further analysis is necessary to confirm the statistical significance of these observations.

The shape of the nucleus can indicate the mechanical state of the surrounding tissue, as nuclear deformation often correlates with altered gene expression and cellular function (Lammerding, 2011). Analysis of nuclear morphology revealed the presence of more elongated nuclei at the retinal periphery compared to the centre, suggesting increased tissue mechanical strain. Although nuclear orientation appears generally stable across regions, larger fields of view with more segmented nuclei are needed to confirm the lack of a relationship between region-dependent cellular mechanics and nuclear orientation. The characterisation of monolayer organisation in the central part showed the importance of intercellular stability, provided by tight junctional proteins, in regulating RPE structural integrity and mechanical homeostasis.

Actin and keratin form two distinct but interconnected cytoskeletal networks within epithelial cells. The actin network connects to adherens junctions, allowing for force transmission between cells and enabling coordinated cell movements. Meanwhile, the keratin network links to desmosomes, which helps distribute mechanical energy across the tissue, preserving overall integrity and barrier function (Rübsam et al., 2023). Additionally, this network was proposed to define tissue textile nature (Di Russo et al., 2023). Hence, the varying arrangements of the keratin network within the RPE, as presented in our paper (Kozyrina et al., 2024), suggest that towards the periphery, the actin cytoskeleton plays a more significant role in the epithelial mechanical status. Altogether, this evidence strongly indicates higher epithelial contractility at the far periphery compared to the centre. This difference could influence the ability of RPE cells to maintain their structural integrity and functional capacity to withstand the required tissue functional load.

2. Stem cell-derived model is an optimal *in vitro* system to study retinal pigmented epithelium mechanobiology

The distinct arrangements of the keratin network within the RPE, particularly towards the periphery, suggest an increased contribution of the actin cytoskeleton to the mechanical status of the epithelium. This together with morphological differences implies higher epithelial contractility at the far periphery compared to the centre. Due to technical limitations in directly quantifying mechanical properties and contractility *in vivo*, I developed an *in vitro* model using laminin-functionalized polyacrylamide (PAA) gels. The approach allowed me to reduce the experimental complexity of the *in vivo* system and

modulate ECM-derived parameters in a controlled manner. The flexibility of PAA hydrogels in achieving the desired stiffness, combined with controlled surface modification, allowed us to create conditions that resemble the native ECM. By using NHS-ester functionalization, I attached laminin proteins at various concentrations onto a hydrogel surface. Consequently, these conditions allowed me to mimic the ECM of different retinal regions accurately in a two-dimensional system.

When developing an *in vitro* system to mimic native conditions, the ARPE-19 cell line presents both benefits and limitations. One of the primary advantages of using ARPE-19 cells is their ease of culture, making them a convenient choice. Additionally, ARPE-19 cells are well-characterized and have been extensively used in various studies, providing a wealth of comparative data. However, a significant limitation is that they do not fully replicate the phenotype and functionality of primary RPE cells. Studies have shown that ARPE-19 cells may lack certain characteristics critical for accurately modelling native retinal conditions. For instance, they exhibit a relatively high proliferation rate (30% in 12 hours, (Tsujinaka et al., 2015)) and take approximately one month after reaching confluence to mature and polarize (Lehmann et al., 2014). Additionally, their expression of RPE-specific genes may differ from that of primary RPE cells (Lehmann et al., 2014; Strunnikova et al., 2010). These discrepancies can significantly limit the translational relevance of findings obtained from ARPE-19-based models.

In contrast, human induced pluripotent stem cell-derived RPE (hiPSC-RPE) cells offer a more suitable alternative for our requirements. hiPSC-RPE cells can be generated from patient-specific iPSCs, providing a personalized model that closely mimics the genetic and functional properties of native RPE cells (Müller et al., 2018; M. J. Song et al., 2023). These cells exhibit proper morphological features, gene expression patterns, and physiological functions that are more representative of the *in vivo* environment. Therefore, transitioning to hiPSC-RPE cells in our *in vitro* system allows us to achieve a more accurate and reliable representation of native retinal conditions, enhancing the validity and applicability of our research findings.

In this work, I developed both 2D and 3D cell culture models to study the effect of ECM on RPE mechanobiology. First, I aimed to characterise the effect of ECM composition using an epithelial spheroid model. The suspension culture offered an ideal platform to study the biochemical signalling from the ECM independently of its mechanical

properties. I employed the most commonly used technique based on the hanging drop method for spheroid formation. While the formation of spheroids was efficient, the prolonged formation times posed challenges for maintaining optimal culture conditions. For more consistent and controlled spheroid size and cultural conditions, I later used 3D agarose moulds. This method enhanced reproducibility and allowed for better manipulation of the biochemical microenvironment, thus offering a more accurate model for studying the behaviour of RPE cells. Overall, 3D cultures allowed us to observe complex cell-matrix interactions and spatial cell organization, offering valuable insights into how the environment, driven solely by biochemical stimulation, can regulate cellular mechanics in a three-dimensional context. Nonetheless, further characterization using standardized protocols is essential to fully elucidate the intricate interplay between ECM biochemical composition and epithelial mechanics and functionality.

In contrast, cells in the two-dimensional system sense and respond to both biochemical and mechanical stimuli from the substrate. To address this, we cultured cells on soft polyacrylamide (PAA) hydrogels, which allowed for precise control of substrate stiffness and biochemistry, creating conditions that more closely resemble the natural ECM environment. This approach provided a simplified yet informative platform to study cell-matrix interactions, focusing on cellular traction forces, adhesion properties, and phagocytic capacity in a controlled manner. When combined with a physiologically relevant stem cell-derived culture system, this bottom-up approach became an ideal setup to examine the effects of ECM laminin isoforms and densities on RPE cell homeostasis.

3. Laminin isoforms modulate epithelial mechanical homeostasis

A human-relevant model based on hiPSC-derived RPE cells on hydrogels has provided significant insights into the intricate role of ECM components in modulating RPE cell behaviour. This model has highlighted the direct impact of laminin 511 on enhancing RPE contractility, as evidenced by increased traction forces and elevated monolayer stress. These changes coincide with a notable reduction in phagocytic efficiency, a crucial function of RPE cells. However, despite this increase in contractility, there were no alterations in cell shape or topology observed. This finding suggests that the variability of monolayer organisation *in vivo* might be influenced by additional factors beyond ECM composition alone. For instance, the anchorage of RPE cells to the ora serrata at the retinal

periphery likely plays a crucial role in maintaining the structural integrity and organization of the monolayer (Nobeschi et al., 2006).

Additionally, the characterization of spheroid sphericity highlighted the distinct effects of laminin isoforms in regulating multicellular collective self-organization. Specifically, there was a slight increase in sphericity during incubation with laminin 521 and a decrease with laminin 111 compared to conditions without additional ECM components. It was shown that strong cell-matrix adhesion and weak cell-cell adhesion play crucial roles in modulating branching morphogenesis in stratified epithelia (S. Wang et al., 2021). Therefore, different laminin isoforms may promote varying degrees of intercellular adhesion, potentially affecting the overall spheroid structure. Laminin isoform 111 is the most prevalent ECM protein during embryogenesis and remains present as a major epithelial laminin in some adult tissues (Ekblom et al., 1998; Patton et al., 1997). Laminin 111 facilitates epithelial-to-mesenchymal transition during development by competitively binding to α3β1 integrin, leading to the overexpression of the intercellular junction protein E-cadherin (Horejs et al., 2014; Scott et al., 2019). In contrast to the role of adhesion in branching morphogenesis—where stratified epithelial budding is driven by strong cell-matrix adhesion combined with weak cell-cell adhesion (S. Wang et al., 2021)—laminin 111 in spheroid suspension may promote stronger cell-cell adhesion by upregulating E-cadherin, leading to less uniform spheroid shapes. However, further studies are needed to more accurately assess spheroid sphericity and identify any molecular changes related to the differential expression of junctional proteins.

The impact of laminin α5 on cellular mechanics aligns with previous findings. Laminin α5-containing isoforms enhance cell stiffness and support better mechanotransduction (Di Russo et al., 2016) and intercellular tightness (J. Song et al., 2017) in endothelial cells. Additionally, laminin 511 enhances hiPSC colony density and retinal differentiation through actomyosin contraction, leading to cell density-dependent YAP inactivation and increased MLC phosphorylation, colony compaction, and neuroectoderm differentiation (Shibata et al., 2018). As for the laminin 332, cellular adhesion on this protein is primarily mediated by α6β4 integrin, which forms hemidesmosomes with keratin as its cytoskeletal binding partner (Jones et al., 1998; Sonnenberg et al., 1991). Hemidesmosomes, which serve as anchoring points, are crucial in organizing the keratin network—an essential component for maintaining the

mechanical integrity of epithelial tissues, as highlighted in numerous studies(Hahn & Labouesse, 2001; Di Russo et al., 2023; Walko et al., 2015). Recent studies have shown that hemidesmosomes and the keratin network play a vital role in reducing cellular traction force (W. Wang et al., 2020) and protecting the nucleus from mechanical strain (Z. Kechagia et al., 2023).

Altogether, these findings highlight the critical role of ECM composition in regulating RPE mechanobiology. Consistent with the tensegrity model, cellular mechanics is governed by a balance of cytoskeleton-driven forces, where the contractile actin cytoskeleton is counterbalanced by intermediate filaments (Ingber, 1993). This intricate interplay is essential for maintaining proper cellular homeostasis. Furthermore, the differential interactions of integrins with specific laminin isoforms reveal how ECM components can finely tune cellular behaviour and function. Understanding these dynamics provides valuable insights into the mechanobiological processes underlying RPE functionality.

4. Surface nanostructure controls epithelial monolayer mesoscale properties through modulation of cell-adhesion receptors

Substrate nanostructure plays a crucial role in controlling cellular mechanobiology by influencing cell collective behaviour. Nanoscale features on substrates interact directly with cell receptors and their clusters, impacting downstream mechanotransduction signalling pathways and regulating cell responses (X. Li et al., 2021; Di Russo et al., 2021; J. L. Young et al., 2020). The density of ECM protein fragments on the surface significantly influences cellular behaviour by affecting integrin lateral nanospacing, which in turn influences single-cell spreading, migration speed, and persistence (Cavalcanti-Adam et al., 2007; Oria et al., 2017). Therefore, the observed decrease in laminin density and its relation to the functional capacity of RPE cells in vivo can be explained by changes in cell-ECM interaction mediated by the density of adhesion receptors.

In this study, the data revealed a divergent effect of low-density laminin 511 and laminin 332 on RPE mechanical properties and functionality. Specifically, cells cultured on laminin 511 exhibited significantly higher traction forces, elevated levels of active RhoA, and reduced functional capacity compared to those cultured on laminin 332 at the same concentration. The fundamental difference between laminin 511 and laminin 332 lies in the specific integrin receptors involved in cellular adhesion.

Adhesion to laminin 511 is primarily mediated by β1 integrins, with a higher affinity for α3β1 over α6β1, and it can additionally interact with α6β4 integrin. Meanwhile, laminin 332 exhibits a stronger affinity for integrin α6β4 compared to α3β1, highlighting distinct integrin-binding preferences between the two laminin isoforms (Nishiuchi et al., 2006; Sugawara et al., 2008; Yap et al., 2019). The variations in RPE cell behaviour are likely dependent on the differential engagement of these laminin-binding integrins. The different binding affinities of these integrins alter the balance between β1- and β4-mediated adhesion on the laminin substrates, which might explain the mesoscale differences in RPE cell mechanics and functionality.

Integrins are pivotal in cell adhesion and mechanics, acting as critical connectors between the ECM and the cytoskeleton to facilitate bidirectional mechanotransduction. According to the molecular clutch model (Mitchison & Kirschner, 1988), integrins bind directly to ECM proteins, forming catch bonds that strengthen under force, clustering, and recruiting other adhesion proteins. This process activates various signalling pathways, including Src-FAK, Ras-MEK-MAPK, and Akt/PI3K, by engaging kinases and adaptor proteins (Schiller & Fässler, 2013; Zent & Pozzi, 2010). Integrins also dynamically interact with the actomyosin system through proteins such as talin and vinculin, converting kinetic energy from actin retrograde flow and contractility into traction forces that pull on the ECM (Z. Sun et al., 2016).

The molecular clutch model was initially proposed for β1 integrin in freely moving cells, where its role in mediating cell-ECM interactions and mechanotransduction is well-established. β1 integrin, primarily interacting with the actin cytoskeleton, is involved in dynamic processes such as cell migration, mechanosensing, and signalling, particularly through the FAK/Rac/p21-activated kinase pathway. For example, in mammary epithelium, integrin α3β1 is critical for regulating the contraction/relaxation cycle by inhibiting MLCK activity, with its absence leading to impaired functions like milk ejection (K. Raymond et al., 2011). Additionally, the α3β1 integrin–CD151 complex enhances cadherin-mediated cell-cell adhesion, illustrating its dual role in both ECM interactions and intercellular connections (Chattopadhyay et al., 2003). Furthermore, blocking α3β1 can inhibit the adhesion, invasion, and survival of circulating tumour cells, highlighting its importance in cancer progression (Stipp, 2010). The α6β1 integrin, another β1 subunit pairing, is also implicated in mechanosensing, as seen in lens cortical fiber cells where it responds to shear stress, triggering hemichannel opening critical for glucose and

glutathione transport (J. Liu et al., 2020). In immune cells, α6β1 plays a role in adhesion and migration, influencing immune surveillance and response (Dangerfield et al., 2005). Its complementary role with α3β1 is evident in wound healing, where the enhanced migration speed of keratinocytes lacking α3 integrin is compensated by increased α6β1 expression (Margadant et al., 2008).

In contrast, the β4 integrin subunit, particularly in the α6β4 heterodimer, is less involved in dynamic cell movements and instead contributes to stable, long-lasting adhesions in epithelial tissues. Unlike β1 integrin, β4 integrin uniquely associates with cytokeratins rather than F-actin, forming a critical component of hemidesmosomes that anchor epithelial cells to the basement membrane. This interaction with cytokeratins through plectin provides mechanical stability to epithelial tissues, enabling cells to withstand shear stress and maintain tissue integrity (Rezniczek et al., 1998). Moreover, it was proposed that α6β4-mediated compression forces are crucial for epithelial cells to remodel basement membranes (Rabinovitz et al., 2001). Notably, the absence of α6β4 integrin has been associated with the induction of tumorigenic properties in epithelial cells, such as increased proliferation, migration, and apoptosis resistance *in vitro*, along with increased metastatic capacity *in vivo* (Wenta et al., 2022; Yu et al., 2005). This contrast between β1 and β4 integrins emphasises their distinct roles in cellular mechanics, with β1 integrins driving dynamic cellular responses and β4 integrins providing structural stability in tissue-specific contexts.

The flow cytometry data indicated that RPE cells cultured on laminin 332 exhibited a notably higher ratio of integrin β4 to β1 compared to cells on laminin 511. In the context of RPE cells, this elevated β4/β1 integrin ratio in cells adhering to low-density laminin 332 may account for the observed low traction forces, contrasting with the higher traction forces promoted by low-density laminin 511. Moreover, during the β1 antibody feeding assay, there was a noticeable decrease in the number of internalized vesicles in cells cultured on laminin 511 compared to laminin 332. This finding, along with the overall higher β1 expression in cells on laminin 511, highlights the substantial difference in integrin recycling speed between these conditions. This suggests variations in receptor affinity and the strength of the cell-receptor bond. These differences underscore the distinct roles of various laminin isoforms in influencing cellular mechanics. Additionally, *in vivo* observations of RPE cells in the far periphery showed a thinner and tenser keratin

network, along with elongated nuclei. This indicates a greater contribution of the contractile actin cytoskeleton to tissue mechanics in this region.

Despite these insights, several technical challenges remain unresolved. One open question is whether the relative amounts of laminin isoforms vary along the visual axis and if the ratio between β4 integrins (associated with hemidesmosomes) and β1 integrins decreases with the distance from the optic nerve. Addressing these questions will require advanced imaging techniques and molecular analyses to map the distribution of laminin isoforms and integrin subunits across different regions of the retina. Additionally, exploring the interplay between other ECM components and cytoskeletal elements could provide a more comprehensive understanding of how RPE cells maintain their structural integrity and function under varying environmental conditions.

During the flow cytometry analysis, I encountered challenges with signal overlap between several antibodies and the autofluorescence of RPE cells, highlighting the need for a more optimized antibody panel and additional samples to improve the clarity and accuracy of the data. Moreover, the antibody-feeding assay requires further standardization and proper characterization of the internalization processes. To better understand integrin β1 recycling, higher imaging resolution and possibly live imaging with conjugated antibodies are needed. These improvements will help to address current limitations and provide more definitive insights into the dynamics of integrin internalization and the influence of cellular mechanics.

5. Cellular actomyosin contractility levels control apical phagocytosis of retinal pigment epithelium

In the results of this study, I demonstrated that the traction levels defined by laminin significantly modulate the efficiency of RPE cells to phagocytose photoreceptor outer segments (POS), a fundamental physiological function of RPE cells. By modulating the level of cellular contractility through changes in surface mechanical cues (substrate stiffness) and biochemical coatings (laminin versus vitronectin), we observed clear differences in phagocytic efficiency. To isolate the exclusive role of cellular contractility from the potential converging effects of ECM signalling, I further manipulated cellular actomyosin contractility using a ROCK inhibitor and a RhoA activator.

Quantitative analysis revealed a direct correlation between actomyosin contractility level and the efficiency of RPE monolayers in POS phagocytosis. Specifically,

increased contractility was associated with reduced phagocytosis efficiency. These findings were consistent across various experimental conditions, indicating that higher traction forces, induced by low densities of laminin 511 as opposed to laminin 332, impair RPE functional capacity.

During the phagocytosis of POS, RPE cells initially recognise and bind to shed POS via specific receptors such as integrin αvβ5 and Mer tyrosine kinase receptor (MerTK) (Kwon & Freeman, 2020). When MerTK binds with ligands such as Gas6 or Protein S, it undergoes multimerization and autophosphorylation, initiating a cascade of events essential for phagocytosis. Once bound, RPE cells engulf and internalize POS, a process where the actin cytoskeleton is essential. During phagocytosis, the actin filaments undergo dynamic reorganization to form pseudopods that extend around and envelop the POS (Kwon & Freeman, 2020; Umapathy et al., 2023). Phosphorylated MerTK anchors the recruitment of F-actin to the phagocytic cup and stimulates Rac activation, promoting the branching of the F-actin cytoskeleton via the Arp2/3 complex.

The actin cytoskeleton's branched networks, necessary for effective phagocytosis, are stabilized by molecular clutches (Kwon & Freeman, 2020). One such clutch involves the binding of RPE cadherins to neural cell adhesion molecule (N-CAM) on the POS. Another critical clutch is the αvβ5 integrin, which binds to POS by interacting with the milk globular factor E-8 (MFG-E8) protein secreted by RPE cells. The αvβ5 integrin typically exists in a low-affinity conformation but is activated by MerTK through inside-out signalling, involving the recruitment of talin. Talin binds to the β5 subunit of the integrin, providing binding sites for F-actin and proteins like vinculin, linking actin polymerization to the membrane ruffling and ensheathing POS (Kwon & Freeman, 2020).

MerTK-mediated phagocytosis also involves focal adhesion kinase, which, along with αvβ5 integrin receptors, stimulates Rac1-GTPase, leading to the recruitment of actin to the phagocytic cup. These focal adhesion-like structures have been shown to mediate phagocytosis in macrophages and exhibit mechanosensitivity (Jaumouillé et al., 2019). Additionally, MerTK signalling recruits myosin II, which helps close the phagocytic cup and internalize the POS (Klettner & Dithmar, 2020). Although other ancillary molecular clutches may contribute to this process, MerTK remains the central receptor orchestrating POS phagocytosis in RPE cells.

Hence, the formation of this apical molecular clutch may be sensitive to the overall cellular contractility defined by the ECM substrate, explaining the lower efficiency of POS internalization observed in this work. Moreover, a previous study on stem cell-derived RPE has shown that the organization of the actin cytoskeleton can predict the phagocytic ability of differentiated cells. Despite sharing common phagocytic receptors and ligands, RPE cells exhibited diverse phagocytic capacities linked to the distinct cytoskeletal profile characterized by F-actin stress fibres (Müller et al., 2018). This insight aligns with my findings, suggesting that enhanced contractility in RPE cells may compromise their overall homeostasis and function.

VI. Significance

This research provides a novel perspective on the mechanisms that regulate the functionality of the retinal pigment epithelium (RPE), with a particular focus on the role of the extracellular matrix (ECM) in maintaining tissue homeostasis. The RPE is essential for visual function, primarily due to its role in the daily phagocytosis of photoreceptor outer segments (POS). Along the visual axis, the natural decrease in the ratio of photoreceptors to RPE cells indicates a reduced functional demand on the RPE cells from the central retina towards the periphery. However, the processes by which mechanical and biochemical cues from the ECM regulate RPE function remain poorly understood. Within this research, I investigated the hypothesis that the ECM, particularly the composition and density of laminins, plays a crucial role in determining RPE mechanical homeostasis and, consequently, its ability to support retinal function.

A significant aspect of this research builds on previous work conducted in our group, where we identified a laminin-based biochemical gradient within the ECM, which appears to create a corresponding mechanical gradient within the RPE. The current study shows that this gradient modulates cellular contractility and, by extension, phagocytic efficiency. These insights provide a deeper understanding of the ECM as an active regulator of RPE cellular mechanics and function. By demonstrating that variations in laminin density and isoforms differentially engage integrins β1 and β4, this study suggests that the specific laminin assembly within the ECM directly impacts RPE cellular contractility by modulating the balance between actin and keratin cytoskeletal networks. This balance is critical for maintaining tissue mechanical stability and ensuring the RPE's ability to support photoreceptor cells (Figure VI-1).

The reductionist approach using human stem cell-derived RPE models further highlights the significance of this research. The developed stem cell-based *in vitro* systems allow for precise manipulation of ECM properties and detailed analysis of cellular responses. The gained insights are complemented by *in vivo* observations that demonstrate a natural decrease in laminin density towards the retinal periphery, correlating with alteration of cellular morphometry and a reduction in RPE functional demand along the visual axis. Combined, these findings create a coherent picture of how ECM composition influences RPE function, with potential implications for understanding retinal health and disease.

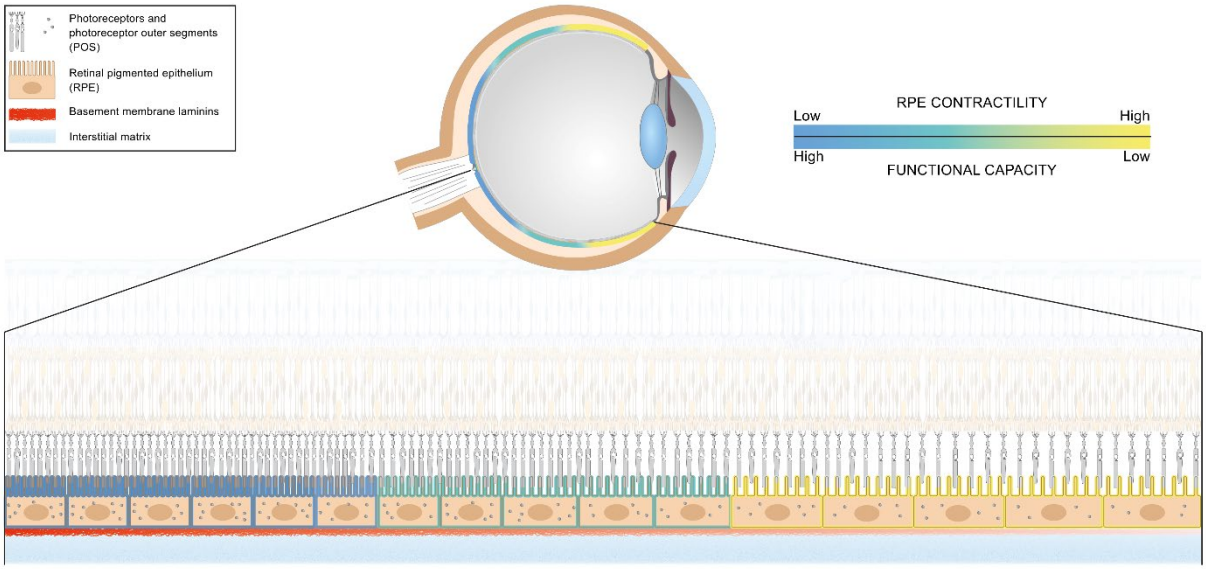

Figure VI-1. *RPE mechanical homeostasis along the visual axis. The schematic illustrates how ECM-orchestrated changes in retinal tissue affect RPE mechanical homeostasis. In the macula, high basement membrane laminin density ensures a mechanical environment that supports the high functional demand. Conversely, low laminin density in the retinal periphery increases RPE contractility, which corresponds to diminished functional capacity.*

On a broader scale, this research extends our understanding of the ECM's role in regulating mechanical homeostasis and functionality, not only in the RPE but in epithelial tissues more generally. The discovery that a laminin-defined mechanical gradient can modulate RPE cellular function suggests that similar mechanisms may influence cellular behaviour in other epithelia. Laminins are key components of the ECM in a variety of epithelial tissues such as the skin, lungs, and gastrointestinal tract, where they influence cellular behaviour, tissue integrity, and response to mechanical stress (Ekblom et al., 1998; Hamill et al., 2009; Shaohua Li et al., 2003). Alterations in ECM composition could affect mechanical balance and lead to functional impairments across a range of tissues.

In summary, this research highlights the importance of mechanical homeostasis in tissue physiology, offering valuable insights not only for retinal biology but also for the broader field of epithelial mechanobiology, emphasizing the importance of mechanical properties in maintaining tissue health.

VII. Limitations and Future Research

Overall, my work highlights the critical importance of ECM-derived signalling and RPE mechanobiology in maintaining retinal function and health. The data obtained with hiPSC-RPE cells supports the existence of a laminin-defined mechanical balance in RPE *in vivo* which gradually shifts to a less prominent keratin contribution and more contractile monolayer toward the retinal periphery. By establishing a link between ECM density, integrin engagement, and cellular mechanics, my research provides a foundation for future studies aimed at unravelling the complex interactions that underline retinal physiology and pathology. This research opens new perspectives on retinal diseases, implementing mechanical status as a parameter to maintain retinal health.

In ageing, ECM undergoes significant remodelling events of its composition, altering the cell-ECM adhesion sites with subsequent putative changes in epithelial functionality (Booij et al., 2010). Age-related Bruch's membrane remodelling mainly includes an increased crosslinking of collagen fibres, calcification of elastic fibres and turnover of glycosaminoglycans (Piskova et al., 2023). By altering cellular adhesion, these changes might shift RPE mechanical homeostasis, potentially leading to phenotypical changes and sight-impairing diseases such as myopia and age-related macular degeneration. Applying the knowledge of this work on a direct connection between cellular contractility levels and RPE phagocytosis capacity, one could explore the possibility of using Rho kinase inhibitors, as in the treatment for glaucoma (L.-C. Liu et al., 2024; J. Wang et al., 2023), to prevent the progression of RPE-specific diseases. Further studies are essential to determine the extent to which RPE contractility contributes to outer retinal diseases and to explore potential therapeutic approaches.

Our two-dimensional *in vitro* model was highly effective in maintaining RPE cells under conditions close to physiological relevance and allowed us to accurately quantify various mechanobiological parameters. However, despite the high efficiency and reproducibility of chemical functionalization, a key limitation is the lack of precise knowledge about the actual density of laminins on the surface of the PAA hydrogels. To study cellular adhesion more accurately, gold nanopatterning or similar techniques could be implemented to control the density and nature of adhesion sites on a hydrogel precisely. For this, laminin peptides or laminin fragments could be used to modulate the cell adhesion receptors. Regarding the further development of 3D models, we can adapt

the methods established in this work for a two-dimensional system, such as flow cytometry to study integrin receptors or force-inference algorithms to evaluate cellular mechanics and employ POS phagocytosis assays to quantify cellular functionality. These established models could also serve as novel platforms for retinal disease modelling, as they recapitulate the main features of retinal tissue and offer relative flexibility.

Given the challenge of directly quantifying mechanical properties and contractility *in vivo*, research must depend on *in vitro* models, which may not perfectly replicate the native environment. Future research should focus on developing more advanced models to better understand the interactions between ECM components and RPE mechanobiology. Additionally, longitudinal studies on retinal ageing and disease progression could offer valuable insights into the temporal dynamics of ECM remodelling and its effects on RPE function.

References

Aboav, D. A. (1970). The arrangement of grains in a polycrystal. *Metallography*, *3*(4), 383–390. https://doi.org/10.1016/0026-0800(70)90038-8

Aboav, D. A. (1980). The arrangement of cells in a net. *Metallography*, *13*(1), 43–58. https://doi.org/10.1016/0026-0800(80)90021-x

Alberts, B., Johnson, A., Lewis, J., Morgan, D., Raff, M., Roberts, K. & Walter, P. (2015). *Molecular Biology of The Cell Sixth Edition*. Garland Science.

Arcangelis, A. D., Mark, M., Kreidberg, J., Sorokin, L. & Georges-Labouesse, E. (1999). Synergistic activities of α3 and α6 integrins are required during apical ectodermal ridge formation and organogenesis in the mouse. *Development*, *126*(17), 3957–3968. https://doi.org/10.1242/dev.126.17.3957

Aumailley, M. (2012). The laminin family. *Cell Adhesion & Migration*, *7*(1), 48–55. https://doi.org/10.4161/cam.22826

Aumailley, M. (2021). Laminins and interaction partners in the architecture of the basement membrane at the dermal-epidermal junction. *Experimental Dermatology*, *30*(1), 17–24. https://doi.org/10.1111/exd.14239

Balcioglu, H. E., Balasubramaniam, L., Stirbat, T. V., Doss, B. L., Fardin, M.-A., Mège, R.-M. & Ladoux, B. (2020). A subtle relationship between substrate stiffness and collective migration of cell clusters. *Soft Matter*, *16*(7), 1825–1839. https://doi.org/10.1039/c9sm01893j

Belkin, A. M. & Stepp, M. A. (2000). Integrins as Receptors for Laminins. *Microscopy Research and Technique*.

Berens, P. (2009). CircStat: A MATLAB Toolbox for Circular Statistics. *Journal of Statistical Software*. https://doi.org/10.18637/jss.v031.i10

Bhatia, S. K., Rashid, A., Chrenek, M. A., Zhang, Q., Bruce, B. B., Klein, M., Boatright, J. H., Jiang, Y., Grossniklaus, H. E. & Nickerson, J. M. (2016). Analysis of RPE morphometry in human eyes. *Molecular Vision*, *22*, 898–916.

Bi, D., Lopez, J. H., Schwarz, J. M. & Manning, M. L. (2015). A density-independent rigidity transition in biological tissues. *Nature Physics*, *11*(12), 1074–1079. https://doi.org/10.1038/nphys3471

Boekhorst, V. te, Preziosi, L. & Friedl, P. (2016). Plasticity of Cell Migration In Vivo and In Silico. *Annual Review of Cell and Developmental Biology*, *32*(1), 1–36. https://doi.org/10.1146/annurev-cellbio-111315-125201

Bok, D. (1993). The retinal pigment epithelium: a versatile partner in vision. *Journal of Cell Science*, *1993*(Supplement_17), 189–195. https://doi.org/10.1242/jcs.1993.supplement_17.27

Bonilha, V. L., Finnemann, S. C. & Rodriguez-Boulan, E. (1999). Ezrin Promotes Morphogenesis of Apical Microvilli and Basal Infoldings in Retinal Pigment Epithelium. *The Journal of Cell Biology*, *147*(7), 1533–1548. https://doi.org/10.1083/jcb.147.7.1533

Bonnans, C., Chou, J. & Werb, Z. (2014). Remodelling the extracellular matrix in development and disease. *Nature Reviews Molecular Cell Biology*, *15*(12), 786–801. https://doi.org/10.1038/nrm3904

Booij, J. C., Baas, D. C., Beisekeeva, J., Gorgels, T. G. M. F. & Bergen, A. A. B. (2010). The dynamic nature of Bruch's membrane. *Progress in Retinal and Eye Research*, *29*(1), 1–18. https://doi.org/10.1016/j.preteyeres.2009.08.003

Bortz, W. M. (1986). Aging as entropy. *Experimental Gerontology*, *21*(4–5), 321–328. https://doi.org/10.1016/0531-5565(86)90039-2

Boulton, M. & Dayhaw-Barker, P. (2001). The role of the retinal pigment epithelium: Topographical variation and ageing changes. *Eye*, *15*(3), 384–389. https://doi.org/10.1038/eye.2001.141

Bresnick, A. R. (1999). Molecular mechanisms of nonmuscle myosin-II regulation. *Current Opinion in Cell Biology*, *11*(1), 26–33. https://doi.org/10.1016/s0955-0674(99)80004-0

Bridgewater, R. E., Norman, J. C. & Caswell, P. T. (2012). Integrin trafficking at a glance. *Journal of Cell Science*, *125*(16), 3695–3701. https://doi.org/10.1242/jcs.095810

Brodland, G. W., Veldhuis, J. H., Kim, S., Perrone, M., Mashburn, D. & Hutson, M. S. (2014). CellFIT: A Cellular Force-Inference Toolkit Using Curvilinear Cell Boundaries. *PLoS ONE*, *9*(6), e99116. https://doi.org/10.1371/journal.pone.0099116

Cai, Y., Wang, S., Qu, J., Belmonte, J. C. I. & Liu, G.-H. (2022). Rejuvenation of Tissue Stem Cells by Intrinsic and Extrinsic Factors. *Stem Cells Translational Medicine*, *11*(3), 231–238. https://doi.org/10.1093/stcltm/szab012

Cavalcanti-Adam, E. A., Volberg, T., Micoulet, A., Kessler, H., Geiger, B. & Spatz, J. P. (2007). Cell Spreading and Focal Adhesion Dynamics Are Regulated by Spacing of Integrin Ligands. *Biophysical Journal*, *92*(8), 2964–2974. https://doi.org/10.1529/biophysj.106.089730

Chang, J. & Chaudhuri, O. (2019). Beyond proteases: Basement membrane mechanics and cancer invasion. *Journal of Cell Biology*, *218*(8), 2456–2469. https://doi.org/10.1083/jcb.201903066

Chastney, M. R., Conway, J. R. W. & Ivaska, J. (2021). Integrin adhesion complexes. *Current Biology*, *31*(10), R536–R542. https://doi.org/10.1016/j.cub.2021.01.038

Chattopadhyay, N., Wang, Z., Ashman, L. K., Brady-Kalnay, S. M. & Kreidberg, J. A. (2003). α3β1 integrin–CD151, a component of the cadherin–catenin complex, regulates PTPμ

expression and cell–cell adhesion. *The Journal of Cell Biology*, *163*(6), 1351–1362. https://doi.org/10.1083/jcb.200306067

Chaudhari, P. R. & Vaidya, M. M. (2014). Versatile hemidesmosomal linker proteins: structure and function. *Histology and Histopathology*, *30*(4), 425–434. https://doi.org/10.14670/hh-30.425

Chaudhuri, O., Cooper-White, J., Janmey, P. A., Mooney, D. J. & Shenoy, V. B. (2020). Effects of extracellular matrix viscoelasticity on cellular behaviour. *Nature*, *584*(7822), 535–546. https://doi.org/10.1038/s41586-020-2612-2

Chen, M., Rajapakse, D., Fraczek, M., Luo, C., Forrester, J. V. & Xu, H. (2016). Retinal pigment epithelial cell multinucleation in the aging eye – a mechanism to repair damage and maintain homoeostasis. *Aging Cell*, *15*(3), 436–445. https://doi.org/10.1111/acel.12447

Chiu, S. N. (1995). Aboav-Weaire's and Lewis' laws—A review. *Materials Characterization*, *34*(2), 149–165. https://doi.org/10.1016/1044-5803(94)00081-u

Chong, N. H. V., Keonin, J., Luthert, P. J., Frennesson, C. I., Weingeist, D. M., Wolf, R. L., Mullins, R. F. & Hageman, G. S. (2005). Decreased Thickness and Integrity of the Macular Elastic Layer of Bruch's Membrane Correspond to the Distribution of Lesions Associated with Age-Related Macular Degeneration. *The American Journal of Pathology*, *166*(1), 241–251. https://doi.org/10.1016/s0002-9440(10)62248-1

Chouhan, G., Lewis, N. S., Ghanekar, V., Ainavarapu, S. R. K., Inamdar, M. M. & Sonawane, M. (2024). Cell-size-dependent regulation of Ezrin dictates epithelial resilience to stretch by countering myosin-II-mediated contractility. *Cell Reports*, *43*(6), 114271. https://doi.org/10.1016/j.celrep.2024.114271

Citalán-Madrid, A. F., García-Ponce, A., Vargas-Robles, H., Betanzos, A. & Schnoor, M. (2013). Small GTPases of the Ras superfamily regulate intestinal epithelial homeostasis and barrier function via common and unique mechanisms. *Tissue Barriers*, *1*(5), e26938. https://doi.org/10.4161/tisb.26938

Clark, E. A. & Brugge, J. S. (1995). Integrins and Signal Transduction Pathways: the Road Taken. *Science*, *268*(5208), 233–239. https://doi.org/10.1126/science.7716514

Cox, T. R. & Erler, J. T. (2011). Remodeling and homeostasis of the extracellular matrix: implications for fibrotic diseases and cancer. *Disease Models & Mechanisms*, *4*(2), 165–178. https://doi.org/10.1242/dmm.004077

Curcio, C. A. & Allen, K. A. (1990). Topography of ganglion cells in human retina. *Journal of Comparative Neurology*, *300*(1), 5–25. https://doi.org/10.1002/cne.903000103

Curcio, C. A. & Johnson, M. (2013). Retina. *2: Basic Science and Translation to Therapy: Section 1Anatomy and Physiology: Section 1: Anatomy and Physiology*, 465–481. https://doi.org/10.1016/b978-1-4557-0737-9.00020-5

Dangerfield, J. P., Wang, S. & Nourshargh, S. (2005). Blockade of α6 integrin inhibits IL-1β- but not TNF-α-induced neutrophil transmigration in vivo. *Journal of Leukocyte Biology*, *77*(2), 159–165. https://doi.org/10.1189/jlb.0704421

Delwel, G. O., Melker, A. A. de, Hogervorst, F., Jaspars, L. H., Fles, D. L., Kuikman, I., Lindblom, A., Paulsson, M., Timpl, R. & Sonnenberg, A. (1994). Distinct and overlapping ligand specificities of the alpha 3A beta 1 and alpha 6A beta 1 integrins: recognition of laminin isoforms. *Molecular Biology of the Cell*, *5*(2), 203–215. https://doi.org/10.1091/mbc.5.2.203

Diaz-de-la-Loza, M.-C., Ray, R. P., Ganguly, P. S., Alt, S., Davis, J. R., Hoppe, A., Tapon, N., Salbreux, G. & Thompson, B. J. (2018). Apical and Basal Matrix Remodeling Control Epithelial Morphogenesis. *Developmental Cell*, *46*(1), 23-39.e5. https://doi.org/10.1016/j.devcel.2018.06.006

Di Persio, C. M., Hodivala-Dilke, K. M., Jaenisch, R., Kreidberg, J. A. & Hynes, R. O. (1997). α3β1 Integrin Is Required for Normal Development of the Epidermal Basement Membrane. *The Journal of Cell Biology*, *137*(3), 729–742. https://doi.org/10.1083/jcb.137.3.729

Di Persio, C. M., Neut, R. van der, Georges-Labouesse, E., Kreidberg, J. A., Sonnenberg, A. & Hynes, R. O. (2000). α3β1 and α6β4 integrin receptors for laminin-5 are not essential for epidermal morphogenesis and homeostasis during skin development. *Journal of Cell Science*, *113*(17), 3051–3062. https://doi.org/10.1242/jcs.113.17.3051

Di Russo, J. D., Luik, A., Yousif, L., Budny, S., Oberleithner, H., Hofschröer, V., Klingauf, J., Bavel, E. van, Bakker, E. N., Hellstrand, P., Bhattachariya, A., Albinsson, S., Pincet, F., Hallmann, R. & Sorokin, L. M. (2016). Endothelial basement membrane laminin 511 is essential for shear stress response. *The EMBO Journal*, *36*(2), 183–201. https://doi.org/10.15252/embj.201694756

Di Russo, J. D., Magin, T. M. & Leube, R. E. (2023). A keratin code defines the textile nature of epithelial tissue architecture. *Current Opinion in Cell Biology*, *85*, 102236. https://doi.org/10.1016/j.ceb.2023.102236

Di Russo, J. D., Young, J. L., Wegner, J. W., Steins, T., Kessler, H. & Spatz, J. P. (2021). Integrin α5β1 nano-presentation regulates collective keratinocyte migration independent of substrate rigidity. *ELife*, *10*, e69861. https://doi.org/10.7554/elife.69861

Dowling, J., Yu, Q. C. & Fuchs, E. (1996). Beta4 integrin is required for hemidesmosome formation, cell adhesion and cell survival. *The Journal of Cell Biology*, *134*(2), 559–572. https://doi.org/10.1083/jcb.134.2.559

DuFort, C. C., Paszek, M. J. & Weaver, V. M. (2011). Balancing forces: architectural control of mechanotransduction. *Nature Reviews Molecular Cell Biology*, *12*(5), 308–319. https://doi.org/10.1038/nrm3112

Eisenhoffer, G. T., Loftus, P. D., Yoshigi, M., Otsuna, H., Chien, C.-B., Morcos, P. A. & Rosenblatt, J. (2012). Crowding induces live cell extrusion to maintain homeostatic

cell numbers in epithelia. *Nature*, *484*(7395), 546–549. https://doi.org/10.1038/nature10999

Ekblom, M., Falk, M., Salmivirta, K., Durbeej, M. & Ekblom, P. (1998). Laminin Isoforms and Epithelial Development. *Annals of the New York Academy of Sciences*, *857*(1), 194–211. https://doi.org/10.1111/j.1749-6632.1998.tb10117.x

Eyckmans, J., Boudou, T., Yu, X. & Chen, C. S. (2011). A Hitchhiker's Guide to Mechanobiology. *Developmental Cell*, *21*(1), 35–47. https://doi.org/10.1016/j.devcel.2011.06.015

Feng, W., Yasumura, D., Matthes, M. T., LaVail, M. M. & Vollrath, D. (2002). Mertk Triggers Uptake of Photoreceptor Outer Segments during Phagocytosis by Cultured Retinal Pigment Epithelial Cells*. *Journal of Biological Chemistry*, *277*(19), 17016–17022. https://doi.org/10.1074/jbc.m107876200

Fields, M. A., Priore, L. V. D., Adelman, R. A. & Rizzolo, L. J. (2020). Interactions of the choroid, Bruch's membrane, retinal pigment epithelium, and neurosensory retina collaborate to form the outer blood-retinal-barrier. *Progress in Retinal and Eye Research*, *76*, 100803. https://doi.org/10.1016/j.preteyeres.2019.100803

Finnemann, S. C. (2003). Focal adhesion kinase signaling promotes phagocytosis of integrin-bound photoreceptors. *The EMBO Journal*, *22*(16), 4143–4154. https://doi.org/10.1093/emboj/cdg416

Flier, A. van der & Sonnenberg, A. (2001). Function and interactions of integrins. *Cell and Tissue Research*, *305*(3), 285–298. https://doi.org/10.1007/s004410100417

Foty, R. (2011). A Simple Hanging Drop Cell Culture Protocol for Generation of 3D Spheroids. *Journal of Visualized Experiments*, *51*, 2–6. https://doi.org/10.3791/2720

Frantz, C., Stewart, K. M. & Weaver, V. M. (2010). The extracellular matrix at a glance. *Journal of Cell Science*, *123*(24), 4195–4200. https://doi.org/10.1242/jcs.023820

Funaki, M. & Janmey, P. A. (2017). Chapter 23 - Technologies to Engineer Cell Substrate Mechanics in Hydrogels. In A. Vishwakarma & J. M. Karp (Eds.), *Biology and Engineering of Stem Cell Niches* (pp. 363–373). Academic Press. https://doi.org/10.1016/b978-0-12-802734-9.00023-8

Gardner, H., Kreidberg, J., Koteliansky, V. & Jaenisch, R. (1996). Deletion of Integrin α1 by Homologous Recombination Permits Normal Murine Development but Gives Rise to a Specific Deficit in Cell Adhesion. *Developmental Biology*, *175*(2), 301–313. https://doi.org/10.1006/dbio.1996.0116

Geiger, B., Spatz, J. P. & Bershadsky, A. D. (2009). Environmental sensing through focal adhesions. *Nature Reviews Molecular Cell Biology*, *10*(1), 21–33. https://doi.org/10.1038/nrm2593

German, O. L., Buzzi, E., Rotstein, N. P., Rodríguez-Boulan, E. & Politi, L. E. (2008). Retinal pigment epithelial cells promote spatial reorganization and differentiation of retina

photoreceptors. *Journal of Neuroscience Research*, *86*(16), 3503–3514. https://doi.org/10.1002/jnr.21813

Ghatak, S., Niland, S., Schulz, J.-N., Wang, F., Eble, J. A., Leitges, M., Mauch, C., Krieg, T., Zigrino, P. & Eckes, B. (2016). Role of Integrins α1β1 and α2β1 in Wound and Tumor Angiogenesis in Mice. *The American Journal of Pathology*, *186*(11), 3011–3027. https://doi.org/10.1016/j.ajpath.2016.06.021

Gordon, M. K. & Hahn, R. A. (2009). Collagens. *Cell and Tissue Research*, *339*(1), 247. https://doi.org/10.1007/s00441-009-0844-4

Gumbiner, B. M. (2005). Regulation of cadherin-mediated adhesion in morphogenesis. *Nature Reviews Molecular Cell Biology*, *6*(8), 622–634. https://doi.org/10.1038/nrm1699

Hahn, B.-S. & Labouesse, M. (2001). Tissue integrity: Hemidesmosomes and resistance to stress. *Current Biology*, *11*(21), R858–R861. https://doi.org/10.1016/s0960-9822(01)00516-4

Hamill, K. J., Kligys, K., Hopkinson, S. B. & Jones, J. C. R. (2009). Laminin deposition in the extracellular matrix: a complex picture emerges. *Journal of Cell Science*, *122*(24), 4409–4417. https://doi.org/10.1242/jcs.041095

Hanayama, R., Tanaka, M., Miwa, K., Shinohara, A., Iwamatsu, A. & Nagata, S. (2002). Identification of a factor that links apoptotic cells to phagocytes. *Nature*, *417*(6885), 182–187. https://doi.org/10.1038/417182a

Harburger, D. S. & Calderwood, D. A. (2008). Integrin signalling at a glance. *Journal of Cell Science*, *122*(2), 159–163. https://doi.org/10.1242/jcs.018093

Hardin, C., Rajendran, K., Manomohan, G., Tambe, D. T., Butler, J. P., Fredberg, J. J., Martinelli, R., Carman, C. V. & Krishnan, R. (2013). Glassy Dynamics, Cell Mechanics, and Endothelial Permeability. *The Journal of Physical Chemistry B*, *117*(42), 12850–12856. https://doi.org/10.1021/jp4020965

Holle, A. W., Kalafat, M., Ramos, A. S., Seufferlein, T., Kemkemer, R. & Spatz, J. P. (2017). Intermediate filament reorganization dynamically influences cancer cell alignment and migration. *Scientific Reports*, *7*(1), 45152. https://doi.org/10.1038/srep45152

Horejs, C.-M., Serio, A., Purvis, A., Gormley, A. J., Bertazzo, S., Poliniewicz, A., Wang, A. J., DiMaggio, P., Hohenester, E. & Stevens, M. M. (2014). Biologically-active laminin-111 fragment that modulates the epithelial-to-mesenchymal transition in embryonic stem cells. *Proceedings of the National Academy of Sciences*, *111*(16), 5908–5913. https://doi.org/10.1073/pnas.1403139111

Hussey, K. A., Hadyniak, S. E. & Johnston, R. J. (2022). Patterning and Development of Photoreceptors in the Human Retina. *Frontiers in Cell and Developmental Biology*, *10*, 878350. https://doi.org/10.3389/fcell.2022.878350

Hynes, R. O. (1992). Integrins: Versatility, modulation, and signaling in cell adhesion. *Cell*, *69*(1), 11–25. https://doi.org/10.1016/0092-8674(92)90115-s

Hynes, R. O. (2002). Integrins Bidirectional, Allosteric Signaling Machines. *Cell*, *110*(6), 673–687. https://doi.org/10.1016/s0092-8674(02)00971-6

Ingber, D. E. (1993). Cellular tensegrity: defining new rules of biological design that govern the cytoskeleton. *Journal of Cell Science*, *104*(3), 613–627. https://doi.org/10.1242/jcs.104.3.613

Ingber, D. E., Wang, N. & Stamenović, D. (2014). Tensegrity, cellular biophysics, and the mechanics of living systems. *Reports on Progress in Physics*, *77*(4), 046603. https://doi.org/10.1088/0034-4885/77/4/046603

Iskratsch, T., Wolfenson, H. & Sheetz, M. P. (2014). Appreciating force and shape — the rise of mechanotransduction in cell biology. *Nature Reviews Molecular Cell Biology*, *15*(12), 825–833. https://doi.org/10.1038/nrm3903

Jaumouillé, V., Cartagena-Rivera, A. X. & Waterman, C. M. (2019). Coupling of β2 integrins to actin by a mechanosensitive molecular clutch drives complement receptor-mediated phagocytosis. *Nature Cell Biology*, *21*(11), 1357–1369. https://doi.org/10.1038/s41556-019-0414-2

Jones, J. C. R., Hopkinson, S. B. & Goldfinger, L. E. (1998). Structure and assembly of hemidesmosomes. *BioEssays*, *20*(6), 488–494. https://doi.org/10.1002/(sici)1521-1878(199806)20:6<;488::aid-bies7>3.0.co;2-i

Kechagia, J. Z., Ivaska, J. & Roca-Cusachs, P. (2019). Integrins as biomechanical sensors of the microenvironment. *Nature Reviews Molecular Cell Biology*, *20*(8), 457–473. https://doi.org/10.1038/s41580-019-0134-2

Kechagia, Z., Sáez, P., Gómez-González, M., Canales, B., Viswanadha, S., Zamarbide, M., Andreu, I., Koorman, T., Beedle, A. E. M., Elosegui-Artola, A., Derksen, P. W. B., Trepat, X., Arroyo, M. & Roca-Cusachs, P. (2023). The laminin–keratin link shields the nucleus from mechanical deformation and signalling. *Nature Materials*, *22*(11), 1409–1420. https://doi.org/10.1038/s41563-023-01657-3

Keese, C. R. & Giaever, I. (1991). Substrate mechanics and cell spreading. *Experimental Cell Research*, *195*(2), 528–532. https://doi.org/10.1016/0014-4827(91)90406-k

Kim, J. M., Jo, Y., Jung, J. W. & Park, K. (2021). A mechanogenetic role for the actomyosin complex in branching morphogenesis of epithelial organs. *Development*, *148*(6), dev190785. https://doi.org/10.1242/dev.190785

Kim, J. S., Lee, C.-H., Su, B. Y. & Coulombe, P. A. (2012). Mathematical Modeling of the Impact of Actin and Keratin Filaments on Keratinocyte Cell Spreading. *Biophysical Journal*, *103*(9), 1828–1838. https://doi.org/10.1016/j.bpj.2012.09.016

Kim, S., Cai, M. & Hilgenfeldt, S. (2014). Lewis' law revisited: the role of anisotropy in size–topology correlations. *New Journal of Physics*, *16*(1), 015024. https://doi.org/10.1088/1367-2630/16/1/015024

Kim, Y.-K., Yu, H., Summers, V. R., Donaldson, K. J., Ferdous, S., Shelton, D., Zhang, N., Chrenek, M. A., Jiang, Y., Grossniklaus, H. E., Boatright, J. H., Kong, J. & Nickerson, J. M. (2021). Morphometric Analysis of Retinal Pigment Epithelial Cells From C57BL/6J Mice During Aging. *Investigative Ophthalmology & Visual Science*, *62*(2), 32. https://doi.org/10.1167/iovs.62.2.32

Kiritsi, D., Has, C. & Bruckner-Tuderman, L. (2013). Laminin 332 in junctional epidermolysis bullosa. *Cell Adhesion & Migration*, *7*(1), 135–141. https://doi.org/10.4161/cam.22418

Kivelä, T., Jääskeläinen, J., Vaheri, A. & Carpén, O. (2000). Ezrin, a membrane-organizing protein, as a polarization marker of the retinal pigment epithelium in vertebrates. *Cell and Tissue Research*, *301*(2), 217–223. https://doi.org/10.1007/s004410000225

Klettner, A. K. & Dithmar, S. (2020). *Retinal Pigment Epithelium in Health and Disease* (A. K. Klettner & S. Dithmar, Eds.). https://doi.org/10.1007/978-3-030-28384-1

Klöditz, K., Chen, Y.-Z., Xue, D. & Fadeel, B. (2017). Programmed cell clearance: From nematodes to humans. *Biochemical and Biophysical Research Communications*, *482*(3), 491–497. https://doi.org/10.1016/j.bbrc.2016.12.005

Klymkowsky, M. W., Miller, R. H. & Lane, E. B. (1983). Morphology, behavior, and interaction of cultured epithelial cells after the antibody-induced disruption of keratin filament organization. *The Journal of Cell Biology*, *96*(2), 494–509. https://doi.org/10.1083/jcb.96.2.494

Kozyrina, A. N., Piskova, T. & Di Russo, J. (2020). Mechanobiology of Epithelia From the Perspective of Extracellular Matrix Heterogeneity. *Frontiers in Bioengineering and Biotechnology*, *8*, 596599. https://doi.org/10.3389/fbioe.2020.596599

Kozyrina, A. N., Piskova, T., Semeraro, F., Doolaar, I. C., Prapty, T., Haraszti, T., Hubert, M., Windoffer, R., Leube, R. E., Smith, A.-S. & Di Russo, J. (2024). Laminin-defined Mechanical Status Modulates Retinal Pigment Epithelium Functionality. *BioRxiv*, 2023.02.24.529913. https://doi.org/10.1101/2023.02.24.529913

Kreidberg, J. A., Donovan, M. J., Goldstein, S. L., Rennke, H., Shepherd, K., Jones, R. C. & Jaenisch, R. (1996). Alpha 3 beta 1 integrin has a crucial role in kidney and lung organogenesis. *Development*, *122*(11), 3537–3547. https://doi.org/10.1242/dev.122.11.3537

Kwon, W. & Freeman, S. A. (2020). Phagocytosis by the Retinal Pigment Epithelium: Recognition, Resolution, Recycling. *Frontiers in Immunology*, *11*, 604205. https://doi.org/10.3389/fimmu.2020.604205

Lakkaraju, A., Umapathy, A., Tan, L. X., Daniele, L., Philp, N. J., Boesze-Battaglia, K. & Williams, D. S. (2020). The Cell Biology of the Retinal Pigment Epithelium. *Progress in*

Retinal and Eye Research, *78*, 100846. https://doi.org/10.1016/j.preteyeres.2020.100846

Lammerding, J. (2011). Mechanics of the Nucleus. *Comprehensive Physiology*, *1*(2), 783–807. https://doi.org/10.1002/cphy.c100038

Lauffenburger, D. A. & Horwitz, A. F. (1996). Cell Migration: A Physically Integrated Molecular Process. *Cell*, *84*(3), 359–369. https://doi.org/10.1016/s0092-8674(00)81280-5

Le, A. P., Rupprecht, J.-F., Mège, R.-M., Toyama, Y., Lim, C. T. & Ladoux, B. (2021). Adhesion-mediated heterogeneous actin organization governs apoptotic cell extrusion. *Nature Communications*, *12*(1), 397. https://doi.org/10.1038/s41467-020-20563-9

Lee, J. L. & Streuli, C. H. (2014). Integrins and epithelial cell polarity. *Journal of Cell Science*, *127*(15), 3217–3225. https://doi.org/10.1242/jcs.146142

Lehmann, G. L., Benedicto, I., Philp, N. J. & Rodriguez-Boulan, E. (2014). Plasma membrane protein polarity and trafficking in RPE cells: Past, present and future. *Experimental Eye Research*, *126*, 5–15. https://doi.org/10.1016/j.exer.2014.04.021

Lewis, F. T. (1926). The correlation between cell division and the shapes and sizes of prismatic cells in the epidermis of Cucumis. *The Anatomical Record*.

Li, Shaohua, Edgar, D., Fässler, R., Wadsworth, W. & Yurchenco, P. D. (2003). The Role of Laminin in Embryonic Cell Polarization and Tissue Organization. *Developmental Cell*, *4*(5), 613–624. https://doi.org/10.1016/s1534-5807(03)00128-x

Li, Shun, Liu, Z.-Y., Li, H., Zhou, S., Liu, J., Sun, N., Yang, K.-F., Dougados, V., Mangeat, T., Belguise, K., Feng, X.-Q., Liu, Y. & Wang, X. (2024). Basal actomyosin pulses expand epithelium coordinating cell flattening and tissue elongation. *Nature Communications*, *15*(1), 3000. https://doi.org/10.1038/s41467-024-47236-1

Liu, J., Riquelme, M. A., Li, Z., Li, Y., Tong, Y., Quan, Y., Pei, C., Gu, S. & Jiang, J. X. (2020). Mechanosensitive collaboration between integrins and connexins allows nutrient and antioxidant transport into the lens. *Journal of Cell Biology*, *219*(12), e202002154. https://doi.org/10.1083/jcb.202002154

Liu, L.-C., Chen, Y.-H. & Lu, D.-W. (2024). The Application of Rho Kinase Inhibitors in the Management of Glaucoma. *International Journal of Molecular Sciences*, *25*(11), 5576. https://doi.org/10.3390/ijms25115576

Liu, Y.-J., Le Berre, M., Lautenschlaeger, F., Maiuri, P., Callan-Jones, A., Heuzé, M., Takaki, T., Voituriez, R. & Piel, M. (2015). Confinement and Low Adhesion Induce Fast Amoeboid Migration of Slow Mesenchymal Cells. *Cell*, *160*(4), 659–672. https://doi.org/10.1016/j.cell.2015.01.007

Li, X., Klausen, L. H., Zhang, W., Jahed, Z., Tsai, C.-T., Li, T. L. & Cui, B. (2021). Nanoscale Surface Topography Reduces Focal Adhesions and Cell Stiffness by Enhancing

Integrin Endocytosis. *Nano Letters*, *21*(19), 8518–8526. https://doi.org/10.1021/acs.nanolett.1c01934

López-Otín, C., Blasco, M. A., Partridge, L., Serrano, M. & Kroemer, G. (2023). Hallmarks of aging: An expanding universe. *Cell*, *186*(2), 243–278. https://doi.org/10.1016/j.cell.2022.11.001

Macara, I. G., Guyer, R., Richardson, G., Huo, Y. & Ahmed, S. M. (2014). Epithelial Homeostasis. *Current Biology*, *24*(17), R815–R825. https://doi.org/10.1016/j.cub.2014.06.068

Mack, N. A. & Georgiou, M. (2014). The interdependence of the Rho GTPases and apicobasal cell polarity. *Small GTPases*, *5*(2), e973768. https://doi.org/10.4161/21541248.2014.973768

Malinverno, C., Corallino, S., Giavazzi, F., Bergert, M., Li, Q., Leoni, M., Disanza, A., Frittoli, E., Oldani, A., Martini, E., Lendenmann, T., Deflorian, G., Beznoussenko, G. V., Poulikakos, D., Ong, K. H., Uroz, M., Trepat, X., Parazzoli, D., Maiuri, P., … Scita, G. (2017). Endocytic reawakening of motility in jammed epithelia. *Nature Materials*, *16*(5), 587–596. https://doi.org/10.1038/nmat4848

Mao, Yanlan & Wickström, S. A. (2024). Mechanical state transitions in the regulation of tissue form and function. *Nature Reviews Molecular Cell Biology*, 1–17. https://doi.org/10.1038/s41580-024-00719-x

Mao, Yingyu & Finnemann, S. C. (2015). Regulation of phagocytosis by Rho GTPases. *Small GTPases*, *6*(2), 89–99. https://doi.org/10.4161/21541248.2014.989785

Mao, Yingyu & Finnemann, S. C. (2021). Acute RhoA/Rho Kinase Inhibition Is Sufficient to Restore Phagocytic Capacity to Retinal Pigment Epithelium Lacking the Engulfment Receptor MerTK. *Cells*, *10*(8), 1927. https://doi.org/10.3390/cells10081927

Margadant, C., Raymond, K., Kreft, M., Sachs, N., Janssen, H. & Sonnenberg, A. (2008). Integrin α3β1 inhibits directional migration and wound re-epithelialization in the skin. *Journal of Cell Science*, *122*(2), 278–288. https://doi.org/10.1242/jcs.029108

Martin, A. C. & Goldstein, B. (2014). Apical constriction: themes and variations on a cellular mechanism driving morphogenesis. *Development*, *141*(10), 1987–1998. https://doi.org/10.1242/dev.102228

Maruthamuthu, V., Sabass, B., Schwarz, U. S. & Gardel, M. L. (2011). Cell-ECM traction force modulates endogenous tension at cell–cell contacts. *Proceedings of the National Academy of Sciences*, *108*(12), 4708–4713. https://doi.org/10.1073/pnas.1011123108

Mashburn, D. N., Lynch, H. E., Ma, X. & Hutson, M. S. (2012). Enabling user-guided segmentation and tracking of surface-labeled cells in time-lapse image sets of living tissues. *Cytometry Part A*, *81A*(5), 409–418. https://doi.org/10.1002/cyto.a.22034

Mescher, A. L. (2013). *Junqueira's Basic Histology* (13th ed.). McGraw-Hill Education.

Mitchison, T. & Kirschner, M. (1988). Cytoskeletal dynamics and nerve growth. *Neuron*, *1*(9), 761–772. https://doi.org/10.1016/0896-6273(88)90124-9

Mongera, A., Rowghanian, P., Gustafson, H. J., Shelton, E., Kealhofer, D. A., Carn, E. K., Serwane, F., Lucio, A. A., Giammona, J. & Campàs, O. (2018). A fluid-to-solid jamming transition underlies vertebrate body axis elongation. *Nature*, *561*(7723), 401–405. https://doi.org/10.1038/s41586-018-0479-2

Mouw, J. K., Ou, G. & Weaver, V. M. (2014). Extracellular matrix assembly: a multiscale deconstruction. *Nature Reviews Molecular Cell Biology*, *15*(12). https://doi.org/10.1038/nrm3902

Müller, C., Charniga, C., Temple, S. & Finnemann, S. C. (2018). Quantified F-Actin Morphology Is Predictive of Phagocytic Capacity of Stem Cell-Derived Retinal Pigment Epithelium. *Stem Cell Reports*, *10*(3), 1075–1087. https://doi.org/10.1016/j.stemcr.2018.01.017

Murrell, M., Oakes, P. W., Lenz, M. & Gardel, M. L. (2015). Forcing cells into shape: the mechanics of actomyosin contractility. *Nature Reviews Molecular Cell Biology*, *16*(8), 486–498. https://doi.org/10.1038/nrm4012

Nagatomi, J. (2011). *Mechanobiology Handbook* (C. Press, Ed.). CRC Press. https://doi.org/10.1201/b10780-10

Nandrot, E. F., Kim, Y., Brodie, S. E., Huang, X., Sheppard, D. & Finnemann, S. C. (2004). Loss of Synchronized Retinal Phagocytosis and Age-related Blindness in Mice Lacking αvβ5 Integrin. *The Journal of Experimental Medicine*, *200*(12), 1539–1545. https://doi.org/10.1084/jem.20041447

Newsome, D. A., Huh, W. & Green, W. R. (1987). Bruch's membrane age-related changes vary by region. *Current Eye Research*, *6*(10), 1211–1221. https://doi.org/10.3109/02713688709025231

Nievers, M. G., Schaapveld, R. Q. J. & Sonnenberg, A. (1999). Biology and function of hemidesmosomes. *Matrix Biology*, *18*(1), 5–17. https://doi.org/10.1016/s0945-053x(98)00003-1

Nishiuchi, R., Takagi, J., Hayashi, M., Ido, H., Yagi, Y., Sanzen, N., Tsuji, T., Yamada, M. & Sekiguchi, K. (2006). Ligand-binding specificities of laminin-binding integrins: A comprehensive survey of laminin–integrin interactions using recombinant α3β1, α6β1, α7β1 and α6β4 integrins. *Matrix Biology*, *25*(3), 189–197. https://doi.org/10.1016/j.matbio.2005.12.001

Nobes, C. D. & Hall, A. (1995). Rho, Rac, and Cdc42 GTPases regulate the assembly of multimolecular focal complexes associated with actin stress fibers, lamellipodia, and filopodia. *Cell*, *81*(1), 53–62. https://doi.org/10.1016/0092-8674(95)90370-4

Nobes, C. D. & Hall, A. (1999). Rho GTPases Control Polarity, Protrusion, and Adhesion during Cell Movement. *The Journal of Cell Biology*, *144*(6), 1235–1244. https://doi.org/10.1083/jcb.144.6.1235

Nobeschi, L., Freymuller, E. & Smith, R. L. (2006). Intercellular Junctions in Rabbit Eye Ora Serrata. *Anatomia, Histologia, Embryologia*, *35*(5), 287–292. https://doi.org/10.1111/j.1439-0264.2006.00679.x

Ohashi, T., Ichihara, H., Sakamoto, N. & Sato, M. (2009). *Specify of traction forces to extracellular matrix in smooth muscle cells*. 2192–2193. https://doi.org/10.1007/978-3-540-92841-6_548

Oria, R., Wiegand, T., Escribano, J., Elosegui-Artola, A., Uriarte, J. J., Moreno-Pulido, C., Platzman, I., Delcanale, P., Albertazzi, L., Navajas, D., Trepat, X., García-Aznar, J. M., Cavalcanti-Adam, E. A. & Roca-Cusachs, P. (2017). Force loading explains spatial sensing of ligands by cells. *Nature*, *552*(7684), 219–224. https://doi.org/10.1038/nature24662

Ortolan, D., Sharma, R., Volkov, A., Maminishkis, A., Hotaling, N. A., Huryn, L. A., Cukras, C., Marco, S. D., Bisti, S. & Bharti, K. (2022). Single-cell–resolution map of human retinal pigment epithelium helps discover subpopulations with differential disease sensitivity. *Proceedings of the National Academy of Sciences*, *119*(19), e2117553119. https://doi.org/10.1073/pnas.2117553119

Palamidessi, A., Malinverno, C., Frittoli, E., Corallino, S., Barbieri, E., Sigismund, S., Beznoussenko, G. V., Martini, E., Garre, M., Ferrara, I., Tripodo, C., Ascione, F., Cavalcanti-Adam, E. A., Li, Q., Fiore, P. P. D., Parazzoli, D., Giavazzi, F., Cerbino, R. & Scita, G. (2019). Unjamming overcomes kinetic and proliferation arrest in terminally differentiated cells and promotes collective motility of carcinoma. *Nature Materials*, *18*(11), 1252–1263. https://doi.org/10.1038/s41563-019-0425-1

Parinot, C., Rieu, Q., Chatagnon, J., Finnemann, S. C. & Nandrot, E. F. (2014). Large-Scale Purification of Porcine or Bovine Photoreceptor Outer Segments for Phagocytosis Assays on Retinal Pigment Epithelial Cells. *Journal of Visualized Experiments*, *94*, 1–8. https://doi.org/10.3791/52100

Park, J.-A. A., Kim, J. H., Bi, D., Mitchel, J. A., Qazvini, N. T., Tantisira, K., Park, C. Y., McGill, M., Kim, S.-H. H., Gweon, B., Notbohm, J., Steward, R., Burger, S., R, ell, S. H., Kho, A. T., Tambe, D. T., Hardin, C., Shore, S. A., … Fredberg, J. J. (2015). Unjamming and cell shape in the asthmatic airway~epithelium. *Nat Mater*, *14*(10), 1040–1048. https://doi.org/10.1038/nmat4357

Park, J.-A., Atia, L., Mitchel, J. A., Fredberg, J. J. & Butler, J. P. (2016). Collective migration and cell jamming in asthma, cancer and development. *Journal of Cell Science*, *129*(18), 3375–3383. https://doi.org/10.1242/jcs.187922

Patton, B. L., Miner, J. H., Chiu, A. Y. & Sanes, J. R. (1997). Distribution and Function of Laminins in the Neuromuscular System of Developing, Adult, and Mutant Mice. *The Journal of Cell Biology*, *139*(6), 1507–1521. https://doi.org/10.1083/jcb.139.6.1507

Piskova, T., Kozyrina, A. N. & Di Russo, J. (2023). Mechanobiological implications of age-related remodelling in the outer retina. *Biomaterials Advances*, *147*, 213343. https://doi.org/10.1016/j.bioadv.2023.213343

Pora, A., Yoon, S., Dreissen, G., Hoffmann, B., Merkel, R., Windoffer, R. & Leube, R. E. (2020). Regulation of keratin network dynamics by the mechanical properties of the environment in migrating cells. *Scientific Reports*, *10*(1), 4574. https://doi.org/10.1038/s41598-020-61242-5

Pozzi, A., Yurchenco, P. D. & Iozzo, R. V. (2016). The nature and biology of basement membranes. *Matrix Biology : Journal of the International Society for Matrix Biology*, *57–58*, 1–11. https://doi.org/10.1016/j.matbio.2016.12.009

Przybyla, L., Lakins, J. N., Sunyer, R., Trepat, X. & Weaver, V. M. (2016). Monitoring developmental force distributions in reconstituted embryonic epithelia. *Methods*, *94*, 101–113. https://doi.org/10.1016/j.ymeth.2015.09.003

Rabinovitz, I., Gipson, I. K. & Mercurio, A. M. (2001). Traction Forces Mediated by α6β4 Integrin: Implications for Basement Membrane Organization and Tumor Invasion. *Molecular Biology of the Cell*, *12*(12), 4030–4043. https://doi.org/10.1091/mbc.12.12.4030

Raymond, K., Cagnet, S., Kreft, M., Janssen, H., Sonnenberg, A. & Glukhova, M. A. (2011). Control of mammary myoepithelial cell contractile function by α3β1 integrin signalling. *The EMBO Journal*, *30*(10), 1896–1906. https://doi.org/10.1038/emboj.2011.113

Raymond, S. M. & Jackson, I. J. (1995). The retinal pigmented epithelium is required for development and maintenance of the mouse neural retina. *Current Biology*, *5*(11), 1286–1295. https://doi.org/10.1016/s0960-9822(95)00255-7

Rezniczek, G. A., Pereda, J. M. de, Reipert, S. & Wiche, G. (1998). Linking Integrin α6β4-based Cell Adhesion to the Intermediate Filament Cytoskeleton: Direct Interaction between the β4 Subunit and Plectin at Multiple Molecular Sites. *The Journal of Cell Biology*, *141*(1), 209–225. https://doi.org/10.1083/jcb.141.1.209

Rice, A. J., Cortes, E., Lachowski, D., Cheung, B. C. H., Karim, S. A., Morton, J. P. & Hernández, A. del R. (2017). Matrix stiffness induces epithelial–mesenchymal transition and promotes chemoresistance in pancreatic cancer cells. *Oncogenesis*, *6*(7), e352–e352. https://doi.org/10.1038/oncsis.2017.54

Ridley, A. J., Schwartz, M. A., Burridge, K., Firtel, R. A., Ginsberg, M. H., Borisy, G., Parsons, J. T. & Horwitz, A. R. (2003). Cell Migration: Integrating Signals from Front to Back. *Science*, *302*(5651), 1704–1709. https://doi.org/10.1126/science.1092053

Rivier, N. (1985). Statistical crystallography Structure of random cellular networks. *Philosophical Magazine B*, *52*(3), 795–819. https://doi.org/10.1080/13642818508240637

Rousselle, P. & Beck, K. (2013). Laminin 332 processing impacts cellular behavior. *Cell Adhesion & Migration*, *7*(1), 122–134. https://doi.org/10.4161/cam.23132

Rübsam, M., Broussard, J. A., Wickström, S. A., Nekrasova, O., Green, K. J. & Niessen, C. M. (2017). Adherens Junctions and Desmosomes Coordinate Mechanics and Signaling to

Orchestrate Tissue Morphogenesis and Function: An Evolutionary Perspective. *Cold Spring Harbor Perspectives in Biology*, *10*(11), a029207. https://doi.org/10.1101/cshperspect.a029207

Rübsam, M., Püllen, R., Tellkamp, F., Bianco, A., Peskoller, M., Bloch, W., Green, K. J., Merkel, R., Hoffmann, B., Wickström, S. A. & Niessen, C. M. (2023). Polarity signaling balances epithelial contractility and mechanical resistance. *Scientific Reports*, *13*(1), 7743. https://doi.org/10.1038/s41598-023-33485-5

Ruggiero, L., Connor, M. P., Chen, J., Langen, R. & Finnemann, S. C. (2012). Diurnal, localized exposure of phosphatidylserine by rod outer segment tips in wild-type but not Itgb5−/− or Mfge8−/− mouse retina. *Proceedings of the National Academy of Sciences*, *109*(21), 8145–8148. https://doi.org/10.1073/pnas.1121101109

Saraswathibhatla, A., Indana, D. & Chaudhuri, O. (2023). Cell–extracellular matrix mechanotransduction in 3D. *Nature Reviews Molecular Cell Biology*, *24*(7), 495–516. https://doi.org/10.1038/s41580-023-00583-1

Schiller, H. B. & Fässler, R. (2013). Mechanosensitivity and compositional dynamics of cell–matrix adhesions. *EMBO Reports*, *14*(6), 509–519. https://doi.org/10.1038/embor.2013.49

Scott, L. E., Weinberg, S. H. & Lemmon, C. A. (2019). Mechanochemical Signaling of the Extracellular Matrix in Epithelial-Mesenchymal Transition. *Frontiers in Cell and Developmental Biology*, *7*, 135. https://doi.org/10.3389/fcell.2019.00135

Seltmann, K., Fritsch, A. W., Käs, J. A. & Magin, T. M. (2013). Keratins significantly contribute to cell stiffness and impact invasive behavior. *Proceedings of the National Academy of Sciences*, *110*(46), 18507–18512. https://doi.org/10.1073/pnas.1310493110

Serna-Morales, E., Sánchez-Sánchez, B. J., Marcotti, S., Nichols, A., Bhargava, A., Dragu, A., Hirvonen, L. M., Díaz-de-la-Loza, M.-C., Mink, M., Cox, S., Rayfield, E., Lee, R. M., Hobson, C. M., Chew, T.-L. & Stramer, B. M. (2023). Extracellular matrix assembly stress initiates Drosophila central nervous system morphogenesis. *Developmental Cell*, *58*(10), 825-835.e6. https://doi.org/10.1016/j.devcel.2023.03.019

Shibata, S., Hayashi, R., Okubo, T., Kudo, Y., Katayama, T., Ishikawa, Y., Toga, J., Yagi, E., Honma, Y., Quantock, A. J., Sekiguchi, K. & Nishida, K. (2018). Selective Laminin-Directed Differentiation of Human Induced Pluripotent Stem Cells into Distinct Ocular Lineages. *Cell Reports*, *25*(6), 1668-1679.e5. https://doi.org/10.1016/j.celrep.2018.10.032

Simič, R., Mandal, J., Zhang, K. & Spencer, N. D. (2021). Oxygen inhibition of free-radical polymerization is the dominant mechanism behind the "mold effect" on hydrogels. *Soft Matter*, *17*(26), 6394–6403. https://doi.org/10.1039/d1sm00395j

Song, J., Zhang, X., Buscher, K., Wang, Y., Wang, H., Di Russo, J., Li, L., Lütke-Enking, S., Zarbock, A., Stadtmann, A., Striewski, P., Wirth, B., Kuzmanov, I., Wiendl, H., Schulte, D., Vestweber, D. & Sorokin, L. (2017). Endothelial Basement Membrane Laminin 511

Contributes to Endothelial Junctional Tightness and Thereby Inhibits Leukocyte Transmigration. *Cell Reports*, *18*(5), 1256–1269. https://doi.org/10.1016/j.celrep.2016.12.092

Song, M. J., Quinn, R., Nguyen, E., Hampton, C., Sharma, R., Park, T. S., Koster, C., Voss, T., Tristan, C., Weber, C., Singh, A., Dejene, R., Bose, D., Chen, Y.-C., Derr, P., Derr, K., Michael, S., Barone, F., Chen, G., … Bharti, K. (2023). Bioprinted 3D outer retina barrier uncovers RPE-dependent choroidal phenotype in advanced macular degeneration. *Nature Methods*, *20*(1), 149–161. https://doi.org/10.1038/s41592-022-01701-1

Sonnenberg, A., Calafat, J., Janssen, H., Daams, H., Raaij-Helmer, L. M. van der, Falcioni, R., Kennel, S. J., Aplin, J. D., Baker, J. & Loizidou, M. (1991). Integrin alpha 6/beta 4 complex is located in hemidesmosomes, suggesting a major role in epidermal cell-basement membrane adhesion. *The Journal of Cell Biology*, *113*(4), 907–917. https://doi.org/10.1083/jcb.113.4.907

Stamenović, D. & Ingber, D. E. (2008). Tensegrity-guided self assembly : from molecules to living cells. *Soft Matter*, *5*(6), 1137–1145. https://doi.org/10.1039/b806442c

Stipp, C. S. (2010). Laminin-binding integrins and their tetraspanin partners as potential antimetastatic targets. *Expert Reviews in Molecular Medicine*, *12*, e3. https://doi.org/10.1017/s1462399409001355

Strauss, O. (2005). The Retinal Pigment Epithelium in Visual Function. *Physiological Reviews*, *85*(3), 845–881. https://doi.org/10.1152/physrev.00021.2004

Strunnikova, N. V., Maminishkis, A., Barb, J. J., Wang, F., Zhi, C., Sergeev, Y., Chen, W., Edwards, A. O., Stambolian, D., Abecasis, G., Swaroop, A., Munson, P. J. & Miller, S. S. (2010). Transcriptome analysis and molecular signature of human retinal pigment epithelium. *Human Molecular Genetics*, *19*(12), 2468–2486. https://doi.org/10.1093/hmg/ddq129

Sugawara, K., Tsuruta, D., Ishii, M., Jones, J. C. R. & Kobayashi, H. (2008). Laminin-332 and -511 in skin. *Experimental Dermatology*, *17*(6), 473–480. https://doi.org/10.1111/j.1600-0625.2008.00721.x

Sun, B. (2021). The mechanics of fibrillar collagen extracellular matrix. *Cell Reports Physical Science*, *2*(8), 100515. https://doi.org/10.1016/j.xcrp.2021.100515

Sun, Z., Guo, S. S. & Fässler, R. (2016). Integrin-mediated mechanotransduction. *Journal of Cell Biology*, *215*(4), 445–456. https://doi.org/10.1083/jcb.201609037

Swaminathan, V. & Waterman, C. M. (2016). The molecular clutch model for mechanotransduction evolves. *Nature Cell Biology*, *18*(5), 459–461. https://doi.org/10.1038/ncb3350

Tarau, I.-S., Berlin, A., Curcio, C. A. & Ach, T. (2019). The Cytoskeleton of the Retinal Pigment Epithelium: from Normal Aging to Age-Related Macular Degeneration.

International Journal of Molecular Sciences, *20*(14), 3578. https://doi.org/10.3390/ijms20143578

Totaro, A., Panciera, T. & Piccolo, S. (2018). YAP/TAZ upstream signals and downstream responses. *Nature Cell Biology*, *20*(8), 888–899. https://doi.org/10.1038/s41556-018-0142-z

Tsujinaka, H., Itaya-Hironaka, A., Yamauchi, A., Sakuramoto-Tsuchida, S., Ota, H., Takeda, M., Fujimura, T., Takasawa, S. & Ogata, N. (2015). Human retinal pigment epithelial cell proliferation by the combined stimulation of hydroquinone and advanced glycation end-products via up-regulation of VEGF gene. *Biochemistry and Biophysics Reports*, *2*, 123–131. https://doi.org/10.1016/j.bbrep.2015.05.005

Tulla, M., Pentikäinen, O. T., Viitasalo, T., Käpylä, J., Impola, U., Nykvist, P., Nissinen, L., Johnson, M. S. & Heino, J. (2001). Selective Binding of Collagen Subtypes by Integrin α1I, α2I, and α10I Domains*. *Journal of Biological Chemistry*, *276*(51), 48206–48212. https://doi.org/10.1074/jbc.m104058200

Ulanova, M., Gravelle, S. & Barnes, R. (2008). The Role of Epithelial Integrin Receptors in Recognition of Pulmonary Pathogens. *Journal of Innate Immunity*, *1*(1), 4–17. https://doi.org/10.1159/000141865

Umapathy, A., Torten, G., Paniagua, A. E., Chung, J., Tomlinson, M., Lim, C. & Williams, D. S. (2023). Spatiotemporal Live-Cell Analysis of Photoreceptor Outer Segment Membrane Ingestion by the Retinal Pigment Epithelium Reveals Actin-Regulated Scission. *The Journal of Neuroscience*, *43*(15), 2653–2664. https://doi.org/10.1523/jneurosci.1726-22.2023

Vishwakarma, M., Di Russo, J., Probst, D., Schwarz, U. S., Das, T. & Spatz, J. P. (2018). Mechanical interactions among followers determine the emergence of leaders in migrating epithelial cell collectives. *Nature Communications*, *9*(1), 3469. https://doi.org/10.1038/s41467-018-05927-6

Volland, S., Esteve-Rudd, J., Hoo, J., Yee, C. & Williams, D. S. (2015). A Comparison of Some Organizational Characteristics of the Mouse Central Retina and the Human Macula. *PLoS ONE*, *10*(4), e0125631. https://doi.org/10.1371/journal.pone.0125631

Walko, G., Castañón, M. J. & Wiche, G. (2015). Molecular architecture and function of the hemidesmosome. *Cell and Tissue Research*, *360*(2), 363–378. https://doi.org/10.1007/s00441-014-2061-z

Walma, D. A. C. & Yamada, K. M. (2020). The extracellular matrix in development. *Development*, *147*(10), dev175596. https://doi.org/10.1242/dev.175596

Wang, J., Wang, H. & Dang, Y. (2023). Rho-Kinase Inhibitors as Emerging Targets for Glaucoma Therapy. *Ophthalmology and Therapy*, *12*(6), 2943–2957. https://doi.org/10.1007/s40123-023-00820-y

Wang, S., Matsumoto, K., Lish, S. R., Cartagena-Rivera, A. X. & Yamada, K. M. (2021). Budding epithelial morphogenesis driven by cell-matrix versus cell-cell adhesion. *Cell*, *184*(14), 3702-3716.e30. https://doi.org/10.1016/j.cell.2021.05.015

Wang, W., Zuidema, A., Molder, L. te, Nahidiazar, L., Hoekman, L., Schmidt, T., Coppola, S. & Sonnenberg, A. (2020). Hemidesmosomes modulate force generation via focal adhesions. *Journal of Cell Biology*, *219*(2), e201904137. https://doi.org/10.1083/jcb.201904137

Watt, F. M. & Huck, W. T. S. (2013). Role of the extracellular matrix in regulating stem cell fate. *Nature Reviews Molecular Cell Biology*, *14*(8), 467–473. https://doi.org/10.1038/nrm3620

Weaver, V. M., Lelièvre, S., Lakins, J. N., Chrenek, M. A., Jones, J. C. R., Giancotti, F., Werb, Z. & Bissell, M. J. (2002). β4 integrin-dependent formation of polarized three-dimensional architecture confers resistance to apoptosis in normal and malignant mammary epithelium. *Cancer Cell*, *2*(3), 205–216. https://doi.org/10.1016/s1535-6108(02)00125-3

Wei, S. C., Fattet, L., Tsai, J. H., Guo, Y., Pai, V. H., Majeski, H. E., Chen, A. C., Sah, R. L., Taylor, S. S., Engler, A. J. & Yang, J. (2015). Matrix stiffness drives epithelial–mesenchymal transition and tumour metastasis through a TWIST1–G3BP2 mechanotransduction pathway. *Nature Cell Biology*, *17*(5), 678–688. https://doi.org/10.1038/ncb3157

Wenta, T., Schmidt, A., Zhang, Q., Devarajan, R., Singh, P., Yang, X., Ahtikoski, A., Vaarala, M., Wei, G.-H. & Manninen, A. (2022). Disassembly of α6β4-mediated hemidesmosomal adhesions promotes tumorigenesis in PTEN-negative prostate cancer by targeting plectin to focal adhesions. *Oncogene*, *41*(30), 3804–3820. https://doi.org/10.1038/s41388-022-02389-5

Wen, T., Zhang, Z., Yu, Y., Qu, H., Koch, M. & Aumailley, M. (2010). Integrin α3 subunit regulates events linked to epithelial repair, including keratinocyte migration and protein expression. *Wound Repair and Regeneration*, *18*(3), 325–334. https://doi.org/10.1111/j.1524-475x.2010.00590.x

Wickström, S. A. & Niessen, C. M. (2018). Cell adhesion and mechanics as drivers of tissue organization and differentiation: local cues for large scale organization. *Current Opinion in Cell Biology*, *54*, 89–97. https://doi.org/10.1016/j.ceb.2018.05.003

Wyatt, T. P. J., Harris, A. R., Lam, M., Cheng, Q., Bellis, J., Dimitracopoulos, A., Kabla, A. J., Charras, G. T. & Baum, B. (2015). Emergence of homeostatic epithelial packing and stress dissipation through divisions oriented along the long cell axis. *Proceedings of the National Academy of Sciences*, *112*(18), 5726–5731. https://doi.org/10.1073/pnas.1420585112

Yalcin, E. G., He, Y., Orhan, D., Pazzagli, C., Emiralioglu, N. & Has, C. (2015). Crucial role of posttranslational modifications of integrin α3 in interstitial lung disease and nephrotic syndrome. *Human Molecular Genetics*, *24*(13), 3679–3688. https://doi.org/10.1093/hmg/ddv111

Yamada, K. M. & Sixt, M. (2019). Mechanisms of 3D cell migration. *Nature Reviews Molecular Cell Biology*, *20*(12), 738–752. https://doi.org/10.1038/s41580-019-0172-9

Yang, S., Zhou, J. & Li, D. (2021). Functions and Diseases of the Retinal Pigment Epithelium. *Frontiers in Pharmacology*, *12*, 727870. https://doi.org/10.3389/fphar.2021.727870

Yap, L., Tay, H. G., Nguyen, M. T. X., Tjin, M. S. & Tryggvason, K. (2019). Laminins in Cellular Differentiation. *Trends in Cell Biology*, *29*(12), 987–1000. https://doi.org/10.1016/j.tcb.2019.10.001

Young, J. L., Holle, A. W. & Spatz, J. P. (2016). Nanoscale and mechanical properties of the physiological cell–ECM microenvironment. *Experimental Cell Research*, *343*(1), 3–6. https://doi.org/10.1016/j.yexcr.2015.10.037

Young, J. L., Hua, X., Somsel, H., Reichart, F., Kessler, H. & Spatz, J. P. (2020). Integrin Subtypes and Nanoscale Ligand Presentation Influence Drug Sensitivity in Cancer Cells. *Nano Letters*, *20*(2), 1183–1191. https://doi.org/10.1021/acs.nanolett.9b04607

Young, R. W. & Bok, D. (1969). Participation of the retinal pigment epithelium in the rod outer segment renewal process. *The Journal of Cell Biology*, *42*(2), 392–403. https://doi.org/10.1083/jcb.42.2.392

Yousif, L. F., Di Russo, J. & Sorokin, L. (2013). Laminin isoforms in endothelial and perivascular basement membranes. *Cell Adhesion & Migration*, *7*(1), 101–110. https://doi.org/10.4161/cam.22680

Yurchenco, P. D. (2011). Basement Membranes: Cell Scaffoldings and Signaling Platforms. *Cold Spring Harbor Perspectives in Biology*, *3*(2), a004911. https://doi.org/10.1101/cshperspect.a004911

Yu, W., Datta, A., Leroy, P., O'Brien, L. E., Mak, G., Jou, T.-S., Matlin, K. S., Mostov, K. E. & Zegers, M. M. P. (2005). β1-Integrin Orients Epithelial Polarity via Rac1 and Laminin. *Molecular Biology of the Cell*, *16*(2), 433–445. https://doi.org/10.1091/mbc.e04-05-0435

Zent, R. & Pozzi, A. (2010). *Cell-Extracellular Matrix Interactions in Cancer*. https://doi.org/10.1007/978-1-4419-0814-8

Abbreviations

ARPE-19 cells – spontaneously arising retinal pigment epithelia cell line

AAV – adeno-associated virus

AFM – atomic force microscopy

AMD – age related macular degeneration

APTES – (3-Aminopropyl)triethoxysilane

APS – ammoniumpersulphate

BM – basement membrane

BSA – bovine serum albumin

ddH_2O – double distilled water

DMA – dynamic mechanical analysis

DMSO – dimethyl sulfoxide

ECM – extracellular matrix

EDTA – ethylenediaminetetraacetic acid

FBS – filtrated bovine serum

hiPSC-RPE – human induced pluripotent stem cell-derived retinal pigment epithelial cells

IM – interstitial matrix

LN – laminin

LSM – laser scanning microscopy

MLC – myosin light chain

MSM – monolayer stress microscopy

PAA – polyacrylamide (hydrogel)

PBS – phosphate buffer saline

pMLC - phosphorylated myosin light chain

POS – photoreceptors' outer segment

PtdSer – phosphatidylserine

ROCK – Rho-associated protein kinase

ROI – region of interest

RPE – retinal pigment epithelium

TEM – transmission electron microscopy

TEMED – N,N,N′,N′-tetramethylethylenediamine

TFM – traction force microscopy

TRIS – tris(hydroxymethyl)aminomethane

VN – vitronectin

SDS – sodium dodecyl sulphate

SEM – scanning electron microscopy

UV – ultraviolet

List of figures

List of tables

Appendix 1.

Fiji macro for files adjustment

Description:

These ImageJ macro scripts are designed for processing and adjusting image files according to specific requirements. The macros include operations such as resizing, contrast enhancement, and conversion to 8-bit format.

Script:

```
  macro "adjustment files from Gloria [a]" {

titel = getTitle();
run("Size...", "width=1500 height=1251 depth=1 constrain average
interpolation=Bilinear");
setOption("ScaleConversions", true);
run("Enhance Contrast", "saturated=0.35");
run("8-bit");
}
  macro "adjustment files from Gloria_Sasha [d]" {
run("Slice Keeper", "first=1 last=1 increment=1");
run("Size...", "width=1500 height=1251 depth=1 constrain average
interpolation=Bilinear");
setOption("ScaleConversions", true);
run("Enhance Contrast", "saturated=0.35");
run("8-bit");
  }
```

MATLAB scripts for traction force microscopy analysis

Traction force plotting script

Description:

This MATLAB script is designed to load and process particle image velocimetry (PIV) data, specifically for analysing traction forces. It allows the user to select a PIV data file from Fiji containing velocity information, processes the data to assign velocities to grid points, and plots the interpolated magnitude of velocity (|V|) using a heatmap. The script generates a heatmap of the interpolated velocity field (Vq), visualizing the traction forces, with customizable color scaling (cmin, cmax) and a colormap (parula).

Script (Traction_Plot_Newflo):

```
clear all;

cmin = 0;
cmax = 500;

pixScale = 0.8995; % micron/pixel
isRotate = 0;
```

```
isLateral = 1;
plotTitle = 'Lateral Correlation Function';
setRoI = 0;
setMax = 3000;
setMin = 0;

% Select the velocity data file in the targeted folder and read its path
and file name
[flname, pathname] = uigetfile('*.txt','Select the PIV data file');
flpathname = strcat(pathname,flname);
PIVdat = load(flpathname);
tic
% Create an
datLen = length(PIVdat(:,1));
xmax = PIVdat(datLen,1); ymax = PIVdat(datLen,2);
x0 = PIVdat(1,1); y0 = PIVdat(1,2); gridspace = PIVdat(2,1)-PIVdat(1,1);
numBoxY = round(((xmax-x0)/gridspace)+1); numBoxX = round(((ymax-
y0)/gridspace)+1);

% Read and assign the center of each PIV Box
boxCenter = zeros(numBoxY, numBoxX, 2);
A = reshape(PIVdat(:,1),numBoxY,numBoxX); boxCenter(:,:,1) = A;
A = reshape(PIVdat(:,2),numBoxY,numBoxX); boxCenter(:,:,2) = A;

% Read and assign velocity parameters (Vx,Vy,|V|,dVx,dVy) and assign to the
% center of the box
Vx = (reshape(PIVdat(:,3),numBoxY,numBoxX))';
Vy = (reshape(PIVdat(:,4),numBoxY,numBoxX))';
V = (reshape(PIVdat(:,5),numBoxY,numBoxX))';
dVx = Vx - mean(mean(Vx));
dVy = Vy - mean(mean(Vy));

[X,Y] = meshgrid(1:numBoxY,1:numBoxX);
[Xq,Yq] = meshgrid(1:0.2:numBoxY,1:0.2:numBoxX);
Vq = interp2(X,Y,V,Xq,Yq,'cubic');
figure
colormap parula
imagesc(Vq)
colorbar
caxis([cmin cmax])
```

Traction force values extraction

Description:

This MATLAB script is designed to analyse traction forces within a circular region of interest (ROI). It processes data extracted from traction force measurements, calculates mean values within the defined ROI, and optionally plots the results.

Script (CircROI_T3DS_REMeD):

```
%.....................................................................
% Circular ROI of Traction and 3d Stresses
% Florian Huhnke 2017
clear all
close all
```

```
%Set =1 what you want to analyse, if you want to plot your result, set
%PlotT=1 for traction or PlotS, respectively
TractionVal = 1; StressVal = 0; PlotT = 1; PlotS = 0;

%Set the prefered file name below
Flname = 'Traction.csv';

%Set initN = 1 if you change radius or switch between traction and stress
%quantification
initN = 1;

%Set minimum and Maximum of your Colormap in case you plot the new graphs
cminT = 0; cmaxT = 1000;
cminS = 0; cmaxS = 10;

if initN ~= 1
    Data = load(Flname);
end

if StressVal ~= 1 && TractionVal ~=0

        Traction_Plot_Extraction;

           xpos = 45;
           ypos = 35;
           rad = 63;
%              xpos = input('Please select X position: ');
%              ypos = input('Please select Y position: ');
%  rad = input('Please select the radius (Odd number only!): ');

            [ mean, ROI, cir_mask ] = CircROI_mean(V,[ypos xpos], rad);
            RoundROIT = ROI.*cir_mask;
            ResultTraction = RoundROIT(RoundROIT~=0);

            mean

    elseif StressVal ~= 0 && TractionVal ~=1

            [s3D_flname, s3D_pathname] = uigetfile('*.mat','Select the 3D
Stress File');
            s3D_flpathname = strcat(s3D_pathname,s3D_flname);
load(s3D_flpathname);

            surf(savg2d);colormap jet; colorbar; caxis([cminS cmaxS]);
            shading Interp;

            xpos = input('Please select X position: ');
            ypos = input('Please select Y position: ');
            rad = input('Please select the radius (Odd number only!): ');

            [ mean, ROI, cir_mask ] = CircROI_mean(savg2d,[ypos xpos],
rad);
            RoundROIS = ROI.*cir_mask;
            ResultStress = RoundROIS(RoundROIS~=0);

    else

            h = msgbox('Please select either Traction or Stress analysis!',
...
```

```
            'ERROR', 'error');

end

if StressVal ~= 1 && TractionVal ~=0

            flpathname = strcat(pathname,flname); load(flpathname);
            k = strfind(flpathname, '.txt');
            svflname = flpathname(1:k-1);
            save([svflname '_RoI_TractionData' '.mat'], 'ResultTraction',
...
                'RoundROIT', 'xpos', 'ypos', 'rad' )

                    if initN ~=1
                        Mydata = [Data(:,:), ResultTraction(:,:)];
                        csvwrite(Flname, Mydata);
                    else
                        csvwrite(Flname, ResultTraction);
                    end

    elseif StressVal ~= 0 && TractionVal ~=1

            s3D_flpathname = strcat(s3D_pathname,s3D_flname);
load(s3D_flpathname);
            k = strfind(s3D_flpathname, '_3DStress'); svflname =
s3D_flpathname(1:k-1);
            save([svflname '_RoI_3DStress' '.mat'], 'ResultStress', ...
                'RoundROIS', 'xpos', 'ypos', 'rad' )

                    if initN ~=1
                        Mydata = [Data(:,:), ResultStress(:,:)];
                        csvwrite(Flname, Mydata);

                    else
                         csvwrite(Flname, ResultStress);
                    end
end

if PlotS ~= 1 && PlotT ~=0 && TractionVal ~=0;

             figure
             colormap jet;imagesc(RoundROIT);colorbar;caxis([cminT cmaxT]);

    elseif PlotS ~= 0 && PlotT ~=1 && StressVal ~= 0;

             figure
             surf(RoundROIS);colormap jet;colorbar;caxis([cminS
cmaxS]);shading Interp;

    elseif PlotS ~= 0 && PlotT ~=0;

             h = msgbox('Select only one Graph to show results! Either
Stress or Traction!', ...
            'ERROR', 'error');
    else
        close all;
end

% binranges = [0: 5: 250] ;
```

```
% [N, binranges] = histcounts(ResultTraction,binranges);
% Nh=[0, N];
% histable= [Nh', binranges']
%
% ModeFrequency = max (Nh)

close all;
```

MATLAB scripts for monolayer stress microscopy analysis

Identification of cell-free regions in traction force data

Description:

This MATLAB script processes traction force data and an associated image to identify and record cell-free areas. It reads in an image and a traction force data file, compares the positions from the traction force data with pixel values in the image, and determines whether each point lies within a cell-free region. The results are saved for further analysis.

Script (cell_free_boundary_flo):

```
% Select the velocity data file in the targeted folder and read its path
and
% file name
[cf_flname, cf_pathname] = uigetfile('*.tif','select the image with black
cell-free area');
cf_flpathname = strcat(cf_pathname,cf_flname);
cf_image = imread(cf_flpathname);


% Select the traction force data file in the targeted folder and read its
path and
% file name
[tf_flname, tf_pathname] = uigetfile('*.txt','Select the traction force
file');
tf_flpathname = strcat(tf_pathname,tf_flname);
TF = load(tf_flpathname);
k = strfind(tf_flpathname, '.txt');
svflname = tf_flpathname(1:k-1);


numberNodes = size(TF(:,1));
cell_free = zeros(numberNodes(1),2);

for i=1:numberNodes

        cell_free(i,1) = i;

        if cf_image(TF(i,2),TF(i,1))<=5
            cell_free(i,2) = 1;
        else
            cell_free(i,2) = 0;
        end

end
```

```
save cell_free_info cell_free

save([svflname '_cell_free_info' '.mat'],'cell_free');
```

Monolayer stresses calculation

Description:

This MATLAB script is designed for analyzing monolayer stress microscopy data using previously measured traction forces. It processes traction force data, generates a mesh for finite element analysis (FEA), applies boundary conditions, computes the system stiffness matrix, solves for displacements, and calculates stresses at nodes.

Script (MSM_generic_Noise_flo):

```
%.....................................................................
% MATLAB codes for Monolayer Stress Microscopy
% Tamal Das 2014

% Clear memory
tic
clear all
isCellFree = 0; % If there are cell unoccupied areas, set this to 1 else 0

invCalc = 1; % for T = force on substrate, invCalc = 1 else invCalc = -1;

% Maximum iteration
maxIterate = 1000; % 1000 for noisy data, 500 in general
accuLimit = 1e-06; % accuLimit = 1e-06

%pixel factor
px = 0.8995-06;

% TFM substrate properties
E  = 0.4e4; poisson = 0.50;

% Average height of cell monolayer
h = 15; % 5 um

% Matrix C
C=E/(1-poisson^2)*[1 poisson 0;poisson 1 0;0 0 (1-poisson)/2];

% Select the traction force data file in the targeted folder
% and read its path and file name
[tf_flname, tf_pathname] = uigetfile('*.txt','Select the traction force
file');
tf_flpathname = strcat(tf_pathname,tf_flname);
TF = load(tf_flpathname);
k = strfind(tf_flname, '.txt');
svflname = tf_flname(1:k-1);

% Mesh generation
nodeCoordinates = TF(:,1:2);
xx=nodeCoordinates(:,1);
```

```
yy=nodeCoordinates(:,2);
scaleFactor = 0.1; %(xx(2)-xx(1))*0.65;

numberNodes = size(xx,1);
% numberNodesX = round(numberNodes^0.5);
% numberNodesY = numberNodesX;
numberNodesX = round(((max(xx)-min(xx))/(xx(2)-xx(1)))) + 1;
numberNodesY = round(numberNodes/numberNodesX);

numberElementsX=numberNodesX-1;
numberElementsY=numberNodesY-1;
numberElements=numberElementsX*numberElementsY;

elementNodes = zeros(numberElements,4);
for i=1:numberElements;
    currRow = ceil(i/numberElementsX); currColumn = rem(i,numberElementsX);
    if currColumn == 0
        currColumn = numberElementsX;
    end
    elementNodes(i,1) = (currRow-1)*numberNodesX+ currColumn;
    elementNodes(i,2) = (currRow-1)*numberNodesX+ currColumn + 1;
    elementNodes(i,3) = currRow*numberNodesX + currColumn + 1;
    elementNodes(i,4) = currRow*numberNodesX + currColumn;
end

step = 1;
toc

% GDof: global number of degrees of freedom
GDof=2*numberNodes;

% Computation of the system stiffness matrix
stiffness=formStiffness2D(GDof,numberElements,...
    elementNodes,numberNodes,nodeCoordinates,C,1,1);

step = 2;
toc

% Boundary conditions
load('cell_free_info.mat');

if isCellFree == 0
    cfree = cell_free(:,2);
    cfree2D = reshape(cfree,[numberNodesY numberNodesX]);
    cfree2D(1,:) = 1; cfree2D(numberNodesY,:)=1;
    cfree2D(:,1) = 1; cfree2D(:,numberNodesX)=1;
    cfree = reshape(cfree2D, [numberNodes 1]);
    cell_free(:,2) = cfree;
end

cellfreeNode = find(cell_free(:,2)==1);
numberCFNode = size(cellfreeNode,1);
cellfreeDof = zeros(2*numberCFNode,1);
for i=1:numberCFNode
    cellfreeDof(i)=cellfreeNode(i);
    cellfreeDof(i+numberCFNode)=cellfreeNode(i)+numberNodes;
end
% Write code for image boundary
prescribedDof=[cellfreeDof];
```

```
% Force vector
force=zeros(GDof,1);
Tx = TF(:,3); Ty = TF(:,4);

%set cutoff for noise----------
Tnoise = 0;
noiseNodes = find(TF(:,5)<Tnoise);
Tx(noiseNodes) = 0; Ty(noiseNodes) = 0;
%-------------------------

for i=1:numberCFNode;
    currNode = cellfreeNode(i);
    Tx(currNode) = 0; Ty(currNode) = 0;
end
for i=1:numberNodes;
    force(i) = -invCalc*Tx(i)/h;
    force(i+numberNodes)=-invCalc*Ty(i)/h;
end
Tr = (Tx.^2 + Ty.^2).^0.5;

% Solution
displacements=solution(GDof,prescribedDof,stiffness,force,maxIterate,accuLi
mit);

step = 3;
toc

% Displacements and deformed shape
UX=displacements(1:numberNodes);
UY=displacements(numberNodes+1:GDof);

% Stresses at nodes
stress=stresses2D(GDof,numberElements,...
    elementNodes,numberNodes,nodeCoordinates,...
    displacements,UX,UY,C,scaleFactor);

save([tf_pathname svflname
'.mat'],'px','E','poisson','nodeCoordinates','numberNodesX',...
    'elementNodes','GDof','prescribedDof','displacements','stress', 'Tr');
toc

%load chirp, sound(y,1/2*Fs)
```

Monolayer stresses plotting script

Description:

This MATLAB script processes and visualizes stress data obtained from a monolayer stress microscopy experiment. It loads precomputed stress results, retrieves mesh information, calculates various stress components, and generates visualizations. The script also saves the processed data for further analysis.

Script (MSM_post_processing_Medhavi):

```
%.....................................................................
% MATLAB codes for Monolayer Stress Microscopy
% Tamal Das 2014
```

```
% Clear memory
%clear all

[msm_flname, msm_pathname] = uigetfile('*.mat','Select the monolayer stress
file');
msm_flpathname = strcat(msm_pathname,msm_flname);
load(msm_flpathname);
k = strfind(msm_flpathname, '.mat');
svflname = msm_flpathname(1:k-1);

%Set minimum and Maximum of your Colormap below
cmin = -5;
cmax = 5;

% Retrieving the mesh information
xx=nodeCoordinates(:,1);
yy=nodeCoordinates(:,2);
numberNodes = size(xx,1);
numberNodesY = round(numberNodes/numberNodesX);
numberElementsX=numberNodesX-1;
numberElementsY=numberNodesY-1;
numberElements=numberElementsX*numberElementsY;

UX=displacements(1:numberNodes);
UY=displacements(numberNodes+1:GDof);

% Relevant output parameters: smax, smin, tau etc.
sXX=mean(stress(:,:,1),2);
nX = numberNodesY - 1; nY = numberNodesX - 1;
sXX2d = reshape(sXX, [nY nX]);
sYY = mean(stress(:,:,2),2);
sYY2d = reshape(sYY, [nY nX]);
tXY = mean(stress(:,:,3),2);
tXY2d = reshape(tXY, [nY nX]);
% smax = (abs(sXX)+abs(sYY))/2+(((abs(sXX)-abs(sYY))/2).^2+tXY.^2).^0.5;
% smax2d =  reshape(smax, [nY nX]);
% smin = (abs(sXX)+abs(sYY))/2-(((abs(sXX)-abs(sYY))/2).^2+tXY.^2).^0.5;
% smin2d =  reshape(smin, [nY nX]);
smax = (sXX+sYY)/2+(((sXX-sYY)/2).^2+tXY.^2).^0.5;
smax2d =  reshape(smax, [nY nX]);
smin = (sXX+sYY)/2-(((sXX-sYY)/2).^2+tXY.^2).^0.5;
smin2d =  reshape(smin, [nY nX]);
savg = -(smax + smin)/2;   % changed to negative sign to have compression =
positive = red on colorbar
savg2d = reshape(savg, [nY nX]);
tXY_max = (smax-smin)/2;
tXY_max2d =  reshape(tXY_max, [nY nX]);

%theta_p = atan(2*tXY./(sXX-sYY))/2;
theta_p = atan2(2*tXY, (sXX-sYY))/2;   % gives angle between y axis and the
major principal axis
%theta_p = atan2(2*tXY, -(sXX-sYY))/2;   % gives angle between x axis and
the major principal axis

%sXXf = stress(:,:,1); sYYf = stress(:,:,2); tXYf = stress(:,:,3);
%smaxf = (abs(sXXf)+abs(sYYf))/2+(((abs(sXXf)-
abs(sYYf))/2).^2+tXYf.^2).^0.5;
%sminf = (abs(sXXf)+abs(sYYf))/2-(((abs(sXXf)-
abs(sYYf))/2).^2+tXYf.^2).^0.5;
```

```
%savgf = (smaxf+sminf)/2;
%tXY_maxf = (smaxf-sminf)/2;

%figure
 %drawingField(nodeCoordinates,...
  %   elementNodes,'Q4',savgf);
 %colormap jet
 %colorbar
 %caxis([cmin cmax])
 %hold on

xcen = zeros(numberElements,1);
ycen = zeros(numberElements,1);

for i=1:numberElements

   xcen(i) = mean(xx(elementNodes(i,:)));
   ycen(i) = mean(yy(elementNodes(i,:)));

%    ra = 12;   % constant ra
%    rb = ra*smin(i)/smax(i);
%    ang = theta_p(i);
%    C = 'r';
%    Nb = 100;
%
%    ellipse_h = ellipse(ra,rb,ang,xcen(i),ycen(i),C,Nb);

end

save stressvalues xcen ycen savg tXY_max theta_p smin smax nY nX sXX sYY
tXY;

%save 3dstress savg2d;

%stressname= '3dstress';

save([svflname '_stressvalues.mat'], 'xcen', 'ycen', 'savg', ...
    'tXY_max','theta_p', 'smin', 'smax', 'nY', 'nX', 'sXX', 'sYY', 'tXY')

save([svflname '_3DStress.mat'],'savg2d');

figure
surf(savg2d)
%imshow(savg2d')
colormap parula
colorbar
caxis([cmin cmax])
shading Interp
zoom (3)
view([-40 62]);
box off
grid off
axis off

 %hold on
%Angle between stress ellipse and velocity vector

%[cd_flname, cd_pathname] = uigetfile('*.txt','Select the cell displacement
file');
```

```
%cd_flpathname = strcat(cd_pathname,cd_flname);
%CD = load(cd_flpathname);
 %dx = CD(:,3); dy = CD(:,4);

 %dx_el = zeros(numberElements,1); dy_el = zeros(numberElements,1);

 %for i=1:numberElements
    %dx_el(i) = mean(dx(elementNodes(i,:)));
     %dy_el(i) = mean(dy(elementNodes(i,:)));
%end

 %dx_el2d = reshape(dx_el, [nY nX]); dy_el2d = reshape(dy_el, [nY nX]);
 %qvX = xcen(1:1); qvY = qvX;
 %theta_v = atan(dy_el./dx_el);

 %quiver(qvX,qvY,dx_el2d',dy_el2d','w');
 %hold off

 %theta_diff = abs(abs(theta_p)-abs(theta_v))*180/pi;

  %figure
  %plot(tXY_max,theta_diff,'o');
  %> 60% quantiles of maximum shear stress
 %qtXY = quantile(tXY_max,4);
 %q2 = qtXY(3);
 %k = find(tXY_max>=q2);
 %q2_theta_diff = zeros(size(k,1));
 %q2_theta_diff = theta_diff(k);

%figure
 %h = rose(q2_theta_diff*pi/180,96);
 %xrose = get(h,'Xdata');
 %yrose = get(h,'Ydata');
 %g=patch(xrose,yrose,'y');

%load chirp, sound(y,1/2*Fs)
```

Monolayer stresses values extraction

Description:

This MATLAB script is designed to load stress data and perform analysis within a defined circular region of interest (ROI). The user can load pre-existing stress data, reshape it into a matrix, and calculate the mean and absolute mean stress values in the ROI. The results can be saved and appended to an existing dataset or stored in a new file.

Script (Stress_valuesROI_JDR_AK):

```
clear all
%If you run the Script for the first time, set InitN=1
initN = 1;

%load stressvalues in workspace
uiload;
%load corrisponding monolayer stress microscopy figure
uiopen('*.fig');
```

```
figure;
plot (xcen);

%insert matrix dimension from xcen or ycen frequency (combine xcen
frequency and x frequency / number
%of elements in ycen)

pause

StressV = reshape (savg,[75 90]);

if initN ~= 1
Data = load('StressValues.csv');
end

%insert xpos and ypos for center of ROI
xpos = 45;
ypos = 35;
rad = 63;
[ mean, ROI, cir_mask ] = CircROI_mean(StressV,[ypos xpos], rad);
[ absmean, ROI, cir_mask ] = CircROI_absmean(StressV,[ypos xpos], rad);
Res1 = ROI.*cir_mask;

mean;
absmean;

if  initN ~=1
    noround = Res1(Res1~=0);
    ROIstress = [Data(:,:), noround(:,:)];
    csvwrite('StressValues.csv', ROIstress);
else
    noround = Res1(Res1~=0);
    ROIstress = noround(:,:);
    csvwrite('StressValues.csv', ROIstress);

end

close all;
```

MATLAB scripts for analysis of correlation length of stress vectors

Calculation and visualization of correlation length of monolayer stresses

Description:

This MATLAB script calculates and visualizes the correlation length of stress data from a selected file. It computes the correlation function, fits it to an exponential decay model, and plots the results. The script also calculates correlation lengths based on the fitted model.

Script (Stress_CorrLenP):

```
% Output: xi_diameter = Correlation length as defined in our Merlin paper
% xi_radius = Correlation length following the definition C(r) = e^(-r/xi)
% Figure 1: Black Square = Actual Correlation Function;
```

```
% Red Dot = Fitted Correlation Function to a curve C(r) = e^(-r/xi)

% Approximate Run Time: 20X20 = 0.8s, 30X30 = 4s, 40X40 = 16s, 50X50 = 52s,
% 60X60 = 150s

% WARNING: Change the pixScale parameter for your image setting

clear all

pixScale = 0.8995; % micron/pixel
isNormal = 1;
setMax = 1000;

% Select the stress data file in the targeted folder and read its path and
file name
[flname, pathname] = uigetfile('*.mat','Select the stress file');
disp(flname)
flpathname = strcat(pathname,flname);
load(flpathname);
tic
datLen = length(savg);
totBoxCnt = datLen;

if isNormal == 1
    dsgma = savg - mean(savg);
    plotTitle = 'Correlation Function of Average Normal Stress';
else
    dsgma = tXY_max - mean(tXY_max);
    plotTitle = 'Correlation Function of Maximum Shear Stress';
end

combBoxCnt = totBoxCnt*(totBoxCnt-1)/2;
dr2 = zeros(combBoxCnt,1);
dsg1sq = zeros(combBoxCnt,1);
dsg2sq = zeros(combBoxCnt,1);
dsg1dsg2 = zeros(combBoxCnt,1);

theta_p_abs = zeros(totBoxCnt,1);
theta_p_abs = theta_p;
for i=1:totBoxCnt
    if theta_p(i)<0
        theta_p_abs(i)=pi+theta_p(i);
    end
end
p1sq = zeros(combBoxCnt,1); p2sq = zeros(combBoxCnt,1);
p1p2 = zeros(combBoxCnt,1);

pntCnt = 0;
for i=1:totBoxCnt
    % complete=i*100/totBoxCnt
    for j=i:totBoxCnt
    pntCnt = pntCnt + 1;
    dr2(pntCnt) = ((xcen(i)-xcen(j))^2 + (ycen(i)-ycen(j))^2);
    dsg1sq(pntCnt) = dsgma(i)^2; dsg2sq(pntCnt) = dsgma(j)^2;
dsg1dsg2(pntCnt) = dsgma(i)*dsgma(j);
    p1sq(pntCnt) = theta_p_abs(i)^2; p2sq(pntCnt)=theta_p_abs(j)^2;
    p1p2(pntCnt) = theta_p_abs(i)*theta_p_abs(j);
    end
end
```

```
[sq_r,avg_dsg1dsg2] = consolidator(dr2, dsg1dsg2,@mean);
i=1*(100/7)
[sq_r,rCnt] = consolidator(dr2, [],'count');
[sq_r,avg_dsg1] = consolidator(dr2, dsg1sq,@mean);
i=3*(100/7)
[sq_r,avg_dsg2] = consolidator(dr2, dsg2sq,@mean);
avg_dsg1 = abs(avg_dsg1); avg_dsg2 = abs(avg_dsg2);
[sq_r,avg_p1sq] = consolidator(dr2, p1sq,@mean);
i=5*(100/7)
[sq_r,avg_p2sq] = consolidator(dr2, p2sq,@mean);
[sq_r,avg_p1p2] = consolidator(dr2, p1p2,@mean);
i=7*(100/7)
avg_p1sq = abs(avg_p1sq); avg_p2sq = abs(avg_p2sq);

angleCorr = avg_p1p2./((avg_p1sq.*avg_p2sq).^0.5);
corrFunc = avg_dsg1dsg2./((avg_dsg1.*avg_dsg2).^0.5);
corrFuncMod = corrFunc.*angleCorr;

dr = (sq_r.^0.5)*pixScale;

figure(1)
plot(dr,corrFunc,'ks-');
set(gca,'FontSize',16,'fontWeight','bold')
hold on
plot(dr,corrFuncMod,'bo-');

% Curve fitting to exp(-dr): To evaluate xi = Correlation length
% truncCurve = 25 is an arbitrary value, which is to restrict the curve to
the
% exponential part of the correlation function
truncCurve = 25;
xdata = dr(1:truncCurve); ydata = corrFunc(1:truncCurve);
[estimates, model] = fitcurvedemo(xdata, ydata);

xi_diameter = -log(0.01)/estimates % Correlation function becomes 0.01,
which is approx. zero
xi_radius = 1/estimates % Correlation function becomes 1/e --> e^(-r/xi)

FittedCurve = exp(-dr*estimates);
plot(dr, FittedCurve,'r.-')

title(plotTitle,'FontSize',24,'FontWeight','bold','Color','k')
xlabel('r (\mum)','FontSize',24,'FontWeight','bold','Color','k');
ylabel('C(r)','FontSize',24,'FontWeight','bold','Color','k');
xaxmin = 0; xaxmax = 500; yaxmin = -1; yaxmax = 1.2;
axis([xaxmin xaxmax yaxmin yaxmax]);
corLineX(1:51) = xi_diameter; corLineY = yaxmin:(yaxmax-yaxmin)/50:yaxmax;
zeroLineY(1:(xaxmax-xaxmin)+1) = 0;
plot(xaxmin:1:xaxmax,zeroLineY,'b--');
plot(corLineX,corLineY,'b--');
hold off

slope = (corrFunc(truncCurve)-1)/(dr(truncCurve)-1);
exterpDia = -(1/slope) % Extrapolated from first 25 points slope

save CorrFuncFileM xi_diameter xi_radius dr corrFunc corrFuncMod
FittedCurve

toc
load chirp, sound(y,1/2*Fs)
```

Appendix 2.

Plasmid maps

Vector Summary

Vector ID	VB230129-1083pte
Vector Name	pAAV[shRNA]-mCherry-U6>hITGB1[shRNA#1]
Vector Size	5344 bp
Viral Genome Size	2205 bp
Vector Type	Mammalian shRNA Knockdown AAV Vector
Inserted ORF	mCherry
Inserted shRNA	hITGB1[shRNA#1]
Target Sequence	TTTGTAGGAAGAGGGATAATA
Plasmid Copy Number	High
Antibiotic Resistance	Ampicillin
Cloning Host	VB UltraStable (or alternative strain)

Vector map

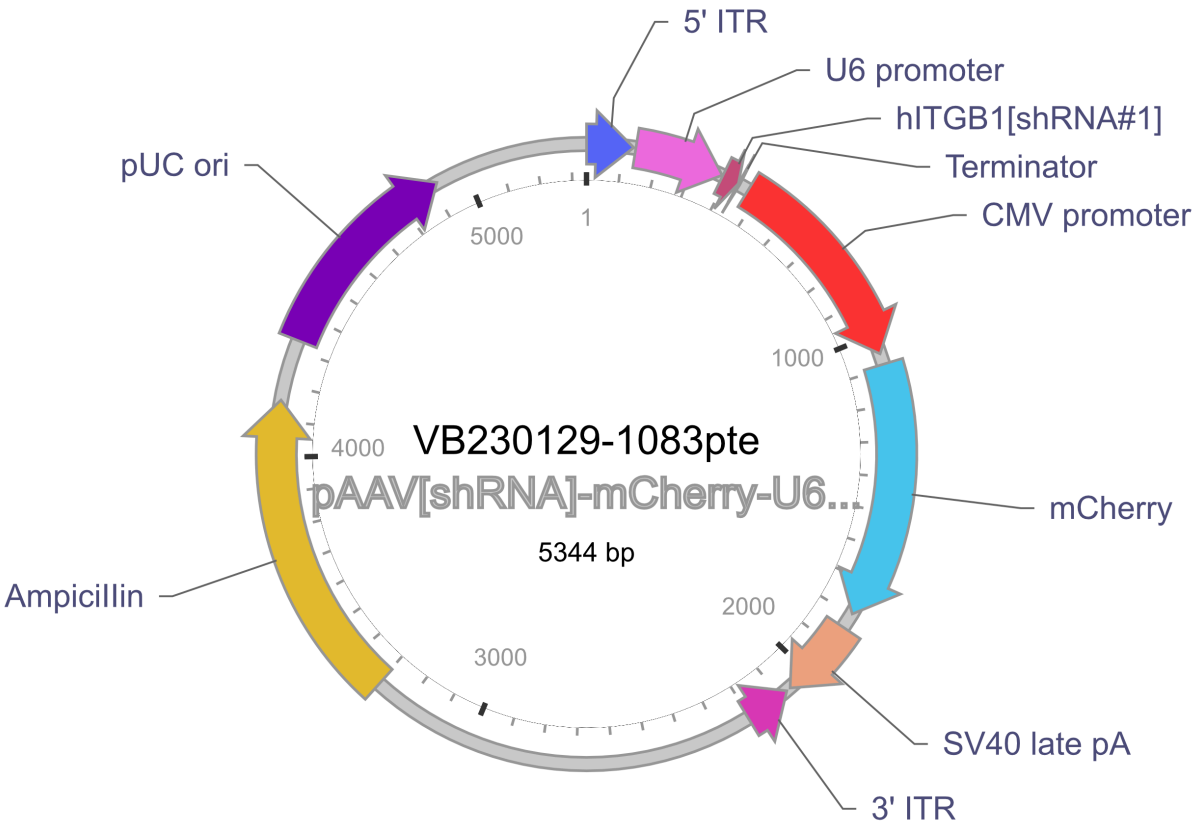

Vector Summary

Vector ID	VB230129-1084bae
Vector Name	pAAV[shRNA]-mCherry-U6>hITGB1[shRNA#2]
Vector Size	5344 bp
Viral Genome Size	2205 bp
Vector Type	Mammalian shRNA Knockdown AAV Vector
Inserted ORF	mCherry
Inserted shRNA	hITGB1[shRNA#2]
Target Sequence	TAGGTAGCTTTAGGGCAATAT
Plasmid Copy Number	High
Antibiotic Resistance	Ampicillin
Cloning Host	VB UltraStable (or alternative strain)

Vector map

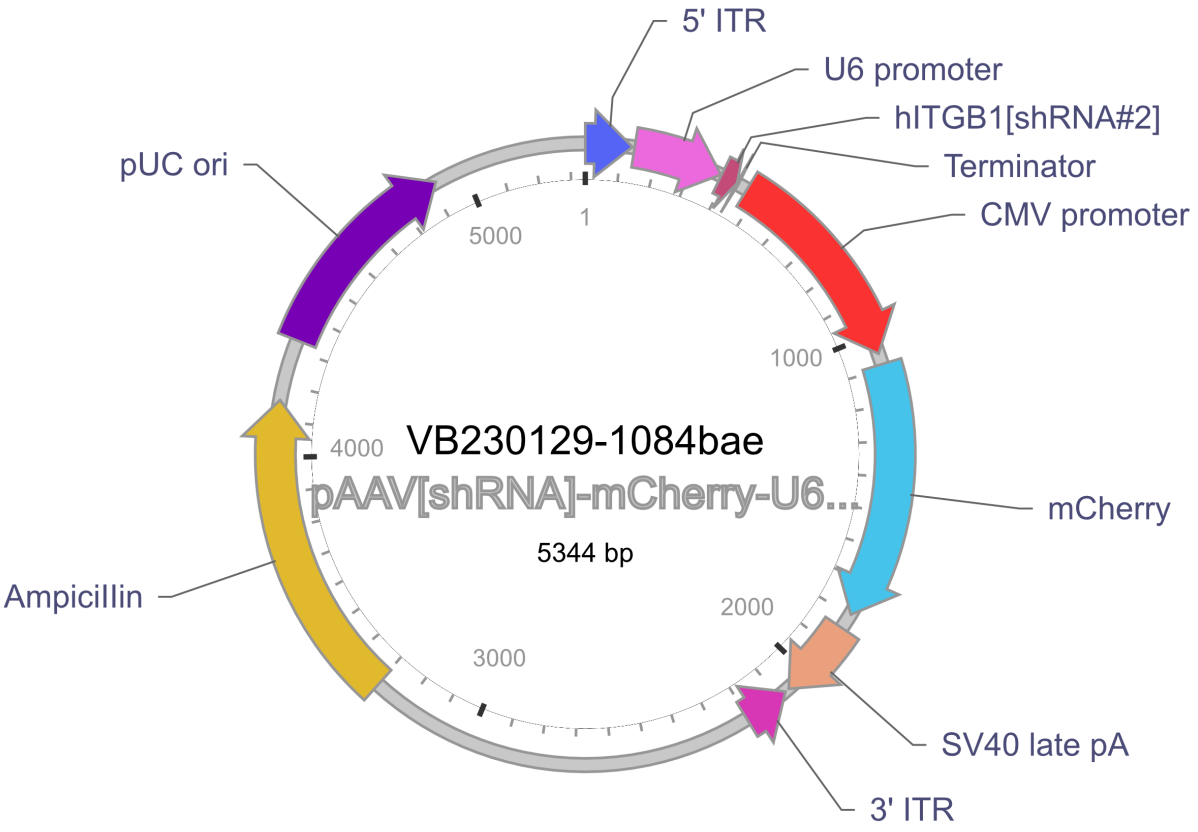

Vector Summary

Vector ID	VB230129-1085nbd
Vector Name	pAAV[shRNA]-mCherry-U6>hITGB1[shRNA#3]
Vector Size	5344 bp
Viral Genome Size	2205 bp
Vector Type	Mammalian shRNA Knockdown AAV Vector
Inserted ORF	mCherry
Inserted shRNA	hITGB1[shRNA#3]
Target Sequence	GCCTTGCATTACTGCTGATAT
Plasmid Copy Number	High
Antibiotic Resistance	Ampicillin
Cloning Host	VB UltraStable (or alternative strain)

Vector map

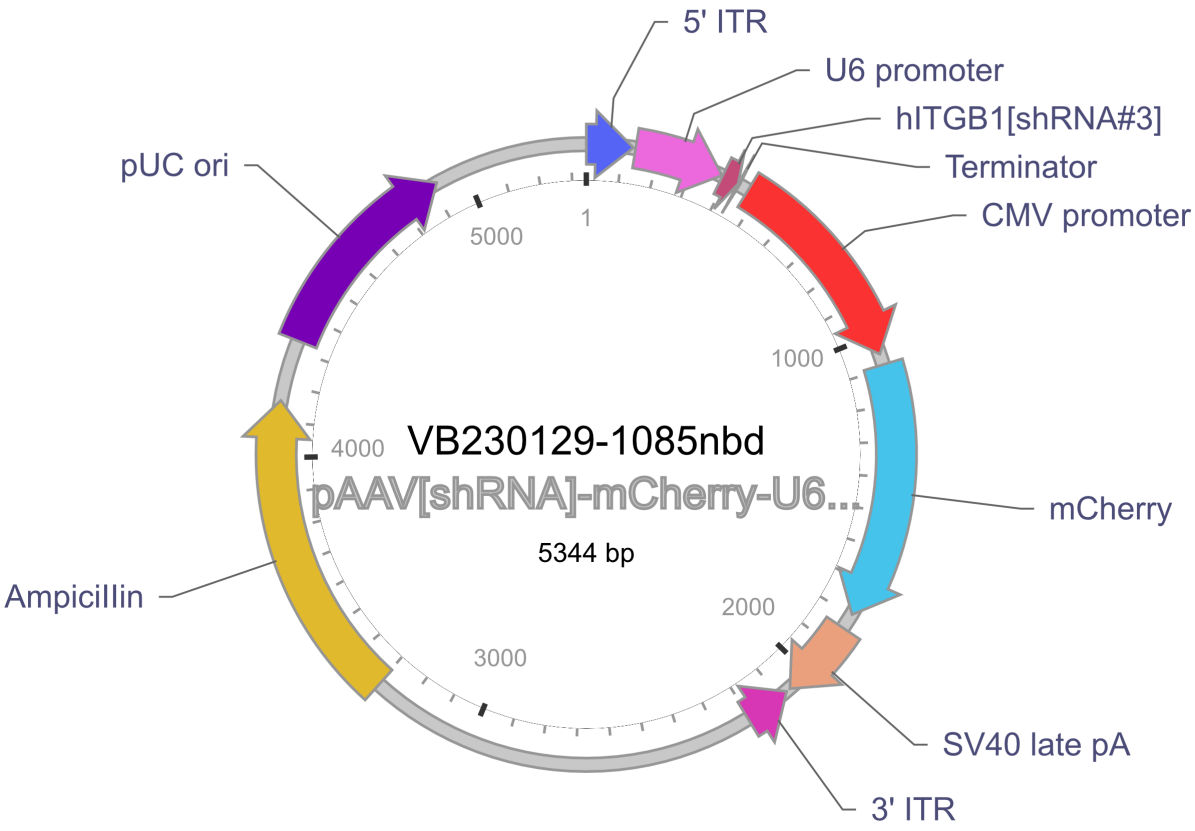

Vector Summary

Vector ID	VB010000-0024wah
Vector Name	pAAV[shRNA]-mCherry-U6>Scramble_shRNA
Vector Size	5344 bp
Viral Genome Size	2205 bp
Vector Type	Mammalian shRNA Knockdown AAV Vector
Inserted Marker	mCherry
Inserted shRNA	Scramble_shRNA#1
Target Sequence	CCTAAGGTTAAGTCGCCCTCG
Plasmid Copy Number	High
Antibiotic Resistance	Ampicillin
Cloning Host	VB UltraStable (or alternative strain)

Vector map